POLITECHNIKA GDAŃSKA

Imię i nazwisko autora rozprawy: mgr inż. Anna Grzegórska
Dyscyplina naukowa: Nauki Chemiczne

ROZPRAWA DOKTORSKA

Tytuł rozprawy w języku polskim: Projektowanie, synteza i charakterystyka fotokatalizatorów nowej generacji na bazie związku $Ti_3C_2T_x$ do usuwania aktywnych substancji farmaceutycznych

Tytuł rozprawy w języku angielskim: Design, synthesis and characterization of new-generation photocatalysts based on a $Ti_3C_2T_x$ for the degradation of active pharmaceutical ingredients

Promotor *podpis*
dr hab. inż. Anna Zielińska-Jurek, prof. PG

Gdańsk, 2023

POLITECHNIKA GDAŃSKA

OŚWIADCZENIE

Autor rozprawy doktorskiej: Anna Grzegórska

Ja, niżej podpisany(a), oświadczam, iż jestem świadomy(a), że zgodnie z przepisem art. 27 ust. 1 i 2 ustawy z dnia 4 lutego 1994 r. o prawie autorskim i prawach pokrewnych (t.j. Dz.U. z 2021 poz. 1062), uczelnia może korzystać z mojej rozprawy doktorskiej zatytułowanej:
Projektowanie, synteza i charakterystyka fotokatalizatorów nowej generacji na bazie związku $Ti_3C_2T_x$ do usuwania aktywnych substancji farmaceutycznych

do prowadzenia badań naukowych lub w celach dydaktycznych.[1]

Świadomy(a) odpowiedzialności karnej z tytułu naruszenia przepisów ustawy z dnia 4 lutego 1994 r. o prawie autorskim i prawach pokrewnych i konsekwencji dyscyplinarnych określonych w ustawie Prawo o szkolnictwie wyższym i nauce (Dz.U.2021.478 t.j.), a także odpowiedzialności cywilno-prawnej oświadczam, że przedkładana rozprawa doktorska została napisana przeze mnie samodzielnie.

Oświadczam, że treść rozprawy opracowana została na podstawie wyników badań prowadzonych pod kierunkiem i w ścisłej współpracy z promotorem dr hab. inż. Anną Zielińska-Jurek, prof. PG.

Niniejsza rozprawa doktorska nie była wcześniej podstawą żadnej innej urzędowej procedury związanej z nadaniem stopnia doktora.

Wszystkie informacje umieszczone w ww. rozprawie uzyskane ze źródeł pisanych i elektronicznych, zostały udokumentowane w wykazie literatury odpowiednimi odnośnikami, zgodnie z przepisem art. 34 ustawy o prawie autorskim i prawach pokrewnych.

Potwierdzam zgodność niniejszej wersji pracy doktorskiej z załączoną wersją elektroniczną.

Gdańsk, dnia ....

podpis doktoranta

Ja, niżej podpisany(a), wyrażam zgodę/nie wyrażam zgody* na umieszczenie ww. rozprawy doktorskiej w wersji elektronicznej w otwartym, cyfrowym repozytorium instytucjonalnym Politechniki Gdańskiej.

Gdańsk, dnia ....

podpis doktoranta

[1] Art. 27. 1. Instytucje oświatowe oraz podmioty, o których mowa w art. 7 ust. 1 pkt 1, 2 i 4–8 ustawy z dnia 20 lipca 2018 r. – Prawo o szkolnictwie wyższym i nauce, mogą na potrzeby zilustrowania treści przekazywanych w celach dydaktycznych lub w celu prowadzenia działalności naukowej korzystać z rozpowszechnionych utworów w oryginale i w tłumaczeniu oraz zwielokrotniać w tym celu rozpowszechnione drobne utwory lub fragmenty większych utworów.
2. W przypadku publicznego udostępniania utworów w taki sposób, aby każdy mógł mieć do nich dostęp w miejscu i czasie przez siebie wybranym korzystanie, o którym mowa w ust. 1, jest dozwolone wyłącznie dla ograniczonego kręgu osób uczących się, nauczających lub prowadzących badania naukowe, zidentyfikowanych przez podmioty wymienione w ust. 1.

POLITECHNIKA GDAŃSKA

OPIS ROZPRAWY DOKTORSKIEJ

Autor rozprawy doktorskiej: Anna Grzegórska

Tytuł rozprawy doktorskiej w języku polskim: Projektowanie, synteza i charakterystyka fotokatalizatorów nowej generacji na bazie związku $Ti_3C_2T_x$ do usuwania aktywnych substancji farmaceutycznych

Tytuł rozprawy w języku angielskim: Design, synthesis and characterization of new generation photocatalysts based on a $Ti_3C_2T_x$ for the degradation of active pharmaceutical ingredients

Język rozprawy doktorskiej: polski

Promotor rozprawy doktorskiej: dr hab. inż. Anna Zielińska-Jurek, prof. PG

Data obrony:

Słowa kluczowe rozprawy doktorskiej w języku polskim: aktywne substancje farmaceutyczne, fotokataliza, MXeny, tlenek tytanu(IV)

Słowa kluczowe rozprawy doktorskiej w języku angielskim: active pharmaceutical ingredients, MXene, photocatalysis, titanium(IV) oxide

Streszczenie rozprawy w języku polskim: Celem niniejszej pracy było zastosowanie materiałów nowej generacji na bazie związku $Ti_3C_2T_x$ w procesach fotokatalitycznej degradacji aktywnych substancji farmaceutycznych: karbamazepiny, acetaminofenu i ibuprofenu. Zakres prac badawczych obejmował syntezę fotokatalizatorów, charakterystykę ich właściwości fizykochemicznych, oraz ocenę aktywności fotokatalitycznej. Przedstawiono możliwość zastosowania węglika tytanu jako kokatalizatora procesów fotokatalitycznych oraz prekursora do otrzymania kompozytu TiO_2/Ti_3C_2. Ponadto zaproponowano metody modyfikacji kompozytów TiO_2/Ti_3C_2 za pomocą metali takich jak żelazo i miedź oraz związku z grupy ferrytów spinelowych – $MnFe_2O_4$, celem poprawy ich właściwości. Modyfikacja powierzchni kompoztów za pomocą metali prowadziła do osiągnięcia wyższej aktywności fotokatalitycznej degradacji farmaceutyków w świetle UV-vis. Dzięki wprowadzeniu nanocząstek magnetycznych $MnFe_2O_4$ możliwa była efektywna separacja fotokatalizatora po procesie. Finalnie, synergizm degradacji substancji farmaceutycznych uzyskano w wyniku kombinacji procesu fotokatalizy z aktywacją nadtlenomonosiarczanu za pomocą Cu lub $MnFe_2O_4$, prowadzącą do wytworzenia reaktywnych rodników siarczanowych.

Streszczenie rozprawy w języku angielskim: This study aimed to use new-generation materials based on $Ti_3C_2T_x$ for the photocatalytic degradation of pharmaceuticals: carbamazepine, acetaminophen, and ibuprofen. The scope of this research includes synthesizing photocatalysts, characterization of their physicochemical properties, and assessment of photocatalytic activity. The possibility of using titanium carbide as a cocatalyst for photocatalytic processes and as a precursor to obtain TiO_2/Ti_3C_2 composites was presented. Moreover, methods of modifying TiO_2/Ti_3C_2 composites with metal particles, such as iron and copper, and a compound from the spinel ferrite group ($MnFe_2O_4$) have been proposed to improve their properties. Modification of the surface of the composites with metals led to higher photocatalytic activity for the degradation of pharmaceutical substances under UV-vis irradiation. Meanwhile, owing to the introduction of magnetic $MnFe_2O_4$ nanoparticles, the effective separation of the photocatalyst after the process was possible. Finally, synergism for the degradation of pharmaceutical substances was obtained as a result of the combination of photocatalysis and the activation of peroxymonosulfate with Cu or $MnFe_2O_4$, leading to the production of highly reactive sulfate radicals.

Podziękowania

Serdeczne podziękowania składam mojej Promotor dr hab. inż. Annie Zielińskiej-Jurek za niezwykle cenną wiedzę, motywację i wsparcie, którego udzielała mi przez cały okres trwania studiów doktoranckich jak i w trakcie przygotowań rozprawy doktorskiej.

Dziękuję również wszystkim Współpracownikom z Katedry Inżynierii Procesowej i Technologii Chemicznej za wszelką pomoc, rady, i przyjazną atmosferę. W szczególności dziękuję dr inż. Izabeli Wysockiej, za nieocenioną pomoc w trakcie prac badawczych, wsparcie, oraz wszelkie wskazówki.

Z całego serca chciałabym podziękować również moim Rodzicom, Siostrze oraz Przyjaciołom za nieustanne zrozumienie i motywację. Dziękuję, że zawsze jesteście obok mnie i wspieracie mnie w każdej decyzji. To dzięki Wam udało mi się osiągnąć ten cel.

Spis treści

Dorobek naukowy

Publikacje wchodzące w skład rozprawy doktorskiej:

1. A. Grzegórska, I. Wysocka, P. Głuchowski, J. Ryl, J. Karczewski, A. Zielińska-Jurek, Novel composite of Zn/Ti-layered double hydroxide coupled with MXene for the efficient photocatalytic degradation of pharmaceuticals, Chemosphere 308 (2022) 136191. https://doi.org/10.1016/j.chemosphere.2022.136191

   Punktacja MNiSW=140, IF_{2022}=8,8

2. A. Grzegórska, P. Głuchowski, J. Karczewski, J. Ryl, I. Wysocka, K. Siuzdak, G. Trykowski, K. Grochowska, A. Zielińska-Jurek, Enhanced photocatalytic activity of accordion-like layered Ti_3C_2 (MXene) coupled with Fe-modified decahedral anatase particles exposing {101} and {001} facets, Chem. Eng. J. 426 (2021) 130801. https://doi.org/10.1016/j.cej.2021.130801

   Punktacja MNiSW=200, IF_{2021}=16,744

3. A. Grzegórska, A. Gajewicz-Skrętna, G. Trykowski, K. Sikora, A. Zielińska-Jurek, Design and synthesis of TiO_2/Ti_3C_2 composites for highly efficient photocatalytic removal of acetaminophen: The relationships between synthesis parameters, physicochemical properties, and photocatalytic activity. Catal. Today 413-415 (2023) 113980. https://doi.org/10.1016/j.cattod.2022.12.011

   Punktacja MNiSW=140, IF_{2022}=5,3

4. A. Grzegórska, J. Chibueze Ofoegbu, L. Cervera-Gabalda, C. Gómez-Polo, D. Sannino, A. Zielińska-Jurek, Magnetically recyclable TiO_2/MXene/$MnFe_2O_4$ photocatalyst for enhanced peroxymonosulphate-assisted photocatalytic degradation of carbamazepine and ibuprofen under simulated solar light. J. Environ. Chem. Eng. 11 (2023) 110660. https://doi.org/10.1016/j.jece.2023.110660

   Punktacja MNiSW=140, IF_{2022}=7,968

5. A. Grzegórska, J. Karczewski, A. Zielińska-Jurek, Modelling and optimisation of MXene-derived TiO_2/Ti_3C_2 synthesis parameters using Response Surface Methodology based on the Box–Behnken factorial design. Enhanced carbamazepine degradation by the Cu-modified TiO_2/Ti_3C_2 photocatalyst, Process Saf. Environ. Prot. 179 (2023) 449. https://doi.org/10.1016/j.psep.2023.09.028

   Punktacja MNiSW=100, IF_{2022}=7,8

   Sumaryczna wartość IF dla prac [P1] - [P5] to: **46,612**
   Sumaryczna wartość punktów MNiSW to: **720**

Pozostałe publikacje:

1. A. Grzegórska, P. Rybarczyk, A. Rogala, D. Zabrocki, Phytoremediation—From Environment Cleaning to Energy Generation—Current Status and Future Perspectives. Energies 13 (2020) 2905. https://doi.org/10.3390/en13112905

   Punktacja MNiSW=140, IF_{2020}=3,004

2. A. Grzegórska, P. Rybarczyk, V. Lukoševičius, J. Sobczak, A. Rogala, Smart Asset Management for District Heating Systems in the Baltic Sea Region. Energies 14 (2021) 314. https://doi.org/10.3390/en14020314

   Punktacja MNiSW=140, IF_{2021}=3,252

3. N. Czaplicka, A. Grzegórska, J. Wajs, J. Sobczak, A. Rogala, Promising Nanoparticle-Based Heat Transfer Fluids—Environmental and Techno-Economic Analysis Compared to Conventional Fluids. Int. J. Mol. Sci. 22 (2021) 9201. https://doi.org/10.3390/ijms22179201

   Punktacja MNiSW=140, IF_{2021}=6,208

4. M. Kowalkińska, A. Fiszka Borzyszkowska, A. Grzegórska, J. Karczewski, P. Głuchowski, M. Łapiński, M. Sawczak, A. Zielińska-Jurek, Pilot-Scale Studies of WO_3/S-Doped g-C_3N_4 Heterojunction toward Photocatalytic NO_x Removal. Materials 15 (2022) 633. https://doi.org/10.3390/ma15020633

   Punktacja MNiSW=140, IF_{2022}=3,4

5. A. Kubiak, A. Grzegórska, J. Zembrzuska, A. Zielińska-Jurek, K. Siwińska-Ciesielczyk, M. Janczarek, P. Krawczyk, T. Jesionowski, Design and Microwave-Assisted Synthesis of TiO_2-Lanthanides Systems and Evaluation of Photocatalytic Activity under UV-LED Light Irradiation. Catalysts 12 (2023) 8. https://doi.org/10.3390/catal12010008

   Punktacja MNiSW=100, IF_{2022}=3,9

6. A. Kubiak, A. Grzegórska, E. Gabała, J. Zembrzuska, M. Szybowicz, H. Fuks, A. Szymczyk, A. Zielińska-Jurek, M. Sikorski, T. Jesionowski, TiO_2-C nanocomposite synthesized via facile surfactant-assisted method as a part of less energy-consuming LED-based photocatalytic system for environmental applications. J. Photochem. Photobiol., A 437 (2023) 114428. https://doi.org/10.1016/j.jphotochem.2022.114428

   Punktacja MNiSW=70, IF_{2022}=4,3

7. A. Grzegórska, N. Czaplicka, J. Antonkiewicz, P. Rybarczyk, A. Baran, K. Dobrzyński, D. Zabrocki, A. Rogala, Remediation of soils on municipal rendering plant territories using Miscanthus × giganteus. Environ. Sci. Pollut. Res. 30 (2023) 22305. https://doi.org/10.1007/s11356-022-23724-z

   Punktacja MNiSW=100, IF_{2022}=5,8

8. A. Kubiak, A. Grzegórska, E. Gabała, J. Zembrzuska, A. Zielińska-Jurek, M. Cegłowski, Unraveling a novel microwave strategy to fabricate exposed {001}/{101} facets anatase nanocrystals: Potential for use to the elimination of environmentally toxic metronidazole waste, Mater. Res. Bull. 167 (2023) 112438. https://doi.org/10.1016/j.materresbull.2023.112438

   Punktacja MNiSW=100, IF_{2022}=5,4

Sumaryczna wartość IF wszystkich moich prac to: **81,876**
Sumaryczna wartość punktów MNiSW wszystkich moich prac to: **1650**
Indeks Hirscha według bazy Scopus: 6

Udział w grantach:

1. Projektowanie, synteza oraz badanie struktur 2D fotokatalizatorów hybrydowych do degradacji farmaceutyków w fazie wodnej (NCN SONATA BIS)
2. Ekologiczne asfalty (Program Operacyjny Inteligentny Rozwój) w Konsorcjum z ORLEN S.A.
3. Improving quality of BSR waters by advanced treatment processes, Interreg BSR (Europejska Współpraca Terytorialna 2021-2025)
4. Projektowanie i synteza multifunkcjonalnych materiałów do termo-fotokatalitycznej redukcji dwutlenku węgla oraz fotodegradacji trwałych zanieczyszczeń organicznych (NCN OPUS)
5. Baltic Phytoremediation (Europejska Współpraca Terytorialna)
6. Baltic Smart Asset Management (Europejska Współpraca Terytorialna)

Udział w konferencjach:

1. A. Grzegórska, A. Zielińska-Jurek, *Boosting the synthesis conditions of novel TiO_2/Ti_3C_2 composite for efficient photocatalytic degradation of acetaminophen*, 11th European Conference on Solar Chemistry and Photocatalysis: Environmental Applications, Turyn, Włochy, 06-10.06.2022 – prezentacja ustna
2. A. Grzegórska, I. Wysocka, A. Zielińska-Jurek, *Coupling of Zn/Ti-layered double hydroxide with novel MXene compound for efficient photocatalytic removal of pharmaceuticals*, 15th Pannonian International Symposium on Catalysis, Jastrzębia Góra, Polska, 04-08.09.2022– poster
3. A. Grzegórska, A. Zielińska-Jurek, *The synergistic process of photocatalysis coupled with PMS activation using novel TiO_2/MXene/$MnFe_2O_4$ magnetic composite towards effective removal of pharmaceuticals*, 24. Ogólnopolska Konferencja Inżynierii Chemicznej i Procesowej, Szczecin, Polska, 13-16.06.2023 – poster

Staż naukowo-badawczy

03.2022-05.2022; Uniwersytet w Strasburgu (ICPEES), Strasburg, Francja; opiekun stażu: prof. Nicolas Keller, tematyka: Badania nad modyfikacją związków z grupy MXenów i ich zastosowaniem w procesach foto-termo-katalitycznych.

Wykaz skrótów i oznaczeń

ACT – acetaminofen, N-(4-hydroksyfenylo)acetamid

AOP – zaawansowane procesy utleniania (z ang. advanced oxidation processes)

API – aktywne substancje farmaceutyczne (z ang. active pharmaceutical ingredients)

CB – pasmo przewodnictwa (z ang . conduction band)

CBZ – karbamazepina, 5H-dibenzo[b,f]azepino-5-karboksyamid

DR/UV-vis – spektroskopia odbicia rozproszonego w zakresie ultrafioletu i światła widzialnego (z ang. UV–vis diffuse reflectance spectroscopy)

EIS – elektrochemiczna spektroskopia impedancyjna (z ang. electrochemical impedance spectroscopy)

FTIR – spektroskopia w podczerwieni z transformacją Fouriera (z ang. Fourier-transform infrared spectroscopy)

IBP – ibuprofen, kwas (RS)-2-[4-(2-metylopropylo)fenylo]propanowy

LDH – warstwowe podwójne wodorotlenki (z ang. layered double hydroxide)

LSPR – zlokalizowany powierzchniowy rezonans plazmonowy (z ang. localized surface plasmon resonance)

LZO – lotne związki organiczne

MO – tlenek metalu (z ang. metal oxide)

NIR – bliska podczerwień (z ang. near-infrared)

NLPZ – niesteroidowe leki przeciwzapalne

P25 – komercyjny tlenek tytanu (IV) produkowany przez firmę Evonik (Niemcy)

PMS – nadtlenomonosiarczan potasu (z ang. potassium peroxymonosulphate) o wzorze $KHSO_5 \cdot 0{,}5KHSO_4 \cdot 0{,}5K_2SO_4$

ROS – reaktywne formy tlenu (z ang. reactive oxygen species)

RQ – iloraz ryzyka (z ang. risk quotient)

SEM – skaningowa mikroskopia elektronowa (z ang. scanning electron microscopy)

TEM – transmisyjna mikroskopia elektronowa (z ang. transmission electron microscopy)

UE – Unia Europejska

UV – promieniowanie ultrafioletowe (z ang. ultraviolet)

VB – pasmo walencyjne (z ang . valence band)

XPS – spektroskopia fotoelektronów w zakresie promieniowania X (z ang. X-ray photoelectron spectroscopy)

Rozdział I. Wstęp

1. Problem zanieczyszczenia wód

Jednym z wyzwań współczesnego świata jest zapewnienie dostępu do czystej wody. Wzrost demograficzny sprawia, że zapotrzebowanie na wodę jest coraz większe, a zmiany klimatyczne, rosnąca antropopresja i związane z nią zanieczyszczenie zasobów wodnych powodują, że zasoby te systematycznie maleją. Zgodnie z prognozami Organizacji Narodów Zjednoczonych (ONZ) do 2050 roku zapotrzebowanie na wodę wzrośnie dwukrotnie, a w ciągu najbliższych lat dostępność wody zdatnej do spożycia może zmniejszyć się nawet o 40% [1]. W związku z tym, czystość i jakość wód jest jednym z najważniejszych wyzwań globalnych XXI wieku.

Przede wszystkim rozwój przemysłu, rolnictwa, czy wzrost urbanizacji, a więc czynniki antropogeniczne, przyczyniają się do wyższego zanieczyszczenia wód, stanowiąc zagrożenie dla zdrowia ludzi oraz ekosystemów. Do głównych zanieczyszczeń należą barwniki, jony metali ciężkich, związki powierzchniowo czynne, pestycydy, petrochemikalia, mikroplastiki oraz aktywne substancje farmaceutyczne [2]. Zastosowanie konwencjonalnych metod oczyszczania ścieków, nie zawsze jest wystarczające wobec niektórych grup zanieczyszczeń, między innymi takich jak substancje farmaceutyczne niepodatne na rozkład biologiczny. W raporcie Komisji Ochrony Środowiska Morskiego Bałtyku (HELCOM) „*Pharmaceuticals in the aquatic environment of the Baltic Sea region*" [3] z 2017 roku stwierdzono, że tylko 9 z 118 analizowanych substancji farmaceutycznych było efektywnie usuwane (>95%) ze ścieków podczas procesu oczyszczania, z kolei dla blisko połowy związków efektywność oczyszczania wynosiła poniżej 50%.

Aktywne substancje farmaceutyczne (API) są jedną z najważniejszych i najobszerniejszych grup związków należących do potencjalnych antropogenicznych źródeł zanieczyszczenia wody. API są powszechnie wykrywane w wodach powierzchniowych, wodach gruntowych, czy wodzie pitnej. Ich stężenie w ekosystemach wodnych mieści się w zakresie od nanogramów na decymetr sześcienny do mikrogramów na decymetr sześcienny i co istotne, z roku na rok rośnie [4]. Zanieczyszczenia te mogą pochodzić z różnych źródeł. W szczególności, z odpadów poprodukcyjnych w zakładach farmaceutycznych, co wynika z braku regulacji prawnych w zakresie dopuszczalnych stężeń API w ściekach, jak również stosowania często nieefektywnych metod ich usuwania po procesie produkcyjnym. Także ścieki komunalne, a w szczególności ścieki szpitalne, zawierają duże zawartości substancji farmaceutycznych wydalanych z organizmu, w formie niezmienionej lub w postaci ich metabolitów. Źródłem

substancji farmaceutycznych w wodzie są także przeterminowane leki, które często zamiast prawidłowej utylizacji trafiają do ścieków.

Jedne z najnowszych badań przeprowadzonych w Polsce w 2022 roku przez Kucharskiego i współautorów [5] wykazały obecność 130 aktywnych substancji farmaceutycznych w osadach pobranych z 70 punktów zlokalizowanych na Zalewie Szczecińskim. Najwyższe poziomy stężeń zidentyfikowano w pobliżu miejsc zrzutu ścieków z oczyszczalni, portu i stoczni. Jako najczęściej występujące farmaceutyki zidentyfikowano: amisulpryd – lek przeciwpsychotyczny, karbamazepinę – lek przeciwpadaczkowy, bisoprolol – lek beta-adrenolityczny, oraz klindamycynę – antybiotyk. Natomiast najwyższe średnie stężenia zidentyfikowano dla metoprololu - leku beta-adrenolitycznego oraz sulpirydu – leku przeciwpsychotycznego. Stężenia oznaczonych API mieściły się w zakresie od 5 ng/g do 120 ng/g [5].

Aktywne substancje farmaceutyczne stanowią szczególne zagrożenie, gdyż mogą wykazywać aktywność farmaceutyczną, a ich metabolity często wykazują wyższą toksyczność niż związek macierzysty. W znacznym stopniu są to związki trudno degradowalne, a także co istotne niepodatne na rozkład biologiczny w konwencjonalnych oczyszczalniach ścieków. Ponadto, w środowisku ulegają procesom *bioakumulacji* czyli gromadzeniu w tkankach organizmów roślinnych i zwierzęcych oraz *biomagnifikacji* czyli wzrostowi stężenia danej substancji w następujących po sobie ogniwach łańcucha pokarmowego na kolejnych poziomach troficznych. Obecność substancji farmaceutycznych potwierdzono między innymi w roślinach jadalnych, takich jak ogórek, cebula, sałata, kukurydza oraz w tkankach ryb [6,7].

Występowanie farmaceutyków w środowisku ma kluczowe znaczenie i budzi obawy ponieważ zakres ich zagrożenia, a także wpływ na zdrowie ludzi, faunę i florę jest w dużej mierze nieznany. Substancje farmaceutyczne i ich pochodne mogą wywoływać niepożądane efekty biologiczne wśród organizmów żywych. Liczne badania potwierdziły, że mogą wykazywać działanie mutagenne, kancerogenne czy neurotoksyczne [4]. Ponadto, niektóre substancje farmaceutyczne mogą zakłócać działanie układu hormonalnego lub powodować zaburzenia reprodukcji [8]. Co ważne, dla mieszaniny różnych substancji farmaceutycznych, w wyniku szeregu interakcji zachodzących między nimi, może występować tak zwany synergiczny efekt toksyczności.

Obecnie nie ma regulacji prawnych określających dozwolone maksymalne stężenia substancji farmaceutycznych w środowisku [9]. Niemniej jednak problem ten jest coraz częściej identyfikowany i podejmowanych jest coraz więcej działań mających na celu zwrócenie uwagi na konieczność redukcji stężeń API oraz monitorowanie narażenia na skutek

długotrwałej ekspozycji. Między innymi w Stanach Zjednoczonych, Agencja Ochrony Środowiska (EPA) ustanowiła wytyczne dotyczące bezpiecznych poziomów niektórych leków w wodzie pitnej i opracowała program monitorowania farmaceutyków w ściekach [10]. Ponadto, Agencja Ochrony Środowiska i Agencja ds. Żywności i Leków (FDA) wydały wytyczne dotyczące bezpiecznego usuwania niezużytych leków oraz wdrażania programów zwrotu leków [11]. Dyrektywa Unii Europejskiej 2013/39/UE uznaje zanieczyszczenie wody pozostałościami substancji farmaceutycznych za pojawiający się problem środowiskowy [12]. Substancje takie jak diklofenak, 17-betaestradiol, 17-alfa-etynyloestradiol i estron oraz trzy antybiotyki makrolidowe: erytromycyna, klarytromycyna i azytromycyna znajdują się na tak zwanej „Liście Obserwacyjnej". Ma to na celu gromadzenie danych dotyczących monitorowania środowiska wodnego w Unii Europejskiej. To z kolei pozwala na dobór odpowiednich środków, aby rozwiązać problem zagrożenia, jakie te substancje stanowią.

W związku z tym, wprowadzenie monitoringu i identyfikacji występujących substancji farmaceutycznych oraz ścieżek ich przemian w środowisku, a także systemu zarządzania zanieczyszczonymi akwenami, stanowi szczególnie istotny aspekt w procesie poprawy jakości wody. Ponadto, poszukiwanie efektywnych, przyjaznych dla środowiska i uzasadnionych z punktu widzenia ekonomicznego procesów oczyszczania ścieków jest kluczowe w odniesieniu do ograniczenia stężenia środków farmaceutycznych w ściekach i wodach powierzchniowych.

2. Charakterystyka wybranych aktywnych substancji farmaceutycznych

Liczne badania wskazują, że karbamazepina, ibuprofen, oraz acetaminofen należą do farmaceutyków powszechnie wykrywanych w ekosystemach wodnych na całym świecie [13]. Ponadto, karabamazepina uznawana jest za antropogeniczny marker jakości wody, ze względu na trwałość, niepodatność na rozkład biologiczny w konwencjonalnych oczyszczalniach ścieków, jak i powszechną obecność w zbiornikach wodnych [14].

2.1. Właściwości i zastosowanie

Wzory strukturalne wybranych substancji farmaceutycznych przedstawiono na Rysunku 1. Karbamazepina - 5H-dibenzo[b,f]azepino-5-karboksyamid, należy do grupy leków przeciwpadaczkowych. Z kolei ibuprofen - kwas (RS)-2-[4-(2-metylopropylo)fenylo]propanowy należy do grupy niesteroidowych leków przeciwzapalnych. Acetaminofen - N-(4-

hydroksyfenylo)acetamid, powszechnie znany jako paracetamol, to lek o działaniu przeciwbólowym i przeciwgorączkowym. Jednakże w odróżnieniu od typowych niesteroidowych leków przeciwzapalnych (NLPZ), acetaminofen wykazuje bardzo słabe działanie przeciwzapalne. W Tabeli 1 porównano podstawowe właściwości aktywnych substancji farmaceutycznych: karbamazepiny, ibuprofenu, oraz acetaminofenu.

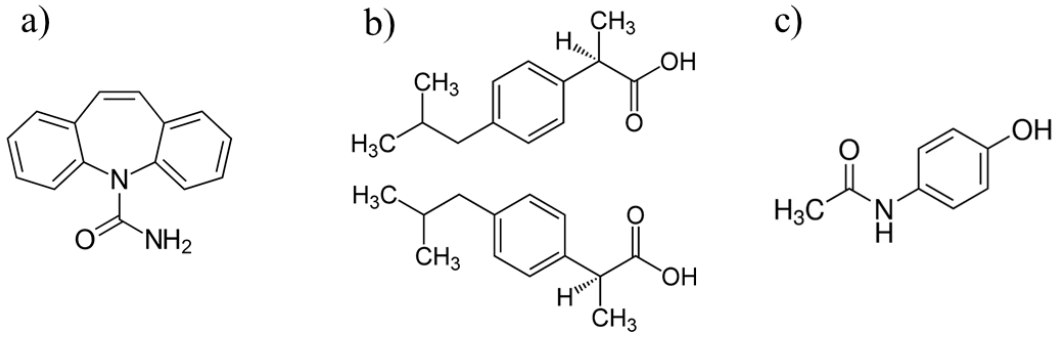

Rysunek 1. Wzór strukturalny karbamazepiny (a), ibuprofenu (b) i acetaminofenu (c)

Tabela 1. Zestawienie właściwości karbamazepiny, ibuprofenu, i acetaminofenu

Właściwości	*Karbamazepina*	*Ibuprofen*	*Acetaminofen*
Masa	236,27 g/mol	206,13 g/mol	151,16 g/mol
pKa	15,96	4,85	9,46
Rozpuszczalność w wodzie	0,15 g/dm^3	0,068 g/dm^3	4,15 g/dm^3
Biodostępność po podaniu doustnym	85% [15]	99% [16]	79% [17]
Produkty metabolizmu	10,11-epoksyd karbamazepiny [15]	hydroksyibuprofen, karboksyibuprofen, [16]	glukuronid acetaminofenu, siarczan acetaminofenu, N-Acetylo-p-benzochinonoimina [18]
Okres półtrwania w środowisku	71-93 dni [19]	5–32 dni [20]	1-2 dni [21]
Podatność na usuwanie w konwencjonalnych oczyszczalniach ścieków	<10% [22]	Około 90% [23]	86-100% [24]

2.2. Stężenia w ekosystemach wodnych

Na podstawie raportu „*Pharmaceuticals in the aquatic environment of the Baltic Sea region*", sporządzonego przez HELCOM [3] i opublikowanego w 2017, acetaminofen, ibuprofen i karbamazepina należą do grupy 20 najczęściej sprzedawanych leków w krajach regionu Morza Bałtyckiego. Ponadto, związki te należą do grupy 20 substancji farmaceutycznych występujących w najwyższym stężeniu w ściekach wypływających z oczyszczalni ścieków, co

przedstawiono na Rysunku 2. Wszystkie trzy substancje wykryto zarówno w ściekach wypływających z oczyszczalni, jak i w wodzie morskiej (Rysunek 2 i 4). Najwyższe stężenie odnotowano dla acetaminofenu (powyżej 500 µg/dm^3 w wodzie z oczyszczalni i powyżej 0,5 µg/dm^3 w wodzie morskiej). Ponadto, ACT i CBZ wykryto także w wodzie rzecznej (Rysunek 3). W tych akwenach najwyższe stężenie zaobserwowano dla karbamazepiny (około 5000 µg/dm^3).

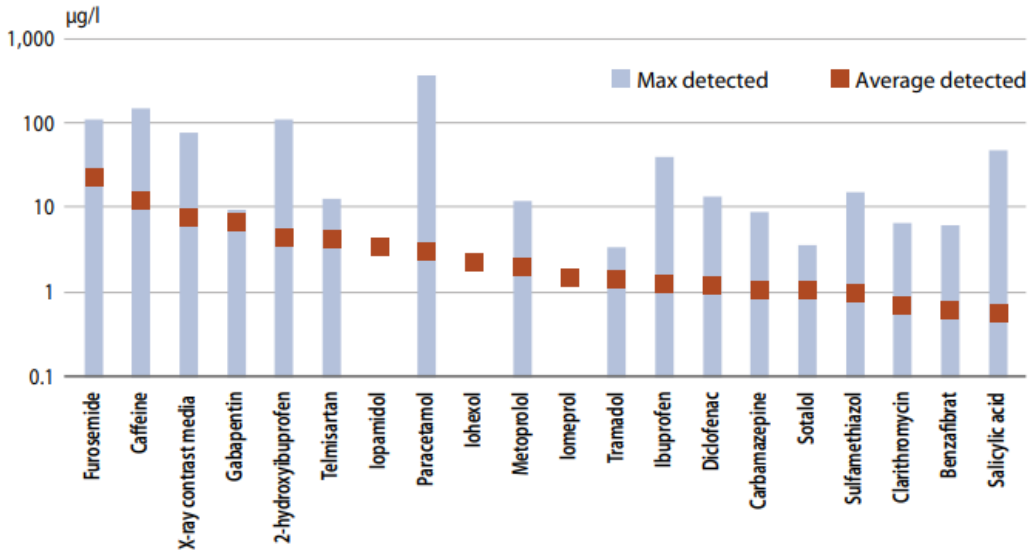

Rysunek 2. Stężenie API w ściekach z oczyszczalni z regionu Morza Bałtyckiego [3]

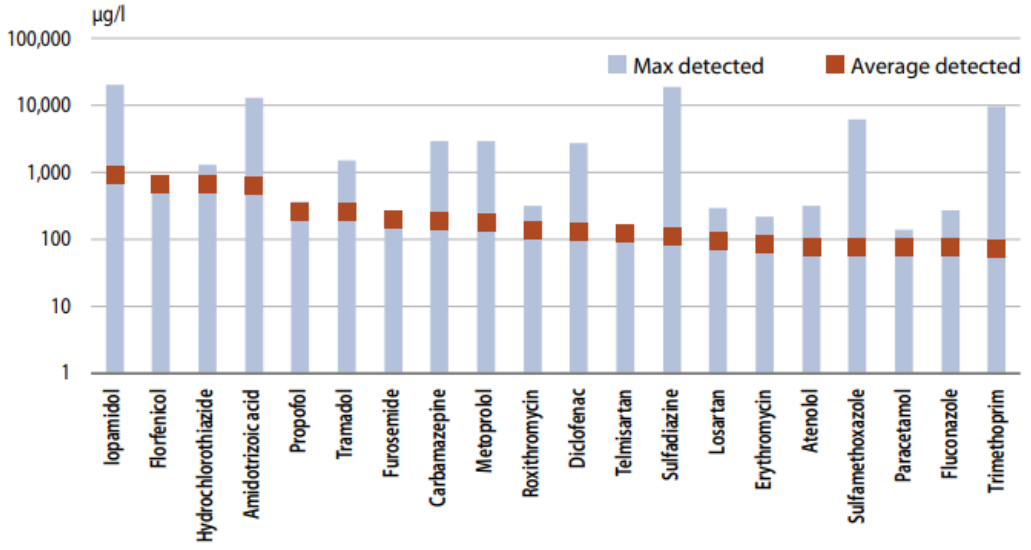

Rysunek 3. Stężenie API w rzekach z regionu Morza Bałtyckiego [3]

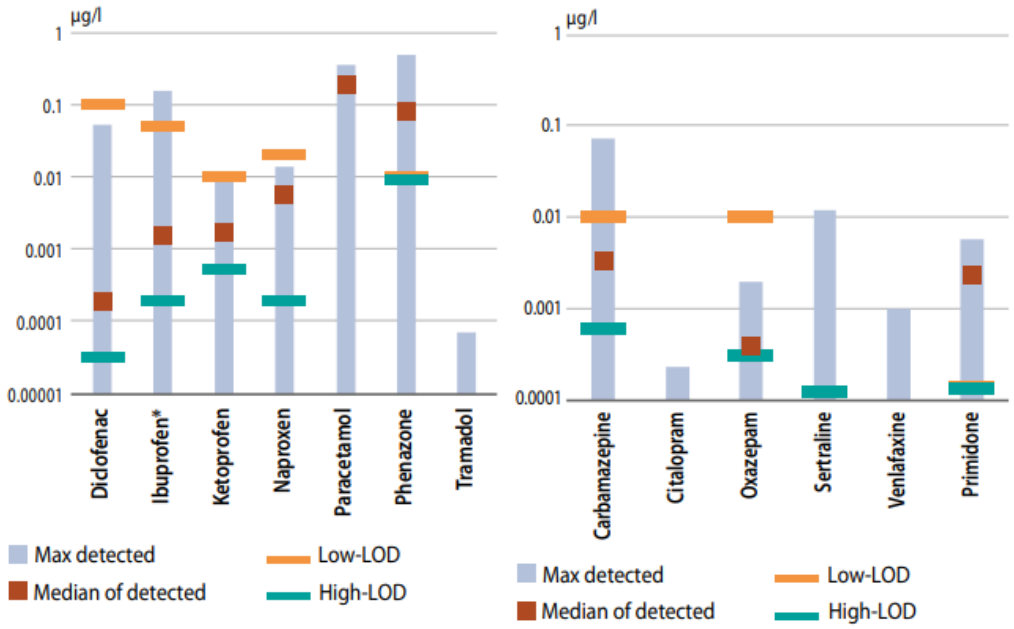

Rysunek 4. Stężenie API w wodach Morza Bałtyckiego [3]

2.3. Toksyczność

Qiang i in. [19] stwierdzili, że obecność karbamazepiny w stężeniu od 1 do 5 µg/dm^3 znacząco wpłynęła na przyspieszenie rozwoju zarodkowego, a także zaburzyła zachowanie zarodków i larw ryby danio pręgowanego (*Brachydanio rerio*). Wykazano, że obecność CBZ może wpływać na nieprawidłową ekspresję genów nerwowych i upośledzać zachowanie ryb, co z kolei może wpływać na strukturę ich populacji w ekosystemie. Badania przeprowadzone przez Oliveira i współautorów [25] wykazały, że obecność karbamazepiny nie indukuje stresu oksydacyjnego. Jednakże zauważono, że w przypadku ekspozycji chronicznej, parametry gonadosomatyczne uległy pogorszeniu, co wskazuje, że CBZ może upośledzać zdolności reprodukcyjne, a w efekcie może mieć wpływ na trwałość populacji.

W przypadku acetaminofenu, Guiloski i współautorzy [26] zaobserwowali zakłócenie działania osi podwzgórze-przysadka-gonady u samców suma srebrnego (*Rhamdia quelen*), a także zmienione parametry hematologiczne i hepatotoksyczność w wyniku ekspozycji na acetaminofen o stężeniu 0,25 i 2,5 µg/dm^3 przez 21 dni. Z kolei Brandão i współautorzy [27] stwierdzili, że acetaminofen nie spowodował wzrostu śmiertelności małż słodkowodnych (*Corbicula fluminea*) zarówno w przypadku krótkotrwałej (96 godzin), jak i długotrwałej ekspozycji (28 dni).

Toksyczność ibuprofenu wobec suma afrykańskiego (*Clarias gariepinus*) określono w badaniach Ogueji i współautorów [28]. Śmiertelność na poziomie 50% w ciągu 96 godzin ekspozycji zaobserwowano dla stężenia ibuprofenu wynoszącego 0,38 mg/dm^3. W przypadku

ryb narażonych na obecność ibuprofenu zaobserwowano nadpobudliwość, utratę równowagi, zmianę zabarwienia skóry, zwiększone wydzielanie śluzu czy nieregularne ruchy płetw (0,38-0,48 mg/dm^3). Dodatkowo obecność ibuprofenu spowodowała wzrost liczby erytrocytów i leukocytów, poziomu hemoglobiny, oraz znaczny spadek liczby neutrofili. Potwierdzono negatywny wpływ IBU na funkcjonowanie ryb i wskazano na konieczność monitorowania jego poziomu w wodach. W badaniach Xia i współautorów [29] porównano toksyczność ACT i IBP (5-500 µg/dm^3) wobec wylęgania i ruchliwości danio pręgowanego po 6 godzinach od zapłodnienia. W przypadku ibuprofenu zaobserwowano znaczną redukcję wskaźnika wylęgania o około 63% przy stężeniu 500 µg/dm^3. Ponadto, ekspozycja na wysokie stężenie IBP spowodowała zmniejszenie spontanicznych ruchów oraz odległości, czasu trwania i prędkości swobodnego pływania. Z kolei w przypadku acetaminofenu nie zaobserwowano znaczącego wpływu na rozwój organizmów.

Jednym z najczęściej wykorzystywanych narzędzi do oceny zagrożenia środowiskowego wynikającego z występowania farmaceutyków w ściekach oczyszczonych jest tak zwany iloraz ryzyka (RQ) wyznaczany na podstawie wytycznych Europejskiej Agencji Leków [30]. Wartość RQ obliczana jest poprzez podzielenie maksymalnego zmierzonego stężenia dla danego API przez przewidywane stężenie niewywołujące negatywnych efektów wśród organizmów wodnych (np. alg, rozwielitek, ryb). Gdy RQ < 0,1 nie ma zagrożenia dla organizmów wodnych lub jest ono znikome, gdy 0,1 ≤ RQ ≤ 1,0 ryzyko jest średnie, natomiast, gdy RQ ≥ 1,0 istnieje potencjalnie wysokie ryzyko dla organizmów wodnych. W pracy Khasawneh i Palaniandy [31], ACT i IBP zostały sklasyfikowane jako substancje wysokiego ryzyka (RQ > 1), natomiast CBZ jako substancja wykazująca średnie ryzyko (RQ < 1). Z kolei w badaniach Bouissou-Schurtz i współautorów [32] oszacowano, że parametr RQ dla ACT równy jest 1,6, dla ibuprofenu wynosi 600, zaś dla karbamazepiny wynosi 3,2. Wskazuje to, że wszystkie trzy API należą do grupy substancji wysokiego ryzyka zagrożenia środowiskowego, a w szczególności obecność ibuprofenu stwarza realne ryzyko dla organizmów żywych.

3. Fotokataliza

Do nowych i zaawansowanych procesów efektywnych w degradacji substancji niepodatnych na rozkład biologiczny, w tym zanieczyszczeń farmaceutycznych należą Zaawansowane Procesy Utleniania (*z ang. advanced oxidation processes, AOP*). AOP charakteryzują się wytwarzaniem in-situ wysoce reaktywnych form tlenu, takich jak: rodniki hydroksylowe, nadtlenek wodoru, ozon, czy anionorodniki ponadtlenkowe, które umożliwiają

efektywną degradację i mineralizację zanieczyszczeń do prostych związków nieorganicznych. Podział technik AOP przedstawiono na Rysunku 5.

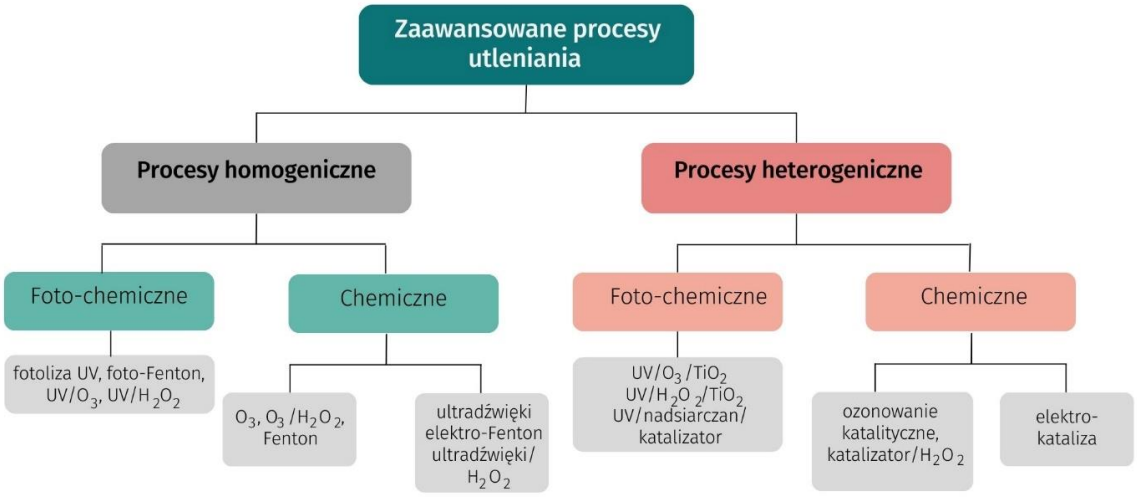

Rysunek 5. Podział zaawansowanych procesów utleniania – [opracowanie własne]

Fotokataliza heterogeniczna należy do grupy Zaawansowanych Procesów Utleniania. W tym procesie dochodzi do przekształcania szeregu związków chemicznych m.in. aktywnych substancji farmaceutycznych do prostych związków nieorganicznych, tlenku węgla(IV) i wody. Proces zachodzi w obecności fotokatalizatora, aktywowanego za pomocą promieniowania elektromagnetycznego.

W procesie fotokatalizy, półprzewodnik absorbuje światło o określonej długości fali, o energii równej bądź wyższej wartości jego przerwy wzbronionej. W wyniku absorpcji światła przez półprzewodnik dochodzi do wzbudzenia elektronu (e^-) z pasma walencyjnego do pasma przewodnictwa. Efektem czego jest wytworzenie dziur (h^+) w pasmie walencyjnym. Elektrony z pasma przewodnictwa reagują z cząsteczkami tlenu, tworząc anionorodniki ponadtlenkowe. Z kolei dziury, z pasma walencyjnego reagują z cząsteczkami wody na powierzchni półprzewodnika, tworząc rodniki hydroksylowe.

Reakcje zachodzące w trakcie procesu fotokatalizy przedstawiono w oparciu o Równania 1-5.

$$\boldsymbol{Fotokatalizator + h\nu \rightarrow h^+ + e^-} \quad (1)$$

$$\boldsymbol{h^+ + H_2O \rightarrow OH^\bullet + H^+} \quad (2)$$

$$\boldsymbol{h^+ + OH^- \rightarrow OH^\bullet} \quad (3)$$

$$\boldsymbol{e^- + O_2 \rightarrow O_2^{\bullet -}} \quad (4)$$

$$\boldsymbol{API + reaktywne\ formy\ tlenu \rightarrow produkty\ degradacji} \quad (5)$$

W Tabeli 2 porównano wady i zalety poszczególnych metod stosowanych do usuwania aktywnych substancji farmaceutycznych. Obecnie coraz większą uwagę poświęca się fotokatalizie, co wynika przede wszystkim z wysokiej efektywności degradacji API oraz stopnia ich mineralizacji do prostych związków nieorganicznych. Korzystnym rozwiązaniem jest też opracowywanie hybrydowych technologii na przykład poprzez sprzęganie metod biologicznych czy adsorpcji z fotokatalizą. Takie rozwiązanie często pozwala na osiągnięcie wysoce wydajnego procesu degradacji [33].

Tabela 2. Porównanie wad i zalet różnych obecnie stosowanych metod do usuwania substancji farmaceutycznych [33,34]

Metoda	*Zalety*	*Wady*
Procesy biologiczne	-Niski koszt	- Powolny proces -Niska wydajność procesu
Adsorpcja	-Niski koszt -Wysoka efektywność - Prosta obsługa	- Niska selektywność -Generowanie odpadu
Ozonowanie	-Wysoce efektywna metoda dla ścieków o wysokim pH -Ozon rozkłada się do tlenu i wody, dzięki czemu nie wprowadza wtórnych zanieczyszczeń do ścieków	-Ozon stanowi wysoce toksyczny gaz – wymaga ścisłej kontroli - Wysoki wkład finansowy oraz koszty operacyjne
Fenton/foto-Fenton	- Fe^{2+} i Fe^{3+} mogą pełnić funkcję nie tylko utleniającą ale też koagulacyjną -Stosunkowo tanie reagenty -Metoda efektywna także w wysokiej temperaturze	- Możliwość wykorzystania w zakresie pH 2-4 lub 3-6 w przypadku metody foto-Fentona -Tworzenie osadu $Fe(OH)_3$
Fotokataliza	-Wysoka efektywność względem szerokiego spektrum zanieczyszczeń - Fotokatalizator może być odzyskiwany i wielokrotnie wykorzystywany - Fotokatalizator np. TiO_2 jest stabilny i stosunkowo tani	- Zabarwienie i mętność ścieków mogą ograniczać aktywność -Problemy z separacją fotokatalizatora po procesie -Fotokatalizatory aktywowane przez światło UV -Szybka rekombinacja nośników ładunku ogranicza aktywność

Większość znanych i zbadanych półprzewodników stosowanych w fotokatalizie, w tym najpowszechniej wykorzystywany TiO_2 charakteryzuje się szeroką przerwą energetyczną, a co się z tym wiąże, aktywnością fotokatalityczną w zakresie promieniowania ultrafioletowego. Promieniowanie UV stanowi jedynie od 3 do 5% energii światła słonecznego, co ogranicza zastosowanie naturalnego promieniowania w procesach fotokatalitycznych, a przez to generuje koszty związane z koniecznością stosowania energochłonnych źródeł światła.

W związku z tym, jednym z *wyzwań współczesnej fotokatalizy*, jak przedstawiono na Rysunku 6, jest poszukiwanie efektywnych półprzewodników aktywnych w świetle widzialnym. Przestawione w literaturze rozwiązania dotyczą głównie: 1) inżynierii powierzchni i defektów – optymalizacja struktury krystalicznej, powierzchni właściwej, morfologii cząstek, czy wprowadzanie defektów, 2) domieszkowania – wprowadzania do struktury atomów niemetali (np. O, S, N, C, P) oraz metali (np. Fe, V, Co, Cu), 3) sensybilizacji barwnikami lub kompleksami metali, 4) tworzenia heterozłączy z materiałami aktywnymi w świetle widzialnym [35].

Rysunek 6. Wyzwania współczesnej fotokatalizy [opracowanie własne]

Częstym zjawiskiem jest także rekombinacja elektronów wzbudzonych z pasma przewodnictwa i dziur z pasma walencyjnego, co ogranicza tworzenie wolnych rodników. W związku z czym efektywna separacja nośników ładunku jest również istotnym *wyzwaniem współczesnej fotokatalizy*. Zmniejszenie rekombinacji par elekron-dziura można osiągnąć poprzez 1) tworzenie heterozłączy z innymi materiałami (złącza Schottky'ego, złącza typu p-n, złącza typu II, złącza typu Z), 2) depozycję metali szlachetnych/ko-katalizatora, 3) domieszkowanie, 4) wprowadzanie defektów powierzchniowych, 5) kontrolę morfologii [36–39].

Z punktu widzenia praktycznego zastosowania procesu fotokatalizy do usuwania pozostałości API ze ścieków, *wyzwaniem* jest zapewnienie szybkiej i prostej metody odzysku fotokatalizatora po procesie oczyszczania. Wielkość cząstek fotokatalizatora zawiera się w granicach od kilku mikrometrów, a ostatnio coraz częściej także w granicach od kilku do kilkunastu nanometrów. Wymagane jest zatem stosowanie długotrwałej i kosztownej nanofiltracji, aby zapobiec tworzeniu wtórnych zanieczyszczeń w ściekach w postaci

nanocząstek. W celu ułatwienia separacji fotokatalizatora po procesie oczyszczania, rozwiązaniem może być jego immobilizacja na nośniku (np. granulacie polimerowym, kulkach szklanych, żelu krzemionkowym, włóknie szklanym, ceramice) [40,41], czy też łączenie z materiałem o właściwościach magnetycznych (Fe_3O_4, ferryty spinelowe), co pozwoli na separację za pomocą zewnętrznego pola magnetycznego [42].

4. Synergizm fotokatalizy i aktywacji PMS

Połączenie procesu fotokatalizy z aktywacją nadtlenomonosiarczanu (PMS) jest nowym, obiecującym rozwiązaniem w zakresie oczyszczania wód. Aktywowany PMS może skutecznie wytwarzać rodniki siarczanowe ($\bullet SO_4^-$) o silnych właściwościach utleniających. Rodniki siarczanowe charakteryzują się zbliżonym lub nawet wyższym potencjałem redoks (wynoszący 2,5–3,1 V), w porównaniu z rodnikami hydroksylowymi (E^0= 1,8–2,8 V) [43]. Ponadto, rodniki siarczanowe wykazują wyższą selektywność, dłuższy okres półtrwania (30–40 μs) i mogą być aktywowane w szerszym zakresie pH (od 2 do 8) niż rodniki $\bullet OH$ [44]. Aktywacja PMS zachodzi w wyniku działania energii zewnętrznej, w tym ciepła, ultradźwięków, promieniowania UV, promieniowania gamma, reakcji katalitycznej w obecności metali przejściowych (np. Fe, Mn, Cu, Co), materiałów węglowych (np. grafen, węgiel aktywowany) oraz procesu fotokatalizy [45]. W tym odniesieniu, kombinacja fotokatalizy z aktywacją PMS może umożliwić osiągnięcie synergicznego działania obu procesów w celu zwiększenia wydajności procesu degradacji zanieczyszczeń niepodatnych na rozkład biologiczny.

5. MXeny

5.1. Ogólna charakterystyka MXenów

MXeny to grupa materiałów nowej generacji, które zostały po raz pierwszy opisane w 2011 roku przez zespół Profesora Yury Gogotsi'ego (patrz Rysunek 7).

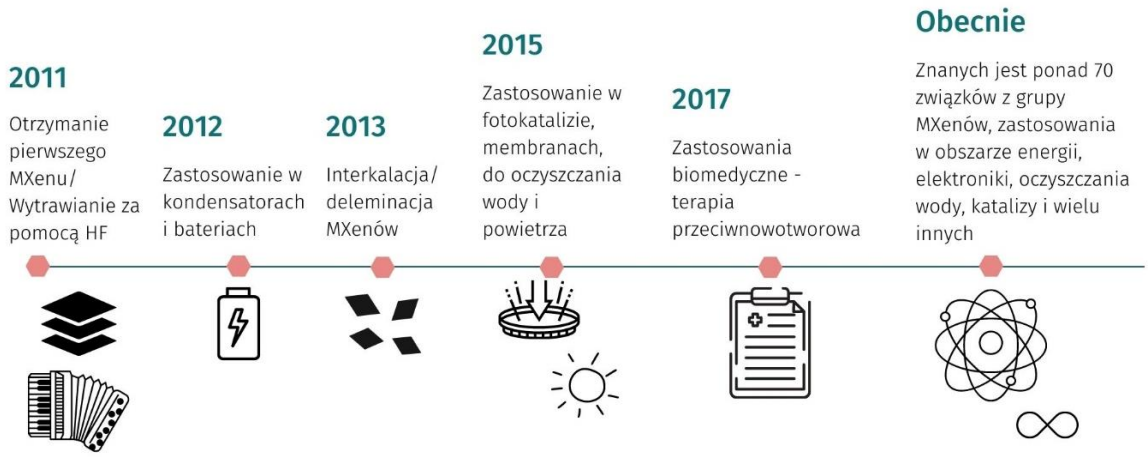

Rysunek 7. Historia MXenów [opracowanie własne]

Aktualnie do grupy poznanych i opisanych MXenów zalicza się ponad 70 materiałów. MXeny to materiały stanowiące węgliki, azotki lub węgliko-azotki metali przejściowych. Prekursorem do otrzymywania MXenów są związki fazy MAX o wzorze ogólnym $\boldsymbol{M_{n+1}AX_n}$, gdzie ***M*** to metal przejściowy, taki jak: Ti, Zr, Sc, V, Mo, Cr, Hf, Nb, Ta, ***A*** to Al, Si, Ga (pierwiastki grup 13-14), natomiast ***X*** to C lub/oraz N, a **n**= 1-3 [46]. Wiązania M-X są dużo silniejsze niż wiązania M-A, w związku z czym warstwa metalu A, może być z łatwością usunięta bez niszczenia wiązań M-X. Dzięki czemu MXeny otrzymywane są na drodze selektywnego usuwania metalu (A) ze struktury związków fazy MAX, najczęściej poprzez wytrawianie za pomocą kwasu fluorowodorowego lub mieszanin fluorku litu, sodu, potasu, i kwasu chlorowodorowego (kwas fluorowodorowy tworzony in-situ) [47]. W przypadku zastosowania soli fluoru dodatkowo dochodzi do interkalacji kationów metali: Na^+, K^+, Li^+ pomiędzy warstwami MXenów, powodując zwiększenie odległości międzypłaszczyznowych [48]. Proces wytrawiania glinu, na przykładzie Ti_3AlC_2, odbywa się zgodnie z reakcją przedstawioną Równaniem 6. Dodatkowo obecność wody i kwasu fluorowodorowego wpływa na wytworzenie powierzchniowych grup –OH i –F, zgodnie z Równaniami 7 i 8 [49].

$$Ti_3AlC_2 + 3HF \rightarrow Ti_3C_2 + AlF_3 + 3/2H_2 \quad (6)$$

$$Ti_3C_2 + 2H_2O \rightarrow Ti_3C_2(OH)_2 + H_2 \quad (7)$$

$$Ti_3C_2 + 2HF \rightarrow Ti_3C_2F_2 + H_2 \quad (8)$$

Parametry procesu wytrawiania – temperatura, czas, czy ilość kwasu fluorowodorowego dobierane są w zależności od rodzaju MXenu, a w szczególności od energii wiązań. Nazwa **MX**eny podkreśla usunięcie metalu **A** ze związku fazy **MAX**. Wzór ogólny MXenów to $\boldsymbol{M_{n+1}X_nT_x}$, gdzie $\mathbf{T_x}$ odnosi się do grup funkcyjnych obecnych na powierzchni po procesie wytrawiania,

najczęściej –OH, –O i –F. Obecność takich grup funkcyjnych na powierzchni determinuje szereg właściwości MXenów [50].

5.2. Właściwości fizykochemiczne MXenów

Od czasu odkrycia MXenów aż do dnia dzisiejszego badania nad materiałami z grupy MXenów rozwijają się coraz bardziej dynamicznie w wielu dziedzinach nauki. W 2023 roku liczba publikacji naukowych ze słowem kluczowym „MXene" osiągnęła blisko 93 tysiące. Wiąże się to z ich wieloma unikalnymi i korzystnymi właściwościami, wynikającymi z ich natury zbliżonej do grafenu. Szczególnie korzystne jest to, że ich właściwości mogą być odpowiednio modyfikowane w zależności od wymagań adekwatnych do rodzaju zastosowań. Odbywa się to poprzez dobór kompozycji, powierzchniowych grup funkcyjnych, czy korelacji morfologii i struktury geometrycznej.

W zależności od rodzaju i orientacji grup powierzchniowych, MXeny mogą wykazywać właściwości typowe dla metali, właściwości półmetaliczne, czy też charakterystykę typową dla przewodników wąskopasmowych [51]. MXeny takie jak np. Hf_2CO_2, Zr_2CO_2, V_2CF_2, $V_2C(OH)_2$, Ti_2CO_2, $Sc_2C(OH)_2$, Sc_2CF_2 i Sc_2CO_2 charakteryzują się niezerową przerwą wzbronioną [52,53].

Podobnie grupy funkcyjne na powierzchni wpływają na zmianę pracy wyjścia MXenów. MXeny wykazują ogromny potencjał tworzenia bariery Schottky'ego z półprzewodnikami. Gdy MXen tworzy złącze z półprzewodnikiem, oddziaływania van der Waalsa zapewniają tak zwane słabe „przypięcie" poziomu Fermiego (z ang. *weak Fermi-level pinning*), co w połączeniu z niską/wysoką pracą wyjścia MXenu umożliwia transfer wolnych elektronów/dziur przez barierę Schottky'ego do półprzewodnika [54].

MXeny charakteryzują się także doskonałą wytrzymałością mechaniczną i elastycznością. Parametry takie jak struktura i tekstura (grubości warstwy, odległości między warstwami, wymiary i porowatość), typ (tj. węgliki lub azotki), skład (tj. jedno- lub dwuskładnikowe, domieszkowanie, defekty), a także obecność grup funkcyjnych (-O, -OH i -F) determinują właściwości mechaniczne MXenów [55]. Silne wiązania M–C i/lub M–N w strukturze MXenu charakteryzują się dużą stałą sprężystości, przekraczającą 500 GPa. Ti_2C i Ti_3C_2 mogą wytrzymać do 17% odkształcenia przy naprężeniu jednoosiowym i dwuosiowym. Wartość ta może być wyższa nawet o 28% w wyniku funkcjonalizacji powierzchni grupami funkcyjnymi, które hamują zapadanie się powierzchniowej warstwy atomowej dzięki oddziaływaniom między atomami Ti i powierzchniowymi grupami funkcyjnymi [56].

Ponadto, ze względu na obecność na powierzchni MXenów atomów tlenu i fluoru o dużej elektroujemności, posiadają one ujemny ładunek powierzchniowy. W związku z tym, możliwa

jest interkalacja dodatnio naładowanych jonów poprzez silne oddziaływania kulombowskie między kationami, a MXenem. Dzięki temu MXeny wykazują dobre zdolności adsorpcyjne [57].

MXeny absorbują promieniowanie elektromagnetyczne w zakresie długości fali od 300 do 500 nm (UV-vis). Ponadto wykazują szerokie i silne pasmo absorpcji w zakresie bliskiej podczerwieni (NIR) od 700 do 800 nm. W zakresie energii ultrafioletu MXeny z grupami funkcyjnymi na powierzchni charakteryzują się wyższym współczynnikiem odbicia światła w porównaniu do MXenu bez grup funkcyjnych. Z kolei w zakresie światła widzialnego, MXeny z grupami –O wykazują większą intensywność absorpcji fali elektromagnetycznej i niższy współczynnik odbicia światła, podczas gdy fluorowanie powierzchni bądź obecność grup –OH skutkuje słabszą intensywnością absorpcji w porównaniu z MXenem bez grup funkcyjnych [58].

Związki z grupy MXenów wykazują zdolność do konwersji fototermicznej, co oznacza, że są efektywnym materiałem absorbującym światło i przekształcającym je na energię cieplną. Przeprowadzone badania wykazały, że w przypadku Ti_3C_2 zdolność konwersji światła na ciepło bliska jest 100%. Taki mechanizm przypisywany jest występowaniu efektu zlokalizowanego powierzchniowego rezonansu plazmonowego (LSPR) jaki występuje w przypadku złota czy srebra. Ti_3C_2 wykazuje silną absorpcję w zakresie bliskiej podczerwieni, podobnie jak w przypadku metali szlachetnych [59,60]. Efekt LSPR w MXenach jest związany z kolektywnym drganiem elektronów przewodnictwa w wyniku naświetlania promieniowaniem zwłaszcza w zakresie światła widzialnego lub bliskiej podczerwieni. W MXenach plazmony powierzchniowe są zależne od gęstości nośników ładunku swobodnego na powierzchni. MXeny wykazują wyraźną metaliczną gęstość swobodnych elektronów, która jest ściśle związana z licznymi grupami funkcyjnymi na powierzchni. W przypadku MXenów każda pojedyncza warstwa zachowuje się jak izolowany arkusz, posiadający unikalny zestaw modów plazmonów powierzchniowych, potwierdzając fundamentalną rozbieżność pomiędzy MXenami a „tradycyjnymi" metalami plazmonowymi [61,62].

Ponadto, niektóre z MXenów wykazują właściwości ferromagnetyczne (np. Ti_2C, Ti_2N, Cr_2C) lub antyferromagnetyczne (np. Cr_2N, Mn_2C) [52]. Natura magnetyczna związana jest z przyrostem gęstości elektronów w pobliżu regionu Fermiego. Natomiast funkcjonalizacja powierzchni prowadząca do zmniejszenia gęstości elektronowej wokół poziomu Fermiego skutkuje zanikiem właściwości magnetycznych [63].

MXeny określane jako materiały nowej generacji posiadają nie tylko zalety, ale też wady. Głównym ograniczeniem jest fakt, że pod względem składu chemicznego, MXeny są

termodynamicznie niestabilne, dlatego muszą być przechowywane w miejscach suchych i bez dostępności tlenu. Pojedyncze i kilkuwarstwowe struktury wykazują większą tendencję do utleniania niż struktury wielowarstwowe. Liczne badania potwierdzają, że utlenianie struktury MXenów rozpoczyna się od ich krawędzi z wytworzeniem tlenku metalu, co w konsekwencji prowadzi do zmniejszenia przewodnictwa. Jest to tzw. „efekt domina" prowadzący od utlenienia krawędzi do całej powierzchni, zmieniając właściwości materiału. W związku z tym, efektywną metodą zapobiegającą utlenianiu może być „ochrona" krawędzi np. poprzez kontrolowaną adsorpcję kationów na powierzchni. Inną metodą jest stosowanie węgla do powlekania powierzchni MXenów. Często też konieczne jest przetwarzanie w niskich temperaturach lub w atmosferze gazu obojętnego, aby zapobiec utlenianiu [64,65].

5.3. Struktury MXenów – od 3D do 0D

W zależności od metod otrzymywania MXeny mogą charakteryzować się różną morfologią w postaci:

- *Wielowarstowych arkuszy (3D)*

Podstawową strukturą MXenów otrzymywaną w wyniku usunięcia metalu ze struktury związku fazy MAX są wielowarstwowe arkusze przypominające tzw. harmonijkę z wolnymi przestrzeniami pomiędzy warstwami, co przedstawiono na Rysunku 8. Metody wytrawiania glinu ze struktury Ti_3AlC_2 zestawiono w Tabeli 3.

Rysunek 8. Struktura harmonijkowa MXenu otrzymywana w wyniku procesu wytrawiania związku fazy MAX - Ti_3AlC_2 [zdjęcie własne]

Tabela 3. Zestawienie przykładowych metod usuwania glinu ze struktury związku Ti_3AlC_2

Związek fazy MAX	*Metoda wytrawiania*	*Uwagi*	*Literatura*
Ti_3AlC_2	HF	- obecność fluoru na powierzchni	[66]
	HCl + LiF, NaF, KF, lub NH_4F	- wytwarzanie HF in-situ w trakcie procesu -obecność fluoru i chloru na powierzchni - interkalacja jonów Na^+, K^+, Li^+, NH_4^+	[67]
	$ZnCl_2$	- metoda bez fluoru -obecność chlor na powierzchni i pozostałości cynku	[68]
	NaOH	- metoda bez fluoru - proces prowadzony temperaturze 270°C w 27,5 M NaOH - grupy –OH i –O na powierzchni - reakcja prowadzona w obecności argonu	[69]

- *Hydrożeli/aerożeli (3D)*

Struktury 2D MXenów wykazują znaczną tendencję do agregacji, co ogranicza ich zastosowanie w wielu dziedzinach. Jednym z rozwiązań tego problemu jest integracja arkuszy 2D w makroskopowe struktury o wymiarach 3D. Ze względu na właściwości MXenów, takie jak silna hydrofilowość, przyciąganie w wyniku oddziaływań van der Waalsa, małe rozmiary i wyraźną sztywność, bezpośrednie tworzenie struktur żelu nadal stanowi wyzwanie. Aby utworzyć strukturę hydrożelu z MXenów, często konieczna jest obecność czynnika sieciującego, który kompensuje hydrofilowość arkuszy MXenu i utrzymuje strukturę 3D. W tym celu stosuje się różne substancje, takie jak zredukowany tlenek grafenu, polimery oraz jony metali, na przykład Fe^{2+}, Mg^{2+}, Co^{2+}, Ni^{2+} i Al^{3+} [70-71]. Z kolei, aerożele z MXenów można uzyskać poprzez bezpośrednią liofilizację dyspersji MXenów lub liofilizację hydrożeli [72].

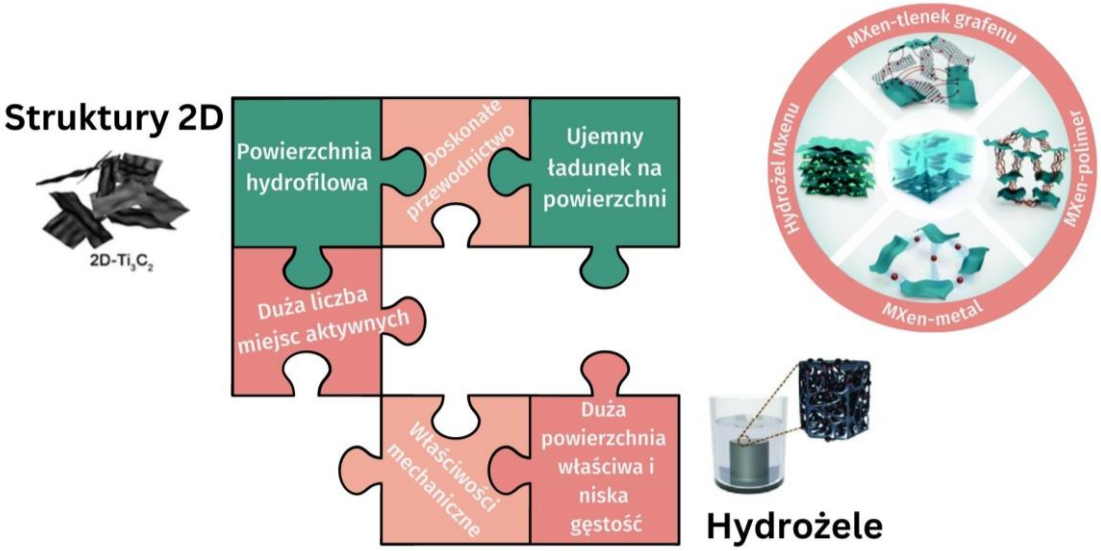

Rysunek 9. Właściwości hydrożeli utworzonych z płatków MXenów, na podstawie [70–72]

Otrzymane hydrożele/aerożele MXenów charakteryzują się niższą gęstością, bardziej rozwiniętą powierzchnią właściwą, lepszymi właściwościami mechanicznymi i elektrochemicznymi niż struktury 2D. Wynika to przede wszystkim z faktu, że:

1) dobrze zorganizowana sieć 3D MXenu zapobiega ponownej agregacji, umożliwiając odsłonięcie miejsc aktywnych na powierzchni oraz lepszą przepuszczalność elektrolitu,

2) sieć MXenu zapewnia ciągłe ścieżki przewodzenia, dla efektywnego transportu elektronów/jonów,

3) silne wiązanie MXenu z elektrolitem lub innymi materiałami w matrycy żelu zapewnia odpowiednią powierzchnię kontaktu na granicy elektrolit/elektroda z niską rezystancją międzyfazową,

4) żele MXenu mają wyjątkową gęstość upakowania, znacznie wyższą niż np. grafit czy komercyjny węgiel aktywowany.

Hydrożele/aerożele znajdują zastosowanie jako kondensatory elektrochemiczne, w bateriach, czujnikach, do kontrolowanego uwalniania leków, w katalizie, do ekranowania zakłóceń elektromagnetycznych oraz do magazynowania energii [71].

- *Jednowarstowe lub kilkuwarstowe arkusze (2D)*

Delaminacja wielowarstwowego MXenu prowadzi do otrzymania pojedynczej lub kilkuwarstwowej struktury MXenu. Najczęściej proces delaminacji odbywa się dzięki zastosowaniu interkalacji dużych polarnych cząsteczek organicznych np. dimetylosulfotlenku (DMSO), wodorotlenku tetrametyloamoniowego (TMAOH), czy wodorotlenku

tetrabutyloamoniowego (TBAOH) w celu zwiększenia odległości międzywarstwowej, osłabiając oddziaływania międzywarstwowe. Han i współautorzy [73] zastosowali wspomagany hydrotermalnie proces interkalacji $Ti_3C_2T_x$ za pomocą TMAOH w obecności przeciwutleniacza. Optymalne warunki prowadzenia procesu to 24 godziny i temperatura 140°C. Potwierdzono, że skuteczność delaminacji jest znacznie wyższa i wynosi około 74%, w porównaniu do konwencjonalnej interkalacji, dla której efektywność delaminacji wynosiła poniżej 20%.

W zależności od zastosowanej metody wytrawiania i interkalacji celem delaminacji wielowarstwowej struktury MXenu, wymagane może być też zastosowanie zewnętrznej siły ścinającej np. ultradźwięków czy wytrząsania [74].

Struktury dwuwymiarowe, w porównaniu do ich wielowarstwowych odpowiedników, charakteryzują się bardziej rozwiniętą powierzchnią właściwą oraz większą liczbą miejsc aktywnych. Ponadto, struktura materiałów 2D zapewnia ekspozycję licznych atomów powierzchniowych oraz skrócona jest droga migracji fotogenerowanych nośników ładunku ze struktury objętościowej do powierzchni. Dzięki temu rekombinacja par elekton-dziura zostaje ograniczona, a w związku z tym większa liczba nośników ładunku może brać udział w reakcji katalitycznej na powierzchni [75].

Rysunek 10. Otrzymywanie arkuszy 2D MXenu [opracowanie własne]

- *Kropek kwantowych*

MXeny można również otrzymywać w formie 0D czyli kropek kwantowych. Kropki kwantowe otrzymane ze struktur dwuwymiarowych nie tylko zachowują korzystne właściwości struktur 2D, ale także wykazują wyższą stabilność chemiczną, łatwiejszą funkcjonalizację, wyższy stosunek powierzchni do objętości czy silniejszą fotoluminescencję, oraz wydajnością kwantową.

Najpopularniejszą metodą otrzymywania kropek kwantowych MXenów jest tak zwana metoda z góry na dół (z ang. top-down). Metoda ta polega na zastosowaniu metod fizycznych

i/lub chemicznych, jak metody hydrotermalne, solwotermalne, mielenie czy ultradźwięki do tzw. „cięcia" prekursora w celu osiągnięcia rozmiarów cząstek poniżej 10 nm. W trakcie syntezy hydro/solwotermalnej rozmiar i grupy funkcyjne kropek kwantowych można modyfikować poprzez dobór czasu reakcji, temperatury, pH, czy rozpuszczalnika. Najczęściej jako rozpuszczalnik stosuje się amoniak, dimetylosulfotlenek, czy etanol [75].

W porównaniu z innymi kropkami kwantowymi, kropki MXenów odznaczają się znacznie większą powierzchnią właściwą, która bogata jest w hydrofilowe grupy funkcyjne umożliwiające łatwe i trwałe łączenie z innymi materiałami. Kropki Ti_3C_2 mają znacznie wyższy potencjał redoks. Typowe półprzewodnikowe kropki kwantowe absorbują promieniowanie z zakresu UV. W przypadku kropek MXenów jest to zakres UV-vis oraz bliska podczerwień (NIR) [76]. Ponadto wykazują one silną fotoluminescencję, która zależna jest od obecności grup funkcyjnych, defektów powierzchniowych, stopnia pasywacji powierzchni, podobnie jak w przypadku kropek kwantowych z węgla czy grafenu [77,78]. Ze względu na szereg korzystnych właściwości, badania nad zastosowaniem kropek kwantowych MXenów prowadzone są w obszarze obrazowania komórek, procesów fototermicznych, czujnikach pH, do wykrywania H_2O_2, w akumulatorach sodowo-jonowych, czy procesach fotokatalitycznej konwersji CO_2, m.in. do CH_4 czy CH_3OH oraz procesach fotogenerowania H_2 [77].

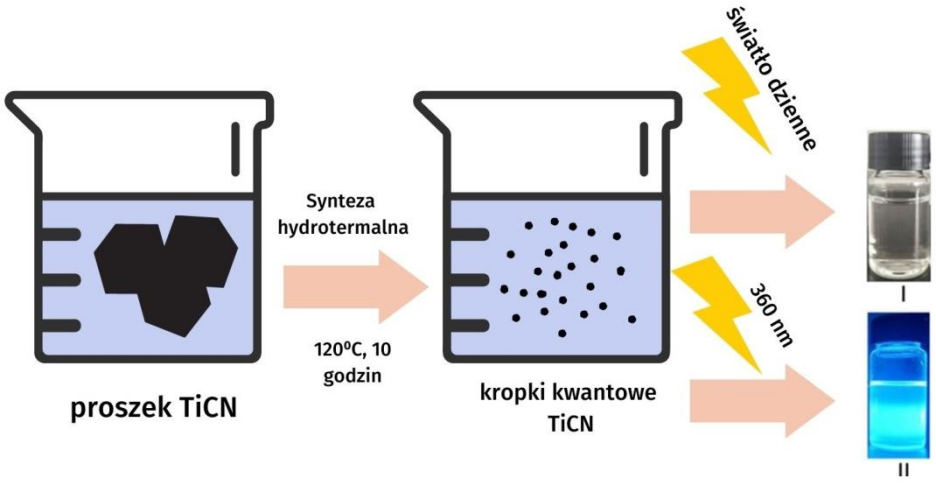

Rysunek 11. Otrzymywanie kropek kwantowych MXenu, na podstawie [79]

5.4. MXeny w fotokatalizie

Ze względu na właściwości metaliczne, półmetaliczne lub typowe dla półprzewodników wąskopasmowych, MXeny na ogół nie wykazują aktywności fotokatalitycznej i nie są samodzielnie stosowane jako fotokatalizatory. Jednak fakt ten nie ogranicza możliwości zastosowania ich w fotokatalizie. MXeny stosowane są przede wszystkim w roli ko-katalizatora

będącego alternatywą dla metali szlachetnych np. złota, platyny czy palladu. Ponadto, MXeny stanowią prekursory do wytworzenia heterozłączy MXen-półprzewodnik in-situ np. Ti_3C_2/TiO_2, V_2C/V_2O_5, Nb_2C/Nb_2O_5 w wyniku utleniania powierzchni MXenu. Na Rysunku 12 zestawiono funkcje MXenów i obszary ich zastosowań w procesach fotokatalitycznych.

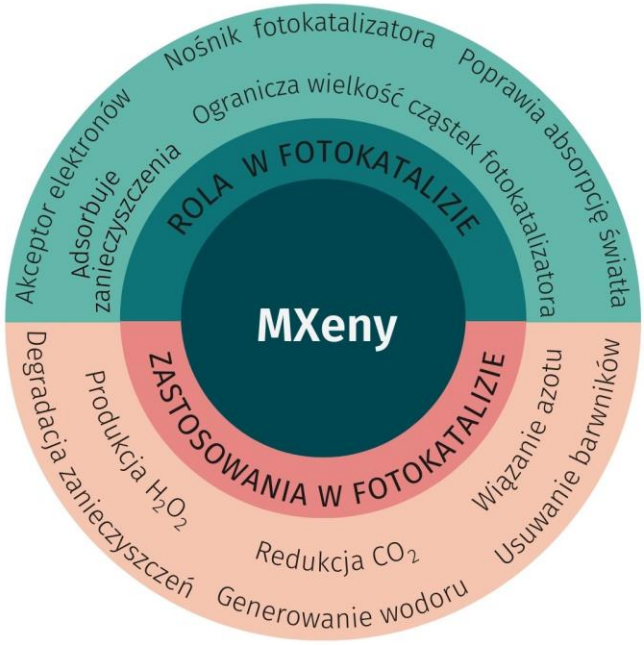

Rysunek 12. Rola i zastosowanie MXenów w fotokatalizie [opracowanie własne]

5.4.1. MXeny w fotokatalizie jako ko-katalizatory

MXeny stosowane są jako ko-katalizatory procesów fotokatalitycznych, czyli związki wspierające działanie właściwego fotokatalizatora. Obecność grup funkcyjnych na powierzchni umożliwia tworzenie bezpośredniej powierzchni kontaktu pomiędzy MXenem i półprzewodnikiem. Ponadto, MXeny mogą stanowić dobre podłoże dla fotokatalizatora, pozwalając na równomierny wzrost i wysoki stopień dyspersji fotokatalizatorów. Dodatkowo, dzięki wspomnianym licznym grupom funkcyjnym na powierzchni, tworzącym swego rodzaju zawadę przestrzenną, MXeny ograniczają rozmiar krystalitów fotokatalizatora. Jedną z istotnych cech MXenów, wykorzystywaną w procesach fotokatalitycznych jest też doskonałe przewodnictwo metaliczne. Na przykład, energia poziomu Fermiego dla $Ti_3C_2T_x$ wynosi około -0.05 V, co jest wartością znacznie bardziej dodatnią niż położenie pasma przewodnictwa dla wielu półprzewodników typu n (wykazujących przewodnictwo elektronowe), co pozwala na transfer i akumulację elektronów, a w konsekwencji na efektywną separację nośników ładunku [80]. Z punktu widzenia fotokatalizy istotny jest też fakt, że MXeny charakteryzują się silną reaktywnością w reakcjach redoks, i mogą być wykorzystywane jako centra aktywne reakcji utleniania/redukcji [81].

Kompozyty z MXenami uzyskuje się w wyniku mieszania mechanicznego, samoorganizacji dwóch komponentów lub strącania półprzewodnika na powierzchni MXenu. W Tabeli 4 zestawiono przykładowe zastosowania MXenów w roli ko-katalizatorów procesów fotokatalitycznych w połączeniach z różnymi półprzewodnikami.

Tabela 4. Przykładowe zastosowania MXenów w roli ko-katalizatorów procesów fotokatalitycznych

Proces	*Materiał*	*Metoda otrzymywania kompozytu/Funkcja MXenu/Główne wnioski*	*Literatura*
Redukcja CO_2	Ti_3C_2/Bi_2WO_6	- Synteza Bi_2WO_6 na powierzchni MXenu - Krótka odległość przenoszenia ładunku i duża powierzchnia kontaktu międzyfazowego zapewnia wydajny transfer elektronów z fotokatalizatora do ko-katalizatora - Blisko 5-krotnie wyższa wydajność redukcji CO_2 do CH_3OH i CH_4 dla kompozytów niż Bi_2WO_6	[82]
	$Ti_3C_2/g\text{-}C_3N_4$	- Kalcynacja mocznika w obecności Ti_3C_2 - Wyższy stopień konwersji CO_2 (około 8-krotnie) dla kompozytu niż dla C_3N_4 - Bezpośredni kontakt między komponentami zapewnia efektywną separację nośników ładunku	[83]
	$Ti_3C_2/CsPbBr_3$	- Synteza $CsPbBr_3$ na powierzchni Ti_3C_2 - Wysoce selektywna redukcja CO_2 do CO i CH_4 - Efektywny transport nośników ładunku pomiędzy MXenem i $CsPbBr_3$	[84]
	Ti_3C_2/TiO_2	- Mieszanie mechaniczne dwóch komponentów - Kompozyt wykazywał 3-krotnie i 277-krotnie wyższa wydajność tworzenia CO i CH_4 niż komercyjny P25 -Doskonałe przewodnictwo elektryczne MXenu ułatwia separację i przenoszenie nośników ładunku - Grupy –OH na powierzchni służą jako miejsca aktywne dla adsorpcji i aktywacji cząsteczek CO_2	[85]
Usuwanie barwników	Ti_3C_2/ZnO	- Synteza ZnO na powierzchni Ti_3C_2 -Kompozyt ZnO/MXen charakteryzował się znacznie większym natężeniem fotoprądu i skuteczniejszą separacją nośników ładunku niż ZnO	[86]
	ZnO/V_2C	- Samoorganizacja komponentów w wyniku przyciągania elektrostatycznego - Stała szybkości degradacji błękitu metylenowego była 16-krotnie wyższa niż dla ZnO - Dobra stabilność fotokatalityczna kompozytu w 4 cyklach degradacji	[87]
	Ti_3C_2/Fe_2O_3	- Samoorganizacja komponentów wspomagana ultradźwiękami - Nanocząstki Fe_2O_3 były dobrze rozproszone i zakotwiczone na warstwach Ti_3C_2, tworząc liczne powierzchnie kontaktu, które pozwalają osiągnąć silną absorpcję światła widzialnego i wysoką wydajność separacji nośników ładunku	[88]
Generowanie wodoru	$Ti_3C_2/g\text{-}C_3N_4$	- Samoorganizacja komponentów wspomagana ultradźwiękami - Kompozyt wykazywał prawie 3-krotnie wyższą efektywność generowania wodoru niż C_3N_4 - Dzięki doskonałemu przewodnictwu MXenu, elektrony z pasma przewodnictwa C_3N_4 mogą być szybko przenoszone do powierzchni MXenu, co sprzyja separacji nośników ładunku	[89]
	Ti_3C_2/ZnS	- Wytwarzanie ZnS na powierzchni Ti_3C_2 w wyniku reakcji solwotermalnej	[90]

		- Wprowadzenie Ti_3C_2 wspomaga przenoszenie ładunku i wydłuża czas życia nośników ładunku, co skutkuje zwiększoną wydajnością produkcji H_2, która jest prawie 4-krotnie wyższa niż dla ZnS	
	CdS/Nb_2C	- Otrzymywanie CdS w obecności Nb_2C w reakcji solwotermalnej - Obecność Nb_2C ograniczyła aglomerację nanocząstek CdS - Kompozyt wykazywał 4-krotnie wyższą efektywność generowania wodoru niż CdS - Wyższa aktywność wolnych rodników w przypadku materiału kompozytowego niż CdS	[91]
Usuwanie LZO	Ti_3C_2/ZnO	- Tworzenie ZnO na powierzchni Ti_3C_2 - Ti_3C_2 stanowi podłoże zapewniające znaczną liczbę miejsc aktywnych umożliwiających osadzanie cząstek ZnO oraz adsorpcje LZO - Zwiększenie powierzchni kontaktu wiąże się z większą liczbą centrów katalitycznych i minimalizuje odległości przenoszenia ładunków - Heterozłącze Schottky'ego ogranicza rekombinację par elektron-dziura - Stała szybkości rozkładu formaldehydu dla kompozytu była blisko 3-krotnie wyższa niż dla ZnO	[92]
	Ti_3C_2/Bi_2WO_6	- Samoorganizacja komponentów w wyniku przyciągania elektrostatycznego - Kompozyt charakteryzował się zwiększonym fotoprądem i słabą fotoluminescencję pod wpływem naświetlania dzięki efektowi pułapkowania elektronów za pomocą Ti_3C_2 - MXen wykazuje silną adsorpcję chemiczną dla HCHO i CH_3COCH_3, podczas gdy Bi_2WO_6 słabą adsorpcję fizyczną - Kompozyt wykazywał 2-krotnie i 7-krotnie wyższą degradację HCHO i CH_3COCH_3 w porównaniu z Bi_2WO_6	[93]
Usuwanie farmaceutyków	Ti_3C_2/MoS_2	- Otrzymywanie MoS_2 na powierzchni Ti_3C_2 w trakcie reakcji solwotermalnej - Tworzenie heterozłącza MoS_2/Ti_3C_2 ułatwia separację par elektron-dziura i przenoszenie ładunku - Kompozyt wykazywał degradację ranitydyny i mineralizację na poziomie odpowiednio 88,4% i 73,58%, co potwierdziło znaczną poprawę w porównaniu do MoS_2	[94]
	$Ti_3C_2/Sm\text{-}C_3N_4$	- Prepolimeryzacja $Sm\text{-}C_3N_4$ a następnie łączenie z Ti_3C_2 - W kompozycie właściwości optyczne oraz wydajność separacji elektronów i dziur uległy poprawie	[95]
	Nb_2C/Bi_2WO_6	- Otrzymywanie Bi_2WO_6 na powierzchni Nb_2C w wyniku reakcji solwotermalnej - Złącze Schottky'ego ogranicza rekombinację par elektron-dziura a elektrony z Bi_2WO_6 przenoszone są na powierzchnię Nb_2C gdzie są akumulowane	[96]
Redukcja metali ciężkich	Ti_3C_2/Bi_2MoO_6	- Synteza Bi_2MoO_6 w obecności Ti_3C_2 w trakcie reakcji solwotermalnej - Silny kontakt międzyfazowy i niewielka odległość transportu ładunku między Bi_2MoO_6 i Ti_3C_2 zapewniają dobrą zdolność przenoszenia ładunku powierzchniowego i międzyfazowego - Szybkości usuwania jonów metali ciężkich Cr(VI) były około 11-krotnie wyższa niż dla Bi_2MoO_6	[97]

	- W kompozycie Bi_2MoO_6/Ti_3C_2 zapewniane są nowe miejsca adsorpcji, co sprzyja wyższym interakcją między zanieczyszczeniami a fotokatalizatorem	
$Ti_3C_2/ZnIn_2S_4$	- Otrzymywanie $ZnIn_2S_4$ na powierzchni MXenu - Silne interakcje między $ZnIn_2S_4$ a MXenem pozwalają na silne wykorzystania energii słonecznej, zwiększoną zdolność separacji ładunków, doskonałe zdolności fotokatalitycznych i stabilności fotokatalizatora	[98]
$Ti_3C_2/Bi_{2.15}WO_6$	- Samoorganizacja komponentów w wyniku przyciąganie elektrostatycznego - Konwersja Cr(VI) dla kompozytu była 3-krotnie wyższa niż dla $Bi_{2.15}WO_6$ - Ti_3C_2 sprzyja separacji nośników, a tym samym znacząco poprawia działanie fotokatalityczne kompozytu	[99]

5.4.2. MXeny w fotokatalizie jako prekursory heterozłączy MXen/tlenek metalu

Heterozłącza MXen/półprzewodnik (tlenek metalu M) otrzymuje się w wyniku utleniania powierzchni MXenu. Otrzymuje się struktury MXen/MO, lub MXen/MO/węgiel amorficzny. Aby kompozyt mógł być wykorzystany w procesach fotokatalitycznych, tlenek metalu musi wykazywać aktywność fotokatalityczną. Proces otrzymywania takich struktur może być realizowany poprzez reakcję hydrotermalną, solwotermalną czy kalcynację. W zależności od zastosowanej metody otrzymane półprzewodniki charakteryzują się zróżnicowaną zawartością MXenu w kompozycie, morfologią, strukturą krystalograficzną, wielkością krystalitów, czy powierzchnią właściwą. Cao i współautorzy [100] zbadali powstawanie struktur TiO_2 na powierzchni Ti_3C_2 podczas reakcji w środowisku wodnym oraz w roztworze NaOH w temperaturze pokojowej. Utlenianie w wodzie prowadziło do uzyskania nanosfer TiO_2, natomiast reakcja w roztworze NaOH skutkowała tworzeniem nanowłókien na powierzchni Ti_3C_2. Z kolei, Low i współautorzy [101] zaproponowali zastosowanie kalcynacji węglika w temperaturze 350-650°C w atmosferze powietrza. Otrzymane struktury przypominały ziarna ryżu osadzone na warstwach Ti_3C_2. Li i współautorzy [102] zaproponowali metodę syntezy TiO_2/Ti_3C_2 poprzez jednoczesne utlenianie i alkalizację warstw Ti_3C_2 w roztworze NaOH i H_2O_2, a następnie wymianę jonową w roztworze HCl i kalcynację w temperaturze 300-500°C. W efekcie uzyskano trójwymiarowe struktury określone jako nanokwiaty o średnim rozmiarze struktur wynoszącym 3µm. Peng i in. [103] otrzymali płytki TiO_2 na powierzchni Ti_3C_2 w wyniku syntezy solwotermalnej prowadzonej w obecności $NaBH_4$ i HCl w 160°C przez 12 godzin. W kolejnej pracy opisali sposób otrzymywania kompozytu TiO_2/Ti_3C_2 w reakcji solwotermalnej [104], w obecności NH_4F i HCl w temperaturze 200°C przez 12-28 godzin. Na powierzchni Ti_3C_2 uzyskano oktaedry TiO_2. Zdjęcia SEM dla opisanych struktur zestawiono na Rysunku 13. Potwierdza to możliwość otrzymania różnych morfologii TiO_2 w wyniku utlenienie prekursora Ti_3C_2.

Morfologia fotokatalizatora i eksponowane płaszczyzny wpływają na jego właściwości fizykochemiczne. Zastosowanie strategii modyfikowania i inżynierii kryształów zapewnia nowe podejście do projektowanie wysoce efektywnych fotokatalizatorów i optymalizację ich aktywności oraz selektywności.

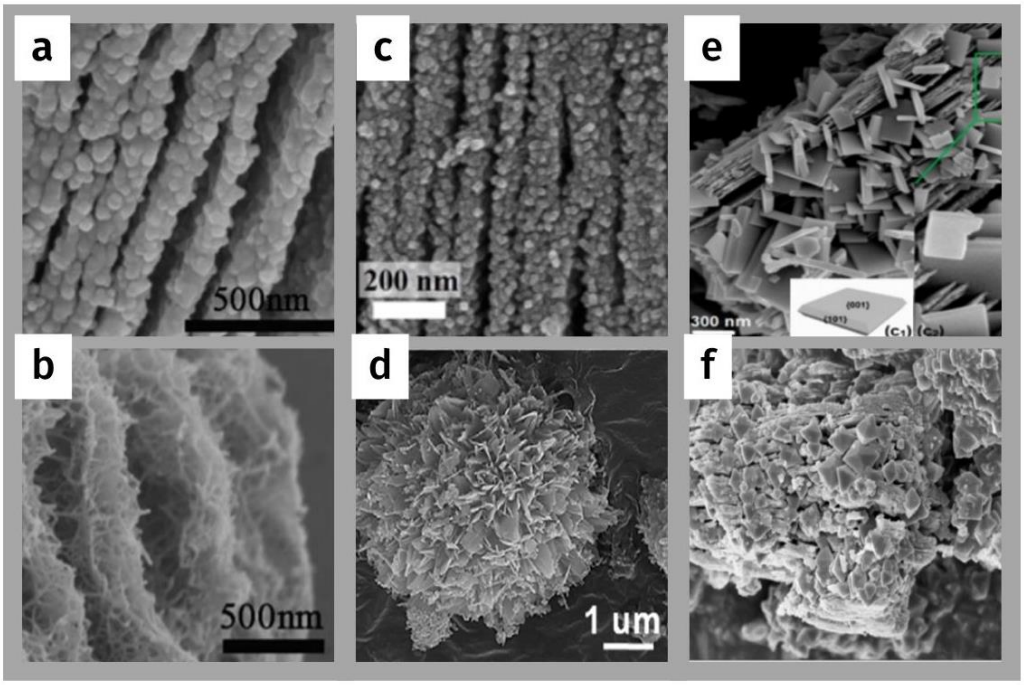

Rysunek 13. Zdjęcia SEM kompozytów Ti_3C_2/TiO_2 dla (a) utleniania wobec H_2O (b) utleniania w obecności NaOH, (c) kalcynacji w 550°C (d) utleniania w obecności NaOH i H_2O_2 (e) utleniania w obecności $NaBH_4$ i HCl (f) utleniania w obecności NH_4F i HCl, na podstawie [100-104]

W heterozłączach MXen/półprzewodnik dzięki występowaniu bezpośredniego kontaktu, możliwe jest utworzenie bariery Schottky'ego, jak przedstawiono na Rysunku 14. W przypadku kompozytu TiO_2/Ti_3C_2 fotogenerowane elektrony są transportowane i akumulowane na powierzchni MXenu, dzięki czemu rekombinacja par elektron-dziura może zostać ograniczona [105].

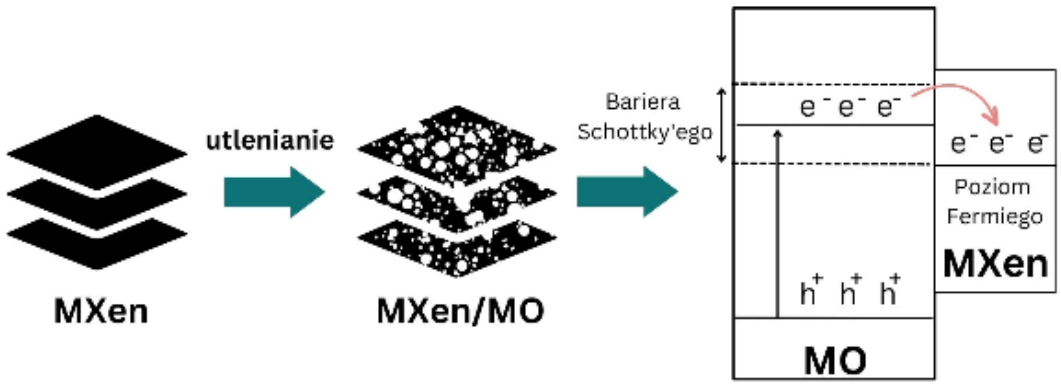

Rysunek 14. Tworzenie heterozłącza MXen/tlenek metalu M [opracowanie własne]

W Tabeli 5 przedstawiono przykłady zastosowań kompozytów MXen/tlenek metalu M w procesach fotokatalitycznych.

Tabela 5. Przykładowe zastosowania MXenów w procesach fotokatalitycznych jako prekursorów kompozytów MXen/tlenek metalu M

Proces	*Materiał*	*Metoda otrzymywania kompozytu/Rola MXenu/Główne wnioski*	*Literatura*
Redukcja CO_2	TiO_2/Ti_3C_2	- Kalcynacja węglika w temperaturze 350-650°C w atmosferze powietrza - Unikalna struktura przypominająca ziarna ryżu ze znaczną liczbą miejsc aktywnych - Kompozyt wykazywał 4-krotnie wyższą wydajność fotokatalitycznej redukcji CO_2 niż P25 - Wysokie przewodnictwo Ti_3C_2 ułatwiło przenoszenie elektronów i ograniczenie rekombinacji	[101]
Usuwanie barwników	TiO_2/Ti_3C_2	- Synteza solwotermalna w obecności $NaBH_4$ i HCl - Blisko 100% usunięcie oranżu metylowego w ciągu 40 minut naświetlania, znacznie wyższa efektywność niż P25 (60% w ciągu 40 minut) -Złącze Schottky'ego pozwala skutecznie transportować i gromadzić generowane elektrony	[106]
	TiO_2/Ti_3C_2	- Synteza solwotermalna w obecności NH_4F i HCl a następnie redukcja za pomocą hydrazyny - Ekspozycja płaszczyzn { 1 1 1 } i { 1 1 0 } rutylu - Efektywna separacja nośników ładunku dzięki obecności Ti_3C_2	[104]
Generowanie wodoru	$Nb_2O_5/C/Nb_2C$	- Utlenianie w atmosferze CO_2 w 850°C - Kompozyt wykazywał najwyższą efektywność generowania wodoru, 4-krotnie wyższą niż dla Nb_2O_5 - Zwiększoną wydajność $Nb_2C/C/Nb_2O_5$ przypisywano bliskiemu kontaktowi między Nb_2O_5 i przewodzącym Nb_2C oraz efektywnej separacji nośników ładunku	[107]
Utlenianie związków organicznych	TiO_2/Ti_3C_2	- Kalcynacja węglika w temperaturze 350-650°C w atmosferze powietrza - Ti_3C_2 może stabilizować wakancje tlenowe i formy Ti^{3+} w kompozycie, co sprzyja wytwarzaniu aktywnych produktów pośrednich podczas fotokatalitycznego utleniania alkoholu benzylowego - Pasmo walencyjne TiO_2 w kompozytach zostało przesunięte w górę, co pozwoliło uniknąć dalszego utleniania benzaldehydu i zwiększenie selektywności - Kompozyt wykazywał wydajność konwersji alkoholu na poziomie 97% i selektywność względem benzaldehydu na poziomie 98%, czyli 3-krotnie i 1,2-krotnie wyższą niż dla TiO_2	[108]
	TiO_2/Ti_3C_2	- Utlenianie Ti_3C_2 w obecności H_2O_2 - Wbudowana struktura gwarantuje bliski kontakt i efektywny przepływ nośników ładunku między komponentami - Obecność Ti^{3+} umożliwia efektywne wykorzystanie światła widzialnego przez kompozyty - 27% aldehydu uległo degradacji w świetle widzialnym, co było znacznie wyższą wartością niż dla P25	[109]

	TiO_2/Ti_3C_2	- Synteza hydrotermalna - W porównaniu z TiO_2, kompozyt wykazywał znacznie lepszą wydajność fotokatalityczną utleniania D-ksylozy do kwasu D-ksylonowego (64,2%) - Transfer elektronów z TiO_2 do Ti_3C_2 znacznie zwiększa czas życia nośników ładunku	[110]
Usuwanie farmaceutyków	Nb_2O_5/Nb_2C	- Synteza hydrotermalna - Kompozyty Nb_2O_5/Nb_2CT_x wykazują doskonałą aktywność fotokatalityczną degradacji tetracykliny - 91,2% w ciągu 180 minut w świetle widzialnym - Złącze Schottky'ego pomiędzy Nb_2O_5 i Nb_2CT_x pozwala na skuteczną separacje fotogenerowanych nośniki ładunku	[111]
	TiO_2/Ti_3C_2	- Synteza solwotermalna w obecności $NaBF_4$ i HCl - Szybkości degradacji tetracykliny dla TiO_2/Ti_3C_2 wynosiła 31,99%, i 28,63% po 150 minutach naświetlania światłem widzialnym i NIR - Tworzenie złącza Schottky'ego na granicy między płaszczyzną {001} TiO_2 i MXenu oraz efekt LSPR MXenu promują skuteczne rozdzielanie elektronów i dziur po fotowzbudzeniu oraz wydłużenie czasu życia nośników	[112]
Usuwanie NO	Nb_2O_5/Nb_2C	- Synteza hydrotermalna a następnie obróbka termiczna w atmosferze H_2/Ar (8% obj. H_2) w 500 C - Otrzymana struktura podobna do aktyni promująca ekspozycją miejsc aktywnych i powiększenie powierzchni kontaktu reakcji - Synergizm wakancji tlenowych i heterozłącza Schottky'ego pozwala na zwiększenie separacji fotogenerowanych elektronów i dziur	[113]

6. Podsumowanie omówienia literatury

Starzenie się społeczeństwa czy wzrost zachorowań przyczyniają się do większej konsumpcji leków, które w niezmienionej formie lub formie metabolitów wydalane są z organizmu do ścieków. W przypadku wielu aktywnych substancji farmaceutycznych procesy oczyszczania w konwencjonalnych oczyszczalniach ścieków są nieefektywne i prowadzą do ich uwalniania do ekosystemu. Jednym z markerów jakości wody jest karbamazepina. Efektywność usuwania karbamazepiny ze ścieków wynosi poniżej 10%. Także los oraz ścieżka przemian API w środowisku nie zawsze są poznane. Produkty degradacji mogą wykazywać aktywność farmaceutyczną, a często także wyższą toksyczność niż związek macierzysty, a zatem mogą mieć znaczący, niekorzystny wpływ na zdrowie ludzi i środowisko. Pomimo tego dopuszczalne stężenia API w ekosystemach wodnych czy wodzie pitnej, nie są jeszcze regulowane przez prawo.

W tym aspekcie kluczowe jest więc monitorowanie występowania i usuwania API w oczyszczalniach. Konieczna jest także poprawa efektywności procesu oczyszczania ścieków poprzez stosowanie innowacyjnych i zrównoważonych procesów technologicznych. Proponowana technologia musi być prosta w obsłudze, stosunkowo tania, efektywna i przede wszystkim przyjazna dla środowiska. Do efektywnych metod usuwania trwałych zanieczyszczeń organicznych zaliczane są zaawansowane procesy utleniania. Wśród AOP to właśnie fotokataliza budzi olbrzymie zainteresowanie. Wynika to przede wszystkim z możliwości zastosowania tej metody do degradacji szerokiego spektrum zanieczyszczeń. Ponadto, istotnym aspektem jest wysoka efektywność. Niemniej jednak, brak aktywności w świetle widzialnym, szybka rekombinacja nośników ładunku czy problemy z separacją fotokatalizatora po procesie wciąż pozostają wyzwaniem do rozwiązania przed wielkoskalowym wykorzystaniem procesów fotokatalitycznych.

Materiałami nowej generacji, które mogą znaleźć zastosowanie w procesach fotokatalitycznych są odkryte w 2011 roku związki z grupy MXenów. Na podstawie dokonanego przeglądu literatury można stwierdzić, że MXeny mogą pełnić dwie istotne role w fotokatalizie. W pracach badawczych wymienia się przede wszystkim ich udział w separacji nośników ładunku, gdzie obecność MXenu pozwala na transport i gromadzenie najczęściej elektronów, zapobiegając rekombinacji par elektron-dziura. Ponadto, wśród istotnych funkcji należy podkreślić również lepszą adsorpcję zanieczyszczeń czy tworzenie większej liczby miejsc aktywnych. Jednocześnie, MXeny stanowią prekursory do tworzenia złączy MXen/tlenek metalu M. Taki kompozyt może być stosowany w fotokatalizie, jeśli tlenek metalu M wykazuje

aktywność fotokatalityczną. Bezpośrednie utlenianie powierzchni MXenu pozwala na utworzenie złącza o bezpośredniej powierzchni kontaktu, zapewniając efektywną separację nośników ładunku oraz znaczną liczbę miejsc aktywnych. Ponadto niektóre z badań wskazują na osiągnięcie aktywności dla tak wytworzonych materiałów w świetle widzialnym.

Pomimo wielu zalet wynikających z zastosowania MXenów liczba publikacji naukowych w tematyce ich zastosowania do fotokatalitycznej degradacji aktywnych substancji farmaceutycznych wciąż pozostaje niewielka. W tym odniesieniu, badania przeprowadzone w ramach pracy doktorskiej dotyczące zastosowania fotokatalizatorów opartych na MXenach do usuwania związków z grupy farmaceutyków w fazie wodnej są nowatorskie i mogą przyczynić się do rozwoju wykorzystania tej grupy związków w procesach fotokatalitycznych.

7. Literatura

[1] A. Boretti, L. Rosa, Reassessing the projections of the World Water Development Report, Npj Clean Water 2 (2019) 15. https://doi.org/10.1038/s41545-019-0039-9

[2] J. Singh, P. Yadav, A.K. Pal, V. Mishra,. Water Pollutants: Origin and Status. In: Pooja, D., Kumar, P., Singh, P., Patil, S. (eds) Sensors in Water Pollutants Monitoring: Role of Material. Advanced Functional Materials and Sensors, (2020) Springer, Singapore. https://doi.org/10.1007/978-981-15-0671-0_2

[3] HELCOM, Pharmaceuticals in the aquatic environment of the Baltic Sea region A status report International Initiative on Water Quality-IIWQ, 2017. http://www.unesco.org/open-access/terms-use-ccbysa-en

[4] P. Chaturvedi, P. Shukla, B.S. Giri, P. Chowdhary, R. Chandra, P. Gupta, A. Pandey, Prevalence and hazardous impact of pharmaceutical and personal care products and antibiotics in environment: A review on emerging contaminants, Environ. Res. 194 (2021) 110664. https://doi.org/10.1016/j.envres.2020.110664

[5] D. Kucharski, G. Nałęcz-Jawecki, P. Drzewicz, A. Skowronek, K. Mianowicz, A. Strzelecka, J. Giebułtowicz, The assessment of environmental risk related to the occurrence of pharmaceuticals in bottom sediments of the Odra River estuary (SW Baltic Sea), Sci. Total Environ. 828 (2022) 154446. https://doi.org/10.1016/j.scitotenv.2022.154446

[6] M. Patel, R. Kumar, K. Kishor, T. Mlsna, C.U. Pittman, D. Mohan, Pharmaceuticals of Emerging Concern in Aquatic Systems: Chemistry, Occurrence, Effects, and Removal Methods, Chem. Rev. 119 (2019) 3510. https://doi.org/10.1021/acs.chemrev.8b00299

[7] P.M. Ondarza, S.P. Haddad, E. Avigliano, K.S.B. Miglioranza, B.W. Brooks, Pharmaceuticals, illicit drugs and their metabolites in fish from Argentina: Implications for protected areas influenced by urbanization, Sci. Total Environ. 649 (2019) 1029. https://doi.org/10.1016/j.scitotenv.2018.08.383

[8] L. Cizmas, V.K. Sharma, C.M. Gray, T.J. McDonald, Pharmaceuticals and personal care products in waters: occurrence, toxicity, and risk, Environ. Chem. Lett. 13 (2015) 381. https://doi.org/10.1007/s10311-015-0524-4

[9] J. Rivera-Utrilla, M. Sánchez-Polo, M.Á. Ferro-García, G. Prados-Joya, R. Ocampo-Pérez, Pharmaceuticals as emerging contaminants and their removal from water. A review, Chemosphere 93 (2013) 1268. https://doi.org/10.1016/j.chemosphere.2013.07.059

[10] G.M. Bruce, R.C. Pleus, S.A. Snyder, Toxicological relevance of pharmaceuticals in drinking water, Environ. Sci. Technol. 44 (2010) 5619. https://doi.org/10.1021/es1004895

[11] E. Brechtelsbauer, S. Shah, Update on pharmaceutical waste disposal regulations: Strategies for success, Am. J. Heal. Pharm. 77 (2020) 574. https://doi.org/10.1093/ajhp/zxz360

[12] A. Rubirola, M.R. Boleda, M.T. Galceran, Formation of new disinfection by-products of priority substances (Directive 2013/39/UE and Watch List) in drinking water treatment. Environ. Sci. Pollut. Res. 26 (2019) 28270. https://doi.org/10.1007/s11356-019-06018-9

[13] R. Hernández-Tenorio, E. González-Juárez, J.L. Guzmán-Mar, L. Hinojosa-Reyes, A. Hernández-Ramírez, Review of occurrence of pharmaceuticals worldwide for estimating concentration ranges in aquatic environments at the end of the last decade, J. Hazard. Mater. Adv. 8 (2022) 100172. https://doi.org/10.1016/j.hazadv.2022.100172

[14] F.I. Hai, S. Yang, M.B. Asif, V. Sencadas, S. Shawkat, M. Sanderson-Smith, J. Gorman, Z.Q. Xu, K. Yamamoto, Carbamazepine as a Possible Anthropogenic Marker in Water: Occurrences,

Toxicological Effects, Regulations and Removal by Wastewater Treatment Technologies, Water 10 (2018) 1. https://doi.org/10.3390/w10020107

[15] I. Fricke-Galindo, A. LLerena, H. Jung-Cook, M. López-López, Carbamazepine adverse drug reactions, Expert Rev. Clin. Pharmacol. 11 (2018) 705. https://doi.org/10.1080/17512433.2018.1486707

[16] S. Chopra, D. Kumar, Ibuprofen as an emerging organic contaminant in environment, distribution and remediation, Heliyon 6 (2020) e04087. https://doi.org/10.1016/j.heliyon.2020.e04087

[17] R.B. Raffa, J. Pawasauskas, J. V. Pergolizzi, L. Lu, Y. Chen, S. Wu, B. Jarrett, R. Fain, L. Hill, K. Devarakonda, Pharmacokinetics of Oral and Intravenous Paracetamol (Acetaminophen) When Co-Administered with Intravenous Morphine in Healthy Adult Subjects, Clin. Drug Investig. 38 (2018) 259. https://doi.org/10.1007/s40261-017-0610-4

[18] M. Lecoeur, G. Rabenirina, N. Schifano, P. Odou, S. Ethgen, G. Lebuffe, C. Foulon, Determination of acetaminophen and its main metabolites in urine by capillary electrophoresis hyphenated to mass spectrometry, Talanta 205 (2019) 120108. https://doi.org/10.1016/j.talanta.2019.07.003

[19] L. Qiang, J. Cheng, J. Yi, J.M. Rotchell, X. Zhu, J. Zhou, Environmental concentration of carbamazepine accelerates fish embryonic development and disturbs larvae behavior, Ecotoxicology 25 (2016) 1426–1437. https://doi.org/10.1007/s10646-016-1694-y

[20] M. Adamczuk, Environmentally realistic concentrations of ibuprofen influence life histories but not population dynamics of Daphnia magna, Sci. Total Environ. 848 (2022) 157783. https://doi.org/10.1016/j.scitotenv.2022.157783

[21] E. Ranieri, P. Verlicchi, T.M. Young, Paracetamol removal in subsurface flow constructed wetlands, J. Hydrol. 404 (2011) 130. https://doi.org/10.1016/j.jhydrol.2011.03.015

[22] Â. Almeida, V. Calisto, M.R.M. Domingues, V.I. Esteves, R.J. Schneider, A.M.V.M. Soares, E. Figueira, R. Freitas, Comparison of the toxicological impacts of carbamazepine and a mixture of its photodegradation products in Scrobicularia plana, J. Hazard. Mater. 323 (2017) 220. https://doi.org/10.1016/j.jhazmat.2016.05.009

[23] N. Paxéus, Removal of selected non-steroidal anti-inflammatory drugs (NSAIDs), gemfibrozil, carbamazepine, b-blockers, trimethoprim and triclosan in conventional wastewater treatment plants in five EU countries and their discharge to the aquatic environment, Water Sci. Technol. 50 (2004) 253. https://doi.org/10.2166/wst.2004.0335

[24] J. Żur, A. Piński, A. Marchlewicz, K. Hupert-Kocurek, D. Wojcieszyńska, U. Guzik, Organic micropollutants paracetamol and ibuprofen—toxicity, biodegradation, and genetic background of their utilization by bacteria, Environ. Sci. Pollut. Res. 25 (2018) 21498. https://doi.org/10.1007/s11356-018-2517-x

[25] P. Oliveira, Â. Almeida, V. Calisto, V.I. Esteves, R.J. Schneider, F.J. Wrona, A.M.V.M. Soares, E. Figueira, R. Freitas, Physiological and biochemical alterations induced in the mussel Mytilus galloprovincialis after short and long-term exposure to carbamazepine, Water Res. 117 (2017) 102. https://doi.org/10.1016/j.watres.2017.03.052

[26] I.C. Guiloski, J.L.C. Ribas, L.D.S. Piancini, A.C. Dagostim, S.M. Cirio, L.F. Fávaro, S.L. Boschen, M.M. Cestari, C. da Cunha, H.C. Silva de Assis, Paracetamol causes endocrine disruption and hepatotoxicity in male fish Rhamdia quelen after subchronic exposure, Environ. Toxicol. Pharmacol. 53 (2017) 111. https://doi.org/10.1016/j.etap.2017.05.005

[27] F.P. Brandão, J.L. Pereira, F. Gonçalves, B. Nunes, The impact of paracetamol on selected biomarkers of the mollusc species Corbicula fluminea, Environ. Toxicol. 29 (2014) 74. https://doi.org/10.1002/tox.20774

[28] E. Ogueji, C. Nwani, S. Iheanacho, C. Mbah, C. Okeke, A. Yaji, Acute toxicity effects of ibuprofen on behaviour and haematological parameters of African catfish Clarias gariepinus (Burchell, 1822), Afr. J. Aquat. Sci. 43 (2018) 293. https://doi.org/10.2989/16085914.2018.1465393

[29] L. Xia, L. Zheng, J.L. Zhou, Effects of ibuprofen, diclofenac and paracetamol on hatch and motor behavior in developing zebrafish (Danio rerio), Chemosphere 182 (2017) 416. https://doi.org/10.1016/j.chemosphere.2017.05.054

[30] A.C. Neves, M.P.G. Mol, Theoretical environmental risk assessment of ten used pharmaceuticals in Belo Horizonte, Brazil, Environ. Monit. Assess. 191 (2019) 275. https://doi.org/10.1007/s10661-019-7386-3

[31] O.F.S. Khasawneh, P. Palaniandy, Occurrence and removal of pharmaceuticals in wastewater treatment plants, Process Saf. Environ. Prot. 150 (2021) 532. https://doi.org/10.1016/j.psep.2021.04.045

[32] C. Bouissou-Schurtz, P. Houeto, M. Guerbet, M. Bachelot, C. Casellas, A.C. Mauclaire, P. Panetier, C. Delval, D. Masset, Ecological risk assessment of the presence of pharmaceutical residues in a French national water survey, Regul. Toxicol. Pharmacol. 69 (2014) 296. https://doi.org/10.1016/j.yrtph.2014.04.006

[33] N. Taoufik, W. Boumya, M. Achak, M. Sillanpää, N. Barka, Comparative overview of advanced oxidation processes and biological approaches for the removal pharmaceuticals, J. Environ. Manage. 288 (2021) 112404. https://doi.org/10.1016/j.jenvman.2021.112404

[34] F. Mansouri, K. Chouchene, N. Roche, M. Ksibi, Removal of Pharmaceuticals from Water by Adsorption and Advanced Oxidation Processes: State of the Art and Trends, Appl. Sci. 11 (2021) 6659. https://doi.org/10.3390/app11146659

[35] J. You, Y. Guo, R. Guo, X. Liu, A review of visible light-active photocatalysts for water disinfection: Features and prospects, Chem. Eng. J. 373 (2019) 624. https://doi.org/10.1016/j.cej.2019.05.071

[36] J. Fang, H. Fan, Y. Ma, Z. Wang, Q. Chang, Surface defects control for ZnO nanorods synthesized by quenching and their anti-recombination in photocatalysis, Appl. Surf. Sci. 332 (2015) 47. https://doi.org/10.1016/j.apsusc.2015.01.139

[37] J. Low, J. Yu, M. Jaroniec, S. Wageh, A.A. Al-Ghamdi, Heterojunction Photocatalysts, Adv. Mater. 29 (2017) 1601694. https://doi.org/10.1002/adma.201601694

[38] G.Z.S. Ling, S. Ng, W. Ong, Tailor-Engineered 2D Cocatalysts: Harnessing Electron–Hole Redox Center of 2D g-C_3N_4 Photocatalysts toward Solar-to-Chemical Conversion and Environmental Purification, Adv. Funct. Mater. 32 (2022) 2111875. https://doi.org/10.1002/adfm.202111875

[30] F. Chen, T. Ma, T. Zhang, Y. Zhang, H. Huang, Atomic-Level Charge Separation Strategies in Semiconductor-Based Photocatalysts, Adv. Mater. 33 (2021) 2005256. https://doi.org/10.1002/adma.202005256

[40] A.T. Le, T.D.H. Le, K.Y. Cheong, S.Y. Pung, Immobilization of zinc oxide-based photocatalysts for organic pollutant degradation: A review, J. Environ. Chem. Eng. 10 (2022) 108505. https://doi.org/10.1016/j.jece.2022.108505

[41] D. Robert, V. Keller, N. Keller, Immobilization of a Semiconductor Photocatalyst on Solid Supports: Methods, Materials, and Applications, in: Photocatalysis and Water Purification, Wiley, 2013: pp. 145–178. https://doi.org/10.1002/9783527645404.ch6

[42] A.M. Ismael, A.N. El-Shazly, S.E. Gaber, M.M. Rashad, A.H. Kamel, S.S.M. Hassan, Novel TiO_2/GO/$CuFe_2O_4$ nanocomposite: a magnetic, reusable and visible-light-driven photocatalyst for efficient photocatalytic removal of chlorinated pesticides from wastewater, RSC Adv. 10 (2020) 34806. https://doi.org/10.1039/D0RA02874F

[43] J. Wang, S. Wang, Activation of persulfate (PS) and peroxymonosulfate (PMS) and application for the degradation of emerging contaminants, Chem. Eng. J. 334 (2018) 1502. https://doi.org/10.1016/j.cej.2017.11.059

[44] S. Guerra-Rodríguez, E. Rodríguez, D.N. Singh, J. Rodríguez-Chueca, Assessment of sulfate radical-based advanced oxidation processes for water and wastewater treatment: A review, Water 10 (2018) 1828. https://doi.org/10.3390/w10121828

[45] V. Hasija, V.H. Nguyen, A. Kumar, P. Raizada, V. Krishnan, A.A.P. Khan, P. Singh, E. Lichtfouse, C. Wang, P. Thi Huong, Advanced activation of persulfate by polymeric g-C_3N_4 based photocatalysts for environmental remediation: A review, J. Hazard. Mater. 413 (2021) 125324. https://doi.org/10.1016/j.jhazmat.2021.125324

[46] C.E. Shuck, A. Sarycheva, M. Anayee, A. Levitt, Y. Zhu, S. Uzun, V. Balitskiy, V. Zahorodna, O. Gogotsi, Y. Gogotsi, Scalable Synthesis of $Ti_3C_2T_x$ MXene, Adv. Eng. Mater. 22 (2020) 1901241. https://doi.org/10.1002/adem.201901241

[47] J.A. Kumar, P. Prakash, T. Krithiga, D.J. Amarnath, J. Premkumar, N. Rajamohan, Y. Vasseghian, P. Saravanan, M. Rajasimman, Methods of synthesis, characteristics, and environmental applications of MXene: A comprehensive review, Chemosphere 286 (2022) 131607. https://doi.org/10.1016/j.chemosphere.2021.131607

[48] N.K. Chaudhari, H. Jin, B. Kim, D. San Baek, S.H. Joo, K. Lee, MXene: an emerging two-dimensional material for future energy conversion and storage applications, J. Mater. Chem. A Mater. 5 (2017) 24564. https://doi.org/10.1039/C7TA09094C

[49] J.C. Lei, X. Zhang, Z. Zhou, Recent advances in MXene: Preparation, properties, and applications, Front. Phys. 10 (2015) 276–286. https://doi.org/10.1007/s11467-015-0493-x

[50] X. Zhan, C. Si, J. Zhou, Z. Sun, MXene and MXene-based composites: synthesis, properties and environment-related applications, Nanoscale Horiz. 5 (2020) 235. https://doi.org/10.1039/C9NH00571D

[51] Z. Qin, T. Su, H. Ji, MXene-Based Photocatalysts, CRC Press, Boca Raton, 2021. https://doi.org/10.1201/9781003156963

[52] K. Luo, X.-H. Zha, Q. Huang, C.-T. Lin, M. Yang, S. Zhou, S. Du, First-principles study of magnetism in some novel MXene materials, RSC Adv. 10 (2020) 44430. https://doi.org/10.1039/D0RA03643A

[53] Y. Zhang, W. Xia, Y. Wu, P. Zhang, Prediction of MXene based 2D tunable band gap semiconductors: GW quasiparticle calculations, Nanoscale 11 (2019) 3993. https://doi.org/10.1039/C9NR01160A

[54] Y. Liu, H. Xiao, W.A. Goddard, Schottky-Barrier-Free Contacts with Two-Dimensional Semiconductors by Surface-Engineered MXenes, J. Am. Chem. Soc. 138 (2016) 15853. https://doi.org/10.1021/jacs.6b10834

[55] Y. Ibrahim, A. Mohamed, A.M. Abdelgawad, K. Eid, A.M. Abdullah, A. Elzatahry, The Recent Advances in the Mechanical Properties of Self-Standing Two-Dimensional MXene-Based

Nanostructures: Deep Insights into the Supercapacitor, Nanomaterials 10 (2020) 1916. https://doi.org/10.3390/nano10101916

[56] U. Yorulmaz, A. Özden, N.K. Perkgöz, F. Ay, C. Sevik, Vibrational and mechanical properties of single layer MXene structures: a first-principles investigation, Nanotechnology 27 (2016) 335702. https://doi.org/10.1088/0957-4484/27/33/335702

[57] H. Kim, Z. Wang, H.N. Alshareef, MXetronics: Electronic and photonic applications of MXenes, Nano Energy 60 (2019) 179. https://doi.org/10.1016/j.nanoen.2019.03.020

[58] G.R. Berdiyorov, Optical properties of functionalized $Ti_3C_2T_2$(T = F, O, OH) MXene: First-principles calculations, AIP Adv. 6 (2016) 055105. https://doi.org/10.1063/1.4948799

[59] D. Xu, Z. Li, L. Li, J. Wang, Insights into the Photothermal Conversion of 2D MXene Nanomaterials: Synthesis, Mechanism, and Applications, Adv. Funct. Mater. 30 (2020) 2000712. https://doi.org/10.1002/adfm.202000712

[60] Z. Huang, X. Cui, S. Li, J. Wei, P. Li, Y. Wang, C.S. Lee, Two-dimensional MXene-based materials for photothermal therapy, Nanophotonics 9 (2020) 2233. https://doi.org/10.1515/nanoph-2019-0571.

[61] S. Hao, H. Han, Z. Yang, M. Chen, Y. Jiang, G. Lu, L. Dong, H. Wen, H. Li, J. Liu, L. Wu, Z. Wang, F. Wang, Recent Advancements on Photothermal Conversion and Antibacterial Applications over MXenes-Based Materials, Nanomicro Lett. 14 (2022) 178. https://doi.org/10.1007/s40820-022-00901-w.

[62] V. Mauchamp, M. Bugnet, E.P. Bellido, G.A. Botton, P. Moreau, D. Magne, M. Naguib, T. Cabioc'h, M.W. Barsoum, Enhanced and tunable surface plasmons in two-dimensional Ti_3C_2 stacks: Electronic structure versus boundary effects, Phys. Rev. B. 89 (2014) 235428. https://doi.org/10.1103/PhysRevB.89.235428

[63] S.S. Siwal, H. Kaur, G. Chauhan, V.K. Thakur, MXene-Based Nanomaterials for Biomedical Applications: Healthier Substitute Materials for the Future, Adv. Nanobiomed Res. 3 (2023) 2200123. https://doi.org/10.1002/anbr.202200123

[64] Y. Wei, P. Zhang, R.A. Soomro, Q. Zhu, B. Xu, Advances in the Synthesis of 2D MXenes, Adv. Mater. 33 (2021) 2103148. https://doi.org/10.1002/adma.202103148

[65] M.P. Browne, D. Tyndall, V. Nicolosi, The potential of MXene materials as a component in the catalyst layer for the Oxygen Evolution Reaction, Curr. Opin. Electrochem. 34 (2022) 101021. https://doi.org/10.1016/j.coelec.2022.101021

[66] O. Mashtalir, M. Naguib, B. Dyatkin, Y. Gogotsi, M.W. Barsoum, Kinetics of aluminum extraction from Ti_3AlC_2 in hydrofluoric acid, Mater. Chem. Phys. 139 (2013) 147. https://doi.org/10.1016/j.matchemphys.2013.01.008

[67] F. Liu, A. Zhou, J. Chen, J. Jia, W. Zhou, L. Wang, Q. Hu, Preparation of Ti_3C_2 and Ti_2C MXenes by fluoride salts etching and methane adsorptive properties, Appl. Surf. Sci. 416 (2017) 781. https://doi.org/10.1016/j.apsusc.2017.04.239

[68] M. Li, J. Lu, K. Luo, Y. Li, K. Chang, K. Chen, J. Zhou, J. Rosen, L. Hultman, P. Eklund, P.O.Å. Persson, S. Du, Z. Chai, Z. Huang, Q. Huang, Element Replacement Approach by Reaction with Lewis Acidic Molten Salts to Synthesize Nanolaminated MAX Phases and MXenes, J. Am. Chem. Soc. 141 (2019) 4730. https://doi.org/10.1021/jacs.9b00574

[69] T. Li, L. Yao, Q. Liu, J. Gu, R. Luo, J. Li, X. Yan, W. Wang, P. Liu, B. Chen, W. Zhang, W. Abbas, R. Naz, D. Zhang, Fluorine-Free Synthesis of High-Purity $Ti_3C_2T_x$ (T=OH, O) via Alkali Treatment, Angewandte Chemie International Edition. 57 (2018) 6115. https://doi.org/10.1002/anie.201800887

[70] W. Zhu, S. Panda, C. Lu, Z. Ma, D. Khan, J. Dong, F. Sun, H. Xu, Q. Zhang, J. Zou, Using a Self-Assembled Two-Dimensional MXene-Based Catalyst (2D-Ni@Ti_3C_2) to Enhance Hydrogen Storage Properties of MgH_2, ACS Appl Mater Interfaces. 12 (2020) 50333. https://doi.org/10.1021/acsami.0c12767

[71] Y.Z. Zhang, J.K. El-Demellawi, Q. Jiang, G. Ge, H. Liang, K. Lee, X. Dong, H.N. Alshareef, MXene hydrogels: fundamentals and applications, Chem. Soc. Rev. 49 (2020) 7229. https://doi.org/10.1039/D0CS00022A

[72] X. Xie, Z. Wu, N. Zhang, Robust and easily retrievable Pd/Ti_3C_2T ⊂graphene hydrogels for efficient catalytic hydrogenation of nitroaromatic compounds, Chinese Chemical Letters. 31 (2020) 1014. https://doi.org/10.1016/j.cclet.2019.10.012

[73] F. Han, S. Luo, L. Xie, J. Zhu, W. Wei, X. Chen, F. Liu, W. Chen, J. Zhao, L. Dong, K. Yu, X. Zeng, F. Rao, L. Wang, Y. Huang, Boosting the Yield of MXene 2D Sheets via a Facile Hydrothermal-Assisted Intercalation, ACS Appl. Mater. Interfaces. 11 (2019) 8443. https://doi.org/10.1021/acsami.8b22339

[74] M. Alhabeb, K. Maleski, B. Anasori, P. Lelyukh, L. Clark, S. Sin, Y. Gogotsi, Guidelines for Synthesis and Processing of Two-Dimensional Titanium Carbide ($Ti_3C_2T_x$ MXene), Chemistry of Materials 29 (2017) 7633. https://doi.org/10.1021/acs.chemmater.7b02847.

[75] K. Zhang, D. Li, H. Cao, Q. Zhu, C. Trapalis, P. Zhu, X. Gao, C. Wang, Insights into different dimensional MXenes for photocatalysis, Chem. Eng. J. 424 (2021) 130340. https://doi.org/10.1016/j.cej.2021.130340

[76] X. Chen, J. Li, G. Pan, W. Xu, J. Zhu, D. Zhou, D. Li, C. Chen, G. Lu, H. Song, Ti_3C_2 MXene quantum dots/TiO_2 inverse opal heterojunction electrode platform for superior photoelectrochemical biosensing, Sens Actuators B Chem. 289 (2019) 131. https://doi.org/10.1016/j.snb.2019.03.052

[77] A.S. Sharbirin, S. Akhtar, J. Kim, Light-emitting MXene quantum dots, Opto-Electronic Advances. 4 (2021) 200077. https://doi.org/10.29026/oea.2021.200077

[78] Q. Xue, H. Zhang, M. Zhu, Z. Pei, H. Li, Z. Wang, Y. Huang, Y. Huang, Q. Deng, J. Zhou, S. Du, Q. Huang, C. Zhi, Photoluminescent Ti_3C_2 MXene Quantum Dots for Multicolor Cellular Imaging, Adv. Mater. 29 (2017) 1604847. https://doi.org/10.1002/adma.201604847

[79] W. Kong, Y. Niu, M. Liu, K. Zhang, G. Xu, Y. Wang, X. Wang, Y. Xu, J. Li, One-step hydrothermal synthesis of fluorescent MXene-like titanium carbonitride quantum dots, Inorg. Chem. Commun. 105 (2019) 151. https://doi.org/10.1016/j.inoche.2019.04.033

[80] P. Kuang, J. Low, B. Cheng, J. Yu, J. Fan, MXene-based photocatalysts, J. Mater. Sci. Technol. 56 (2020) 18. https://doi.org/10.1016/j.jmst.2020.02.037

[81] Z. You, Y. Liao, X. Li, J. Fan, Q. Xiang, State-of-the-art recent progress in MXene-based photocatalysts: a comprehensive review, Nanoscale 13 (2021) 9463. https://doi.org/10.1039/D1NR02224E

[82] S. Cao, B. Shen, T. Tong, J. Fu, J. Yu, 2D/2D Heterojunction of Ultrathin MXene/Bi_2WO_6 Nanosheets for Improved Photocatalytic CO_2 Reduction, Adv. Funct. Mater. 28 (2018) 1800136. https://doi.org/10.1002/adfm.201800136

[83] C. Yang, Q. Tan, Q. Li, J. Zhou, J. Fan, B. Li, J. Sun, K. Lv, 2D/2D Ti_3C_2 MXene/g-C_3N_4 nanosheets heterojunction for high efficient CO_2 reduction photocatalyst: Dual effects of urea, Appl. Catal. B 268 (2020) 118738. https://doi.org/10.1016/j.apcatb.2020.118738

[84] A. Pan, X. Ma, S. Huang, Y. Wu, M. Jia, Y. Shi, Y. Liu, P. Wangyang, L. He, Y. Liu, $CsPbBr_3$ Perovskite Nanocrystal Grown on MXene Nanosheets for Enhanced Photoelectric Detection

and Photocatalytic CO_2 Reduction, J. Phys. Chem. Lett. 10 (2019) 6590. https://doi.org/10.1021/acs.jpclett.9b02605

[85] M. Ye, X. Wang, E. Liu, J. Ye, D. Wang, Boosting the Photocatalytic Activity of P25 for Carbon Dioxide Reduction by using a Surface-Alkalinized Titanium Carbide MXene as Cocatalyst, ChemSusChem 11 (2018) 1606. https://doi.org/10.1002/cssc.201800083

[86] M.F. Khadidja, J. Fan, S. Li, S. Li, K. Cui, J. Wu, W. Zeng, H. Wei, H.G. Jin, N. Naik, Z. Chao, D. Pan, Z. Guo, Hierarchical ZnO/MXene composites and their photocatalytic performances, Colloids Surf. A Physicochem. Eng. Asp. 628 (2021) 127230. https://doi.org/10.1016/j.colsurfa.2021.127230

[87] W. Zhou, B. Yu, J. Zhu, K. Li, S. Tian, Hierarchical ZnO/MXene (Nb_2C and V_2C) heterostructure with efficient electron transfer for enhanced photocatalytic activity, Appl. Surf. Sci. 590 (2022) 153095. https://doi.org/10.1016/j.apsusc.2022.153095

[88] H. Zhang, M. Li, J. Cao, Q. Tang, P. Kang, C. Zhu, M. Ma, 2D a-Fe_2O_3 doped Ti_3C_2 MXene composite with enhanced visible light photocatalytic activity for degradation of Rhodamine B, Ceram Int. 44 (2018) 19958. https://doi.org/10.1016/j.ceramint.2018.07.262.

[89] H. Xu, R. Xiao, J. Huang, Y. Jiang, C. Zhao, X. Yang, In situ construction of protonated g-C_3N_4/Ti_3C_2 MXene Schottky heterojunctions for efficient photocatalytic hydrogen production, Chinese Journal of Catalysis. 42 (2021) 107. https://doi.org/10.1016/S1872-2067(20)63559-8

[90] L. Tie, S. Yang, C. Yu, H. Chen, Y. Liu, S. Dong, J. Sun, J. Sun, In situ decoration of ZnS nanoparticles with Ti_3C_2 MXene nanosheets for efficient photocatalytic hydrogen evolution, J. Colloid. Interface Sci. 545 (2019) 63. https://doi.org/10.1016/j.jcis.2019.03.014

[91] J. Huang, M. Wang, X. Zhang, J. Tao, L. Lu, G. Qiao, G. Liu, Anchoring of 2D CdS on Nb_2CT_X MXene nanosheets for boosting photocatalytic H_2 evolution, J. Alloys Compd. 923 (2022) 166256. https://doi.org/10.1016/j.jallcom.2022.166256

[92] Y. Zhang, Y. Huang, B. Lin, Z. Chen, X. Xu, M. Pan, Ti_3C_2T MXene supported ZnO nanocomposites with highly efficient photocatalytic performance for degradation of VOCs, Diam. Relat. Mater. 133 (2023) 109763. https://doi.org/10.1016/j.diamond.2023.109763

[93] G. Huang, S. Li, L. Liu, L. Zhu, Q. Wang, Ti_3C_2 MXene-modified Bi_2WO_6 nanoplates for efficient photodegradation of volatile organic compounds, Appl. Surf. Sci. 503 (2020) 144183. https://doi.org/10.1016/j.apsusc.2019.144183

[94] X. Zou, X. Zhao, J. Zhang, W. Lv, L. Qiu, Z. Zhang, Photocatalytic degradation of ranitidine and reduction of nitrosamine dimethylamine formation potential over MXene–Ti_3C_2/MoS_2 under visible light irradiation, J. Hazard. Mater. 413 (2021) 125424. https://doi.org/10.1016/j.jhazmat.2021.125424

[95] M. Yu, H. Liang, R. Zhan, L. Xu, J. Niu, Sm-doped g-C_3N_4/Ti_3C_2 MXene heterojunction for visible-light photocatalytic degradation of ciprofloxacin, Chinese Chemical Letters. 32 (2021) 2155. https://doi.org/10.1016/j.cclet.2020.11.069

[96] C. Cui, R. Guo, H. Xiao, E. Ren, Q. Song, C. Xiang, X. Lai, J. Lan, S. Jiang, Bi_2WO_6/Nb_2CT_x MXene hybrid nanosheets with enhanced visible-light-driven photocatalytic activity for organic pollutants degradation, Appl. Surf. Sci. 505 (2020) 144595. https://doi.org/10.1016/j.apsusc.2019.144595

[97] D. Zhao, C. Cai, Preparation of Bi_2MoO_6/Ti_3C_2 MXene heterojunction photocatalysts for fast tetracycline degradation and Cr(VI) reduction, Inorg. Chem. Front. 7 (2020) 2799. https://doi.org/10.1039/D0QI00540A

[98] S. Guo, H. Luo, Y. Bao, Y. Li, H. Guan, Y. Zhu, Construction of hierarchical $Ti_3C_2T_x$ MXene/$ZnIn_2S_4$ heterostructures for efficiently photocatalytic reduction of Cr(VI) under visible light, Appl. Surf. Sci. 575 (2022) 151753. https://doi.org/10.1016/j.apsusc.2021.151753

[99] H. T. Ren, Z. Pan, W.B. Cao, T.T. Li, C.W. Lou, J.H. Lin, X. Han, Facile synthesis of Ti_3C_2 MXene-modified $Bi_{2.15}WO_6$ nanosheets with enhanced reactivity for photocatalytic reduction of Cr(VI), Adv. Powder Technol. 33 (2022) 103722. https://doi.org/10.1016/j.apt.2022.103722

[100] M. Cao, F. Wang, L. Wang, W. Wu, W. Lv, J. Zhu, Room Temperature Oxidation of Ti_3C_2 MXene for Supercapacitor Electrodes, J. Electrochem. Soc. 164 (2017) A3933. https://doi.org/10.1149/2.1541714jes

[101] J. Low, L. Zhang, T. Tong, B. Shen, J. Yu, TiO_2/MXene Ti_3C_2 composite with excellent photocatalytic CO_2 reduction activity, J. Catal. 361 (2018) 255. https://doi.org/10.1016/j.jcat.2018.03.009

[102] Y. Li, X. Deng, J. Tian, Z. Liang, H. Cui, Ti_3C_2 MXene-derived Ti_3C_2/TiO_2 nanoflowers for noble-metal-free photocatalytic overall water splitting, Appl. Mater. Today 13 (2018) 217. https://doi.org/10.1016/j.apmt.2018.09.004

[103] C. Peng, X. Yang, Y. Li, H. Yu, H. Wang, F. Peng, Hybrids of Two-Dimensional Ti_3C_2 and TiO_2 Exposing {001} Facets toward Enhanced Photocatalytic Activity, ACS Appl. Mater. Interfaces 8 (2016) 6051. https://doi.org/10.1021/acsami.5b11973

[104] C. Peng, H. Wang, H. Yu, F. Peng, (111) TiO_{2-x}/Ti_3C_2: Synergy of active facets, interfacial charge transfer and Ti^{3+} doping for enhance photocatalytic activity, Mater. Res. Bull. 89 (2017) 16. https://doi.org/10.1016/j.materresbull.2016.12.049

[105] S. Liu, M. Wang, G. Liu, N. Wan, C. Ge, S. Hussain, H. Meng, M. Wang, G. Qiao, Enhanced NO_2 gas-sensing performance of 2D Ti_3C_2/TiO_2 nanocomposites by in-situ formation of Schottky barrier, Appl. Surf. Sci. 567 (2021) 150747. https://doi.org/10.1016/j.apsusc.2021.150747

[106] V.Q. Hieu, T.K. Phung, T.-Q. Nguyen, A. Khan, V.D. Doan, V.A. Tran, V.T. Le, Photocatalytic degradation of methyl orange dye by Ti_3C_2–TiO_2 heterojunction under solar light, Chemosphere 276 (2021) 130154. https://doi.org/10.1016/j.chemosphere.2021.130154

[107] T. Su, R. Peng, Z.D. Hood, M. Naguib, I.N. Ivanov, J.K. Keum, Z. Qin, Z. Guo, Z. Wu, One-Step Synthesis of Nb_2O_5/C/Nb_2C (MXene) Composites and Their Use as Photocatalysts for Hydrogen Evolution, ChemSusChem 11 (2018) 688. https://doi.org/10.1002/cssc.201702317

[108] X. Bao, H. Li, Z. Wang, F. Tong, M. Liu, Z. Zheng, P. Wang, H. Cheng, Y. Liu, Y. Dai, Y. Fan, Z. Li, B. Huang, TiO_2/Ti_3C_2 as an efficient photocatalyst for selective oxidation of benzyl alcohol to benzaldehyde, Appl. Catal. B 286 (2021) 119885. https://doi.org/10.1016/j.apcatb.2021.119885

[109] X. Wang, Y. Yang, G. Lu, G. Shi, Y. Wang, R. Wang, X. Xie, J. Sun, In-situ preparation of Ti_3C_2/Ti^{3+}-TiO_2 composites with mosaic structures for the adsorption and Photo-degradation of flowing acetaldehyde under visible light, Appl. Surf. Sci. 531 (2020) 147101. https://doi.org/10.1016/j.apsusc.2020.147101

[110] L. Chen, Y. Huang, R. Zou, J. Ma, Y. Yang, T. Li, M. Li, Q. Hao, H. Xie, X. Peng, Regulating TiO_2/MXenes catalysts to promote photocatalytic performance of highly selective oxidation of D-xylose, Green Chemistry 23 (2021) 1382. https://doi.org/10.1039/D0GC03628E

[111] C. Cui, R. Guo, E. Ren, H. Xiao, X. Lai, Q. Qin, S. Jiang, H. Shen, M. Zhou, W. Qin, Facile hydrothermal synthesis of rod-like Nb_2O_5/Nb_2CT_x composites for visible-light driven photocatalytic degradation of organic pollutants, Environ. Res. 193 (2021) 110587. https://doi.org/10.1016/j.envres.2020.110587

[112] Y. Wang, G. Tan, S. Feng, M. Wang, B. Zhang, Y. Liu, W. Liu, Y. Bi, Q. Yang, T. Liu, Y. Liu, A. Xia, H. Ren, L. Lv, Preparation of Exposed (001) Crystal Plane Tio_2/Ti_3C_2 Mxene and Enhanced Full Spectrum Degradation of Antibiotics, SSRN Electronic Journal (2022). https://doi.org/10.2139/ssrn.4109990

[113] Y. Wang, X. Hu, H. Song, Y. Cai, Z. Li, D. Zu, P. Zhang, D. Chong, N. Gao, Y. Shen, C. Li, Oxygen vacancies in actiniae-like Nb_2O_5/Nb_2C MXene heterojunction boosting visible light photocatalytic NO removal, Appl. Catal. B. 299 (2021) 120677. https://doi.org/10.1016/j.apcatb.2021.120677

8. Cel i zakres pracy

8.1. Cel pracy

Celem pracy było zastosowanie materiałów nowej generacji – MXenów w procesie fotokatalitycznej degradacji zanieczyszczeń z grupy aktywnych substancji farmaceutycznych. Ponadto, przeprowadzone prace badawcze miały na celu optymalizację warunków syntezy fotokatalizatorów opartych na MXenach. W kolejnych etapach pracy dążono do określenia wpływu modyfikacji kompozytów na właściwości fizykochemiczne i aktywność fotokatalityczną. Prace badawcze obejmowały preparatykę materiałów, ich charakterystykę fizykochemiczną oraz analizę aktywności fotokatalitycznej w reakcjach degradacji wybranych substancji farmaceutycznych: karbamazepiny, acetaminofenu i ibuprofenu, jak również określenie mechanizmów reakcji fotodegradacji wybranych zanieczyszczeń farmaceutycznych.

8.2. Tezy badawcze

Na podstawie omówienia literatury przedmiotu oraz wstępnych badań własnych zostały sformułowane następujące tezy pracy:

1. Związek z grupy MXenów – $Ti_3C_2T_x$ może być z zastosowany w roli ko-katalizatora lub jako prekursor do otrzymywania fotokatalizatora o zdefiniowanej morfologii do efektywnej degradacji aktywnych substancji farmaceutycznych.
2. Obecność $Ti_3C_2T_x$ działającego jako rezerwuar fotogenerowanych elektronów może wpływać na separację nośników ładunku, a tym samym efektywność procesu fotodegradacji zanieczyszczeń organicznych.
3. Parametry syntezy kompozytu TiO_2/Ti_3C_2, takie jak temperatura, czas, środowisko reakcji determinują właściwości fizykochemiczne otrzymanych materiałów i ich aktywność fotokatalityczną w reakcjach degradacji farmaceutyków.
4. Modyfikacja powierzchni TiO_2/Ti_3C_2 za pomocą Cu oraz Fe może wpływać na wzrost aktywności fotokatalitycznej w zakresie światła UV-vis oraz efektywną separację nośników ładunku.
5. Modyfikacja kompozytu TiO_2/Ti_3C_2 za pomocą ferrytu spinelowego umożliwia separację magnetyczną fotokatalizatora po procesie oczyszczania wody.

6. Modyfikacji powierzchni materiału fotokatalitycznego za pomocą Fe, Mn lub Cu wpływa na aktywację PMS i przyczynia się do wzrostu efektywności fotodegradacji karbamazepiny i ibuprofenu.

8.3. Zakres pracy

8.3.1 Synteza materiałów

– *Otrzymywanie $Ti_3C_2T_x$*

$Ti_3C_2T_x$ otrzymano przez wytrawianie aluminium ze związku fazy MAX – Ti_3AlC_2. 10 g Ti_3AlC_2 dodawano stopniowo do 100 cm^3 48% HF i mieszano w temperaturze pokojowej przez 24 godziny. Następnie materiał odwirowano i przemyto wodą dejonizowaną do odczynu obojętnego. Produkt suszono w temperaturze 50°C do stałej masy.

– *Otrzymywanie kompozytu Zn/Ti LDH/Ti_3C_2*

$Ti_3C_2T_x$ (0,5, 2,5 i 5% wag.) zdyspergowano w 100 cm^3 wody dejonizowanej i poddano działaniu ultradźwięków przez 30 minut. Do powyższej zawiesiny dodano 1,19 g sześciowodnego azotanu cynku. Następnie wkroplono 0,22 cm^3 $TiCl_4$. W kolejnym kroku dodano 3,0 g mocznika i mieszano za pomocą mieszadła magnetycznego przez 30 minut. Następnie zawiesinę przeniesiono do reaktora ze stali nierdzewnej z wkładem teflonowym o pojemności 200 cm^3. Reakcję prowadzono w temperaturze 130°C przez 48 godzin. Otrzymany materiał wielokrotnie odwirowywano i przemywano wodą dejonizowaną do odczynu obojętnego. Produkt suszono w temperaturze 50°C do stałej masy.

– *Otrzymywanie kompozytu TiO_2/Ti_3C_2*

W celu określenia wpływu morfologii TiO_2 na aktywność fotokatalityczną, kompozyty TiO_2/Ti_3C_2 otrzymano z wykorzystaniem czterech metod syntezy:

- *Metoda I.*

0,4 g $Ti_3C_2T_x$ zdyspergowano w mieszaninie 59,2 cm^3 wody dejonizowanej i 0,8 cm^3 kwasu fluoroborowego. Mieszano przez 30 minut a następnie poddano działaniu ultradźwięków przez 10 minut. W kolejnym kroku zawiesinę przeniesiono do reaktora ze stali nierdzewnej z wkładem teflonowym o pojemności 200 cm^3. Reakcję prowadzono w temperaturze od 140 do 220°C przez 12 do 24 godzin. Otrzymany materiał przemyto kilkukrotnie wodą dejonizowaną i suszono w temperaturze 50°C do stałej masy.

- *Metoda II.*

0,4 g $Ti_3C_2T_x$ zdyspergowano w mieszaninie 60 cm^3 wody dejonizowanej, lub 30 cm^3 wody dejonizowanej i 30 cm^3 etanolu, lub 60 cm^3 etanolu . Mieszano przez 30 minut a następnie poddano działaniu ultradźwięków przez 15 minut. W kolejnym kroku zawiesinę przeniesiono do reaktora ze stali nierdzewnej z wkładem teflonowym o pojemności 200 cm^3. Reakcję prowadzono w temperaturze od 180 do 220°C przez 6-24 godzin. Otrzymany materiał przemyto kilkukrotnie wodą dejonizowaną i suszono w temperaturze 50°C do stałej masy.

- *Metoda III.*

W pierwszym kroku zmieszano 60 cm^3 3 M HCl z 0,1 g NH_4F. Następnie do dodano 0,4 g $Ti_3C_2T_x$ i poddano działaniu ultradźwięków przez 10 minut. Następnie zawiesinę mieszano przez 30 minut i przeniesiono do reaktora ze stali nierdzewnej z wkładem teflonowym o pojemności 200 cm^3. Reakcję prowadzono w temperaturze 220°C przez 24 godziny. Otrzymany materiał przemyto kilkukrotnie wodą dejonizowaną i suszono w temperaturze 50°C do stałej masy.

- *Metoda IV.*

0,4 g $Ti_3C_2T_x$ umieszczono w tyglu ceramicznym i poddano kalcynacji w temperaturze 550°C przez 4 godziny.

– *Otrzymywanie kompozytu Fe-TiO_2/Ti_3C_2*

Kompozyt TiO_2/Ti_3C_2 syntetyzowano w temperaturze 140°C przez 12 godzin i w temperaturze 220°C przez 24 godziny zgodnie z metodą I. W kolejnym kroku na szkiełko nałożono cienkie warstwy TiO_2/Ti_3C_2 i suszono w temperaturze 80°C przez 1 godzinę. Osadzanie żelaza na powierzchni TiO_2/Ti_3C_2 przeprowadzono za pomocą magnetronowego systemu napylania katodowego (Q150S, Quorum Technologies, Lewes, Wielka Brytania) z Fe o wysokiej czystości (99,5%, EM-Tec). Grubość Fe kontrolowano za pomocą mikrowagi kwarcowej i ustawiono na 20 nm.

– *Otrzymywanie kompozytu Cu-TiO_2/Ti_3C_2*

W pierwszym etapie 0,4 g $Ti_3C_2T_x$ zdyspergowano w 60 cm^3 mieszaniny woda/etanol (58%:42% obj./obj.). Następnie dodano odpowiednią objętość wodnego roztworu $Cu(NO_3)_2 \cdot 3H_2O$ odpowiadającą 0,25% wag., 0,5% wag. i 1% wag. Cu. Zawiesinę poddano działaniu ultradźwieków przez 10 minut i mieszano przez kolejne 30 min. Kolejno przeniesiono do

reaktora ze stali nierdzewnej z wkładem teflonowym o pojemności 200 cm^3 i syntezę prowadzono przez 17 godzin w temperaturze 220°C.

– *Otrzymywanie kompozytu $TiO_2/Ti_3C_2/MnFe_2O_4$*

Nanocząstki magnetyczne przygotowano poprzez rozpuszczenie w 100 cm^3 wody dejonizowanej, $FeCl_3 \cdot 6H_2O$ i $MnCl_2$ w stosunku molowym 2:1. Następnie wkraplano 0,5 M roztwór NaOH, do osiągnięcia pH 10. Zawiesinę przeniesiono do reaktora ze stali nierdzewnej z wkładem teflonowym. Reakcję prowadzono w temperaturze 180°C przez 6 godzin. Otrzymany materiał oddzielono za pomocą magnesu, przemyto 3 razy wodą dejonizowaną i wysuszono w temperaturze 50°C do stałej masy. TiO_2/Ti_3C_2 otrzymano zgodnie z metodą III. Kompozyty z 5% wag. i 20% wag. $MnFe_2O_4$ przygotowano metodą samoorganizacji wspomaganej ultradźwiękami. W tym celu 0,5 g TiO_2/Ti_3C_2 zdyspergowano w 50 cm^3 mieszaniny woda/etanol (1:4 obj./obj.), natomiast odpowiednią ilość $MnFe_2O_4$ zdyspergowano w 50 cm^3 mieszaniny woda/etanol (1:4 obj./obj.). Obie zawiesiny poddano działaniu ultradźwięków przez 15 minut. Następnie dyspersję $MnFe_2O_4$ wkraplano do zawiesiny TiO_2/Ti_3C_2. Tak przygotowany materiał mieszano przez 1 godzinę mieszadłem mechanicznym. Przygotowany kompozyt oddzielono magnesem i przemyto 3-krotnie wodą dejonizowaną. Na koniec suszono w temperaturze 50°C do stałej masy.

8.3.2. Charakterystyka właściwości fizykochemicznych nanomateriałów

– *Dyfrakcja rentgenowska (XRD)*

Skład fazowy oraz wielkość krystalitów fotokatalizatora określono z wykorzystaniem proszkowej dyfrakcji rentgenowskiej. Analizę przeprowadzono za pomocą aparatu Rigaku Intelligent X-ray diffraction system SmartLab (Rigaku Corporation, Tokio, Japonia), wyposażonego w generator promieni X, działający z zastosowaniem promieniowania Cu Kα (40 kV, 30 mA). Skany wykonywano w zakresie kąta 2θ od 5° do 80°, z szybkością $2°min^{-1}$ i krokiem skanowania 0,01°.

– *Analiza powierzchni właściwej metodą Brunauera-Emmetta-Tellera (BET)*

Izotermy adsorpcji-desorpcji analizowano w temperaturze 77K z wykorzystaniem aparatu Micromeritics Gemini V (model 2365, Norcross, GA, USA). Powierzchnię właściwą oraz objętość porów określono przy użyciu wielopunktowej metody BET.

– *Spektroskopia rozproszonego odbicia w zakresie UV-Vis (DR/UV-vis)*

Widma rozproszonego odbicia rejestrowano w zakresie długości fali 200-800 nm z wykorzystaniem spektrofotometru ThermoScientific Evolution 220 (Waltham, MA, USA). Jako materiał odniesienia wykorzystano siarczan baru. Przerwę energetyczną fotokatalizatorów obliczono w oparciu o funkcję Kubelka-Munka.

– *Pomiary fotoluminescencyjne*

Widma emisyjne i krzywe zaniku luminescencji uzyskano za pomocą spektrografu siatkowego (Princeton Instr. Model Acton 2500i) sprzężonego z kamerą CCD (Hamamatsu Model C5680), która działa w obszarze widmowym 200–1100 nm z rozdzielczością czasową 20 ps. Jako źródło wzbudzenia zastosowano laser femtosekundowy (model koherentny „Libra") sprzężony z optycznym wzmacniaczem parametrycznym (model konwersji światła „OPerA"). Widma fotoluminescencyjne rejestrowano także przy użyciu spektrofluorometru Shimadzu RF-6000 (Kyoto, Japonia). Jako źródło wzbudzenia zastosowano lampę ksenonową o mocy 150 W i długości fali wzbudzenia 300 nm.

– *Spektroskopia w podczerwieni z transformacją Fouriera (FTIR)*

Badanie fotokatalizatora przed i po naświetlaniu przeprowadzono za pomocą spektroskopii w podczerwieni z transformacją Fouriera. Pomiary przeprowadzono za pomocą spektrometru Nicolet iS10 (Thermo Fisher Scientific Waltham) w temperaturze pokojowej. Pomiary prowadzono w zakresie liczby falowej od 4000 do 400 cm^{-1}.

– *Analiza skaningowym mikroskopem elektronowym (SEM)*

Morfologię powierzchni fotokatalizatorów analizowano za pomocą skaningowej mikroskopii elektronowej stosując mikroskop SEM FEI Quanta FEG 250 lub z wykorzystaniem skaningowego mikroskopu elektronowego (Quanta 3D FEG, FEI Europe) z detektorem elektronów wtórnych (detektor Everharta-Thornleya)

– *Analiza transmisyjnym mikroskopem elektronowym (TEM)*

Analizy za pomocą transmisyjnej mikroskopii elektronowej i skaningowej transmisyjnej mikroskopii elektronowej (STEM) przeprowadzono przy użyciu Tecnai G2 200 kV i Thermo-Fisher Scientific Titan Themis Cs-corrector lub za pomocą transmisyjnego mikroskopu elektronowego (model Tecnai F20 X-Twin) sprzężonego z technikami spektroskopowymi (EDS, EELS). W trybie TEM do obrazowania zastosowano detektor ciemnego pola (DF). W trybie

STEM do obrazowania wykorzystano wysokokątowy detektor pierścieniowy ciemnego pola (HAADF) oraz do analizy pierwiastków zastosowano spektrometr z dyspersją energii (EDS) RTEM SN9577+ firmy EDAX (Pleasanton, USA) lub równoległą spektroskopię strat energii elektronów (PEELS) firmy Gatan (Pleasanton, USA).

– *Analiza rentgenowskiej spektroskopii fotoelektronów (XPS)*

Chemię powierzchni próbek analizowano metodą XPS przy użyciu multispektroskopu Escalab 250Xi (ThermoFisher Scientific). Spektroskop pracuje z monochromatycznym źródłem promieniowania rentgenowskiego AlKα. Kompensację ładunku zapewniało bombardowanie elektronami o niskiej energii i jonami Ar+ w trakcie całego pomiaru, z końcową kalibracją dla sygnału pochodzącego od węgla C1s (284,8 eV). Dekonwolucję widm przeprowadzono przy użyciu oprogramowania Avantage 5.9921 (ThermoFisher Scientific). Analizy XPS przeprowadzono także przy użyciu wielokomorowego systemu UHV PREVAC. Źródłem wzbudzenia fotoelektronów była lampa rentgenowska VG Scienta SAX 100 z aluminiową anodą wyposażoną w monochromator VG Scienta XM 780, emitująca promieniowanie Al Kα o energii 1486,6 eV. Dekonwolucję widm przeprowadzono przy użyciu CasaXPS wersja 2.3.25 PR1.

– *Pomiary elektrochemiczne*

Pomiary elektrochemicznej spektroskopii impedancyjnej (EIS) przeprowadzono przy użyciu potentiostatu/galwanostatu Autolab PGSTAT204 (Metrohm Autolab) z zastosowaniem Na_2SO_4 (0,5 M) jako elektrolitu. Materiały fotokatalityczne osadzano na elektrodach weglowych drukowanych metodą sitodruku z elektrodą odniesienia Ag/AgCl (Metrohm Autolab). Średnica elektrody pracującej wynosiła 4 mm. Amplituda napięcia przemiennego wynosiła 0,01 V, a częstotliwość zmieniała się od 0,1 Hz do 100 kHz przy 0V względem elektrody referencyjnej. Analizę Motta Schottky'ego przeprowadzono w celu określenia potencjału pasma płaskiego (Fb). Dane EIS rejestrowano od kierunku anodowego w kierunku katodowym, dla częstotliwości 1000 Hz w zakresie potencjału od 0 do -1,1 V vs. Ag/AgCl.

W przypadku zastosowania drugiej metodyki, fotokatalizatory nanoszono na szkło z tlenku cyny domieszkowanego fluorem (FTO) i stosowano jako elektrodę pracującą w układzie trójelektrodowym, gdzie jako elektrodę odniesienia i przeciwelektrodę zastosowano odpowiednio Ag/AgCl/0,1 M KCl i siatkę Pt. Jako elektrolit zastosowano odpowietrzony 0,5 M roztwór Na_2SO_4. Dane EIS rejestrowano od kierunku anodowego w kierunku katodowym dla zastosowanej częstotliwości 1000 Hz w zakresie potencjałów od 0,1 do 1,2 V vs. Ag/AgCl/0,1 M

KCl przy amplitudzie sygnału AC 10 mV. Warunki kontrolowano za pomocą potencjostatu-galwanostatu Biologic SP-150.

– *Właściwości magnetyczne*

Magnetometr SQUID (Quantum Design MPMS XL7) zastosowano do charakteryzowania właściwości magnetycznych próbek (pętle histerezy w temperaturze pokojowej i namagnesowanie w funkcji temperatury od 10 do 300 K).

8.3.3. Badanie aktywności fotokatalitycznej

Proces fotokatalitycznej degradacji zanieczyszczeń prowadzono w reaktorze szklanym o objętości 25 cm^3 z okienkiem ze szkła kwarcowego. Reaktor wyposażony był w płaszcz wodny umożliwiający utrzymywanie stałej temperatury procesu na poziomie 25°C. Dodatkowo do układu doprowadzano powietrze. Jako źródło światła wykorzystywano lampę ksenonową o mocy 300 W emitującą promieniowanie odpowiadające spektrum światła słonecznego. Stężenie API wynosiło odpowiednio 14 mg/dm^3 dla roztworu karbamazepiny i 20 mg/dm^3 dla roztworu acetaminofenu lub ibuprofenu. Z kolei w przypadku roztworu stanowiącego mieszaninę karbamazepiny i ibuprofenu, stężenie CBZ wynosiło 7 mg/dm^3 a ibuprofenu 10 mg/dm^3. Zawartość fotokatalizatora wynosiła 2g/dm^3. Układ kondycjonowano w ciemności przez 30 minut w celu zapewnienia równowagi procesów adsorpcji-desorpcji. Podczas procesu fotodegradacji pobierano 1 cm^3 zawiesiny w 0, 20, 40 i 60 minucie i fotokatalizator separowano za pomocą filtra strzykawkowego (0,2 µm).

Doświadczenia prowadzono także z dodatkiem PMS do mieszaniny reakcyjnej zawierającej fotokatalizator (stężenie w roztworze równe 0,0625-0,5 mM). Po odseparowaniu fotokatalizatora do próbek roztworu dodawano 200 µl metanolu w celu wygaszenia aktywności wytworzonych rodników.

Dodatkowe analizy przeprowadzono w modelowej wodzie morskiej w celu oceny wpływu jonów nieorganicznych na efektywność procesów fotokatalitycznych. Modelowa woda morska zawierała 2,5% NaCl, 1,1% $MgCl_2$, 0,4% Na_2SO_4, 0,16% $CaCl_2$ w wodzie dejonizowanej.

Ponadto zbadano wpływ pH roztworu. W tym celu pH roztworu korygowano za pomocą 0,1 M HCl lub 0,1 M NaOH.

Celem analizy reaktywnych form tlenu uczestniczących w reakcjach usuwania substancji farmaceutycznych, procesy fotokatalityczne prowadzono w obecności zmiataczy ładunku. Zastosowano szczawian amonu jako zmiatacz dziur (h^+), tert-butanol dla wolnych rodników hydroksylowych (•OH), izopropanol dla rodników hydroksylowych i rodników siarczanowych

(•OH i $•SO_4^-$), p-benzochinon do wychwytywania anionów rodników ponadtlenkowych ($•O_2^-$) oraz $AgNO_3$ do wychwytywania elektronów (e^-). Z kolei, w celu oceny stabilności i możliwości ponownego wykorzystania fotokatalizatora po każdym procesie oddzielano fotokatalizator od roztworu i wlewano świeżą porcję roztworu API. Fotokatalizator zastosowano bez dodatkowej obróbki. Wydajność fotokatalityczną oceniano w czterech kolejnych cyklach degradacji, prowadzonych w tych samych warunkach.

8.3.4. Analiza efektywności degradacji i mineralizacji zanieczyszczeń

Postęp procesu degradacji zanieczyszczeń oraz produkty pośrednie analizowano z wykorzystaniem wysokosprawnej chromatografii cieczowej pracującej w układzie faz odwróconych przy użyciu aparatu Shimadzu UFLC LC-20AD (Kyoto, Japonia) z detektorem PID Shimadzu SPD-M20A. Parametry oznaczeń chromatograficznych zestawiono w Tabeli 6. Zawartość całkowitego węgla organicznego (TOC) po procesie fotokatalitycznym badano za pomocą analizatora Shimadzu TOC Analyzer.

Tabela 6 Parametry oznaczeń produktów fotokatalitycznej degradacji API

Substancja oznaczana	*Temperatura*	*Prędkość przepływu fazy ruchomej*	*Skład fazy ruchomej*
Karbamazepina	45ºC	1,5 $cm^3 \cdot min^{-1}$	60% woda 39,5% acetonitryl 0,5 % kwas ortofosforowy
Acetaminofen	45ºC	0,5 $cm^3 \cdot min^{-1}$	69,9% woda 0,1% kwas mrówkowy 30% metanol
Ibuprofen	45ºC	0,5 $cm^3 \cdot min^{-1}$	70% acetonitryl 29,5% woda 0,5 % kwas ortofosforowy

8.4. Treść pracy

W części doświadczalnej pracy zaprezentowałam wyniki prowadzonych badań w postaci cyklu pięciu oryginalnych prac twórczych w zakresie przedstawionych zagadnień badawczych, opublikowanych w czasopismach z listy JCR, o sumarycznym IF= 46,612. Krótki opis prac został przedstawiony poniżej.

Rozdział II. *A. Grzegórska, I. Wysocka, P. Głuchowski, J. Ryl, J. Karczewski, A. Zielińska-Jurek, Novel composite of Zn/Ti-layered double hydroxide coupled with MXene for the efficient photocatalytic degradation of pharmaceuticals, Chemosphere 308 (2022) 136191. https://doi.org/10.1016/j.chemosphere.2022.136191 [IF=8,8; 140 punktów MNiSW]*

W pracy zastosowano MXen – $Ti_3C_2T_x$ w roli ko-katalizatora procesu fotodegradacji aktywnych substancji farmaceutycznych powszechnie wykrywanych w ściekach, wodach powierzchniowych, czy wodzie pitnej: acetaminofenu i ibuprofenu. Po raz pierwszy otrzymano kompozyt stanowiący połączenie $Ti_3C_2T_x$ z półprzewodnikiem należącym do grupy podwójnych warstwowych wodorotlenków (LDH) – Zn/Ti LDH. Warstwowe podwójne wodorotlenki to grupa naturalnych lub syntetycznych dwuwymiarowych anionowych materiałów gliniastych o strukturze zbliżonej do hydrotalcytu. W ostatnim czasie związki te wzbudziły szerokie zainteresowanie w tematyce fotokatalizy jako nowe materiały półprzewodnikowe. W przypadku związków LDH warstwy kationów najczęściej połączone są za pomocą anionów, a taka struktura sprzyja transportowi nośników ładunku pomiędzy warstwami, zapewniając lepszą adsorpcję zanieczyszczeń, ale także większą liczbę miejsc aktywnych dla reakcji fotokatalitycznych. Niemniej jednak, zastosowanie czystych związków LDH jest wciąż ograniczone ze względu na słabe przewodnictwo, wąski zakres absorpcji światła, czy krótki czas życia nośników ładunku. W związku z tym potencjalną strategią poprawy ich wydajności fotokatalitycznej jest kombinacja z innymi materiałami, takimi jak np. związki z grupy MXenów, która może zapewnić efektywniejszy transfer nośników ładunku oraz pozwolić na ograniczenieć szybkości rekombinacji par elektron-dziura.

W związku z tym, w pracy zbadano wpływ zawartości węglika tytanu (0-5%) na aktywność fotokatalityczną kompozytu oraz wyznaczono jego optymalną zawartość. Celem oceny możliwości wykorzystania takiego materiału w próbkach środowiskowych, zbadano wpływ modelowej wody morskiej, na efektywność procesu fotokatalitycznego. Ponadto, zbadano stabilność otrzymanego materiału i możliwość jego ponownego wykorzystania w czterech następujących po sobie cyklach degradacji. W oparciu o procesy przeprowadzone w obecności zmiataczy ładunku oraz pomiary elektrochemiczne zaproponowano mechanizm degradacji acetaminofenu (ACT) i ibuprofenu (IBP).

Kompozyt Zn/Ti LDH-Ti_3C_2 otrzymano z zastosowaniem metody solwotermalnej. Związek LDH syntezowano w obecności węglika tytanu w ilości od 0 do 5% wagowych, w temperaturze 130°C przez 48 godzin. Na podstawie analizy dyfrakcji rentgenowskiej (XRD) zidentyfikowano jedynie obecność związku Zn/Ti LDH. Na dyfraktogramie zaobserwowano charakterystyczny najbardziej intensywny sygnał dla Zn/Ti LDH przy kącie 2θ = 13,2°, który

odpowiada płaszczyźnie (003). Z kolei nie oznaczono sygnałów pochodzących od węglika tytanu, co mogło wynikać z jego niskiej zawartości w kompozycie czy też wysokiego stopnia dyspersji. Obecność Ti_3C_2 potwierdzono dzięki zastosowaniu analizy spektroskopii fotoelektronowej (XPS) – zarejestrowano sygnały charakterystyczne dla wiązań Ti-C oraz C-Ti-O (odpowiednio dla energii wiązań 455 eV i 457 eV dla Ti2p oraz 283 eV i 284 eV dla C1s). Na podstawie analiz mikroskopowych SEM oraz TEM potwierdzono, że kompozyty tworzą struktury płatkowe o powierzchni właściwej w zakresie od 119 do 134 m^2/g. Na podstawie analizy spektroskopii absorpcyjnej rozproszonego odbicia w zakresie UV/Vis (DR/UV-vis) wykazano, że czysty związek LDH absorbuje światło z zakresu UV do około 400 nm. W przypadku kompozytów, zaobserwowano wzrost absorbancji w zakresie 400-800 nm, co było szczególnie widoczne dla próbki zawierającej 5% węglika tytanu.

Aktywność fotokatalityczną otrzymanych materiałów zbadano w reakcji degradacji dwóch aktywnych substancji farmaceutycznych – acetaminofenu i ibuprofenu. Na podstawie uzyskanych wyników potwierdzono, że czysty związek LDH charakteryzuje się dobrą aktywnością fotokatalityczną. Stopień degradacji acetaminofenu wynosił blisko 100% po 40 minutach naświetlania, a ibuprofenu po 60 minutach naświetlania. Utworzenie heterozłącza pomiędzy Zn/Ti LDH i Ti_3C_2 pozwoliło na poprawę aktywności fotokatalitycznej oraz osiągnięcie wyższego stopnia mineralizacji farmaceutyków. Najlepsze rezultaty osiągnięto, gdy zawartość węglika tytanu w kompozycie wynosiła 2,5%. Wykazano także, że kompozyt Zn/Ti LDH-2,5%Ti_3C_2 charakteryzuje się niezmienioną aktywnością fotokatalityczną w modelowej wodzie morskiej, zawierającej jony nieorganiczne (Na^+, Ca^{2+}, Mg^{2+}, Cl^-, SO_4^{2-}). Potwierdzono także stabilność materiału za pomocą dyfrakcji rentgenowskiej (XRD) oraz spektroskopii w podczerwieni z transformacją Fouriera (FTIR) oraz możliwość ponownego wykorzystania w kolejnych cyklach degradacji. Na podstawie badań aktywności fotokatalitycznej w obecności zmiataczy nośników ładunku wykazano, że głównymi formami uczestniczącymi w degradacji ACT są anionorodniki ponadtlenkowe ($^{\bullet}O_2^-$), natomiast w przypadku ibuprofenu są to dziury (h^+).

W celu potwierdzenia roli MXenów jako ko-katalizatorów procesu fotokatalitycznej degradacji acetaminofenu i ibuprofenu wykonano pomiary fotoluminescencji, czasu życia nośników ładunku oraz pomiary elektrochemiczne. Potwierdzono efektywny transfer ładunku pomiędzy komponentami układu hybrydowego. Ponadto wykazano, że obecność Ti_3C_2 wpływa na zmniejszenie rekombinacji par elektron-dziura.

Rozdział III. *A. Grzegórska, P. Głuchowski, J. Karczewski, J. Ryl, I. Wysocka, K. Siuzdak, G. Trykowski, K. Grochowska, A. Zielińska-Jurek, Enhanced photocatalytic activity of accordion-like layered Ti_3C_2 (MXene) coupled with Fe-modified decahedral anatase particles exposing {1 0 1} and {0 0 1} facets, Chem. Eng. J. 426 (2021) 130801. https://doi.org/10.1016/j.cej.2021.130801 [IF=16,744; 200 punktów MNiSW]*

W pracy zastosowano związek z grupy MXenów – $Ti_3C_2T_x$ jako prekursor do utworzenia heterozłącza TiO_2/Ti_3C_2 poprzez utlenianie in-situ powierzchni węglika. W ramach badań opisanych w publikacji określono wpływ czasu (6-24 godzin) i temperatury (140-220°C) reakcji solwotermalnej prowadzonej w obecności HBF_4 na właściwości fizykochemiczne otrzymanych nanomateriałów oraz ich aktywność fotokatalityczną. Fotokatalizatory zastosowano w reakcji degradacji fenolu jako modelowego zanieczyszczenia organicznego oraz karbamazepiny (CBZ) należącej do grupy aktywnych substancji farmaceutycznych. Ponadto, w kolejnym kroku po raz pierwszy kompozyt TiO_2/Ti_3C_2 zmodyfikowano poprzez napylenie magnetronowe żelaza na powierzchnię i zbadano wpływ modyfikacji powierzchniowej kompozytu na aktywność fotokatalityczną.

Na podstawie analizy dyfrakcji rentgenowskiej (XRD) potwierdzono, że synteza solwotermalna w obecności HBF_4 prowadzi do utlenienia powierzchni węglika i wytworzenia dekaedrów TiO_2. Wraz ze wzrostem temperatury syntezy (140-220°C) oraz czasu syntezy (6-24 godzin) na dyfraktogramie widoczny był znaczny wzrost intensywności sygnału charakterystycznego dla anatazu przy kącie 2θ = 25,1°, odpowiadającym płaszczyznom (101) i zmniejszenie intensywności sygnału dyfrakcyjnego dla Ti3C2 przy kacie 2θ = 8,9°, odpowiadającego płaszczyznom (002). W przypadku próbek modyfikowanych powierzchniowo za pomocą żelaza na dyfraktogramie nie zarejestrowano sygnałów pochodzących od form Fe, co może wynikać z bardzo małej zawartości metalu w stosunku do kompozytu TiO_2/Ti_3C_2. Analizy skaningowej mikroskopii elektronowej (SEM) oraz transmisyjnej mikroskopii elektronowej (TEM) potwierdziły tworzenie cząstek TiO_2 o strukturze dekaedrów, eksponujących wysoce reaktywne płaszczyzny {1 0 1} i {0 0 1}. Również zauważalny był wyższy stopień pokrycia powierzchni MXenu nanocząstkami anatazu wraz ze wzrostem czasu i temperatury syntezy. Analizy mikroskopowa (TEM) oraz spektroskopia fotoelektronów (XPS) potwierdziły także obecność Fe w próbkach modyfikowanych. Żelazo występowało w formie Fe(II) i Fe(III), jako mieszanina obydwu tlenków żelaza. Wyznaczona za pomocą XPS zawartość żelaza wynosiła około 0,7% at.

Aktywność fotokatalityczną otrzymanych materiałów zbadano w reakcji degradacji fenolu jako modelowego zanieczyszczenia organicznego, a następnie karbamazepiny, będącej

wskaźnikiem antropologicznego zanieczyszczenia wód. Zauważalnie najniższą aktywność wykazywały materiały otrzymane w niższej temperaturze i krótszym czasie syntezy, co wiązało się z niewielka zawartościąTiO$_2$ wytworzonego na powierzchni. Najwyższą efektywnością degradacji zanieczyszczeń charakteryzowały się próbki i TiO$_2$/Ti$_3$C$_2$(140,12) i TiO$_2$/Ti$_3$C$_2$(220,24). W przypadku próbki TiO$_2$/Ti$_3$C$_2$(140,12) osiągnięto 96% degradacji CBZ w czasie 60 minut naświetlania. Wykazano, że modyfikacja powierzchni tych kompozytów TiO$_2$/Ti$_3$C$_2$ za pomocą żelaza miała znaczny wpływ na wzrost aktywności fotokatalitycznej. Stała szybkości degradacji CBZ wzrosła o około 49% dla próbki Fe-TiO$_2$/Ti$_3$C$_2$(140,12) i 43% dla TiO$_2$/Ti$_3$C$_2$(220,24), w porównaniu z ich niemodyfikowanymi odpowiednikami. Żelazo działa jak zmiatacz elektronów/dziur i dzięki temu wpływa na zahamowanie rekombinacji fotogenerowanych nośników ładunku. Zarówno w przypadku fenolu, jak i karbamazepiny, wykazano, że głównymi formami uczestniczącymi w procesie degradacji są generowane na powierzchni otrzymanego nanomateriału anionorodniki ponadtlenkowe.

Analiza fotoluminescencji, czasu życia nośników ładunku, oraz pomiary elektrochemiczne potwierdziły transfer nośników ładunku pomiędzy Fe i TiO$_2$/Ti$_3$C$_2$ oraz zmniejszenie stopnia rekombinacji elektron-dziura dla próbek modyfikowanych żelazem. Dodatkowo analiza Motta Schottky'ego wykazała znaczny przyrost gęstości donorów, któremu towarzyszyło dodatnie przesunięcie potencjału pasma płaskiego próbek TiO$_2$/Ti$_3$C$_2$ modyfikowanych Fe, w porównaniu z niemodyfikowanym kompozytem TiO$_2$/Ti$_3$C$_2$.

Rozdział IV. *A. Grzegórska, A. Gajewicz-Skrętna, G. Trykowski, K. Sikora, A. Zielińska-Jurek, Design and synthesis of TiO$_2$/Ti$_3$C$_2$ composites for highly efficient photocatalytic removal of acetaminophen: The relationships between synthesis parameters, physicochemical properties, and photocatalytic activity. Catal. Today 413-415 (2023) 113980. https://doi.org/10.1016/j.cattod.2022.12.011 [IF= 5,3; 140 punktów MNiSW]*

W pracy zastosowano metody chemometryczne do analizy możliwych podobieństw/różnic między kompozytami TiO$_2$/Ti$_3$C$_2$ syntezowanymi w różnych temperaturach i w różnym czasie reakcji solwotermalnej. Zastosowanie takich analiz miało na celu znalezienie ukrytych wzorców w analizowanych danych i określenie związków przyczynowych pomiędzy aktywnością fotokatalityczną kompozytów TiO$_2$/Ti$_3$C$_2$ w reakcji degradacji acetaminofenu (ACT) należącego do grupy farmaceutyków, a morfologią próbek, właściwościami fizykochemicznymi oraz parametrami syntezy. W dalszej części pracy po raz pierwszy porównano wpływ środowiska reakcji syntezy kompozytu TiO$_2$/Ti$_3$C$_2$ (woda, HBF$_4$, NH$_4$F/HCl, oraz kalcynacja) na morfologię otrzymanych cząstek TiO$_2$ oraz efektywność degradacji ACT.

Dla kompozytu charakteryzującego się najlepszymi właściwościami fotokatalitycznymi (otrzymanego w obecności NH_4F i HCl) zaproponowano mechanizm degradacji oraz możliwą ścieżkę degradacji.

Na podstawie analizy dyfrakcji rentgenowskiej (XRD) próbek otrzymanych w trakcie procesu solwotermalnego w obecności HBF_4, prowadzonego w temperaturze 140-220°C, w czasie 6-48 godzin, wyznaczono zawartość TiO_2 w otrzymanych kompozytach TiO_2/Ti_3C_2. W przypadku próbek syntezowanych w temperaturze 140 i 160°C przez 6 godzin, oraz dla próbki syntezowanej w temperaturze 140°C przez 12 godzin, nie zaobserwowano sygnałów pochodzących od TiO_2, co wskazuje na to, że powierzchnia MXenu nie uległa utlenieniu. Dla pozostałych próbek dłuższy czas i wyższa temperatura procesu prowadziły do wyższego stopnia utlenienia Ti_3C_2 do anatazu. Dzięki wykorzystaniu analiz chemometrycznych możliwe było znalezienie podobieństw/różnic między kompozytami TiO_2/Ti_3C_2, oraz określenie zależności między aktywnością fotokatalityczną kompozytów TiO_2/Ti_3C_2 w reakcji degradacji acetaminofenu, a ich morfologią, właściwościami fizykochemicznymi oraz warunkami syntezy. Na podstawie metod hierarchicznej analizy skupień (HCA) i analizy głównych składowych (PCA) wykazano, że degradacja acetaminofenu jest dodatnio skorelowana z zawartością TiO_2 w kompozytach. Ponadto, najwyższe aktywności zaobserwowano dla próbek charakteryzujących się stosunkowo niewielką zawartością Ti_3C_2.

W kolejnym etapie badań porównano wpływ środowiska reakcji syntezy kompozytów TiO_2/Ti_3C_2 na ich aktywność fotokatalityczną. Wykazano, że kompozyt TiO_2/Ti_3C_2 otrzymany w obecności NH_4F i HCl wykazywał najwyższą efektywność degradacji acetaminofenu (92% w ciągu 60 minut naświetlania). Na zdjęciach wykonanych za pomocą skaningowego mikroskopu elektronowego (SEM) zaobserwowano, że wzrastające cząstki tworzą struktury zarówno dekaedrów, jak i oktaedrów eksponujących wysoce aktywne fotokatalitycznie płaszczyzny. Ponadto, na podstawie analizy XRD potwierdzono, że taki kompozyt stanowi mieszaninę dwóch odmian polimorficznych TiO_2 – anatazu i rutylu, co wiąże się z wytworzeniem złącza heterofazowego. Badania fotodegradacji przeprowadzone w obecności zmiataczy ładunku potwierdziły, że głównymi formami uczestniczącymi w procesie usuwania acetaminofenu były anionorodniki ponadtlenkowe. Ponadto, na podstawie analizy chromatografii cieczowej połączonej ze spektrometrią mas (LC/MS) zaproponowano ścieżkę degradacji ACT. Głównym produktem pośrednim degradacji był 3-hydroksy-acetaminofen, co wskazuje na szybkie rozerwanie pierścienia aromatycznego i transformację do kwasów alifatycznych, a finalnie mineralizację do CO_2 i H_2O.

Rozdział V. *A. Grzegórska, J. Chibueze Ofoegbu, L. Cervera-Gabalda, C. Gómez-Polo, D. Sannino, A. Zielińska-Jurek, Magnetically recyclable TiO_2/MXene/$MnFe_2O_4$ photocatalyst for enhanced peroxymonosulphate-assisted photocatalytic degradation of carbamazepine and ibuprofen under simulated solar light. J. Environ. Chem. Eng. 11 (2023) 110660. https://doi.org/10.1016/j.jece.2023.110660. [IF=7,968; 100 punktów MNiSW]*

Celem przezwyciężenia jednego z wyzwań fotokatalizy, jakim jest separacja fotokatalizatora z zawiesiny po procesie oczyszczania, możliwe jest wprowadzenie do struktury kompozytu TiO_2/Ti_3C_2 cząstek o właściwościach magnetycznych. W związku z tym, kompozyt TiO_2/Ti_3C_2 otrzymany w środowisku NH_4F/HCl o strukturze TiO_2 w postaci dekaedrów i oktaedrów zmodyfikowano za pomocą ferrytu manganowego $MnFe_2O_4$ (w ilości 5 i 20% wag.). Utworzenie kompozytu $TiO_2/Ti_3C_2/MnFe_2O_4$ miało na celu (1) poprawę aktywności fotokatalitycznej wspomaganej przez aktywację PMS za pomocą ferrytu manganowego oraz (2) zapewnienie efektywnej separacji magnetycznej po procesie degradacji w zewnętrznym polu magnetycznym. Wśród badanych materiałów o właściwościach magnetycznych, nanocząstki $MnFe_2O_4$ cieszą się dużym zainteresowaniem ze względu na niski koszt, wysoką stabilność chemiczną i nietoksyczność. Jednocześnie jony Mn i Fe umożliwiają aktywację nadtlenomonosiarczanu, dzięki czemu możliwe jest zastosowanie hybrydowego procesu fotokatalizy wspomaganej aktywacją PMS. Aktywność fotokatalityczną zbadano w reakcji degradacji mieszaniny karbamazepiny (CBZ) i ibuprofenu (IBP). Zaproponowano możliwy mechanizm aktywacji PMS oraz degradacji farmaceutyków z zastosowaniem kompozytu $TiO_2/Ti_3C_2/MnFe_2O_4$.

Analiza dyfrakcji rentgenowskiej (XRD) wykazała że synteza solwotermalna w obecności NH_4F i HCl prowadzi do utlenienia powierzchni węglika z wytworzeniem nanocząstek anatazu i rutylu. Stosunek anatazu do rutylu wynosił 40%:60%. Charakterystyczny sygnał dla płaszczyzny (101) anatazu i (110) rutylu zarejestrowano przy kącie 2θ odpowiednio 25,2° i 27,3°. Na dyfraktogramie nie zidentyfikowano sygnałów pochodzących od Ti_3C_2, prawdopodobnie ze względu na niewielki udział fazowy pozostałości węglika po syntezie solwotermalnej. Celem potwierdzenia jego obecności wykonano analizy spektroskopii elektronowej (XPS) oraz analizę termograwimetryczną (TGA). Na widmie Ti 2p zarejestrowano głównie sygnały pochodzące od Ti^{4+} co wskazuje, że większość węglika uległa utlenieniu do TiO_2, niemniej jednak zidentyfikowano także sygnały pochodzące od Ti-C i C-Ti-O w Ti_3C_2 przy energii wiązań odpowiednio 454,5 eV i 457,4 eV. W przypadku analizy TGA prowadzonej w atmosferze powietrza, w zakresie temperatur 200-400°C zaobserwowano niewielki przyrost masy (o około 0,7% wag.) związany z utlenieniem pozostałości Ti_3C_2 do TiO_2. Dla kompozytów

modyfikowanych powierzchniowo na dyfraktogramie XRD zarejestrowano także sygnały pochodzące od ferrytu manganowego, co potwierdza utworzenie kompozytu $TiO_2/Ti_3C_2/MnFe_2O_4$. Na obrazach uzyskanych za pomocą skaningowej mikroskopii elektronowej (SEM) zaobserwowano, że cząstki TiO_2 tworzą formy oktaedrów i dekaedrów o różnych rozmiarach, z kolei $MnFe_2O_4$ występuje w formie cząstek kulistych o średniej wielkości około 80 nm. Na podstawie analizy transmisyjnej mikroskopii elektronowej (TEM) potwierdzono, że cząstki $MnFe_2O_4$ są równomiernie zdyspergowane na powierzchni TiO_2/Ti_3C_2. Modyfikacja powierzchniowa za pomocą ferrytu manganowego miała na celu nadanie fotokatalizatorom właściwości magnetycznych, aby możliwa była efektywna separacja materiału po procesie fotokatalitycznym. Na podstawie analizy pętli histerezy (pomiary magnetyzacji w funkcji przyłożonego pola magnetycznego) wykazano, że kompozyty $TiO_2/Ti_3C_2/MnFe_2O_4$ mogą być z powodzeniem separowane z zawiesiny z wykorzystaniem zewnętrznego pola magnetycznego.

Aktywność fotokatalityczną otrzymanych materiałów zbadano w reakcji degradacji mieszaniny karbamazepiny i ibuprofenu. Kompozyt TiO_2/Ti_3C_2 wykazywał wysoką efektywność degradacji farmaceutyków, co można przypisać powstawaniu złącza heterofazowego między anatazem a rutylem. Taki bezpośredni kontakt pomiędzy dwiema strukturami polimorficznymi TiO_2 może ułatwić międzycząsteczkowy transfer fotogenerowanych ładunków w procesach fotokatalitycznych, a w konsekwencji poprawić aktywność fotokatalityczną. Modyfikacja powierzchni za pomocą ferrytu manganowego w ilości 5% wag. nie wpłynęło negatywnie na efektywność degradacji obu substancji aktywnych farmaceutycznie, która po 60 minutach naświetlania osiągnęła 100%. Taki kompozyt wykazywał również wysoką efektywność mineralizacji zanieczyszczeń. Zaobserwowano 40% redukcji zawartości całkowitego węgla organicznego (TOC) po 60 minutach naświetlania. Jednak wprowadzenie większej ilości $MnFe_2O_4$ (20% wag.) znacznie obniżyło aktywność fotokatalityczną. Zjawisko to można przypisać temu, że nadmierna zawartość nieaktywnych fotokatalitycznie, inertnych cząstek magnetycznych może utrudniać kontakt fotokatalizatora ze światłem lub stawać się nowym centrum rekombinacji elektron-dziura, co skraca czas życia fotogenerowanych nośników ładunku. Poprawę efektywności degradacji farmaceutyków zaobserwowano w wyniku synergicznego efektu działania fotokatalizy i aktywacji PMS za pomocą $MnFe_2O_4$. W przypadku zastosowania 0.25 mM PMS, 100% degradacji CBZ zaobserwowano już po 20 minutach procesu, zaś ibuprofenu po 10 minutach. Ponadto, osiągnięto ponad 50% redukcję TOC po 60 minutach naświetlania. Określono także wpływ pH na aktywność fotokatalityczną w degradacji karbamazepiny i ibuprofenu. W przypadku pH wynoszącego 4,5, aktywność fotokatalityczna

uległa nieznacznej poprawie. Z kolei, zastosowanie zasadowego pH - 9,5 skutkowało obniżeniem efektywności degradacji obu farmaceutyków. W warunkach zasadowego pH, PMS może ulegać samorozkładowi bez wytwarzania reaktywnych rodników siarczanowych. Ponadto, w środowisku zasadowym potencjały redoks rodników siarczanowych i hydroksylowych są niższe niż w środowisku kwasowym oraz krótszy jest ich czas życia.

W kolejnym etapie badań, proces fotokatalityczny przeprowadzono z zastosowaniem $TiO_2/Ti_3C_2/5\%MnFe_2O_4$/PMS w modelowej wodzie morskiej zawierającej nieorganiczne jony przeszkadzające. Zaobserwowano, że w tych warunkach degradacja CBZ wyniosła 100% już po 5 minutach naświetlania, z kolei w przypadku IBP uległa nieznacznemu pogorszeniu. Obecność jonów chlorkowych może wpływać na poprawę aktywności fotokatalitycznej wspomaganej PMS, co może być związane z wytwarzaniem rodników chlorkowych w wyniku reakcji pomiędzy Cl^- i $\bullet SO_4^-$. Z drugiej strony jony nieorganiczne mogą działać jak zmiatacze rodników hydroksylowych, a tym samym obniżać aktywność fotokatalityczną. Niemniej jednak, w przypadku obu API efektywność degradacji w modelowej wodzie morskiej pozostała wysoka. Dodatkowo, na podstawie procesów degradacji przeprowadzonych w obecności zmiataczy ładunku wykazano, że głównymi formami uczestniczącymi w procesie degradacji CBZ są rodniki siarczanowe i anionorodniki ponadtlenkowe, a w przypadku IBP rodniki siarczanowe i dziury.

Analiza dyfrakcji rentgenowskiej (XRD) i spektroskopii w podczerwieni z transformacją Fouriera (FTIR) dla próbki fotokatalizatora po procesie degradacji nie wykazała żadnych zmian w strukturze materiału. Ponadto, wysoka aktywność w czterech kolejnych cyklach degradacji potwierdziła, że materiał ten może być odzyskiwany za pomocą separacji magnetycznej i ponownie wykorzystywany w kolejnym procesach fotodegradacji zanieczyszczeń organicznych.

Rozdział VI. *A. Grzegórska, J. Karczewski, A. Zielińska-Jurek, Modelling and optimisation of MXene-derived TiO_2/Ti_3C_2 synthesis parameters using Response Surface Methodology based on the Box–Behnken factorial design. Enhanced carbamazepine degradation by the Cu-modified TiO_2/Ti_3C_2 photocatalyst, Process Saf. Environ. Prot. 179 (2023) 449. https://doi.org/10.1016/j.psep.2023.09.028 [IF= 7,8; 100 punktów MNiSW]*

W pracy przedstawiono optymalizację procesu otrzymywania kompozytu TiO_2/Ti_3C_2 na podstawie planu czynnikowego Box-Behnken (BBD) połączonego z analizą powierzchni odpowiedzi (RSM). Model BBD opiera się na trzech poziomach, dla każdej z 3 zmiennych niezależnych opisujących proces: temperatura syntezy, czas syntezy, i stosunek woda/etanol.

Na podstawie wykonanych doświadczeń i analizy otrzymanych danych wyznaczono parametry determinujące aktywność fotokatalityczną, efektywność redukcji zawartości całkowitego węgla organicznego (TOC), wielkość krystalitów oraz powierzchnię właściwą wyznaczoną metodą BET. Na podstawie optymalizacji odpowiedzi wyznaczono wartości parametrów, dla których przewidywana jest najwyższa aktywność fotokatalityczna. Dodatkowo, w kolejnym etapie zoptymalizowaną próbkę zmodyfikowano za pomocą miedzi (0,25 – 1% wag.). Porównano efektywność procesu fotokatalitycznego oraz procesu fotokatalitycznego wspomaganego aktywacją PMS.

Zgodnie z planem czynnikowym Boxa-Behnkena wykonano 15 doświadczeń uwzględniających trzy zmienne niezależne na trzech poziomach. Zbadano wpływ czasu syntezy (6, 15 lub 24 godziny), temperatury (180, 200 i 220°C) oraz środowiska reakcji (woda, etanol, woda/etanol 50%:50% obj./obj.) na aktywność fotokatalityczną degradacji CBZ, efektywność redukcji TOC, wielkość krystalitów oraz powierzchnię właściwą BET. Na podstawie analizy powierzchni odpowiedzi (RSM) połączonej z analizą wariancji (ANOVA) stwierdzono, że największy wpływ na wszystkie cztery odpowiedzi ma zawartość etanolu zastosowanego w procesie solwotermalnym.

W wyniku syntezy solwotermalnej w obecności wody, etanolu, lub mieszaniny woda/etanol dochodziło do utlenienia powierzchni węglika z wytworzeniem sferycznych cząstek TiO_2, co potwierdzono na podstawie analizy mikroskopowej SEM. Na dyfraktogramach rentgenowskich dla wszystkich próbek zaobserwowano sygnały pochodzące zarówno od anatazu, jak i Ti_3C_2. Na podstawie analizy XRD wykazano, że wyższa temperatura i czas syntezy są pozytywnie skorelowane ze stopniem utlenienia powierzchni. Ponadto, większą zawartość anatazu zaobserwowano w próbkach syntezowanych w wodzie dejonizowanej, następnie w mieszaninie woda/etanol i najmniejszą w środowisku etanolu. Wielkość krystalitów TiO_2 zawierała się w zakresie od 11,5 nm do 25 nm. Podobnie, największe krystality anatazu zaobserwowano dla syntezy prowadzonej w wodzie, a najmniejsze w etanolu. Powierzchnia właściwa fotokatalizatorów wyznaczona w oparciu o metodę BET wynosiła w zakresie od 24 do 70 m^2/g. Największe rozwinięcie powierzchni właściwej zaobserwowano dla próbek syntezowanych w etanolu, a najmniejsze dla otrzymywanych w wodzie. Aktywność fotokatalityczną otrzymanych materiałów scharakteryzowano w reakcji degradacji karbamazepiny. Efektywność degradacji CBZ wynosiła od 48 do 97%, w czasie 60 minut naświetlania. Z kolei stopień mineralizacji, wyznaczany jako redukcja zawartości całkowitego węgla organicznego wynosił od 3 do 31%. Najwyższą aktywność fotokatalityczną uzyskano dla próbki syntezowanej w temperaturze 200°C, przez 15 godzin w środowisku woda/etanol.

Z kolei najwyższy stopień mineralizacji dla próbki syntezowanej w temperaturze 220°C, przez 24 godziny w środowisku woda/etanol. Celem osiągnięcia najwyższej aktywności fotokatalitycznej w oparciu o optymalizację odpowiedzi wyznaczono parametry, dla których przewidywana jest najlepsza efektywność procesu: temperatura 220°C, czas 17 godzin i stosunek woda etanol 58%:42% obj./obj. Przewidywania te zostały potwierdzone doświadczalnie i dla takiej próbki uzyskano 100% degradacji w czasie 60 minut.

Aby dodatkowo poprawić aktywność fotokatalityczną i umożliwić aktywację PMS otrzymano fotokatalizatory TiO_2/Ti_3C_2 modyfikowane miedzią w ilości od 0,25 do 1% wag. Próbki otrzymano zgodnie z wyznaczonymi optymalnymi parametrami. Na podstawie analizy dyfrakcji rentgenowskiej nie potwierdzono obecności miedzi w kompozytach, prawdopodobnie ze względu na bardzo małą zawartość na powierzchni kompozytu. Obecność miedzi potwierdzono za pomocą analizy SEM/EDS i XPS. Stwierdzono, że miedź znajduje się w postaci Cu(0)/Cu(I) i Cu(II). Obecność miedzi metalicznej lub na pierwszym stopniu utlenienia wskazuje na częściową redukcję w trakcie syntezy na powierzchni węglika. Zaobserwowano, że modyfikacja za pomocą Cu wpłynęła na poprawę aktywności fotokatalitycznej, przy czym najwyższą aktywność zaobserwowano dla próbki TiO_2/Ti_3C_2 modyfikowanej 0,5% wag. miedzi. Stała szybkości degradacji CBZ wzrosła o około 50%, w porównaniu do próbki niemodyfikowanej. W kolejnym etapie zbadano efektywność degradacji fotokatalitycznej wspomaganej aktywacją PMS (0,5 mM). Potwierdzono synergistyczny efekt działania obu procesów. Zaobserwowano 100% degradacji CBZ w czasie 20 minut, a stała szybkości degradacji CBZ wzrosła prawie 4-krotnie, w porównaniu do procesu prowadzonego bez dodatku PMS. Na podstawie reakcji ze zmiataczami ładunku wykazano, że głównymi formami odpowiedzialnymi za proces degradacji zanieczyszczeń organicznych są rodniki siarczanowe i anionorodniki ponadtlenkowe.

Na podstawie pomiarów fotoluminenscencji, elektrochemicznej spektroskopii impedancyjnej oraz odpowiedzi fotoprądowej potwierdzono, że wprowadzenie miedzi wpływa na powierzchnię kompozytu wpływa na zmniejszenie rekombinacji nośników ładunku, a w efekcie poprawę właściwości fotokatalitycznych. Potwierdzono także, że układ 0,5%Cu-TiO_2/Ti_3C_2/PMS charakteryzuje się wysoką stabilnością w kolejnych cyklach degradacji, a analizy dyfrakcji rentgenowskiej (XRD) i spektroskopii w podczerwieni z transformacją Fouriera (FTIR) po procesie nie wykazały zmian w strukturze kompozytu.

Rozdział VII: *Podsumowanie i wnioski*

W rozdziale VII przedstawiono podsumowanie i wnioski z przeprowadzonych prac badawczych.

Rozdział II. Novel composite of Zn/Ti-layered double hydroxide coupled with MXene for the efficient photocatalytic degradation of pharmaceuticals

Chemosphere 308 (2022) 136191

Contents lists available at ScienceDirect

Chemosphere

journal homepage: www.elsevier.com/locate/chemosphere

Novel composite of Zn/Ti-layered double hydroxide coupled with MXene for the efficient photocatalytic degradation of pharmaceuticals

Anna Grzegórska [a,**], Izabela Wysocka [a], Paweł Głuchowski [b], Jacek Ryl [c], Jakub Karczewski [c], Anna Zielińska-Jurek [a,*]

[a] Department of Process Engineering and Chemical Technology, Faculty of Chemistry, Gdańsk University of Technology, G. Narutowicza 11/12, Gdańsk, 80-233, Poland
[b] Institute of Low Temperature and Structural Research, Polish Academy of Sciences, Okólna 2, Wrocław, 50-422, Poland
[c] Institute of Nanotechnology and Materials Engineering, Faculty of Applied Physics and Mathematics, Gdańsk University of Technology, G. Narutowicza 11/12, Gdańsk, 80-233, Poland

HIGHLIGHTS

- Zn/Ti layered double hydroxide coupled with MXene was synthesized for the first time.
- Effective photodegradation of commonly detected pharmaceuticals in a model seawater.
- LDH/MXene containing 2.5 wt% of MXene revealed the highest photoactivity.
- The main oxidizing species responsible for ibuprofen degradation are OH.• and holes (h^-).
- Acetaminophen degradation by Zn/Ti LDH-Ti_3C_2 proceeded in the presence of .•O_2^-.

GRAPHICAL ABSTRACT

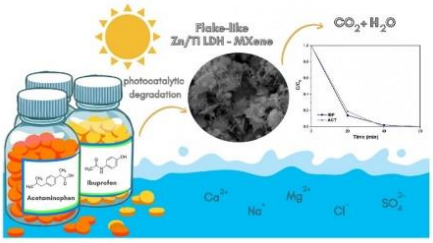

ARTICLE INFO

Handling editor: Sergi Garcia-Segura

Keywords:
Acetaminophen
Ibuprofen
MXene
Pharmaceuticals removal
Photocatalysis
Ti_3C_2
Zn/ti LDH

ABSTRACT

In the present study, a hybrid photocatalyst of Zn/Ti layered double hydroxide (LDH) coupled with MXene – Ti_3C_2 was synthesized for the first time and applied in photocatalytic degradation of acetaminophen and ibuprofen, two commonly present in the natural environment and prone to accumulate in the aquatic ecosystem pharmaceuticals. The effect of MXene content (0.5 wt%, 2.5 wt%, and 5 wt%) on the photocatalytic activity of LDH/MXene composite was investigated. The composite of LDH/MXene containing 2.5 wt% of MXene revealed the highest photocatalytic activity in the degradation of acetaminophen (100% within 40 min) and ibuprofen (99.7% within 60 min). Furthermore, an improvement in acetaminophen and ibuprofen mineralization was observed for the composite material. Meanwhile, the introduction of interfering ions (Na^+, Ca^{2+}, Mg^{2+}, Cl^-, SO_4^{2-}) in the model seawater did not affect the removal efficiency of both pharmaceuticals. The photocatalytic experiment performed in the four subsequent cycles, as well as FTIR, TEM, and XPS analyses after the photodegradation process confirmed the excellent stability and reusability of the prepared composite material. In order to evaluate the effect of various reactive oxidizing species (ROS) on the photocatalytic process, the trapping experiment was applied. It was noticed that •O_2^- had the main contribution in photocatalytic degradation of

* Corresponding author. Department of Process Engineering and Chemical Technology, Faculty of Chemistry, Gdańsk University of Technology, G. Narutowicza 11/12, Gdańsk, 80-233, Poland.,
** Corresponding author.
E-mail addresses: anna.grzegorska@pg.edu.pl (A. Grzegórska), annjurek@pg.edu.pl (A. Zielińska-Jurek).

https://doi.org/10.1016/j.chemosphere.2022.136191
Received 17 June 2022; Received in revised form 8 August 2022; Accepted 21 August 2022
Available online 26 August 2022

acetaminophen, while •OH and h^+ mainly affected the degradation of ibuprofen. Finally, based on the results of Mott Schottky analysis, bandgap calculation, and ROS trapping experiment, the possible mechanism for pharmaceuticals degradation was proposed. This research illustrates the feasibility and novelty of the treatment of pharmaceuticals by LDH/MXene composites, implying that MXene plays a significant role in the electron-hole separation and thus high photocatalytic activity.

1. Introduction

Water pollution is one of the present concerns for humans and the environment (Naz et al., 2021). The major impact is attributed to residues of pharmaceuticals, pesticides, nutrients, micro-plastics, and petroleum (Priya et al., 2022; Rasheed et al., 2020; Singh et al., 2021). Particularly, the important group includes pharmaceuticals, which concentration in water systems is continuously growing due to higher consumption and discharging as metabolites or unchanged forms into the environment (Desbiolles et al., 2018; Xiang et al., 2021). The contamination of water sources such as seawater or lake water brings the potential risk of chronic exposure of aquatic organisms, bioaccumulation, biomagnification, and thereby harmful effects on human health (Pemberthy M et al., 2020; Branchet et al., 2021).

Acetaminophen (ACT), commonly known as paracetamol, is an analgesic and antipyretic compound, while ibuprofen (IBP) belongs to the group of non-steroidal anti-inflammatory drugs (Dey et al., 2018). These pharmaceuticals are common in the natural environment and prone to accumulate in the aquatic ecosystem (Zur et al., 2011). Moreover, they have been detected in surface waters, wastewaters, as well as drinking waters around the world (Sousa et al., 2018). In Latin America, acetaminophen concentration was in the range of 0.016–46.6 μg/dm^3 in wastewaters and from 3 to 25,2 ng/dm^3 in surface waters. Meanwhile, ibuprofen concentration ranges from 220 to 13,000 ng/dm^3 in wastewaters and from 2 to 37,000 ng/dm^3 in surface waters (Peña-Guzmán et al., 2019). This shows that the commonly used wastewater treatment processes are ineffective in degrading some pharmaceutical compounds. Depending on the concentration and exposure time, these pollutants may be toxic to bacteria, algae, macrophytes, and fish (Phong Vo et al., 2019). Furthermore, depending on environmental conditions can transform into several more toxic and carcinogenic derivatives, for example, acetaminophen in 4-aminophenol or p-benzoquinone, while ibuprofen into 4-isobutylacetophenone (Liang et al., 2016; Ruggeri et al., 2013).

One of the promising methods for the degradation of emerging contaminants and treatment of active pharmaceutical ingredients is heterogeneous photocatalysis (Akpotu et al., 2019; Klementova et al., 2017). The application of inexpensive, highly available, chemically stable, and non-toxic photocatalysts classified it as a green remediation technology (Article et al., 2015; Xu et al., 2019).

The prospective materials in the field of photocatalysis are layered double hydroxides belonging to a class of two-dimensional semiconductors consisting of mixed metal hydroxide layers with anions or solvent molecules intercalated between them (Razzaq et al., 2020; Guo et al., 2010). However, the major drawbacks of LDH are low efficiency in the utilization of visible light and fast recombination of electron-hole pairs (Motlagh et al., 2020). Thus, the combination of LDH with other materials has been developed to overcome these limitations. For example, Zn/Ti-LDH were applied for methylene blue decomposition, rhodamine B and NO decomposition (Shao et al., 2011; Zhu et al., 2018), oxidation of benzyl alcohol (Zou et al., 2020) and photocatalytic toluene degradation in the gas phase (Liu et al., 2022). Zhu et al. (2017) proposed the combination of Zn/Ti LDH with C60 molecules. The synthesized material was applied for the photocatalytic decomposition of Orange II under simulated solar light. Furthermore, carbon-based materials are increasingly being used in photocatalytic processes (Tayyab et al., 2022; Liu et al., 2021a). The heterojunction of Zn/Ti LDH with g-C_3N_4 improved the photocatalytic efficiency of ceftriaxone sodium degradation and hydrogen generation under visible light (Sun et al., 2019).

Recently, MXene compounds with graphene-like morphology have become promising materials instead of platinum or palladium as noble-metal-free co-catalyst. These structures can inhibit the recombination of charge carriers, improve interfacial charge transfer, and increase photocatalytic activity. Previously, LDH/MXene composites were used for high-performance supercapacitors, adsorbents, sensors, electromagnetic wave absorbers, and catalysts in oxygen evolution reactions (OER) (Hao et al., 2019; Li et al., 2019a; Zhou et al., 2020). There are only a few studies on the application of LDH/MXene composites in photocatalysis. Chen et al. (2020) proposed the implementation of Co–Co LDH/$Ti_3C_2T_x$ for visible-light-driven photocatalytic CO_2 reduction. Wang et al. (2021a) applied a 3D marigold-like CoAl-LDH/Ti_3C_2 for the degradation of tetracycline hydrochloride, chloramphenicol, and terramycin. Meanwhile, Ma et al. (2022) used NiFe-LDH/MXene for photocatalytic removal of norfloxacin.

In this study, for the first time, Zn/Ti LDH-MXene composite was synthesized and used for photocatalytic degradation of two commonly detected pharmaceuticals - acetaminophen and ibuprofen under simulated solar light. The photocatalytic process of active pharmaceutical ingredients degradation was performed in model seawater to evaluate the effect of the multiple interfering ions on the removal efficiency. Furthermore, the physicochemical properties and optimal content of Ti_3C_2 in the hybrid photocatalyst were determined and the mechanism of photocatalytic degradation in the presence of reactive oxygen species was proposed.

2. Experimental

2.1. Materials

The MAX phase compound - Ti_3AlC_2 was provided by Luoyang Tongrun Info Technology Co. (China). The hydrofluoric acid (ACS reagent, 48%), $Zn(NO_3)_2{\cdot}6H_2O$ (reagent grade, 98%), $TiCl_4$ (Reagent-Plus®, 99.9% trace metals basis), and urea (ReagentPlus®, ≥99.5%, pellets) were purchased from Sigma Aldrich. Acetaminophen (BioXtra, ≥99.0%) and Ibuprofen (≥98% (GC)) for the photocatalytic degradation process were provided by Sigma Aldrich. Scavengers: p-benzoquinone (reagent grade, ≥98%) and ammonium oxalate monohydrate (ACS reagent, ≥99%) were purchased from Sigma Aldrich, while isopropanol (99.7%, pure p. a.) and H_2O_2 (30%, pure p. a.) from Avantor Performance Materials Poland. The reagents were used as received with no further purification. Deionized water (DI) was used in all experiments.

2.2. The synthesis procedure of photocatalyst

2.2.1. Etching of Al from Ti_3AlC_2

First, the 10 g of MAX phase compound - Ti_3AlC_2 was added to 100 cm^3 of HF and mixed at room temperature. The material was rinsed with DI water and centrifuged until pH of 7. The powder was dried at 50 °C for 2 h under air conditions.

2.2.2. Synthesis of Zn/Ti LDH

In a typical procedure, 1.19 g of zinc nitrate hexahydrate was dissolved in 100 cm^3 DI water. Next, 0.22 cm^3 of $TiCl_4$ was added dropwise. The molar ratio of Zn to Ti was 2:1. Then 3.0 g of urea was added, and the mixture was magnetically stirred for 30 min. Subsequently, the

mixture was transferred to the 200 cm^3 Teflon-lined stainless steel autoclave. The reaction was performed at 130 °C for 48 h. Finally, the obtained material was centrifuged and washed with DI water until neutral pH. The powder was dried at 50 °C for 2 h under air condition.

2.2.3. Synthesis of Zn/Ti LDH-MXene

$Ti_3C_2T_x$ (0.5, 2.5, and 5 wt%) was dispersed in 100 cm^3 DI water and sonicated for 30 min. Then 1.19 g of zinc nitrate hexahydrate was dissolved in the above mixture. Next, 0.22 cm^3 of $TiCl_4$ was added dropwise. Then 3.0 g of urea was added, and the mixture was magnetically stirred for 30 min. Subsequently, the mixture was transferred to the 200 cm^3 Teflon-lined stainless steel autoclave. The reaction was performed at 130 °C for 48 h. Finally, the obtained material was repeatedly centrifuged and washed with DI water until neutral pH. The powder was dried at 50 °C for 2 h under air conditions. To evaluate the effect of synthesis conditions on the physicochemical properties of $Ti_3C_2T_x$, pure $Ti_3C_2T_x$ was solvothermal treated in the same conditions without precursors of Zn/Ti LDH. The scheme of the synthesis procedure is shown in Fig. 2a.

2.3. Characterization of photocatalytic materials

The crystalline phase was characterized by the Rigaku Intelligent X-ray diffraction (XRD) system SmartLab (Rigaku Corporation, Tokyo, Japan). Scans were recorded in the 2θ range from 5° to 80°, with a speed of $2°{\cdot}min^{-1}$ and a step of 0.01°. Specific surface area and pore volume of the samples were evaluated through Brunauer-Emmett-Teller (BET) method by N_2 adsorption at 77 K (boiling point of liquid nitrogen) with the Micromeritics Gemini V apparatus (model 2365) (Norcross, GA, USA). Firstly a pretreatment at 200 °C for 2 h under nitrogen flow was performed. The light absorption properties were measured in the wavelength range from 200 nm to 800 nm by the ThermoScientific Evolution 220 spectrophotometer (Waltham, MA, USA) using barium sulfate as a standard reference. The bandgap energy was calculated using the Kubelka-Munk function, $(R)^{0.5}E_{ph}^{0.5}$ against E_{ph}, where E_{ph} is photon energy. The photocatalysts' surface morphology was measured by scanning electron microscopy (SEM) using SEM Microscope FEI Quanta FEG 250. Fourier-transform infrared spectroscopy (FTIR) analysis was performed using FTIR Nicolet iS10 (Thermo Fisher Scientific Waltham, MA, USA) spectrometer in the wavenumber from 400 to 4000 cm^{-1}. The surface chemistry of the samples was analyzed by X-ray photoelectron spectroscopy (XPS) using Escalab 250Xi multispectroscope (ThermoFisher Scientific). The spectroscope operates with a monochromatic AlKα X-ray source (spot size 650 μm). The high-resolution spectra were collected in the core-level binding energy range of Zn2p, Ti2p, C1s, and O1s, at pass energy of 20 eV. The charge compensation was provided by low-energy electron and Ar + ions bombardment throughout the measurement, with a final calibration at adventitious carbon C1s peak (284.8 eV). Spectral deconvolution was done using Avantage 5.9921 software (ThermoFisher Scientific). Transmission electron microscopy (TEM) and scanning transmission electron microscopy (STEM) analyses were carried out using Tecnai G2 200 kV and Thermo-Fisher Scientific Titan Themis Cs-corrector. Samples were dispersed in ethanol and subsequently placed on a carbon-coated copper grid.

The photoluminescence spectra (PL) and luminescence kinetic were registered using a spectrograph (Princeton Instr. Model Acton 2500i) coupled to a CCD streak camera (Hamamatsu Model C5680) operating in the 200–1100 nm spectral region with a temporal resolution of 20 ps. As an excitation source, a femtosecond laser was used (Coherent Model "Libra") equipped with an optical parametric amplifier (Light Conversion Model "OPerA").

Electrochemical impedance spectroscopy (EIS) measurements were performed using Potentiostat/Galvanostat Autolab PGSTAT204 (Metrohm Autolab) with a Na_2SO_4 (0.5 M) as an electrolyte. The photocatalytic materials were deposited on the carbon screen-printed electrodes with Ag/AgCl reference electrode (Metrohm Autolab). The diameter of the working electrode area was 4 mm. The AC voltage amplitude was 0.01 V, and the frequency ranged from 0.1 Hz to 100 kHz at 0 V *vs.* OCP (open circuit potential). The Mott Schottky analysis was performed to determine the flat band (F_b) potential of the Zn/Ti LDH. The EIS data were recorded from the anodic towards a cathodic direction. EIS data were recorded for the applied frequency of 1000 Hz in the potential range from 0 to −1.1 V vs. Ag/AgCl.

2.4. Photocatalytic activity

In a typical experiment, 0.05 g of the photocatalyst was dispersed in 25 cm^3 of 20 $mg{\cdot}dm^3$ acetaminophen or ibuprofen aqueous solution. The properties of both pharmaceuticals were summarized in Table 1S in the Supporting Materials. The photocatalytic process was carried out in a 25 cm^3 quartz reactor equipped with an air supply mode. A 300 W Xe lamp (LOT Oriel, Darmstadt, Germany) with the light flux in the UV range (310 nm < λ < 380 nm) equalled 30 mW cm^{-2} was used as a light source, imitating the sunlight spectrum. Before the experiment, the photocatalyst suspension was kept in the dark for 30 min under continuous magnetic stirring to reach adsorption-desorption equilibrium before irradiation. During the photodegradation process, 1 cm^3 of the suspension was separated every 20 min using a 0.2 μm syringe filter. The photocatalytic processes were performed for 60 min. The rate of acetaminophen and ibuprofen degradation was monitored using reverse-phase high-performance liquid chromatograph Shimadzu UFLC LC-20AD (Kyoto, Japan) with photodiode array detector Shimadzu SPD-M20A. The measurements were performed at 45 °C and under isocratic flow conditions of 0.5 cm^3 min^{-1}. A volume composition of the mobile phase of 70% acetonitrile, 29.5% water, and 0.5% orthophosphoric acid was applied to determine ibuprofen concentration, while 0.1% formic acid, 69.9% water, and 30% methanol to determine acetaminophen concentration. The total organic carbon (TOC) change in the photocatalytic process of acetaminophen and ibuprofen degradation was investigated using Shimadzu TOC Analyzer.

The additional experiments were performed in the model seawater to evaluate the effect of interfering ions on the efficiency of photocatalytic processes of acetaminophen and ibuprofen degradation. The composition of the model seawater was: 2.5% NaCl, 1.1% $MgCl_2$, 0.4% Na_2SO_4, 0.16% $CaCl_2$ in DI water (Wang et al., 2019). The concentration of ibuprofen or acetaminophen in model seawater was 20 mg/dm^3.

In the next step, the photocatalytic process was performed in the presence of scavengers to study the mechanism of acetaminophen and ibuprofen photodegradation. Ammonium oxalate was applied as holes scavenger (h^+), H_2O_2 for electrons (e^-), isopropyl alcohol for free hydroxyl radicals (·OH), and p-benzoquinone for superoxide radical anions ($\cdot O_2^-$).

3. Results and discussion

The SEM analysis was performed to show the morphology of MXene -$Ti_3C_2T_x$, Zn/Ti LDH, and Zn/Ti LDH-Ti_3C_2 composite. The formation of an accordion-like structure of MXene is presented in Fig. 1a. The obtained samples of pure LDH and Zn/Ti LDH-2.5% Ti_3C_2 composite present a flake-like morphology (Fig. 1b–c). However, there is no clearly visible difference between the morphology of the samples with various content of MXene (Fig. 1S in the Supporting Materials). The TEM images of Zn/Ti LDH-2.5% Ti_3C_2 (Fig. 1 d-e) confirmed the formation of Zn/Ti LDH flakes (brighter area) with and inclusions of MXene flakes (darker area). The TEM elemental mapping is presented in Fig. 2S in the Supporting Materials.

The XRD patterns of MAX, MXene and combined MXene/LDHs materials are presented in Fig. 2 b-c. After the etching of aluminium from Ti_3AlC_2, the synthesized $Ti_3C_2T_x$ showed the main diffraction peaks centred at 2θ = 8.8°, 18.1°, and 27.4°, corresponding to (002), (004), and (006) planes, indicating the MAX phase compound has been

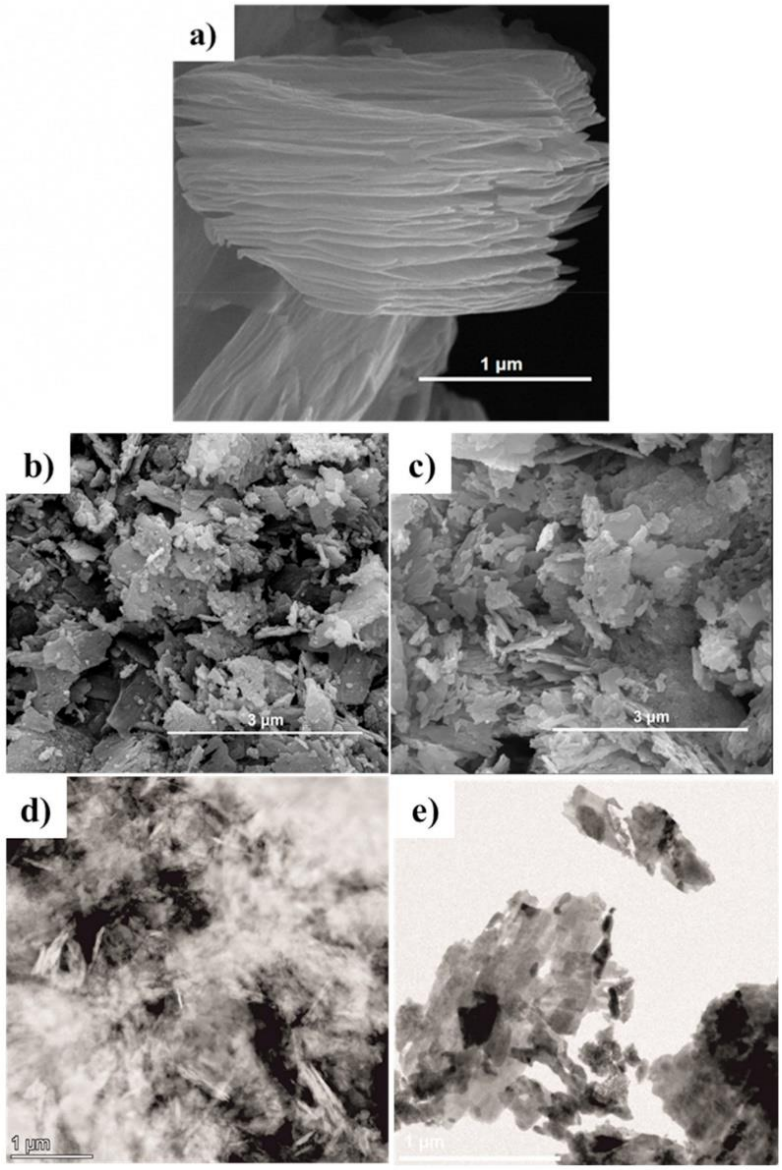

Fig. 1. SEM image of accordion-like $Ti_3C_2T_x$ (a), pure Zn/Ti LDH (b), Zn/Ti LDH-2.5% Ti_3C_2 (c), and TEM images of Zn/Ti LDH-2.5% Ti_3C_2 (d–e).

successfully transformed to Ti_3C_2 (Fig. 2a). The XRD analysis of $Ti_3C_2T_x$, which underwent a solvothermal reaction in the presence of urea, performed at 130 °C for 48 h, revealed the shifting of the MXene main diffraction peak to lower values of 2θ from 8.8° to 6.8° (Fig. 2b). This phenomenon of *d*-spacing increase may be related to the intercalation of urea and exfoliation during the solvothermal process (Yang et al., 2019). Furthermore, Zhao et al. stated that the presence of urea in the solvothermal reaction might prevent MXene from oxidation (Zhao et al., 2022).

Moreover, the X-ray diffraction (XRD) analysis confirmed the formation of Zn/Ti LDH, as shown in Fig. 2c. The narrow and symmetric peak characteristic for LDH at $2\theta = 13.2°$ corresponding to the (003) reflection can be observed in all the obtained samples. The reflections of (006), (009), (110), and (113) can be assigned to LDH. For all composites materials, no diffraction signals corresponding to the MXene are noticed. A similar effect of no diffraction peaks identified for Ti_3C_2 was reported by Li et al. (2020) for Bi_3TaO_7/Ti_3C_2 composite, Cai et al. (2018) for Ag_3PO_4/Ti_3C_2, and Cheng et al. (2020) for $CdLa_2S_4/Ti_3C_2$ and Fang et al. (2019) for Ag_2WO_4/Ti_3C_2. This phenomenon is attributed to its ultra-thick surface property, low amount, and high dispersion. The incorporation of Ti_3C_2 did not affect the crystal structure of Zn/Ti LDH, excluding the influence of the crystal structure on photocatalytic activity. However, analyzing the crystallite size of Zn/TiLDH, it can be seen that the presence of MXene promotes the growth of LDHcrystallites, as presented in Table 2S in Supporting Materials.

The diffuse reflectance UV–vis spectroscopy (DR/UV–vis) was performed to investigate the optical absorption characteristics of the prepared materials. All results were normalized for better clarity and

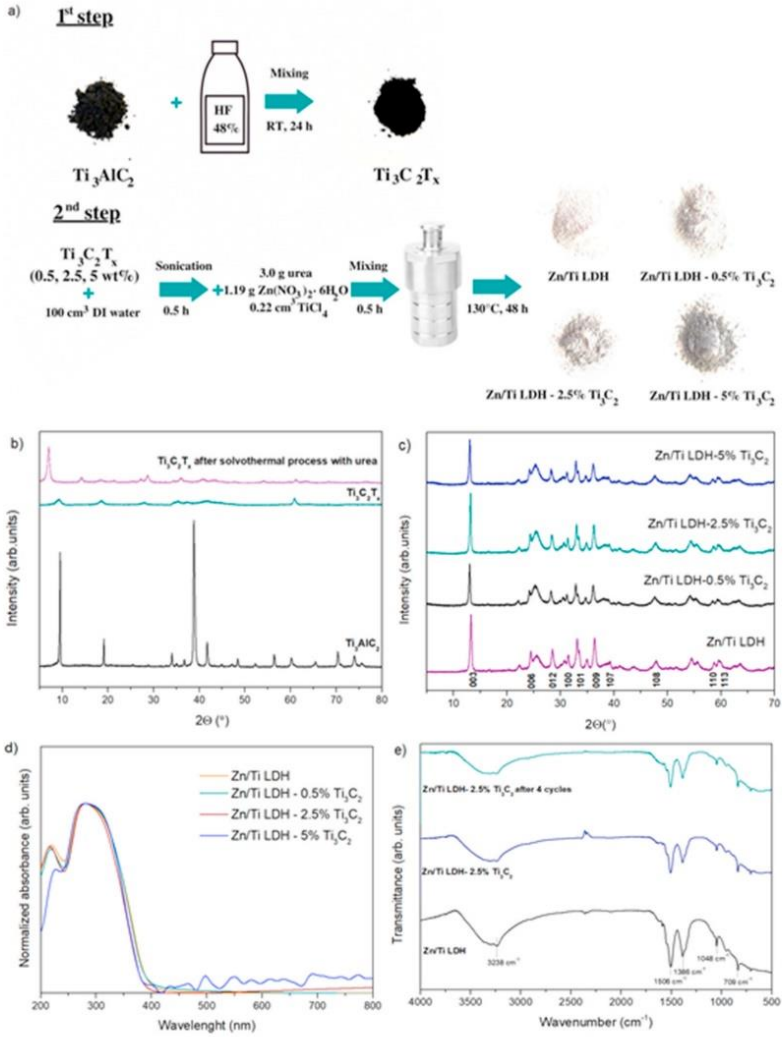

Fig. 2. Synthesis scheme (a), XRD diffractograms of Ti_3AlC_2, $Ti_3C_2T_x$, and $Ti_3C_2T_x$ after the solvothermal process with urea (b), XRD diffractograms of pure Zn/Ti LDH and Zn/Ti LDH-2.5%Ti_3C_2 (c), DR/UV–Vis spectra of Zn/Ti LDH and Zn/Ti LDH-Ti_3C_2 (d), and FTIR spectra of pure Zn/Ti LDH and Zn/Ti LDH-2.5%Ti_3C_2 (e).

comparison of the values. As shown in Fig. 2d, pure LDH exhibited strong absorption intensity only in the UV range with a threshold of about 400 nm. For the composite materials, a significant increase in the absorption in the range of 400–800 nm may be attributed to the presence of MXene and its absorption in the UV–Vis light range. It can be further observed by the gradually darker colour with higher content of MXene (inset in Fig. 2a). The Kubelka-Munk plots for obtained composites are presented in Fig. 3S in Supporting Materials. For samples containing MXene in the composition, the bandgap values were similar to pure LDH material. The physicochemical characteristics of pure MXene, Zn/TiLDH, and Zn/Ti LDH-Ti_3C_2 composites are presented in Table 2S in Supporting Materials. The BET surface area of pure MXene and Zn/Ti LDH was about 10.2 $m^2 \cdot g^{-1}$ and 129.4 $m^2 \cdot g^{-1}$, respectively. For the composite containing 0.5% of MXene, a slight decrease in surface area and pore volume was observed. The highest BET surface area of about 134.5 $m^2 \cdot g^{-1}$ was noticed for Zn/Ti LDH-5% Ti_3C_2.

Fig. 2e represents the FTIR spectra of pure Ti/Zn LDH and Zn/Ti LDH-2.5%Ti_3C_2. There is no difference between the spectra of pure LDH and the composite material. The strong, wide absorption band with a maximum at 3238 cm^{-1} is attributed to the O–H stretching mode. The characteristic signals at 1506 cm^{-1} and 1386 cm^{-1} are assigned to the interlayer carbonate anions (CO_3^{2-}) (Sun et al., 2019). Furthermore, weaker signals at 1048 cm^{-1} and 709 cm^{-1} are assigned to the carbonate and free carbonate ions (Egambaram et al., 2019).

The photoluminescence (PL) spectra of Zn/Ti-LDH and Zn/Ti-LDH-Ti_3C_2 photocatalysts were analyzed under 350 nm excitation wavelength (see Fig. 3a). The pure Zn/Ti-LDH showed a broad emission band with a maximum of about 450 nm, similar to Zn (Zhang et al., 2013) or Ti (Chowdhury and Bhattacharyya, 2015) doped LDH. The similar profiles of luminescence spectra of Zn or Ti-doped LDH powders suggest that the origin of the PL phenomenon may be the same. The emission in this region in the above-mentioned materials results from surface defects. The pure Zn/Ti-LDH catalyst shows strong photoluminescence attributed to the presence of either oxygen vacancies and/or defects in the LDH material. These defects resulting from the incorporation of Zn or Ti into the lattice have a strong impact on photocatalytic activity.

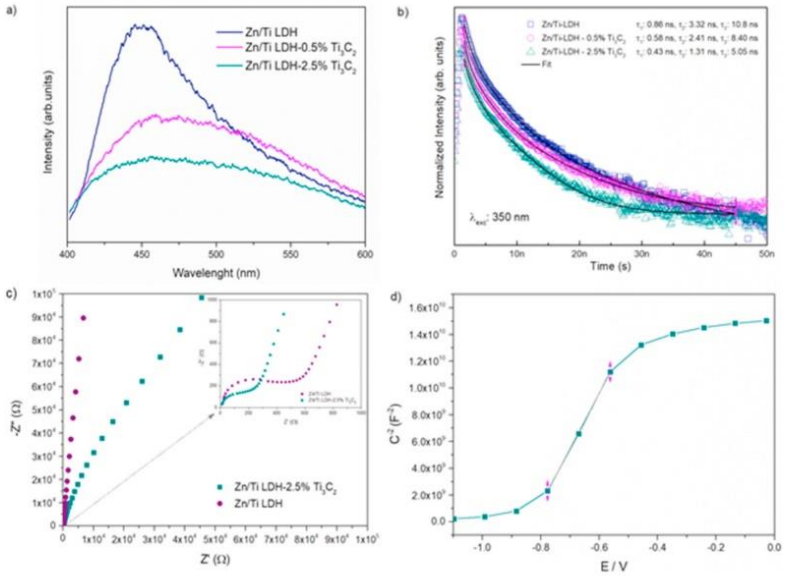

Fig. 3. Photoluminescence spectra (a), photoluminescence decay curves (b), EIS Nyquist plots (c) for Zn/Ti LDH-Ti_3C_2 composites, and Mott-Schottky plot (d) for sample Zn/Ti LDH.

Oxygen vacancies and defects are reported to bind the photo-induced electrons easily to form excitons, and PL signals may be easily observed. The broadened single-band emission spectrum observed instead of two or three narrower bands typical for emissions from semiconductor defects suggests the presence of hydroxyl groups and water molecules in LDH (Prestopino et al., 2019). For the composites of LDH with Ti_3C_2, the emission band is strongly broadened and slightly shifted toward longer wavelengths. The deconvolution of the broad band observed for the composite shows that it consists of three components. The first and third components (approx. 450 nm and sideband at 510 nm) are related to the emission from Zn/Ti-LDH, while the second component (observed at approx. 480 nm) overlapping the emission spectrum of the composite is assigned to the luminescence from surface defects in Ti_3C_2. The emission sum of both compounds leads to the broadening of the luminescence band, and the emission from Ti_3C_2 observed at longer wavelengths causes a slight redshift of the band. The lower PL intensity for composite material than pure Zn/Ti LDH results from a lower number of electron-hole recombination centres, which consequently increases the composites' photocatalytic efficiency.

As the luminescence decays showed a non-exponential character, three components were used for the correct fit of the curves (Fig. 3b). The multiexponential decays suggest that in the samples are different types of recombination centres. As the defects have different energy levels, they trap and release the carriers with variable transport rates. For composites, values of all three components (τ_1, τ_2, τ_3) are lower, and they decrease with the increase of Ti_3C_2 content, which is an effect of energy transfer between LDH and MXene and the distribution of the excitation energy between compounds and the emissions of both.

Fig. 3c shows the EIS Nyquist plot of the prepared photocatalysts. It can be seen that the combination of the LDH with MXene led to a decrease in the semicircle's diameter compared to pure Zn/Ti LDH, suggesting higher separation efficiency of the photo-induced charge carriers (Liu et al., 2020). As shown in Fig. 3d, Zn/Ti LDH-2.5% Ti_3C_2 composite Mott Schottky plot presented n-type characteristics. The potential of flat band edge position was recorded at −0.87 V vs. Ag/AgCl. This value was converted to a value of −0.58 V vs. NHE. Typically, for n-type semiconductors, the F_b potential is almost equal to the conduction band (CB) potential. Thus, the valence band (VB) edge of the composite was calculated as approx. 2.62 eV vs NHE.

The XPS analysis provided information about the oxidation states of elements in the composite material. The survey spectrum for Zn/Ti-LDH-2.5% Ti_3C_2 is presented in Fig. 4S in Supporting Materials. It can be seen that the photocatalyst consists of Zn, Ti, O, and C. The XPS Zn 2p, Ti 2p, O 1s, and C 1s regions for Zn/Ti-LDH-2.5% Ti_3C_2 are shown in Fig. 5S in Supporting Materials. The Zn 2p spectrum shows two characteristic peaks at 1022 eV and 1044 eV attributed to Zn $2p_{3/2}$ and $2p_{1/2}$, respectively, corresponding to the occurrence of zinc in the form of Zn^{2+} in LDH structure (Liu et al., 2021b; Li et al., 2019b). The Ti 2p spectrum may be deconvoluted in four doublet pairs at 455 eV, 457 eV, 457.5 eV, and 459 eV($2p_{3/2}$), which correspond to Ti–C, C–Ti–O, Ti^{3+}, and Ti^{4+}, respectively. The Ti–C and C–Ti–O are related to the presence of MXene (Lu et al., 2021). The signal from Ti^{3+} may be attributed to the Ti_3C_2 or defects in the lattice of Zn/Ti LDH. The formation of Ti^{3+} defects was also noticed in the studies presented by Zhao et al., 2013, 2014 for Ni/Ti LDH and Zn/Ti LDH. The formation of Ti^{3+} defects in the Zn/Ti LDH lattice results from removing oxygen atoms from the surface. The presence of such surface defects results in more oxygen defects, which influence the electronic properties and enhance the separation of electron-hole pairs. Furthermore, it has also been reported that the electron trapped on the Ti^{3+} are able to form superoxide anion radicals from surface-absorbed oxygen (Zhao et al., 2013, 2014). The high-resolution C 1s spectrum is divided into five signals at approximately 283 eV, 284 eV, 285 eV, 286.5 eV, and 289 eV corresponding to Ti–C, C–Ti–O, and C–C/C=C in the MXene structure, and in C–O and C=O bonds in carbonate groups (Ahmed et al., 2016). In the O 1s spectrum, six signals occurred at 528 eV, 529 eV, 530.5 eV, 531.5 eV, 533 eV, and 534 eV, attributed to adsorbed oxygen, metal-oxide bonds, CO_3^{2-}, metal-hydroxide bonds, C=O, and H_2O, respectively (Zheng et al., 2019; Chubar et al., 2013).

The photocatalytic activity of Zn/Ti LDHand Zn/Ti LDH-Ti_3C_2 composites was evaluated in reactions of pharmaceuticals degradation under simulated solar light. Fig. 4a–d and Tables 3S–5S in the Supporting Materials present the results of acetaminophen and ibuprofen removal by direct photolysis and in the presence of photocatalytic material. As can be seen, the photolysis of acetaminophen after 60 min of irradiation was only about 11%. On the contrary, ibuprofen

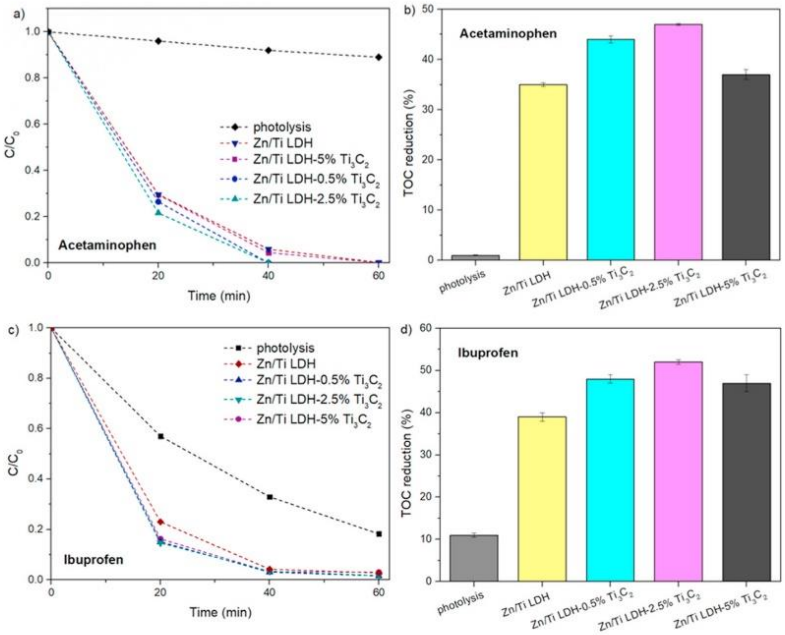

Fig. 4. Efficiency of acetaminophen degradation (C/C_0) (a), TOC reduction (%) for ACT (b), efficiency of ibuprofen degradation (C/C_0) (c) TOC reduction (%) for IBP (d) Zn/Ti LDH and Zn/Ti LDH-Ti_3C_2 photocatalysts.

photodegradation under the same conditions reached about 80%. However, the total organic carbon analysis revealed that after the photolysis of acetaminophen and ibuprofen, the reduction of TOC was equal to 1% and 11.5%, respectively. The application of pure Zn/Ti LDH photocatalyst increased the TOC removal by 34% for ACT degradation and by 27.5% for IBP removal, compared to photolysis. Furthermore, it was observed that coupling of Zn/Ti LDH with the MXene compound led to improved photocatalytic degradation and mineralization of both pharmaceuticals. When the amount of Ti_3C_2 in the composite was 2.5%, the rate constant of acetaminophen degradation increased from 8.1 to 12.8 $min^{-1}{\cdot}10^{-2}$, while TOC reduction increased from 35% to 47% compared to pure Zn/Ti LDH. For this composite, 100% of acetaminophen was removed within 40 min of UV–vis irradiation. In the case of IBP degradation, the rate constant increased from 5.8 to 7.1 $min^{-1}{\cdot}10^{-2}$, while TOC reduction increased from 39% to 52% compared to pure Zn/Ti LDH. Almost complete degradation of IBP was observed within 60 min. The decrease in the activity with the higher content of MXene may be related to the overloading of the photocatalyst surface. The increasing amount of MXene could shield the light absorption of the photocatalyst and thus inhibit photocatalytic activity. A similar Ti_3C_2 overloading effect was observed by Huang et al. (2019) for Bi_2WO_6/Ti_3C_2, Que et al. (2022) for $FAPbBr_3/Ti_3C_2$ composite or Liu et al. (2021c) for C_3N_4/Ti_3C_2 material.

To evaluate the effect of interfering ions on the efficiency of ACT and IBP photocatalytic degradation, the photodegradation of pharmaceuticals was performed in the model seawater containing the following ions: Na^+, Ca^{2+}, Mg^{2+}, Cl^-, and SO_4^{2-}. Some previously reported results showed that inorganic anions such as Cl^- ion in water might reduce photocatalytic activity due to the fact that induced hydroxyl radicals are scavenged by chloride ions or Cl^- can be adsorbed on the surface of photocatalyst and block the active sites (Makita and Harata, 2008; Porcar-Santos et al., 2020). As shown in Fig. 5a–b and in Table 6S in the Supporting Materials in the present study, the degradation efficiency of both pharmaceuticals was unaffected by interfering inorganic ions. This is an important fact about the viability of photocatalytic water treatments using Zn/Ti LDH-2.5%Ti_3C_2 in saline water samples.

In order to elucidate the photocatalytic mechanism, experiments with scavengers for the detection of reactive oxygen species (ROS) participating in the photodegradation process of ACT and IBP were performed (Fig. 5c–d). The content of each scavenger was equal to 0.03 mmol (10-fold concentration of contaminant). Performed experiments showed that the mechanisms of degradation of ACT and IBP are different. In the case of ACT, the inhibitory effect of ammonium oxalate was weak, indicating that holes did not play a significant role in the degradation process. The highest inhibition effect was noticed for p-benzoquinone, suggesting that superoxide anion radicals appear to be the most likely ROS in ACT degradation (Wang et al., 2021b; Fan et al., 2018). Meanwhile, for IBP, the main species involved in the photocatalytic process were holes and hydroxyl radicals due to the limitation of the reaction that occurred in the presence of ammonium oxalate and isopropanol, respectively. These results are consistent with the previous studies of Jiménez-Salcedo et al. (2021) and Sá et al. (2021), who observed that holes are major ROS involved in the degradation of IBP. Also, Liu et al. (Liu et al., 1016) confirmed that holes and hydroxyl radicals are responsible for IBP degradation using niobium-doped TiO_2 nanotubes.

Furthermore, the excellent stability of the prepared LDH/MXene composite was confirmed in the four subsequent photocatalytic cycles of acetaminophen degradation, as shown in Fig. 5e. After the fourth cycle, the efficiency of pollutant removal still reached 100% within 40 min, thus suggesting the high potential of photocatalyst for reusability. Also, the TOC reduction remains unchanged after repetitive photocatalytic cycles. Furthermore, the FTIR (Fig. 2e), TEMTEM (Fig. 3S in Supporting Materials), and XPS (Fig. 5S in Supporting Materials) analyses after the photocatalytic processes did not show any changes in the structure of the photocatalyst.

A schematic illustration of the photocatalytic mechanism of IBP and ACT degradation in the presence of Zn/Ti LDH-2.5% Ti_3C_2 photocatalyst is proposed and presented in Fig. 6. Photogenerated electrons are transferred and accumulated by the MXene, inhibiting the

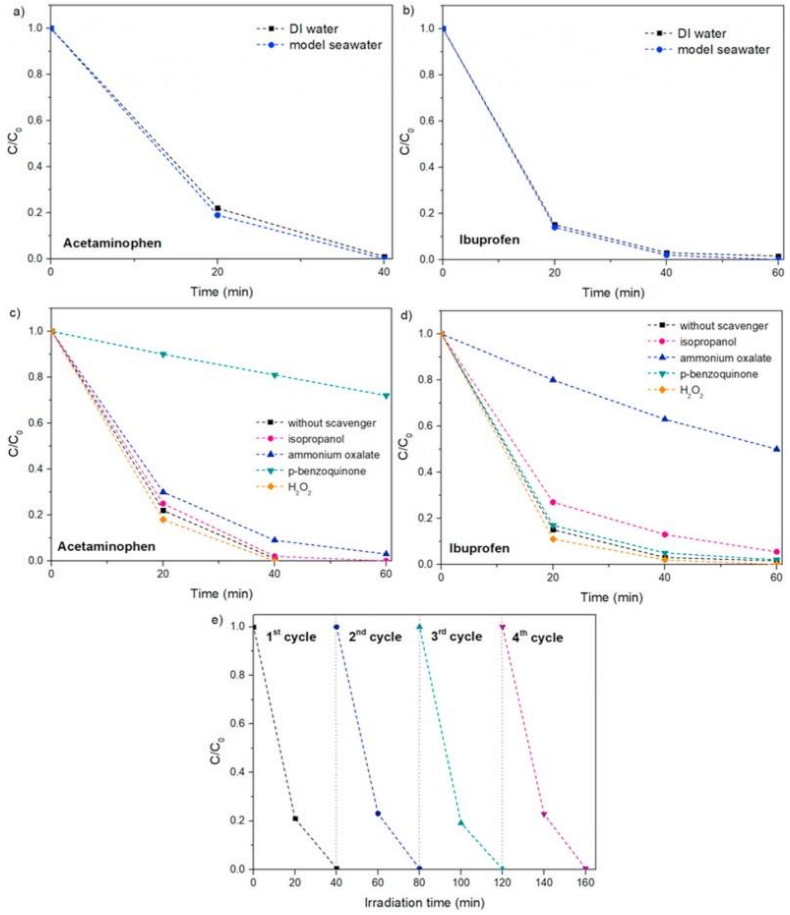

Fig. 5. ACT photocatalytic degradation in DI water and model seawater for Zn/Ti LDH-2.5%Ti_3C_2 (a), ibuprofen degradation in DI water and model seawater for Zn/Ti LDH-2.5%Ti_3C_2 (b), the effect of scavengers on the ACT photocatalytic degradation (c) and IBP degradation for Zn/Ti LDH-2.5%Ti_3C_2 (d), cycling test of the ACT photocatalytic degradation for Zn/Ti LDH-2.5%Ti_3C_2 (e).

recombination of electron-hole pairs. Meanwhile, based on the CB and VB location, the sample Zn/Ti LDH-2.5% Ti_3C_2 may oxidize water molecules to hydroxyl radicals as well as reduce oxygen into superoxide anion radicals.

The performance of the Zn/Ti LDH-2.5% Ti_3C_2 composite was compared with the previously reported photocatalysts used for photodegradation of ACT or IBP, and the results are shown in Table 1. It was found that the Zn/Ti LDH-Ti_3C_2 photocatalyst prepared in our work has excellent performance compared with other materials, especially considering the high degradation efficiency of both pharmaceuticals within 60 min under simulated solar light.

4. Conclusions

In summary, for the first time, the series of novel composites of Zn/Ti LDH coupled with MXene-$Ti_3C_2T_x$ were successfully synthesized and characterized. The important role of the MXene compound as a co-catalyst in photocatalytic water treatment was proven. Specifically, the composite with optimal content of $Ti_3C_2T_x$ equal to 2.5% exhibited superior activity towards degradation of acetaminophen (100% within 40 min) and ibuprofen (99.7% within 60 min), frequently detected pharmaceuticals in surface waters. The presence of MXene - Ti_3C_2 in the composite structure facilitates electron transfer inhibiting the electron-hole recombination process. So far, there are only a few studies concerning the application of LDH/MXene composites in photocatalysis. Thus, the findings presented in this paper enriched the possible application of LDH/MXene photocatalyst for water purification. Furthermore, the essential is the potential use of composite Zn/Ti LDH-2.5% Ti_3C_2 for saline water treatment, where activity was unaffected by interfering inorganic ions, which may have great importance in the environmental aspects. Besides, this composite also shows excellent recycling stability with no changes in photocatalytic efficiency and the material properties in the subsequent cycles of photocatalytic degradation. Finally, we proposed the mechanism of pharmaceuticals degradation based on the trapping experiments with scavengers of ROS, bandgap calculation, and Mott Schottky analysis. The main reactive oxygen species involved in photocatalytic degradation of acetaminophen are superoxide anion radicals (O_2^-), while for ibuprofen holes (h^+) and hydroxyl radicals (OH). Overall, the findings presented in this studies enriched the LDH/MXene photocatalysts, demonstrating highly prospective strategy for pharmaceuticals treatment under solar light.

Author contributions

Conceptualization, AZ-J.; Synthesis, AG; Formal analysis, AG, IW, PG, JR, JK; Funding acquisition, AZ-J.; Investigation, AG; Methodology,

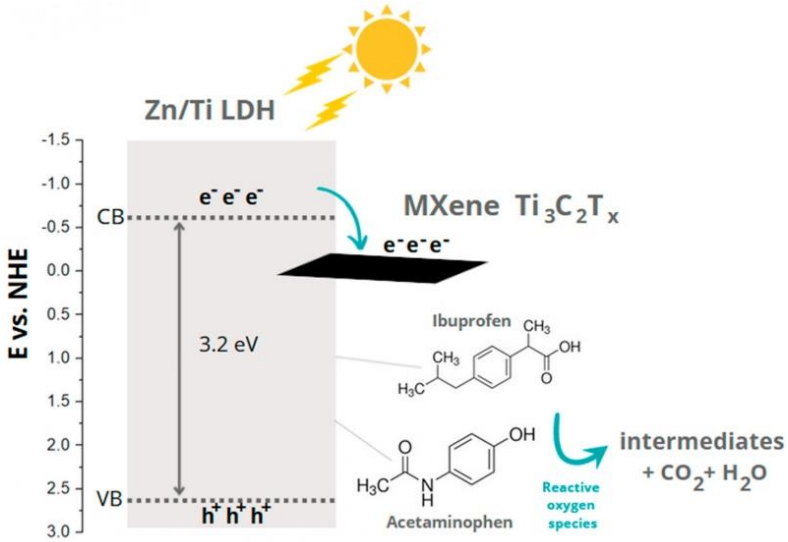

Fig. 6. Schematic illustration of the possible mechanism of ACT and IBP degradation in the presence of Zn/Ti LDH-Ti_3C_2 photocatalyst.

Table 1
The comparison of this work with results presented in recent related papers.

Photocatalyst	Catalyst loading (g/dm^3)	Pharmaceutical concentration (mg/dm^3)	Light source	Degradation efficiency	Ref.
TiO_2/polyethersulphone	n.d. (film - 320 cm^2)	ACT, 10	UV-A lamp	80% in 7 h	Chijioke-Okere et al. (2021)
Sr@TiO_2/UiO-66-NH_2	0.25	ACT, 5	Xe lamp with a 320 nm cut off filter	90% in 4 h	Wang et al. (2022)
carbon xerogel/TiO_2	2	ACT, 25	Hg lamp	96% in 4 h	da Cunha et al. (2021)
noble metal-decorated NH_2-MIL-125	0.25	ACT, 5	Xe lamp with a 290 nm cut off filter	100% in 3 h	Muelas-Ramos et al. (2021)
α-$SnWO_4$/UiO-66(NH_2)/g-C_3N_4	0.5	IBP, 10	Xe lamp	95% in 2 h	Wei et al. (2021)
biochar–$ZnAl_2O_4$	1	IBP, 20	Hg lamp	100% in 2 h	Siara et al. (2022)
Ag/Bi-decorated BiOBr	0.3	IBP, 20	Xe lamp	92.3% within 1 h	Qin et al. (2022)
FeO supported on modified Iranian clinoptilolite	0.3	IBP, 25	Xe lamp	99.8% in 3 h	Mohadesi et al. (2022)
Zn/Ti LDH-2.5%Ti_3C_2	2	ACT, 20/IBP, 20	Xe lamp	100% in 40 min/99.7% in 1 h	this work

AZ-J; Project administration, AZ-J.; Writing – original draft, AG, AZ-J; Writing – review & editing, AG, AZ-J, IW

Declaration of competing interest

The authors declare that they have no known competing financial interests or personal relationships that could have appeared to influence the work reported in this paper.

Data availability

Data will be made available on request.

Acknowledgements

The research was financially supported by Polish National Science Centre (Grant No. NCN 2018/30/E/ST5/00845).

Appendix A. Supplementary data

Supplementary data to this article can be found online at https://doi.org/10.1016/j.chemosphere.2022.136191.

References

Ahmed, B., Anjum, D.H., Hedhili, M.N., Gogotsi, Y., Alshareef, H.N., 2016. H2O2 assisted room temperature oxidation of Ti2C MXene for Li-ion battery anodes. Nanoscale. https://doi.org/10.1039/c6nr00002a.

Akpotu, S.O., Oseghe, E.O., Ayanda, O.S., Skelton, A.A., Msagati, T.A.M., Ofomaja, A.E., 2019. Photocatalysis and biodegradation of pharmaceuticals in wastewater: effect of abiotic and biotic factors. Clean Technol. Environ. Policy 21, 1701–1721. https://doi.org/10.1007/s10098-019-01747-4.

Article, R., Rao, a V.P., Umabala, a M., Suresh, P., 2015. Non-TiO_2 based photocatalysts for remediation of hazardous organic pollutants under green technology-present status. Rev. 4, 1145–1172.

Branchet, P., Arpin-Pont, L., Piram, A., Boissery, P., Wong-Wah-Chung, P., Doumenq, P., 2021. Pharmaceuticals in the marine environment: what are the present challenges in their monitoring? Sci. Total Environ. 766, 142644 https://doi.org/10.1016/j.scitotenv.2020.142644.

Cai, T., Wang, L., Liu, Y., Zhang, S., Dong, W., Chen, H., Yi, X., Yuan, J., Xia, X., Liu, C., Luo, S., 2018. Ag3PO4/Ti3C2 MXene interface materials as a Schottky catalyst with enhanced photocatalytic activities and anti-photocorrosion performance. Appl. Catal. B Environ. 239, 545–554. https://doi.org/10.1016/j.apcatb.2018.08.053.

Chen, W., Han, B., Xie, Y., Liang, S., Deng, H., Lin, Z., 2020. Ultrathin Co-Co LDHs nanosheets assembled vertically on MXene: 3D nanoarrays for boosted visible-light-driven CO2 reduction. Chem. Eng. J. 391, 123519 https://doi.org/10.1016/j.cej.2019.123519.

Cheng, L., Chen, Q., Li, J., Liu, H., 2020. Boosting the photocatalytic activity of CdLa2S4 for hydrogen production using Ti3C2 MXene as a co-catalyst. Appl. Catal. B Environ. 267, 118379 https://doi.org/10.1016/j.apcatb.2019.118379.

Chijioke-Okere, M.O., Mohd Hir, Z.A., Ogukwe, C.E., Njoku, P.C., Abdullah, A.H., Oguzie, E.E., 2021. TiO2/Polyethersulphone films for photocatalytic degradation of acetaminophen in aqueous solution. J. Mol. Liq. 338, 116692 https://doi.org/10.1016/j.molliq.2021.116692.

Chowdhury, P.R., Bhattacharyya, K.G., 2015. Ni/Ti layered double hydroxide: synthesis, characterization and application as a photocatalyst for visible light degradation of aqueous methylene blue. Dalton Trans. 15 https://doi.org/10.1039/C5DT00257E.

Chubar, N., Gerda, V., Megantari, O., Mičušík, M., Omastova, M., Heister, K., Man, P., Fraissard, J., 2013. Applications versus properties of Mg–Al layered double hydroxides provided by their syntheses methods: alkoxide and alkoxide-free sol–gel syntheses and hydrothermal precipitation. Chem. Eng. J. 234, 284–299. https://doi.org/10.1016/j.cej.2013.08.097.

da Cunha, R., do Carmo Batista, W.V.F., de Oliveira, H.L., dos Santos, A.C., dos Reis, P. M., Borges, K.B., Martelli, P.B., Furtado, C.A., de Fátima Gorgulho, H., 2021. Carbon Xerogel/TiO2 composites as photocatalysts for acetaminophen degradation. J. Photochem. Photobiol., A 412, 113248. https://doi.org/10.1016/j.jphotochem.2021.113248.

Desbiolles, F., Malleret, L., Tiliacos, C., Wong-Wah-Chung, P., Laffont-Schwob, I., 2018. Occurrence and ecotoxicological assessment of pharmaceuticals: is there a risk for the Mediterranean aquatic environment? Sci. Total Environ. 639, 1334–1348. https://doi.org/10.1016/j.scitotenv.2018.04.351.

Dey, A., Sandre, V., Marangoni, D.G., Ghosh, S., 2018. Interaction between a nonsteroidal anti-inflammatory drug (ibuprofen) and an anionic surfactant (AOT) and effects of salt (NaI) and hydrotrope (4-4-4). J. Phys. Chem. B 122, 3974–3987. https://doi.org/10.1021/acs.jpcb.8b00687.

Egambaram, O.P., Pillai, S.K., Lategan, M., Ray, S.S., 2019. Nanostructured Zn-Ti layered double hydroxides with reduced photocatalytic activity for sunscreen application. J. Nanoparticle Res. 21 https://doi.org/10.1007/s11051-019-4488-3.

Fan, G., Zheng, X., Luo, J., Peng, H., Lin, H., Bao, M., Hong, L., Zhou, J., 2018. Rapid synthesis of Ag/AgCl@ZIF-8 as a highly efficient photocatalyst for degradation of acetaminophen under visible light. Chem. Eng. J. 351, 782–790. https://doi.org/10.1016/j.cej.2018.06.119.

Fang, Y., Cao, Y., Chen, Q., 2019. Synthesis of an Ag2WO4/Ti3C2 Schottky composite by electrostatic traction and its photocatalytic activity. Ceram. Int. 45, 22298–22307. https://doi.org/10.1016/j.ceramint.2019.07.256.

Guo, X., Zhang, F., Evans, D.G., Duan, X., 2010. Layered double hydroxide films: synthesis, properties and applications, Chem. Commun. Now. 46, 5197–5210. https://doi.org/10.1039/c0cc00313a.

Hao, C., Wu, Y., An, Y., Cui, B., Lin, J., Li, X., Wang, D., Jiang, M., Cheng, Z., Hu, S., 2019. Interface-coupling of CoFe-LDH on MXene as high-performance oxygen evolution catalyst. Mater. Today Energy 12, 453–462. https://doi.org/10.1016/j.mtener.2019.04.009.

Huang, G., Li, S., Liu, L., Zhu, L., Wang, Q., 2019. Ti3C2 MXene-modified Bi2WO6 nanoplates for efficient photodegradation of volatile organic compounds. Appl. Surf. Sci. https://doi.org/10.1016/j.apsusc.2019.144183.

Jiménez-Salcedo, M., Monge, M., Tena, M.T., 2021. Combination of au-ag plasmonic nanoparticles of varied compositions with carbon nitride for enhanced photocatalytic degradation of ibuprofen under visible light. Materials 14. https://doi.org/10.3390/ma14143912.

Klementova, S., Kahoun, D., Doubkova, L., Frejlachova, K., Dusakova, M., Zlamal, M., 2017. Catalytic photodegradation of pharmaceuticals-homogeneous and heterogeneous photocatalysis. Photochem. Photobiol. Sci. 16, 67–71. https://doi.org/10.1039/c6pp00164e.

Li, M., Fang, L., Zhou, H., Wu, F., Lu, Y., Luo, H., Zhang, Y., Hu, B., 2019a. Three-dimensional porous MXene/NiCo-LDH composite for high performance non-enzymatic glucose sensor. Appl. Surf. Sci. 495 https://doi.org/10.1016/j.apsusc.2019.143554.

Li, Y., Xu, J., Liu, Z., Yu, H., 2019b. Performance of amorphous CoSx/oxygen vacancies ZnO heterojunction photocatalytic hydrogen evolution. J. Mater. Sci. Mater. Electron. 30, 246–258. https://doi.org/10.1007/s10854-018-0287-3.

Li, K., Lu, X., Zhang, Y., Liu, K., Huang, Y., Liu, H., 2020. Bi3TaO7/Ti3C2 heterojunctions for enhanced photocatalytic removal of water-borne contaminants. Environ. Res. 185, 109409. https://doi.org/10.1016/j.envres.2020.109409.

Liang, C., Lan, Z., Zhang, X., Liu, Y., 2016. Mechanism for the primary transformation of acetaminophen in a soil/water system. Water Res. 98, 215–224. https://doi.org/10.1016/j.watres.2016.04.027.

W. Liu, W. Zhang, M. Liu, P. Du, C. Dang, J. Liang, Y. Li, Fabrication of Niobium Doped Titanate Nanoflakes with Enhanced Visible-Light-Driven Photocatalytic Activity for Efficient Ibuprofen Degradation https://doi.org/10.1016/j.cclet.2019.07.050.

Liu, Y., Zeng, X., Easton, C.D., Li, Q., Xia, Y., Yin, Y., Hu, X., Hu, J., Xia, D., McCarthy, D. T., Deletic, A., Sun, C., Yu, J., Zhang, X., 2020. An in situ assembled –TiO2 vertical heterojunction for enhanced Z-scheme photocatalytic activity. Nanoscale 12, 8775. https://doi.org/10.1039/d0nr01611j.

Liu, G., Feng, M., Tayyab, M., Gong, J., Zhang, M., Yang, M., Lin, K., 2021a. Direct and efficient reduction of perfluorooctanoic acid using bimetallic catalyst supported on carbon. J. Hazard Mater. 412, 125224 https://doi.org/10.1016/j.jhazmat.2021.125224.

Liu, Y., Zhu, Q., Tayyab, M., Zhou, L., Lei, J., Zhang, J., 2021b. Single-atom Pt loaded zinc vacancies ZnO-ZnS induced type-V electron transport for efficiency photocatalytic H2 evolution. Solar RRL 5, 2100536. https://doi.org/10.1002/solr.202100536.

Liu, W., Sun, M., Ding, Z., Gao, B., Ding, W., 2021c. Ti3C2 MXene embellished g-C3N4 nanosheets for improving photocatalytic redox capacity. J. Alloys Compd. 877, 160233 https://doi.org/10.1016/j.jallcom.2021.160223.

Liu, Y., Chen, S., Li, K., Wang, J., Chen, P., Wang, H., Li, J., Dong, F., 2022. Promote the activation and ring opening of intermediates for stable photocatalytic toluene degradation over Zn-Ti-LDH. J. Colloid Interface Sci. 606, 1435–1444. https://doi.org/10.1016/j.jcis.2021.08.146.

Lu, C., Li, A., Li, G., Yan, Y., Zhang, M., Yang, Q., Zhou, W., Guo, L., 2021. S-decorated porous Ti3C2 MXene combined with in situ forming Cu2Se as effective shuttling interrupter in Na–Se batteries. Adv. Mater. 33 https://doi.org/10.1002/adma.202008414.

Ma, Y., Xu, D., Chen, W., Tang, Y., Wang, X., Li, L., Wang, J., 2022. Oxygen vacancy-embedded 2D/2D NiFe-LDH/MXene Schottky heterojunction for boosted photodegradation of norfloxacin. Appl. Surf. Sci. 572, 151432 https://doi.org/10.1016/j.apsusc.2021.151432.

Makita, M., Harata, A., 2008. Photocatalytic decolorization of rhodamine B dye as a model of dissolved organic compounds: influence of dissolved inorganic chloride salts in seawater of the Sea of Japan. Chem. Eng. Process. Process Intensif. 47, 859–863. https://doi.org/10.1016/j.cep.2007.01.036.

Mohadesi, M., Gouran, A., Seifi, K., 2022. Removal of ibuprofen from synthetic wastewater using photocatalytic method in the presence of FeO photocatalyst supported on modified Iranian clinoptilolite. Environ. Sci. Pollut. Res. 29, 34338–34348. https://doi.org/10.1007/s11356-021-18153-3.

Motlagh, P.Y., Khataee, A., Hassani, A., Sadeghi Rad, T., 2020. ZnFe-LDH/GO nanocomposite coated on the glass support as a highly efficient catalyst for visible light photodegradation of an emerging pollutant. J. Mol. Liq. 302, 112532 https://doi.org/10.1016/j.molliq.2020.112532.

Muelas-Ramos, V., Belver, C., Rodriguez, J.J., Bedia, J., 2021. Synthesis of noble metal-decorated NH2-MIL-125 titanium MOF for the photocatalytic degradation of acetaminophen under solar irradiation. Separ. Purif. Technol. 272, 118896 https://doi.org/10.1016/j.seppur.2021.118896.

Naz, A., Chowdhury, A., Mishra, B.K., 2021. Applications of microbes in bioremediation of point source pollutants from wastewater. IOP Conf. Ser. Earth Environ. Sci. 796 https://doi.org/10.1088/1755-1315/796/1/012039.

Pemberthy M, D., Padilla, Y., Echeverri, A., Peñuela, G.A., 2020. Monitoring pharmaceuticals and personal care products in water and fish from the Gulf of Urabá, Colombia. Heliyon 6. https://doi.org/10.1016/j.heliyon.2020.e04215.

Peña-Guzmán, C., Ulloa-Sánchez, S., Mora, K., Helena-Bustos, R., Lopez-Barrera, E., Alvarez, J., Rodriguez-Pinzón, M., 2019. Emerging pollutants in the urban water cycle in Latin America: a review of the current literature. J. Environ. Manag. 237, 408–423. https://doi.org/10.1016/j.jenvman.2019.02.100.

Phong Vo, H.N., Le, G.K., Hong Nguyen, T.M., Bui, X.T., Nguyen, K.H., Rene, E.R., Vo, T. D.H., Thanh Cao, N.D., Mohan, R., 2019. Acetaminophen micropollutant: historical and current occurrences, toxicity, removal strategies and transformation pathways in different environments. Chemosphere 236, 124391. https://doi.org/10.1016/j.chemosphere.2019.124391.

Porcar-Santos, O., Cruz-Alcalde, A., López-Vinent, N., Zanganas, D., Sans, C., 2020. Photocatalytic degradation of sulfamethoxazole using TiO2 in simulated seawater: evidence for direct formation of reactive halogen species and halogenated by-products. Sci. Total Environ. 736, 139605 https://doi.org/10.1016/j.scitotenv.2020.139605.

Prestopino, G., Arrabito, G., Generosi, A., Mattoccia, A., Paci, B., Perez, G., Verona-Rinati, G., Medaglia, P.G., 2019. Emerging switchable ultraviolet photoluminescence in dehydrated Zn/Al layered double hydroxide nanoplatelets. Sci. Rep. 9, 11498 https://doi.org/10.1038/s41598-019-48012-8.

Priya, A.K., Gnanasekaran, L., Rajendran, S., Qin, J., Vasseghian, Y., 2022. Occurrences and removal of pharmaceutical and personal care products from aquatic systems using advanced treatment- A review. Environ. Res. 204, 112298 https://doi.org/10.1016/j.envres.2021.112298.

Qin, M., Jin, K., Li, X., Wang, R., Li, Y., Wang, H., 2022. Novel highly-active Ag/Bi dual nanoparticles decorated BiOBr photocatalyst for efficient degradation of ibuprofen. Environ. Res. 206, 112628 https://doi.org/10.1016/j.envres.2021.112628.

Que, M., Cai, W., Zhao, Y., Yang, Y., Zhang, B., Yun, S., Chen, J., Zhu, G., 2022. 2D/2D Schottky heterojunction of in-situ growth FAPbBr3/Ti3C2 composites for enhancing photocatalytic CO2 reduction. J. Colloid Interface Sci. 610, 538–545. https://doi.org/10.1016/j.jcis.2021.11.094.

Rasheed, T., Shafi, S., Bilal, M., Hussain, T., Sher, F., Rizwan, K., 2020. Surfactants-based remediation as an effective approach for removal of environmental pollutants—a review. J. Mol. Liq. 318 https://doi.org/10.1016/j.molliq.2020.113960.

Razzaq, A., Ali, S., Asif, M., In, S., 2020. Layered Double Hydroxide (LDH) Based Photocatalytic CO_2 Conversion.

Ruggeri, G., Ghigo, G., Maurino, V., Minero, C., Vione, D., 2013. Photochemical transformation of ibuprofen into harmful 4-isobutylacetophenone: pathways, kinetics, and significance for surface waters. Water Res. 47, 6109–6121. https://doi.org/10.1016/j.watres.2013.07.031.

Sá, A.S., Feitosa, R.P., Honório, L., Peña-Garcia, R., Almeida, L.C., Dias, J.S., Brazuna, L. P., Tabuti, T.G., Triboni, E.R., Osajima, J.A., da Silva-Filho, E.C., 2021. A brief photocatalytic study of zno containing cerium towards ibuprofen degradation. Materials 14. https://doi.org/10.3390/ma14195891.

Shao, M., Han, J., Wei, M., Evans, D.G., Duan, X., 2011. The synthesis of hierarchical Zn-Ti layered double hydroxide for efficient visible-light photocatalysis. Chem. Eng. J. 168, 519–524. https://doi.org/10.1016/j.cej.2011.01.016.

Siara, S., Elvis, C., Harishkumar, R., Velayudhaperumal Chellam, P., 2022. ZnAl2O4 supported on lychee-biochar applied to ibuprofen photodegradation. Mater. Res. Bull. 145, 111530 https://doi.org/10.1016/j.materresbull.2021.111530.

Singh, T., Awasthi, G., Tiwari, Y., 2021. Recruiting endophytic bacteria of wetland plants to phytoremediate organic pollutants. Int. J. Environ. Sci. Technol. https://doi.org/10.1007/s13762-021-03476-y.

Sousa, J.C.G., Ribeiro, A.R., Barbosa, M.O., Pereira, M.F.R., Silva, A.M.T., 2018. A review on environmental monitoring of water organic pollutants identified by EU

guidelines. J. Hazard Mater. 344, 146–162. https://doi.org/10.1016/j.jhazmat.2017.09.058.

Sun, D., Chi, D., Yang, Z., Xing, Z., Yin, J., Li, Z., Zhu, Q., Zhou, W., 2019. Mesoporous g-C3N4/Zn–Ti LDH laminated van der Waals heterojunction nanosheets as remarkable visible-light-driven photocatalysts. Int. J. Hydrogen Energy 44, 16348–16358. https://doi.org/10.1016/j.ijhydene.2019.04.275.

Tayyab, M., Liu, Y., Min, S., Irfan, R.M., Zhu, Q., Zhou, L., Lei, J., Zhang, J., 2022. Simultaneous hydrogen production with the selective oxidation of benzyl alcohol to benzaldehyde by a noble-metal-free photocatalyst VC/CdS nanowires. Chin. J. Catal. 43, 1165–1175. https://doi.org/10.1016/S1872-2067(21)63997-9.

Wang, T., Li, Y., hao Pan, J., ling Zhang, Y., guang Wu, L., ying Dong, C., juan Li, C., 2019. Alcohol solvothermal reduction for commercial P25 to harvest weak visible light and fabrication of the resulting floating photocatalytic spheres. Sci. Rep. 9, 1–11. https://doi.org/10.1038/s41598-019-50457-w.

Wang, T., Yang, Y., Deng, Q., Zhang, X., Xiong, L., Tang, Z., Li, P., Yin, N., Sun, A., Chen, D., Shen, J., 2021a. In situ construction of 3D marigold like CoAl LDH/Ti3C2 heterosystem collaborating with 2D/2D interface for efficient photodegradation of multiple antibiotics. Appl. Surf. Sci. 569, 151084 https://doi.org/10.1016/j.apsusc.2021.151084.

Wang, Y.L., Zhang, S., Zhao, Y.F., Bedia, J., Rodriguez, J.J., Belver, C., 2021b. UiO-66-based metal organic frameworks for the photodegradation of acetaminophen under simulated solar irradiation. J. Environ. Chem. Eng. 9, 106087 https://doi.org/10.1016/j.jece.2021.106087.

Wang, Y.L., Peñas-Garzón, M., Rodriguez, J.J., Bedia, J., Belver, C., 2022. Enhanced photodegradation of acetaminophen over Sr@TiO2/UiO-66-NH2 heterostructures under solar light irradiation. Chem. Eng. J. 446, 137229 https://doi.org/10.1016/j.cej.2022.137229.

Wei, Q., Xiong, S., Li, W., Jin, C., Chen, Y., Hou, L., Wu, Z., Pan, Z., He, Q., Wang, Y., Tang, D., 2021. Double Z-scheme system of α-SnWO4/UiO-66(NH2)/g-C3N4 ternary heterojunction with enhanced photocatalytic performance for ibuprofen degradation and H2 evolution. J. Alloys Compd. 885, 160984 https://doi.org/10.1016/j.jallcom.2021.160984.

Xiang, Y., Wu, H., Li, L., Ren, M., Qie, H., Lin, A., 2021. A review of distribution and risk of pharmaceuticals and personal care products in the aquatic environment in China. Ecotoxicol. Environ. Saf. 213 https://doi.org/10.1016/j.ecoenv.2021.112044.

Xu, C., Ravi Anusuyadevi, P., Aymonier, C., Luque, R., Marre, S., 2019. Nanostructured materials for photocatalysis. Chem. Soc. Rev. 48, 3868–3902. https://doi.org/10.1039/c9cs00102f.

Yang, L., Zheng, W., Zhang, P., Chen, J., Zhang, W., Tian, W.B., Sun, Z.M., 2019. Freestanding nitrogen-doped d-Ti3C2/reduced graphene oxide hybrid films for high performance supercapacitors. Electrochim. Acta 300, 349–356. https://doi.org/10.1016/j.electacta.2019.01.122.

Zhang, Z., Chen, G., Xu, K., 2013. Photoluminescence of colloids of pristine ZnAl layered double hydroxides. Ind. Eng. Chem. Res. 52, 11045–11049. https://doi.org/10.1021/ie4012326.

Zhao, Y., Wang, C.J., Gao, W., Li, B., Wang, Q., Zheng, L., Wei, M., Evans, D.G., Duan, X., O'Hare, D., 2013. Synthesis and antimicrobial activity of ZnTi layered double hydroxide nanosheets. J. Mater. Chem. B. 1, 5988–5994. https://doi.org/10.1039/c3tb21059f.

Zhao, Y., Li, B., Wang, Q., Gao, W., Wang, C.J., Wei, M., Evans, D.G., Duan, X., O'Hare, D., 2014. NiTi-Layered double hydroxides nanosheets as efficient photocatalysts for oxygen evolution from water using visible light. Chem. Sci. 5, 951–958. https://doi.org/10.1039/c3sc52546e.

Zhao, C., Wei, Z., Zhang, J., He, P., Huang, X., Duan, X., Jia, D., Zhou, Y., 2022. Ultrafine SnO_2 nanoparticles on delaminated MXene nanosheets as an anode for lithium-ion batteries. J. Alloys Compd. 907, 164428 https://doi.org/10.1016/j.jallcom.2022.164428.

Zheng, G., Wu, C., Wang, J., Mo, S., Zou, Z., Zou, B., Long, F., 2019. Space-confined effect one-pot synthesis of γ-AlO(OH)/MgAl-LDH heterostructures with excellent adsorption performance. Nanoscale Res. Lett. 14, 281. https://doi.org/10.1186/s11671-019-3112-x.

Zhou, H., Wu, F., Fang, L., Hu, J., Luo, H., Guan, T., Hu, B.S., Zhou, M., 2020. Layered NiFe-LDH/MXene nanocomposite electrode for high-performance supercapacitor. Int. J. Hydrogen Energy 45, 13080–13089. https://doi.org/10.1016/j.ijhydene.2020.03.001.

Zhu, Y., Laipan, M., Zhu, R., Xu, T., Liu, J., Zhu, J., Xi, Y., Zhu, G., He, H., 2017. Enhanced photocatalytic activity of Zn/Ti-LDH via hybridizing with C60. Mol. Catal. 427, 54–61. https://doi.org/10.1016/j.molcata.2016.11.031.

Zhu, Y., Zhu, R., Zhu, G., Wang, M., Chen, Y., Zhu, J., Xi, Y., He, H., 2018. Plasmonic Ag coated Zn/Ti-LDH with excellent photocatalytic activity. Appl. Surf. Sci. 433, 458–467. https://doi.org/10.1016/j.apsusc.2017.09.236.

Zou, J., Wang, Z., Guo, W., Guo, B., Yu, Y., Wu, L., 2020. Photocatalytic selective oxidation of benzyl alcohol over ZnTi-LDH: the effect of surface OH groups. Appl. Catal. B Environ. 260, 118185 https://doi.org/10.1016/j.apcatb.2019.118185.

Żur, U.G.J., Piński, A., Marchlewicz, A., Hupert-Kocurek, K., Wojcieszyńska, D., 2011. Organic micropollutants paracetamol and ibuprofen—toxicity, biodegradation, and genetic background of their utilization by bacteria. Environ. Sci. Pollut. Res. 2284, 1–4. https://link.springer.com/journal/11356.

Supporting Materials

Novel composite of Zn/Ti-layered double hydroxide coupled with MXene for the efficient photocatalytic degradation of pharmaceuticals

Anna Grzegórska[1], Izabela Wysocka[1], Paweł Głuchowski[2], Jacek Ryl[3], Jakub Karczewski[3], Anna Zielińska-Jurek[1]**

[1] Department of Process Engineering and Chemical Technology, Faculty of Chemistry, Gdańsk University of Technology, G. Narutowicza 11/12, 80-233 Gdańsk, Poland

[2] Institute of Low Temperature and Structural Research, Polish Academy of Sciences, Okólna 2, 50-422 Wrocław, Poland

[3] Institute of Nanotechnology and Materials Engineering, Faculty of Applied Physics and Mathematics, Gdańsk University of Technology, G. Narutowicza 11/12, 80-233 Gdańsk, Poland

* Corresponding authors: annjurek@pg.edu.pl, anna.grzegorska@pg.edu.pl

2. Experimental

2.3 Photocatalytic activity

Table 1S. Properties of acetaminophen and ibuprofen

Property	Acetaminophen	Ibuprofen
Chemical structure	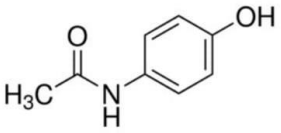	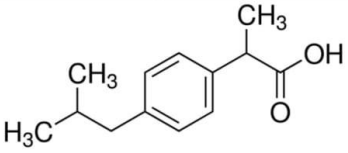
Molecular weight	151.16 g/mol	206.28 g/mol
pK_a	9.38	4.91

3. Results and discussion

Table 2S. Characteristics of prepared Zn/Ti LDH and Zn/Ti LDH-Ti_3C_2 composites.

Sample	Crystallite size (nm)	Bandgap energy (eV)	BET surface area (m^2/g)	Pore volume (cm^3/g)
Ti_3C_2	7	-	10.2	0.005
Zn/Ti LDH	24	3.2	129.4	0.064
Zn/Ti LDH-0.5% Ti_3C_2	34	3.22	119.6	0.059
Zn/Ti LDH-2.5% Ti_3C_2	32	3.25	131.2	0.064
Zn/Ti LDH-5% Ti_3C_2	30	3.25	134.5	0.066

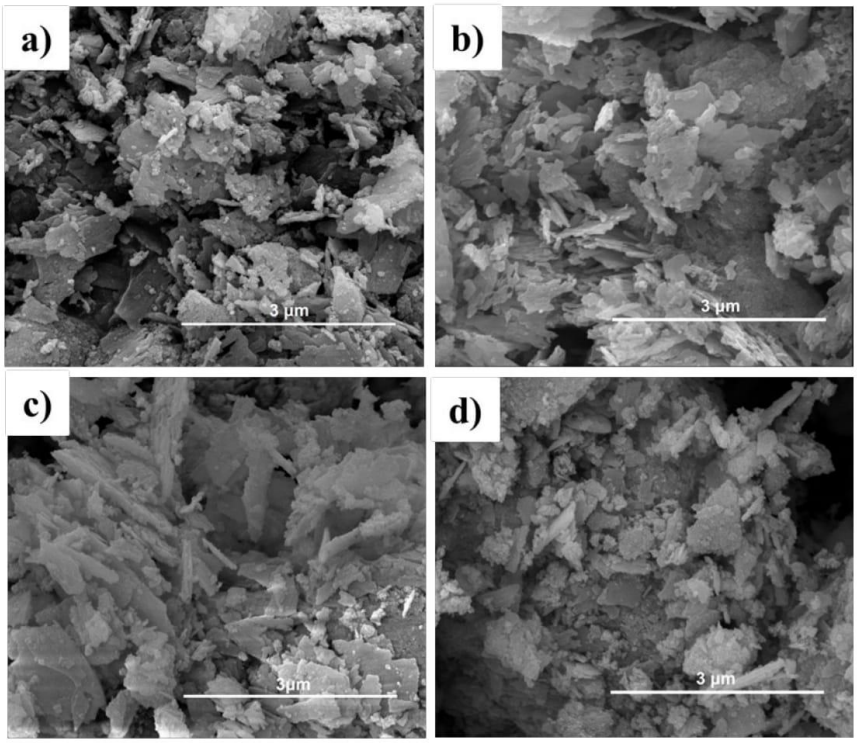

Figure 1S. Comparison of SEM images of pure Zn/Ti LDH (a), Zn/Ti LDH-0.5% (b), Zn/Ti LDH-2.5% (c), and Zn/Ti LDH-5% (d)

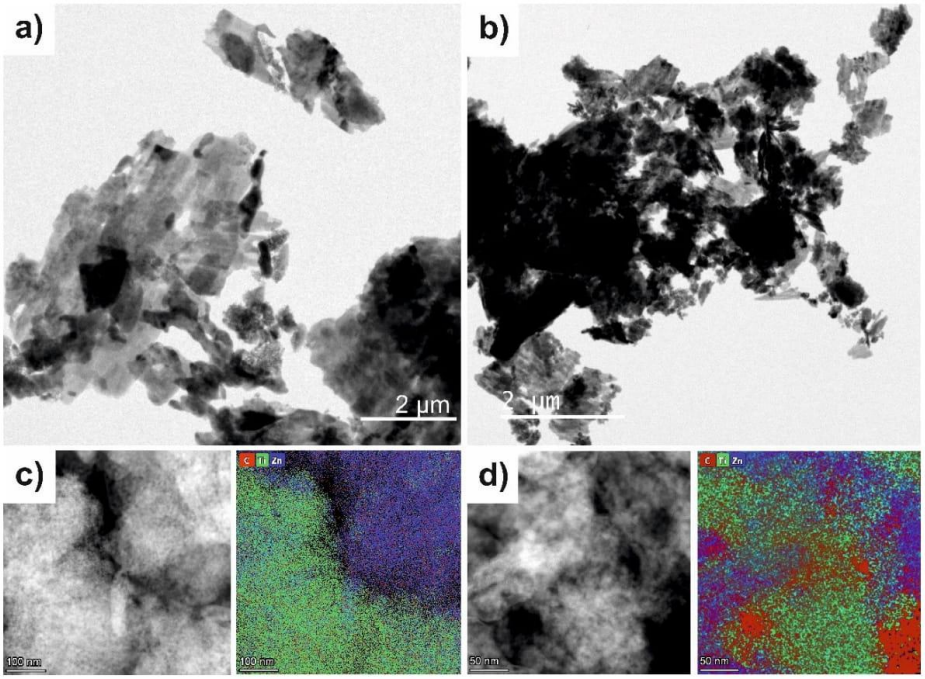

Figure 2S. TEM images before (a) and after fourth photocatalytic cycles (b), elemental mapping (c-d) for Zn/Ti LDH-2.5%

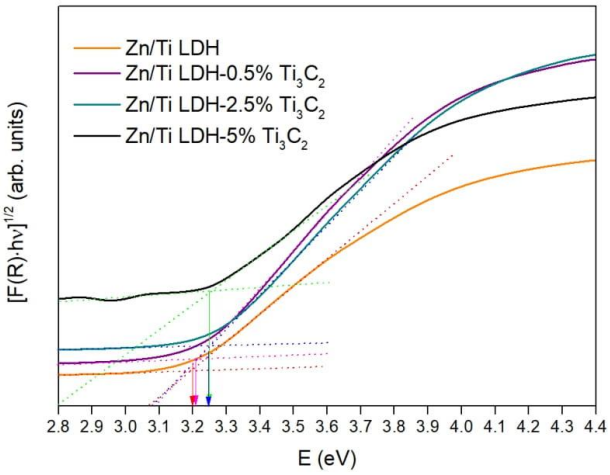

Figure 1S. Kubelka-Munk plots for the bandgap energy calculation of Zn/Ti LDH and Zn/Ti LDH-Ti_3C_2

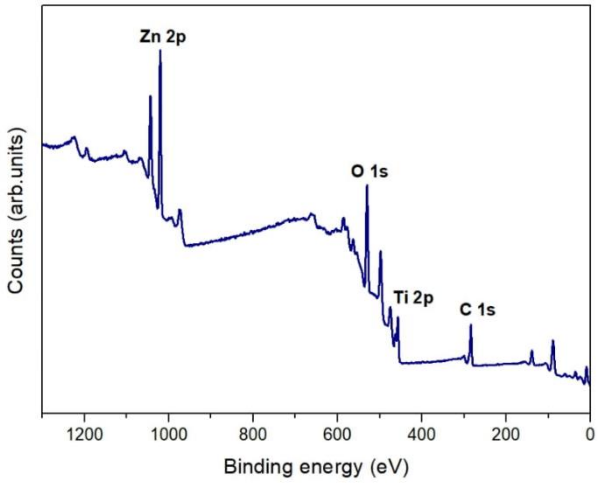

Figure 4S. The XPS survey spectra of Zn/Ti LDH- 2.5% Ti_3C_2

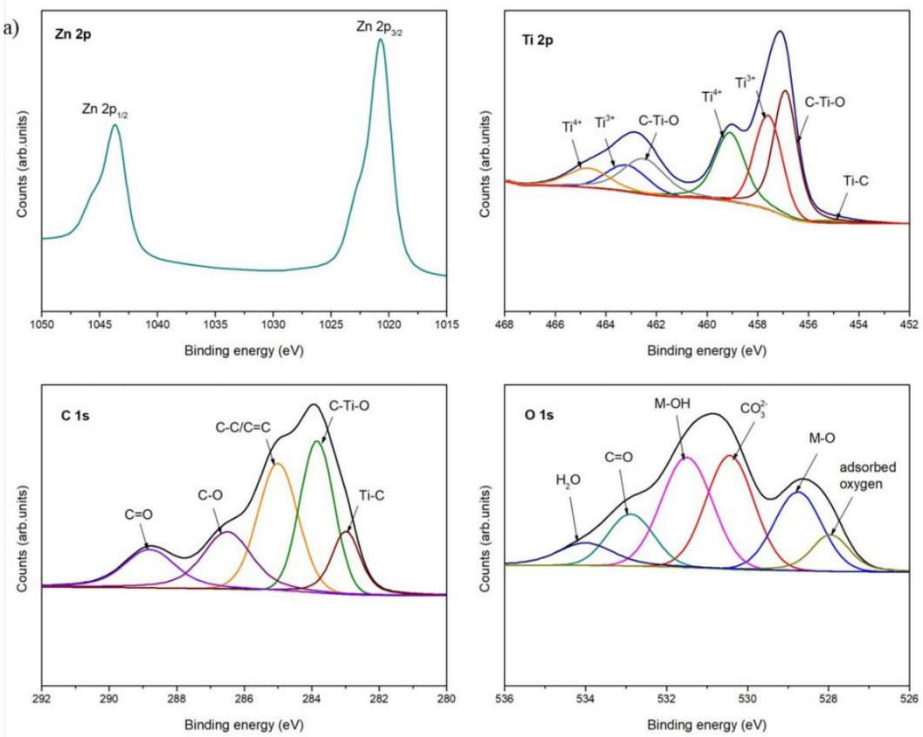

4

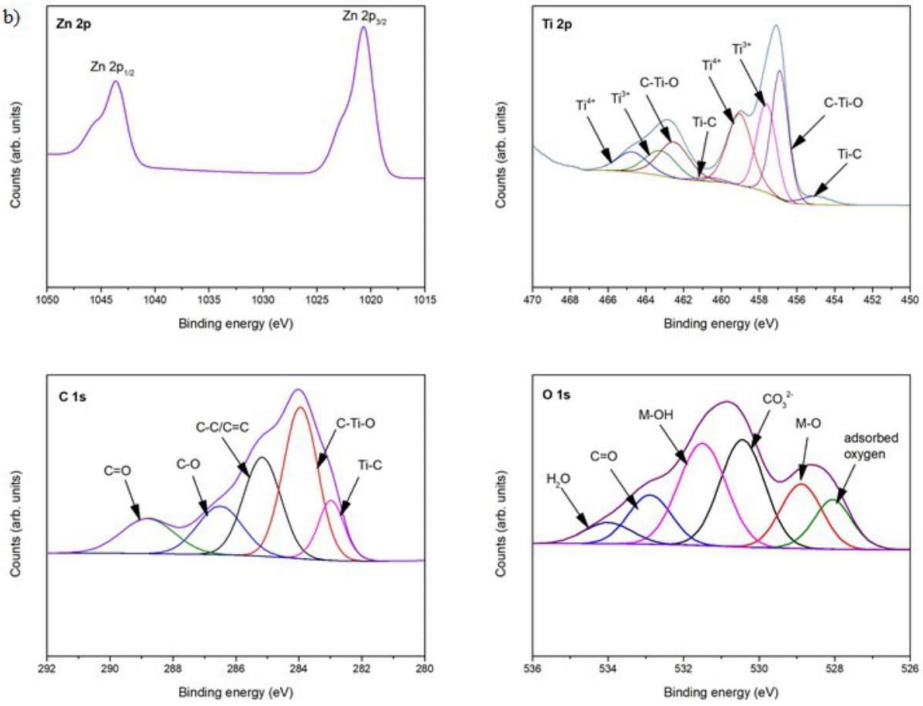

Figure 5S. XPS spectra Zn 2p, Ti 2p, O 1s, and C 1s regions for Zn/Ti-LDH-2.5% Ti_3C_2 before (a) and after 4 photocatalytic cycles (b)

Table 3S. The rate constant of acetaminophen degradation and TOC concentration after the process (initial ACT solution TOC = 11.5 mg/dm^3)

Sample	The rate constant of acetaminophen degradation ($min^{-1}\cdot10^{-2}$)	TOC concentration (mg/dm^3)
photolysis	0.2	11.4
Zn/Ti-LDH	8.1	7.5
Zn/Ti LDH-0.5% Ti_3C_2	11.5	6.4
Zn/Ti LDH-2.5% Ti_3C_2	12.8	6.1
Zn/Ti LDH-5% Ti_3C_2	8.4	7.3

Table 4S. The rate constant of ibuprofen degradation and TOC concentration after the process (initial IBP solution TOC = 12.6 mg/dm^3)

Sample	The rate constant of ibuprofen degradation ($min^{-1} \cdot 10^{-2}$)	TOC concentration (mg/dm^3)
photolysis	2.8	11.2
Zn/Ti LDH	5.8	7.7
Zn/Ti LDH-0.5% Ti_3C_2	7.0	6.6
Zn/Ti LDH-2.5% Ti_3C_2	7.1	6.0
Zn/Ti LDH-5% Ti_3C_2	6.2	6.7

Table 5S. The rate constant of acetaminophen degradation and TOC concentration after the process (initial ACT solution TOC = 11.5 mg/dm^3) for the dose of photocatalyst equal to 1g/dm^3

Sample	The rate constant of acetaminophen degradation ($min^{-1} \cdot 10^{-2}$)	TOC concentration (mg/dm^3)
Zn/Ti LDH	7.0	9.2
Zn/Ti LDH-0.5% Ti_3C_2	9.5	8.1
Zn/Ti LDH-2.5% Ti_3C_2	10.6	7.4
Zn/Ti LDH-5% Ti_3C_2	7.8	8.5

Table 6S. The TOC concentration for ibuprofen and acetaminophen degradation in model seawater (initial ACT solution TOC = 11.6 mg/dm^3, initial IBP solution TOC = 12.9 mg/dm^3)

Sample	TOC concentration (mg/dm^3)
ACT for Zn/Ti LDH-2.5%Ti_3C_2 in model seawater	7.5
IBP for Zn/Ti LDH-2.5%Ti_3C_2 in model seawater	6.8

Rozdział III. Enhanced photocatalytic activity of accordion-like layered Ti_3C_2 (MXene) coupled with Fe-modified decahedral anatase particles exposing {1 0 1} and {0 0 1} facet

Chemical Engineering Journal 426 (2021) 130801

Contents lists available at ScienceDirect

Chemical Engineering Journal

journal homepage: www.elsevier.com/locate/cej

Enhanced photocatalytic activity of accordion-like layered Ti_3C_2 (MXene) coupled with Fe-modified decahedral anatase particles exposing {101} and {001} facets

Anna Grzegórska [a,*], Paweł Głuchowski [b], Jakub Karczewski [c], Jacek Ryl [c], Izabela Wysocka [a], Katarzyna Siuzdak [d], Grzegorz Trykowski [e], Katarzyna Grochowska [d], Anna Zielińska-Jurek [a,*]

[a] Department of Process Engineering and Chemical Technology, Faculty of Chemistry, Gdańsk University of Technology, G. Narutowicza 11/12, 80-233 Gdańsk, Poland
[b] Institute of Low Temperature and Structural Research, Polish Academy of Sciences, Okólna 2, 50-422 Wrocław, Poland
[c] Institute of Nanotechnology and Materials Engineering, Faculty of Applied Physics and Mathematics, Gdańsk University of Technology, G. Narutowicza 11/12, 80-233 Gdańsk, Poland
[d] Centre for Plasma and Laser Engineering, The Szewalski Institute of Fluid-Flow Machinery, Polish Academy of Science, Fiszera 14, 80-231 Gdańsk, Poland
[e] Faculty of Chemistry, Nicolaus Copernicus University, Gagarina 7, 87-100 Toruń, Poland

ARTICLE INFO

Keywords:
Carbamazepine
MXene
Decahedral anatase particles
Titanium carbide
{101} facet
{001} facet

ABSTRACT

New composites consisting of decahedral anatase particles exposing {001} and {101} facets coupled with accordion-like layered Ti_3C_2 with boosted photocatalytic activity towards phenol and carbamazepine degradation were investigated. The photocatalysts were characterized with X-ray diffraction (XRD), diffuse reflectance spectroscopy (DR/UV–Vis), Brunauer-Emmett-Teller (BET) specific surface area, Raman spectroscopy, scanning electron microscopy (SEM), electron paramagnetic resonance (EPR) spectroscopy, emission spectroscopy, luminescence decay analysis, electrochemical impedance spectroscopy (EIS), transmission electron microscopy (TEM), X-ray photoelectron spectroscopy (XPS), thermogravimetric analysis (TGA), and electrophoretic mobility measurements. The effect of hydrothermal reaction parameters on physicochemical, structural, and photocatalytic properties was studied. In all photodegradation processes, *ortho*-hydroxyphenol and *para*-hydroxyphenol were detected as the first intermediates of phenol decomposition. For the TiO_2/Ti_3C_2(140,12) sample containing V_{Ti}, a higher concentration of *para*-hydroxyphenol than *ortho*-hydroxyphenol was observed, whereas for sample TiO_2/Ti_3C_2(220,24) higher concentration of *ortho*-hydroxyphenol was noticed. The formation of surface heterojunction between {101} and {001} facets of decahedral anatase particles grown on Ti_3C_2 surface led to improved photoelectron transfer and enhanced photocatalytic activity towards degradation of carbamazepine - non-biodegradable and susceptible to bioaccumulation in living organisms commonly used pharmaceutical agent. Moreover, modification of TiO_2/Ti_3C_2 surface with iron by magnetron sputtering deposition markedly improved photocatalytic activity in carbamazepine decomposition, with nearly 100% degradation in 60 min of irradiation under simulated solar light.

1. Introduction

Pollution of the aqueous environment with organic compounds from year to year becomes a more significant problem globally. According to the European Environmental Agency report, only about 38% of surface waters are in good chemical condition [1]. There are various organic compounds with potentially adverse health effects on living organisms emitted to the environment, including nonsteroidal anti-inflammatory drugs, antibiotics, hormones, plasticizers, antimicrobials, or surfactants [2].

Among the group of emerging contaminants, carbamazepine (CBZ) is an efficient anticonvulsant and neuropathic painkiller [3] frequently detected in wastewaters in concentrations range from 1 to 3600 ng/dm^3, while in pharmaceutical effluents reaches even up to 443 mg/dm^3 [4]. The CBZ is a low biodegradable and high persistent compound. Thus only below 10% of its content is effectively removed at conventional wastewater treatment plants [5]. Moreover, some recent studies confirmed CBZ toxicity for sludge microbial activity and aquatic

* Corresponding authors.
E-mail addresses: anna.grzegorska@pg.edu.pl (A. Grzegórska), annjurek@pg.edu.pl (A. Zielińska-Jurek).

https://doi.org/10.1016/j.cej.2021.130801
Received 10 January 2021; Received in revised form 13 May 2021; Accepted 7 June 2021
Available online 11 June 2021

organisms like bacteria, algae, invertebrates, and fish [6]. Various methods have been proposed for carbamazepine degradation, including ozonation, extraction, membrane-based separation, or biological processes [7–11]. Furthermore, special attention has been paid to photocatalytic degradation of emerging contaminants and persistent organic pollutants as an efficient and green technology [12].

Heterogeneous photocatalysis is a sustainable and promising strategy intensively investigated for water splitting [13], bacterial disinfection [14], carbon dioxide reduction to energy fuels [15], and degradation of persistent organic pollutants for environment purification [16]. However, it is still challenging to design a durable photocatalyst highly active in solar light (UV–Vis).

The surface chemistry of a photocatalyst is one of the most crucial parameters influencing semiconductor material's surface properties and photocatalytic activity. The most commonly used method to inhibit electron-hole pairs recombination and enhance Vis light activity is a modification of semiconductors, primarily TiO_2 nanoparticles with noble metal nanoparticles [17]. Noble metal nanoparticles (NMNPs) may improve the photocatalytic activity in UV–Vis light due to surface plasmon resonance properties and prolong photo-induced charge carriers due to the formation of Schottky's barrier at the semiconductor–metal interface. Moreover, NMNPs facilitate electron transport by the equilibration of the Fermi levels [17]. Nonetheless, this method is relatively expensive, and the photocatalytic activity of semiconductor material strongly depends on noble metal nanoparticles morphology (size and shape), which is also determined by the reaction environment [18]. Thus less cost and more straightforward solutions are still in demand.

Recently, two-dimensional (2D) materials have attracted great interest in various fields, including electrocatalysis, energy storage, sensors, and photocatalysis [19–23]. Highly anisotropic 2D semiconductors characterized with atom-level thickness, tunable composition, and well-defined structure may offer many desirable properties such as enhanced electron-hole separation, high mobility of charge carriers, and also reduced charge carriers recombination rate [24–25]. The 2D materials possess an improved surface to volume ratio and, as a consequence, significantly developed surface area. Furthermore, 2D semiconductor materials with exposed {1 0 1} and {0 0 1} facets are expected to play a crucial role in enhancing the photocatalytic degradation of emerging contaminants. Another approach is creating interfacial heterojunction to induce an internal electric field, enhancing charge carriers separation [26–29].

MXene compounds with graphene-like morphology have become promising materials instead of platinum or palladium as a noble-metal-free co-catalyst. The MXene group consists of transition metal carbides, nitrides, or carbonitrides [30]. Wei et al. [31] reported the potential application of Ti_3AlC_2 as support for uniform nucleation of lithium particles for Li-based batteries. MXenes are materials with advantageous lithiophilicity, flexibility, mechanical robustness, and good electronic conductivity [31–32]. Due to its properties close to metallic, MXenes may create a Schottky barrier at the MXenes-semiconductor interface and enact as a reservoir for photo-generated electrons [33]. Moreover, they may improve photocatalyst stability, carrier density, and light absorption over a broader spectrum [34–35]. Hybrid MXene photocatalysts have been already successfully combined with Bi_2WO_6 [36], CdS [34], ZnS [37], Ag_3PO_4 [38], g-C_3N_4 [39], Cu_2O [40], BiOBr [41], Fe_2O_3 [42], and TiO_2 [43]. Furthermore, some MXene-derived materials such as MXene/AuNPs, MXene/PdNPs may be prepared by a cost-effective self-assembly technique. The self-assembled composites are characterized by tunable nanoparticles size with uniformly dispersed particles on the MXene substrate, well-controlled by optimized reaction time [44–48]. The application of MXene as a co-catalyst reported in the literature focused on the photocatalytic removal of dyes from the aqueous environment [49–50], hydrogen generation, and CO_2 reduction [51–53].

In this regard, in the present study, MXene compound – $Ti_3C_2T_x$ was used for in-situ preparation of composite photocatalyst consisting of decahedral anatase particles (DAPs) and titanium carbide (Ti_3C_2). DAPs with eight equivalent {1 0 1} facets and two {0 0 1} facets are expected to reveal improved photocatalytic activity. The exposed facets determine photocatalytic activity and degradation pathway of emerging organic pollutants. Therefore, the influence of surface structure properties of TiO_2/Ti_3C_2 layered composite on photocatalytic activity was studied in detail. Moreover, for the first time, in this study, new Fe-modified composites prepared through magnetron sputtering deposition on decahedral anatase particles exposing {0 0 1}, {1 0 1} facets coupled with Ti_3C_2 were obtained and applied for photocatalytic degradation of phenol - a model organic pollutant and carbamazepine anticonvulsant and neuropathic painkiller, which belongs to the group of emerging organic contaminants. The effect of synthesis temperature and time on TiO_2/Ti_3C_2 and Fe-modified TiO_2/Ti_3C_2 composites structural properties and photocatalytic activity was investigated.

2. Experimental

2.1. Materials

The MXenes matrix Ti_2AlC-Ti_3AlC_2 (50 μm) was purchased from NANOGRAFI Co. Ltd. Hydrofluoric acid (48%), and tetrafluoroboric acid (48 wt% in H_2O used for synthesis were purchased from Sigma Aldrich. Phenol (99%) and carbamazepine were purchased from Sigma Aldrich. Scavengers: benzoquinone (reagent grade, $\geq$ 98%) and *tert*-butanol (anhydrous, $\geq$ 99.5%) were purchased from Sigma Aldrich, POCH Gliwice provided $AgNO_3$ (pure p.a.) and EDTA (pure p.a.). Alfa Aestar provided nickel (II) oxide (99.998% metals basis) to determine sample crystallinity. Deionized water (DI) was used in all experiments. All reagents were used as received without further purification.

2.2. Preparation of $Ti_3C_2T_x$

$Ti_3C_2T_x$ (T_x – termination groups -O, –OH, and -F) matrix was prepared by selective etching of the Al layer from Ti_3AlC_2. In this regard, 1 g of Ti_2AlC-Ti_3AlC_2 powder was dispersed in 10 cm^3 of 48% HF solution and continuously stirred at room temperature for 24 h. In the next step, the obtained suspension was centrifuged and washed with DI water until the pH of 7 (neutral pH). The resulting powder was dried under air condition at 80 °C to dry mass.

2.3. Preparation of TiO_2 /Ti_3C_2 layered composite

In a typical experiment, TiO_2/Ti_3C_2 composites were prepared by dispersing 0.4 g of Ti_3C_2 in 59.2 cm^3 DI water and sonication for 10 min to agglomerates breakdown. Then, 0.8 cm^3 of HBF_4 was added dropwise under magnetic stirring. The dispersion was stirred for 30 min and transferred to a 200 cm^3 Teflon-lined stainless-steel autoclave reactor. The reaction temperature was selected from 140 °C to 220 °C. The reaction time equaled 6, 12, or 24 h. The final photocatalyst was centrifuged and washed with DI water until the pH of 7 (neutral pH). Then the sample was dried under air condition at 80 °C to dry mass.

2.4. Preparation of Fe- TiO_2/Ti_3C_2 composite

The Fe-TiO_2/Ti_3C_2 composites were prepared according to the procedure described in paragraph 2.2. The TiO_2/Ti_3C_2 sample was synthesized at 140 °C for 12 h and 220 °C for 24 h. In the next step, thin layers of TiO_2/Ti_3C_2 were applied on the glass slide and dried at 80 °C for 1 h. Iron deposition on the TiO_2/Ti_3C_2 surface was conducted using a magnetron sputtering system (Q150S, Quorum Technologies, Lewes, UK) with mounted highly pure Fe target (99.5%, EM-Tec). The Fe thickness was controlled by quartz microbalance and implemented the program and set to 20 nm.

2.5. Characterization of TiO_2/Ti_3C_2 and Fe- TiO_2/Ti_3C_2 photocatalysts

The crystallinity and average crystallite size were investigated by X-ray powder diffraction. The analysis was performed using Rigaku Intelligent X-ray diffraction system SmartLab (Rigaku Corporation, Tokyo, Japan), equipped with a sealed tube X-ray generator operating with Cu Kα radiation 40 kV and 30 mA. Scans were recorded in the 2θ range from 5° to 80°, with a speed 2°min^{-1} and a step of 0.01°. The crystalline and amorphous phase content was analyzed using an internal standard - NiO.

Nitrogen adsorption–desorption isotherms were measured at 77 K (boiling point of liquid nitrogen) with the Micromeritics Gemini V apparatus (model 2365) (Norcross, GA, USA). The surface area and pore volume were determined by the multipoint BET method. Before each measurement, the samples were degassed at 200 °C under a constant flow of nitrogen. The nitrogen isotherm was measured in a partial pressure range from 0.05 to 0.3.

Diffuse reflectance (DR/UV–Vis) spectra were recorded in the wavelength range from 200 nm to 800 nm using a ThermoScientific Evolution 220 spectrophotometer (Waltham, MA, USA). As a reference, barium sulfate was used. The photocatalysts bandgap energy was calculated from the corresponding Kubelka-Munk function, $(R)^{0.5}E_{ph}^{0.5}$ against E_{ph}, where E_{ph} is photon energy.

Electron paramagnetic resonance (EPR) spectroscopy was used to investigate the structural defects of TiO_2/Ti_3C_2 composites. The EPR analysis was performed at room temperature in a RADIOPAN SE/X-2547 spectrometer. EPR measurements were conducted at X-band (≈ 8.9 GHz), employing a reflection resonator with a modulation frequency of 100 kHz.

The composites' surface morphology was examined by scanning electron microscopy (SEM) using SEM Microscope FEI Quanta FEG 250. Moreover, the images and selected area electron diffraction (SAED) patterns were obtained for the most photocatalytic active samples using the transmission electron microscope (TEM) Tecnai 20F X-Twin, an electron source, cathode with field emission gun (FEG), EHT = 200 keV, camera for TEM Orius, Gatan Inc.

The X-ray photoelectron spectroscopy (XPS) analysis was carried out to determine the elemental composition, types of functional groups, and chemical bonds on photocatalysts' surface. The samples were measured under high vacuum conditions in the multi-chamber UHV system (Prevac, Poland). Before the analysis, the photocatalysts were immobilized on the molybdenum supports. For X-ray excitation of photoelectrons, a monochromatic Al Kα X-ray radiation (E = 1486.7 eV) was applied. All of the binding energies were calibrated by the C 1 s peak at 285.0 eV.

The Mott Schottky analysis was performed to determine the flat band potential of the TiO_2/Ti_3C_2 composites. The prepared material on fluorine-doped tin oxide glass (FTO) was used as a working electrode tested in a three-electrode system, where Ag/AgCl/0.1 M KCl and Pt mesh were used as reference and counter electrode, respectively. The deaerated 0.5 M Na_2SO_4 solution was used as a supporting electrolyte. The electrochemical spectroscopy impedance (EIS) data were recorded from the anodic towards a cathodic direction. EIS data were recorded for the applied frequency of 1000 Hz in the potential range from 0.1 to −1.2 V vs. Ag/AgCl/0.1 M KCl using a 10 mV amplitude of the AC signal. The potentiostat–galvanostat Biologic SP-150 controlled those conditions. The Mott-Schottky plot describing the relation Csc^{-2} vs. E was obtained using the following calculation of the space charge capacitance $C_{SC} = -1/(2\pi f Z_{im})$, where the imaginary part of the impedance Z_{im} was taken into account, f stands for the frequency of AC signal. The flat band potentials' positions were determined based on the tangent's intersection to the Mott-Schottky plot with the potential (E) axis. The value of donor density was calculated according to the theory of space charge capacitance of the semiconductor given by the relation $N_d = 2/(S \times \varepsilon\varepsilon_0 e)$, where ε is the dielectric constant of TiO_2, ε_0 is the vacuum permittivity, e stays for the electron charge, and S stays for the Mott-Schottky plot. In calculations following values were used: $\varepsilon_0 = 8.85 \times 10^{-12}$F/m, $\varepsilon = 38$ for anatase-TiO_2, and $e = 1.602 \times 10^{-19}$C, while S was determined from the run of Mott-Schottky plot.

The photocurrent measurements were carried out in a three-electrode cell, with photocatalyst sample on the FTO glass as the working electrode, Ag|AgCl as the reference electrode, and Pt wire as the counter electrode, in 0.5 M Na_2SO_4 at 20 °C. The electrolyte was purged with argon before the measurements to remove the dissolved oxygen. The photoelectrochemical response was studied in a chronoamperometry measurement at polarization potential of + 0.5 V vs. E_{oc} after the 2000 s of conditioning. Gamry Reference 600+ (Gamry Instruments, USA) potentiostat/galvanostat was used in the experiment.

The Raman spectra were recorded by a confocal micro-Raman spectrometer (InVia Renishaw) with sample excitation using an argon-ion laser emitting at 514 nm and operating at 5% of its total power (50 mW).

Emission spectra and luminescence decay curves were acquired using a grating spectrograph (Princeton Instr. Model Acton 2500i) coupled to a CCD streak camera (Hamamatsu Model C5680) which operates in the 200–1100 nm spectral region with a temporal resolution of 20 ps. As an excitation source, a femtosecond laser (Coherent Model "Libra") coupled to an optical parametric amplifier (Light Conversion Model "OPerA") was used.

The thermogravimetric analysis (TGA) was performed on an SDT 2960 TA analyzer in air atmosphere; heating rate 10° min^{-1}, under 10 cm^3·min^{-1} air flow rate, heating range up to 800 °C with powdered samples in a corundum crucible; sample mass 7–10 mg.

Investigation of photocatalyst functional groups before and after irradiation was conducted using Fourier-transform infrared spectroscopy (FTIR). The measurements were carried out using the Nicolet iS10 (Thermo Fisher Scientific Waltham, MA, USA) spectrometer at room temperature. The measurements were conducted in the wavenumber range from 4000 to 400 cm^{-1}.

2.6. Photocatalytic decomposition of phenol – Model organic pollutant

The photocatalytic activity was evaluated in reaction of phenol decomposition under UV–Vis light. The initial concentration of phenol was equal to 20 mg·dm^{-3} (pH = 6.8). The photodegradation reactions were performed in a quartz reactor equipped with an air supply mode. The photocatalyst at the content of 2 g·dm^{-3} and 25 cm^3 of the aqueous solution of the model pollutant (phenol) was introduced into the reactor and kept in the dark for 30 min under continuous stirring to achieve adsorption–desorption equilibrium before irradiation. A 300 W Xe lamp (LOT Oriel, Darmstadt, Germany) was used as an irradiation source. The light flux in the UV range (310 nm < λ < 380 nm) equaled 30 mW·cm^{-2}. The sample aliquots were collected at 0, 20, 40, and 60 min of irradiation. The photocatalyst particles were separated from the solution using a 0.2 μm syringe filter. The progress of phenol photodegradation and intermediates concentration were analyzed using reverse-phase high-performance liquid chromatograph Shimadzu LC-6A (Kyoto, Japan) with photodiode array detector Shimadzu SPD-M20A. The measurements were performed at 45 °C and under isocratic flow conditions of 0.3 cm^3·min^{-1}. A volume composition of the mobile phase of 70% acetonitrile, 29.5% water, and 0.5% orthophosphoric acid was applied to determine phenol concentration.

2.7. Photocatalytic decomposition of carbamazepine

In the next step, the TiO_2/Ti_3C_2 and Fe-TiO_2/Ti_3C_2 composites' photocatalytic activity was evaluated in reaction of carbamazepine degradation under UV and UV–Vis light. The initial concentration of carbamazepine was equalled to 14 mg/dm^3 (pH = 6.5). The photocatalytic reactions were performed in the 25 cm^3 quartz reactor equipped with an air supply mode. The photocatalyst at the content of 2 g·dm^{-3} was kept in the dark for 30 min under continuous stirring to achieve adsorption–desorption equilibrium before irradiation. A 300 W

Xe lamp (LOT Oriel, Darmstadt, Germany) was used as an irradiation source. The optical path included a water filter and glass filter UG11 to cut off IR and Vis. The glass filter UG11 transmitted light in the range of 250 ÷ 400 nm (max. 330 nm). The temperature during the experiments was maintained at 20 °C. The sample aliquots were collected at 0, 20, 40, and 60 min of irradiation. Furthermore, the photocatalyst particles were separated from the solution using a 0.2 μm syringe filter. The progress of carbamazepine photodegradation was analyzed using reverse-phase high-performance liquid chromatograph Shimadzu LC-6A (Kyoto, Japan) with photodiode array detector Shimadzu SPD-M20A. The measurements were performed at 45 °C and under isocratic flow conditions of 1.5 $cm^3 \cdot min^{-1}$. A volume composition of the mobile phase of 39.5% acetonitrile, 60% water, and 0.5% orthophosphoric acid was applied to determine carbamazepine concentration.

2.8. Verification of the degradation mechanism using scavengers

The charge carriers and reactive oxygen species participating in the photocatalytic reaction were investigated to provide insight into the mechanism of organic contaminants degradation in the presence of TiO_2/Ti_3C_2 layered composites. The photocatalytic activity was evaluated according to the procedure described in paragraphs 2.4 and 2.5 with the addition of a proper amount of scavenger solution to reach concentrations equal to 20 $mg \cdot dm^{-3}$ and 14 $mg \cdot dm^{-3}$ for phenol and carbamazepine, respectively. EDTA was selected as holes scavenger (h^+), $AgNO_3$ for electrons (e), *tert*-butyl alcohol for free hydroxyl radicals (·OH), and benzoquinone for superoxide radical anions ($\cdot O_2^-$).

3. Results and discussion

3.1. Characterization of TiO_2/Ti_3C_2 and Fe-modified TiO_2/Ti_3C_2 photocatalysts

The surface properties of semiconductor material, primarily the surface area, crystallinity, particle size, and exposure of single crystal facets, significantly influenced distinctive physical and chemical properties, including photocatalytic properties in oxidation–reduction reactions.

Fig. 1 shows the TiO_2/Ti_3C_2 composite crystal structure's schematic representation obtained by a two-stage synthesis route. The accordion-like MXene structure was synthesized by selective Al etching from the Ti_3AlC_2-Ti_2AlC matrix. The accordion-like structure of MXene may increase chemical activity and provide unique optical and physicochemical properties arising from the confined thickness and development of the surface area. The surface of MXene was partially oxidized into decahedral anatase particles with exposed {1 0 1} and {0 0 1} facets by the solvothermal reaction in the environment of HBF_4, leading to the formation of the composite structure.

The surface structure determines the efficiency of various groups of pollutants degradation. It also affects the path of their decomposition as a result of differences in (1) the surface density of the excited charge carriers, (2) adsorption capacity of the pollutant, (3) photo-reduction or photo-oxidation properties involving direct pollutants degradation or generation of other reactive oxygen species. Based on our previous study [54], it was assumed that exposed facets are crucial concerning the mineralization efficiency and the pathway of phenol degradation. The TiO_2 octahedral particles exposing {1 0 1} facets favored electron localization on the surface and exhibited the highest phenol mineralization efficiency [54].

The morphological properties were analyzed based on microscopy analysis. The scanning electron microscopy images of TiO_2/Ti_3C_2 composites are shown in Fig. 2 and Fig. 1S in the Supporting Materials. The solvothermal reaction in the presence of HBF_4 aqueous solution led to the oxidation of titanium carbide layers to titanium(IV) oxide. The SEM analysis revealed significant differences between the size of decahedral anatase particles obtained with variable solvothermal reaction time and temperature. An increase in reaction time and temperature caused the formation of smaller, tightly compacted, and differentiated sizes of TiO_2 particles. Furthermore, the reaction performed at the highest temperature of 220°C led to complete oxidation of Ti_3C_2 into the TiO_2 structure. Therefore, for sample TiO_2/Ti_3C_2(220,24) only TiO_2 in the decahedral shape with co-exposed {1 0 1} and {0 0 1} facets was noticed on microscopy images (Fig. 1S and 2S in the Supporting Materials). Exposition of the crystalline planes and surface heterojunction between both facets facilitates inter-facet charge carriers' transport and separation, leading to enhanced photocatalytic activity [55]. Based on scanning microscopy analyzes, co-exposed facets' content was expressed as an average ratio of eight lateral {1 0 1} facets and two vertical {0 0 1} facets, measured for 50 decahedral TiO_2 particles. This value was calculated for two of the most active samples TiO_2/Ti_3C_2(140,12) and TiO_2/Ti_3C_2 (220, 24). The ratio of {1 0 1}/{0 0 1} facets equaled to 45:55. However, due to the agglomeration of anatase decahedral particles, potential exposure of {0 0 1} facets is reduced. According to Yu et al. [56], TiO_2 decahedral particles with the {1 0 1} to {0 0 1} facets ratio equaled to 50:50 possess significantly improved photocatalytic activity. This optimal ratio of facets leads to photogenerated electrons' transfer to {1 0 1} and holes to {0 0 1} facets, hindering the e-h recombination process.

For the most photocatalytic active samples modified with iron species, the TEM analyzes were performed. The SAED pattern of TiO_2/Ti_3C_2(220,24) confirmed the formation of TiO_2. The layer spacing equal to 0.35 nm (Fig. 3-a) referred to (1 0 1) planes found on the exposed {1 0 1} facet of TiO_2. For TiO_2/Ti_3C_2(140,12) composite, two lattice spacings of 0.25 nm and 0.35 nm were also distinguished, indicating the presence of {0 0 6} of Ti_3C_2 and {1 0 1} facet of anatase decahedral particle (Fig. 3-c). The TEM analysis confirmed the presence of Fe at the surface of decahedral anatase particles. Based on the STEM-EDS analysis, the content of iron for Fe-TiO_2/Ti_3C_2(220,24) was about 3 at.%, as shown in Fig. 2S in the Supporting Materials.

The XRD analysis confirmed the presence of 40% of Ti_2AlC and 60% of Ti_3AlC_2 in the MXene precursor – MAX phase. The peaks corresponding to Ti_2CT_x after precursor etching with 48% hydrofluoric acid were not observed, suggesting that Ti_2AlC underwent complete dissolution due to the lower stability compared to Ti_3AlC_2. The XRD patterns of raw Ti_3AlC_2-Ti_2AlC and $Ti_3C_2T_x$ are shown in Fig. 3S in the Supporting Materials. The characteristic reflection attributed to Ti_3AlC_2 at $2\theta = 9.5°$ for the plane (0 0 2) was shifted to a lower value of 8.9° 2θ for

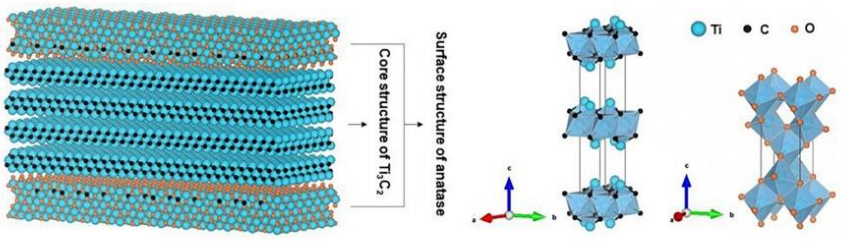

Fig. 1. Visualization of TiO_2-Ti_3C_2 composite crystal structure.

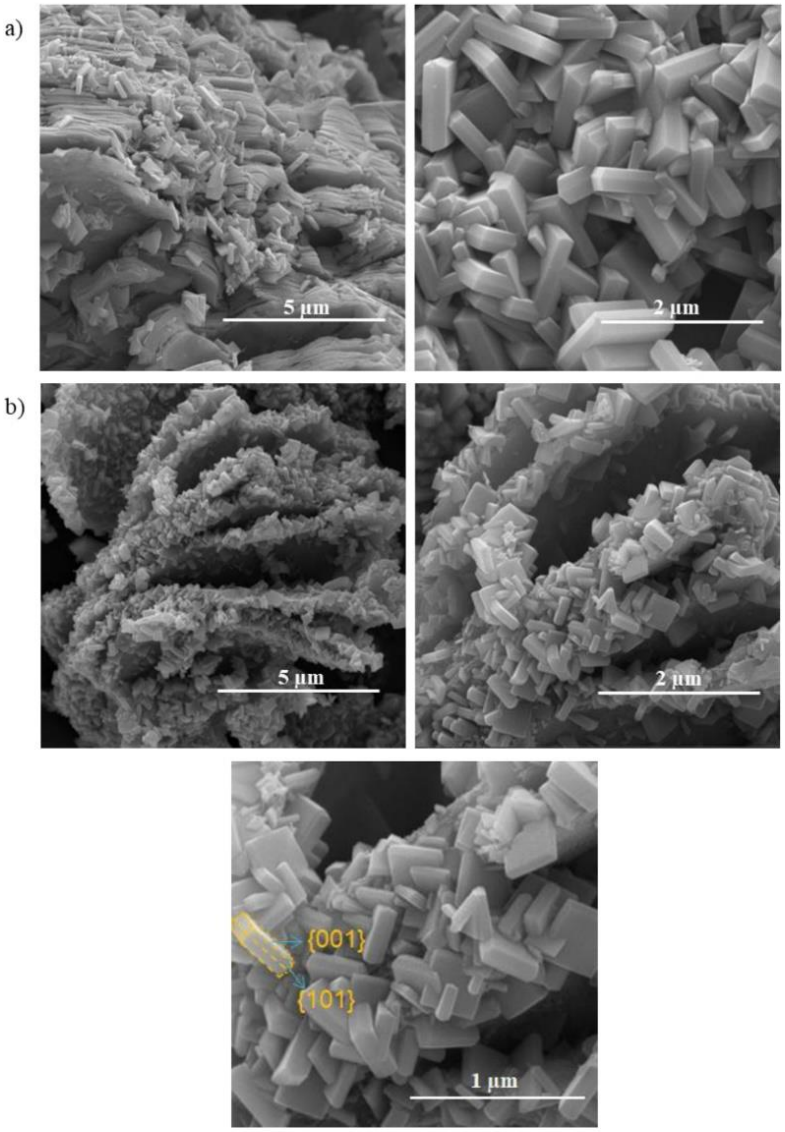

Fig. 2. SEM images of a) TiO_2/Ti_3C_2(160,6) b) TiO_2/Ti_3C_2(140,12).

$Ti_3C_2T_x$. It may be explained as a structural expansion resulting in an increase in *d*-spacing due to the alumina etching from the structure and its substitution with fluoride, oxygen, or hydroxyl terminating groups [57]. The reflection at $2\theta = 25°$ suggesting the presence of a second phase after the etching process using 48% HF, which may be assigned to low quantities of TiO_2 or Al_2O_3. For all the obtained composites, the formation of anatase particles was confirmed. The main diffraction peak of anatase was observed at $2\theta = 25.1°$, corresponding to the (101) plane diffraction, as presented in Fig. 4. Moreover, for anatase particles, the diffraction peak positions attributed to (103), (004), (112), (200), (105), (211), (213), (204), (116), (220), (215), and (301) planes also confirmed the formation of anatase phase, which is in accordance with JCPDS card no. 21–1272. The extension of time and increment of synthesis temperature increased the relative intensity of anatase signals and composites' crystallinity (see Fig. 4 and Table 1S in the Supporting Materials). Furthermore, the reflections specific to Ti_3C_2 at 8.9° 2θ and 18.2° 2θ were observed only for samples TiO_2/Ti_3C_2(140,6), TiO_2/Ti_3C_2(160,6), TiO_2/Ti_3C_2(180,6), TiO_2/Ti_3C_2(140,12). The increase in temperature above 200°C and extended solvothermal reaction time led to oxidation of the $Ti_3C_2T_x$ structure to anatase. Furthermore, signals that occurred at $2\theta = 35.8°$, 41.6°, and 60.4° implied the presence of TiC with crystallite planes (111), (200), and (220), respectively in accordance with JCPDS card no. 65–8417. The diffraction peaks corresponding to lattice plane reflections of iron species should be located at around 25.24°, 35.95°, 36.9°, 47.93°, 54.94°, and 62.0°, but they can be overlapped by peaks attributed to anatase crystallites. Moreover, the presence of iron does not affect the crystal structure of TiO_2/Ti_3C_2 regarding the low amount of Fe loading as well as high dispersion on TiO_2/Ti_3C_2 surface. The intensity of diffraction peaks and anatase crystallite size determined based on the Scherrer equation was similar within the series of samples TiO_2/Ti_3C_2 (140,12), Fe-TiO_2/Ti_3C_2 (140,12), and TiO_2/Ti_3C_2 (220,24), Fe-TiO_2/Ti_3C_2 (220,24) non-

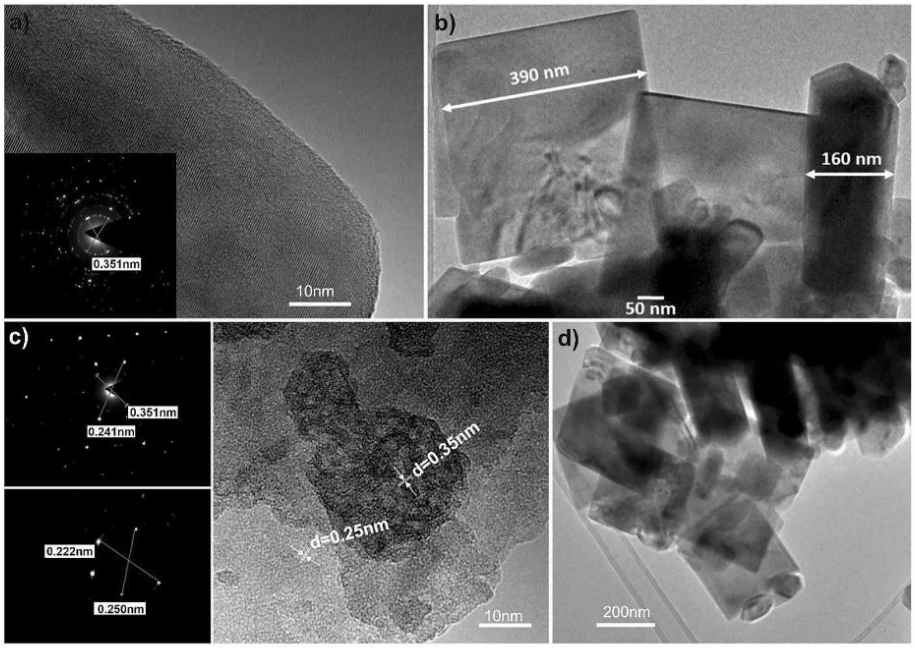

Fig. 3. TEM images and SAED analysis of a) TiO_2/Ti_3C_2(220,24), b) TEM analysis of Fe-TiO_2/Ti_3C_2(220,24), c) SAED and TEM analysis of TiO_2/Ti_3C_2(140,12), d) TEM analysis of Fe-TiO_2/Ti_3C_2(140,12).

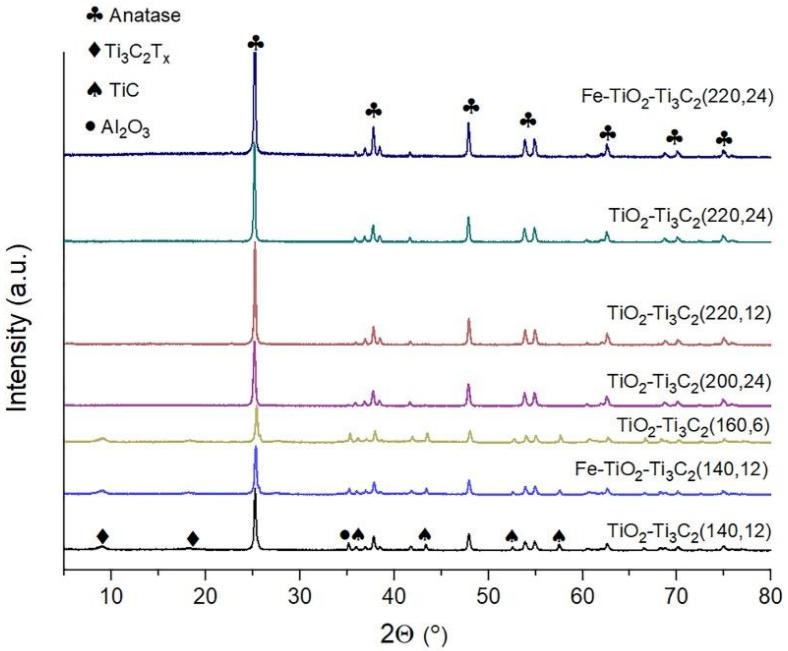

Fig. 4. X-ray diffraction patterns of TiO_2/Ti_3C_2 and Fe-modified TiO_2/Ti_3C_2 composites.

modified and modified with iron (see Table 1).

The TiO_2/Ti_3C_2 photocatalysts' physicochemical properties, e.g., crystallite sizes, indirect band gap values, BET surface areas, are summarized in Table 1. The average anatase crystallite size calculated according to the Scherrer equation varied from about 33 nm to 56 nm for samples TiO_2/Ti_3C_2(200,6) and TiO_2/Ti_3C_2 (140,6), respectively.

The etching of aluminum from Ti_3AlC_2–Ti_2AlC resulted in BET surface area development, which increased 2-fold compared to the raw

Table 1
Characteristics of prepared TiO_2/Ti_3C_2 composites.

No.	Sample	Synthesis conditions		Anatase crystallite size (nm)	BET surface area (m^2/g)	Eg (eV)
		temp. (°C)	time (h)			
1	Ti_3AlC_2-Ti_2AlC	n.d.	n.d.	n.d.	1.7	n.d.
2	$Ti_3C_2T_x$	RT	24	n.d.	3.1	n.d.
3	TiO_2/ Ti_3C_2(140,6)	140	6	56	11.4	n.d.
4	TiO_2/ Ti_3C_2(140,12)	140	12	36	13.5	n.d.
5	TiO_2/ Ti_3C_2(140,24)	140	24	41	6.9	2.4
6	TiO_2/ Ti_3C_2(160,6)	160	6	35	10.2	n.d.
7	TiO_2/ Ti_3C_2(160,12)	160	12	40	8.0	2.4
8	TiO_2/ Ti_3C_2(160,24)	160	24	48	7.1	2.75
9	TiO_2/ Ti_3C_2(180,6)	180	6	47	7.6	1.75
10	TiO_2/ Ti_3C_2(180,12)	180	12	40	8.2	2.65
11	TiO_2/ Ti_3C_2(180,24)	180	24	41	7.0	2.75
12	TiO_2/ Ti_3C_2(200,6)	200	6	33.5	6.9	1.85
13	TiO_2/ Ti_3C_2(200,12)	200	12	38	7.2	2.75
14	TiO_2/ Ti_3C_2(200,24)	200	24	35	5.6	2.95
15	TiO_2/ Ti_3C_2(220,6)	220	6	45	5.3	2.5
16	TiO_2/ Ti_3C_2(220,12)	220	12	48	6.2	2.75
17	TiO_2/ Ti_3C_2(220,24)	220	24	49	5.4	3.0
18	Fe-TiO_2/ Ti_3C_2(140,12)	140	12	35	13.9	n.d.
19	Fe-TiO_2/ Ti_3C_2(220,24)	220	24	50	5.4	3.0

material of Ti_3AlC_2-Ti_2AlC. For TiO_2/Ti_3C_2 composites, the BET surface area varied from 5.3 to 13.5 $m^2 \cdot g^{-1}$. The formation of TiO_2 on the Ti_3C_2 surface resulted in a 2 to 4-fold increase of the specific surface area. Increasing solvothermal reaction time from 6 to 12 h increased the surface area, while 24-hour reactions had the reverse effect, probably due to the formation of tightly compacted agglomerates of TiO_2 structures. Moreover, an increment of reaction temperature led to a reduction of the photocatalyst's surface area from 13.5 $m^2 \cdot g^{-1}$ to 6.2 $m^2 \cdot g^{-1}$ for samples TiO_2/Ti_3C_2(140,12) synthesized at 140 °C, and TiO_2/Ti_3C_2(220,12) obtained at 220 °C, respectively.

The $Ti_3C_2T_x$ functionalized with -F, -O, and –OH terminate groups after the etching process is a material with metallic properties, showing the characteristic of a narrow bandgap semiconductor (0.05–0.1 eV) [58]. Among TiO_2/Ti_3C_2 composites, only the sample synthesized at the highest temperature of 220 °C for 24 h exhibited the bandgap value comparable with decahedral anatase particles (about 3.0 eV) [59], suggesting complete oxidation of Ti_3C_2 to TiO_2. The narrow bandgap of TiO_2/Ti_3C_2 composites (2.4 eV – 2.75 eV) synthesized at lower temperatures of 140 °C, and 160 °C resulted from a Ti_3C_2 presence in the composite structure, while for samples synthesized in solvothermal reaction for 6–12 h at 200 °C – 220 °C the narrower bandgap resulted from the carbonic species present in the structure of TiO_2 (C-doped TiO_2). The deposition of iron at the TiO_2/Ti_3C_2 sample did not change the physicochemical properties (BET surface area, crystallite size, Eg value) of the obtained composite material.

The XPS was used to determine the surface composition and oxidation state of elements in the TiO_2/Ti_3C_2 composites. The XPS analysis confirmed that samples contain the following elements: Ti, O, C, Al, and F. For TiO_2/Ti_3C_2 composites synthesized from Ti_3AlC_2-Ti_2AlC structure at lower temperatures, the presence of alumina and fluorine in the form of AlF_3 and Al_2O_3 was noticed. As presented in Table 2, aluminum and fluorine content in TiO_2/Ti_3C_2(220,24) was 2.94 at.% and 1.94 at.%, respectively. Moreover, for TiO_2/Ti_3C_2(220,24), higher oxygen and lower carbon content were observed than TiO_2/Ti_3C_2(140,12). These results confirmed the formation of the TiO_2 phase from MXene during the solvothermal reaction at the highest temperature of 220 °C. The surface oxidation of MXene was also confirmed by identifying Ti 2p 1/2 and Ti 2p 3/2 peaks at binding energies of 465 eV and 459 eV, which corresponds to Ti^{4+} in TiO_2 structure.

The XPS spectra for high-resolution Ti 2p, O 1 s, C 1 s core levels of TiO_2/Ti_3C_2 composites are presented in Fig. 5. Besides the most intense signal at 459 eV from the Ti-O bond, the Ti 2p3/2 region could be deconvoluted for components centered at 454.8 eV, 455.4 eV, 456.1 eV, 456.8 eV, 458 eV corresponding to Ti-C and C-Ti-O bonds. Similar to research performed by Shen et al. [60], the XPS analysis revealed the presence of C-Ti-F bonds with a signal located at 460.5 eV.

Typical binding energy at about 530.5 eV was related to oxygen in the TiO_2 crystal lattice (Ti–O–Ti). According to Peng et al. [61], the peak at 531.3 eV was assigned to oxygen in Ti–OH/C = O bonds and the peak at 532.3 eV was related to oxygen in the C–OH bonds. Further signals located at 533.2 eV and 534 eV may be attributed to Al_2O_3 and adsorbed water, respectively [62].

The C 1 s region could be deconvoluted for five peaks at 281.9 eV, 283.3 eV, 284.3 eV, 285 eV, 285.6 eV, which can be assigned to Ti-C, C-Ti-O bonding at the interfaces of TiO_2/Ti_3C_2, C = C (sp2), C–C (sp3), C–H (sp3), respectively [63]. Meanwhile, signals at 286.4 eV, 287.2 eV, 289.3 eV correspond to C-OH, C-O-C, and O = C-OH [64]. The Ti-C, C-Ti-O bonds were observed for sample TiO_2/Ti_3C_2(140,12) synthesized at a lower temperature of the solvothermal reaction, while for TiO_2/Ti_3C_2(220,24) were not observed due to complete oxidation of Ti_3C_2 to TiO_2.

The surface properties of photocatalyst modified with iron were similar to pure TiO_2/Ti_3C_2 samples. Meanwhile, the XPS analysis confirmed the presence of 0.7 at.% of iron after magnetron sputtering at sample TiO_2/Ti_3C_2(220,24) and 0.67 at.% of iron for TiO_2/Ti_3C_2(140,12). For Fe-modified TiO_2/Ti_3C_2 photocatalyst broad Fe 2p 3/2 peak with multiplet splitting characteristic for iron oxides was observed, as presented in Fig. 6. The XPS spectrum of Fe 2p can be resolved in two main peaks, which are ascribed to FeO at 711.5 eV and Fe_2O_3 at 712 eV.

The DR/UV–Vis absorption spectra of TiO_2/Ti_3C_2 and Fe-TiO_2/Ti_3C_2 composites are shown in Fig. 7. The TiO_2/Ti_3C_2 composites absorbed both UV and visible light. The threshold around 400 nm was observed on the spectra, indicating the formation of titanium(IV) oxide on the MXene surface. Moreover, the nanocomposites obtained at higher temperatures (200 °C and 220 °C) and with a longer reaction time (12 h or 24 h) were characterized with lower light absorption in the range of 400–800 nm than those obtained at 140 °C and 160 °C. A decrease in visible light absorption and emergence of absorption shoulder with a threshold at 400 nm is correlated with the formation of the TiO_2 phase. The deposition of iron on TiO_2/Ti_3C_2 did not change the shape of spectra and absorption intensity. Compared to TiO_2/Ti_3C_2(220,24) sample containing decahedral anatase particles, higher absorption properties for

Table 2
XPS analysis of Ti, O, C, Al, F content (at.%) for the selected composites TiO_2-Ti_3C_2(140,12) ,TiO_2-Ti_3C_2 (220,24), and Fe-TiO_2-Ti_3C_2(220,24).

Sample	Content (at.%)						
	C 1 s	N 1 s	O 1 s	F 1 s	Al 2p	Ti 2p	Fe 2p
TiO_2/Ti_3C_2(140,12)	24.69	1.03	41.47	6.02	9.01	17.78	–
TiO_2/Ti_3C_2(220,24)	33.50	0.48	43.65	1.69	2.94	17.74	–
Fe-TiO_2/ Ti_3C_2(220,24)	26.2	–	51.6	1.1	–	20.5	0.7

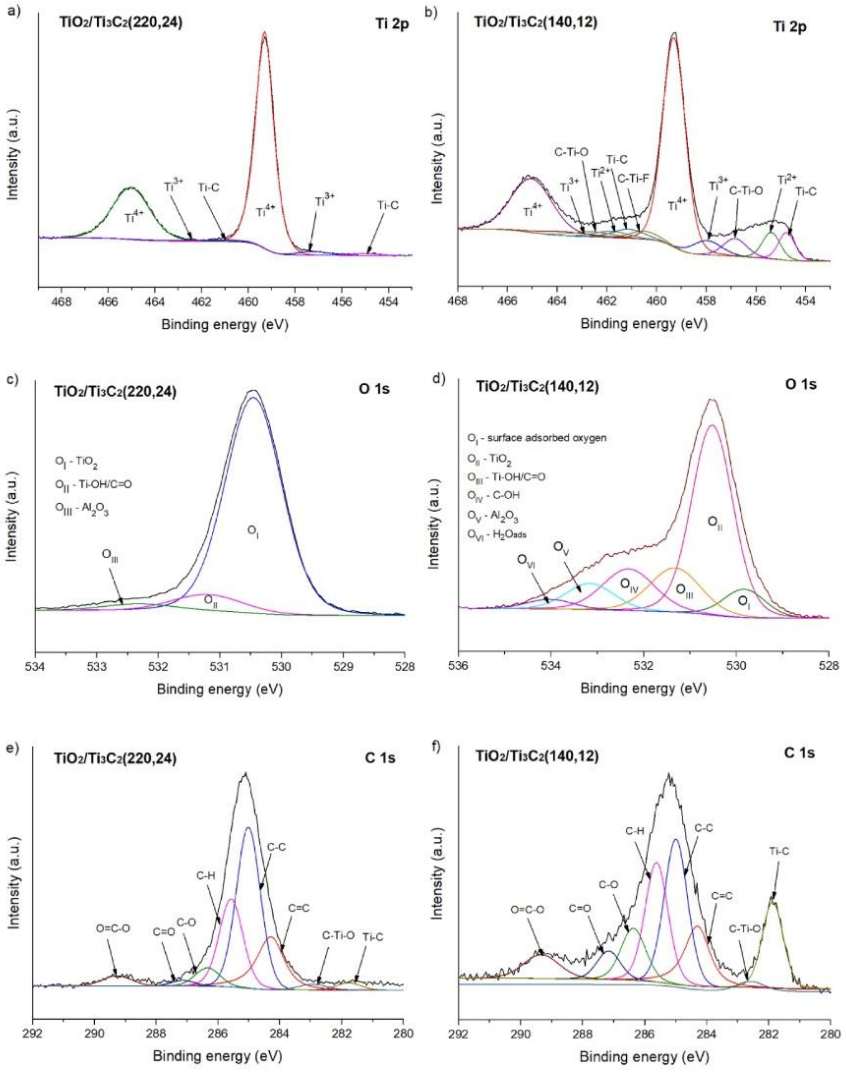

Fig. 5. XPS spectra of titanium (Ti 2p), oxygen (O 1 s), and carbon (C 1 s) region for samples TiO_2/Ti_3C_2(220,24) and TiO_2/Ti_3C_2(140,12).

Fe-modified TiO_2/Ti_3C_2(220,24) sample were observed in the Vis light range of 400–500 nm. Xu et al. [65] reported that the absorption edge for pristine TiO_2 was increased in the visible light region from 390 to 750 nm after ultra-thin Fe_2O_3 surface modification.

The Raman spectra measured for selected photocatalysts presented in Fig. 8 consist of typical anatase active modes [66]. Their detailed interpretation is provided in Table 3. However, it should be underlined that typically the Eg(1) band is observed at 144 cm^{-1} while the maxima were placed at 150 cm^{-1}. Such a blue shift can result from a much smaller grain size (phonon confinement effect) compared to the literature ones or surface coating [67]. The spectra are quite similar in the range from 100 cm^{-1} to 1200 cm^{-1}, and their intensity increased with TiO_2 content. The surface compound can induce some comprehensive stress on the most outer atoms of titanium, and following that, the change in Eg(1) position occurs. Indeed, in most cases, signals typical for carbonaceous species can be easily detected, known as D and G bands [68]. The first one, located at ca. 1363 $cm^{-1,}$ is a breathing mode of A1g symmetry, including phonons near the K zone boundary and originating from the structural defects in the carbon lattice. The G-band present at ca. 1584 cm^{-1} is assigned to the in-plane vibrations of sp^2 carbon atoms and is a doubly degenerated phonon mode (E2g) at the Brillouin zone center. Those features confirm that carbon forms exhibit graphitic character and can also be responsible for the Eg(1) mode shift.

The EPR spectra are presented in Fig. 9 as the signal intensity against the G value. The Lande factor (G) was calculated according to the equation:

$$G = \frac{h\hat{A}\cdot f}{m_B\hat{A}\cdot B} \quad (1)$$

where: G–Lande factor (a.u.); h–Planck's constant ($6.62\cdot10^{-34}$; J·s); f–frequency (Hz); mB–Bohr magneton ($9.2740154\cdot10^{-24}$; $J\cdot T^{-1}$); and B–magnetic field induction (T).

The characteristic G values of about 1.995–2.0 correspond to oxygen (v_o) or carbon vacancies (v_c) and of about 1.94 to the presence of Ti^{3+}, which may have originated from Ti_3C_2. For TiO_2/Ti_3C_2 layered composites, the recorded EPR resonances line was broad and unresolved,

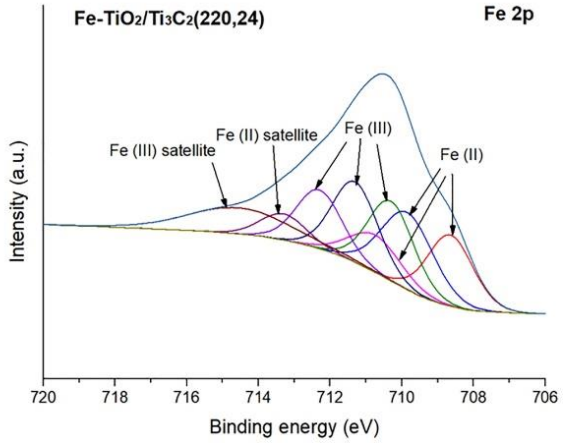

Fig. 6. XPS spectrum of iron (Fe 2p) region for sample Fe-TiO_2/Ti_3C_2.

which demonstrates the formation of a high number of defects [69]. The highest resonance line about g = 1.94 was noticed for the TiO_2/Ti_3C_2(140,12) sample, suggesting a higher concentration of Ti^{3+}. Meanwhile, for the sample TiO_2/Ti_3C_2(220,24), the strongest signal occurred about g = 2.0 and may be assigned to the oxygen or carbon vacancies. Zhang et al. [70] reported that the formation of carbon vacancies, which exposed a large number of active sites, may inhibit the electron-hole recombination process and thus lead to higher photocatalytic activity. Moreover, Shen et al. [60] observed that v_c promotes pollutants adsorption on the photocatalyst surface, modulates the electronic structure, and improves charge carriers accumulation. Carbon vacancies with unpaired electrons represent conversion centers, where photo-generated electrons may absorb oxygen for the generation of photocatalytic active species, e.g., superoxide anion radicals ($\cdot O_2^-$) [71–72]. The active sites – Ti^{3+} species and carbon vacancies may participate in the contaminants' adsorption on the photocatalyst surface. Furthermore, they represent trapping sites for the photo-formed conduction band electrons [73]. Xu et al. [74] proved that the existence of Ti^{3+} defects enhances visible-light-driven photocatalysis due to bandgap narrowing.

The emission spectra of the most photocatalytic active TiO_2/Ti_3C_2 and Fe-TiO_2/Ti_3C_2 composites were measured under 350 nm excitation at room temperature, and the results are presented in Fig. 10. For all compounds, the broad band in the blue region was observed. For samples TiO_2/Ti_3C_2(140,12) and Fe-TiO_2/Ti_3C_2(140,12) synthesized at 140 °C, the peak maximum was about 460 nm, while for TiO_2/Ti_3C_2(220,24) and Fe-TiO_2/Ti_3C_2(220,24) samples obtained at a higher temperature of 220 °C the peak was shifted to 470 nm. As the emission spectra strongly depend on the particles surrounding the environment [75], it may suggest that higher synthesis temperature leads to the changes of the photocatalyst surface. The emission of the composites was similar to the luminescence of anatase (TiO_2) [76] and can be assigned to charge transfer transition from Ti^{4+} to O^- at the sites near defects [77] and emission from the surface oxygen vacancies or defects [78]. The blue shift observed for presented photocatalysts may also be the result of the Burstein-Moss effect. The effect is even more expected as the Fe-modified samples are slightly more blue-shifted compared to unmodified samples. It is also important to notice that time and laser power may also lead to the bathochromic effect [79].

The decay curves of the composites' luminescence were registered under 350 fs pulse laser at room temperature. It can be noted that the decay profiles showed the non-exponential character. The non-exponential profiles of luminescence decays suggest the existence of carrier trapping sites with different energy levels, leading to a distribution of the carrier transport rates [77]. To calculate decays for all samples, two-phase exponential decay function with time constant parameters were used:

$$y = y_0 + A_1 e^{-x/t_1} + A_2 e^{-x/t_2}$$

The analysis of the decay curves showed that longer time and higher synthesis temperature led to shortening of the luminescence lifetimes (see Fig. 11). This may suggest a decrease in the number of luminescent centers (defects) after a more prolonged synthesis at the higher temperature. Analysis of the luminescence decay time showed that Fe-modified samples revealed longer decays, suggesting energy transfer between TiO_2 and Fe species.

As presented in Fig. 12, the Mott Schottky plots' positive slope demonstrated the n-type semiconductivity characteristic of TiO_2/Ti_3C_2 composites [80]. According to Xu et al. [81], regions 1, 2, and 3 correspond to the potential ranges in which the capacitance is dominated by the FTO substrate FTO/layer interface and the semiconducting

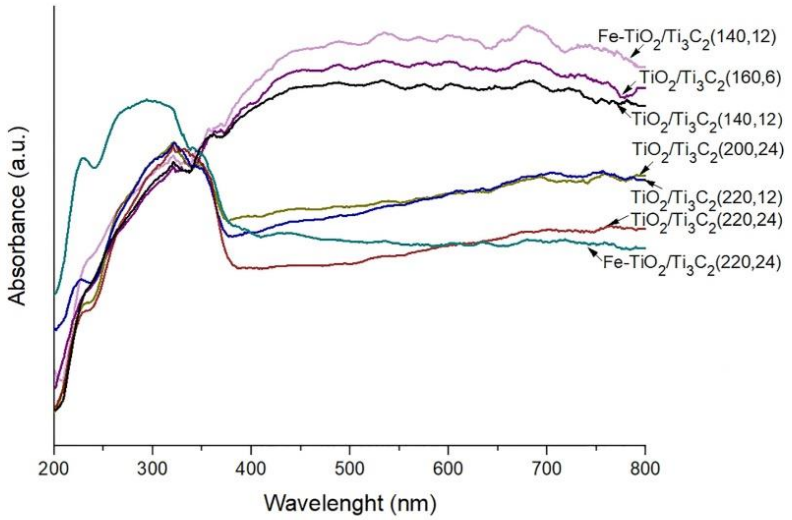

Fig. 7. DR/UV–Vis spectra of the selected TiO_2/Ti_3C_2 and Fe-TiO_2/Ti_3C_2 composites.

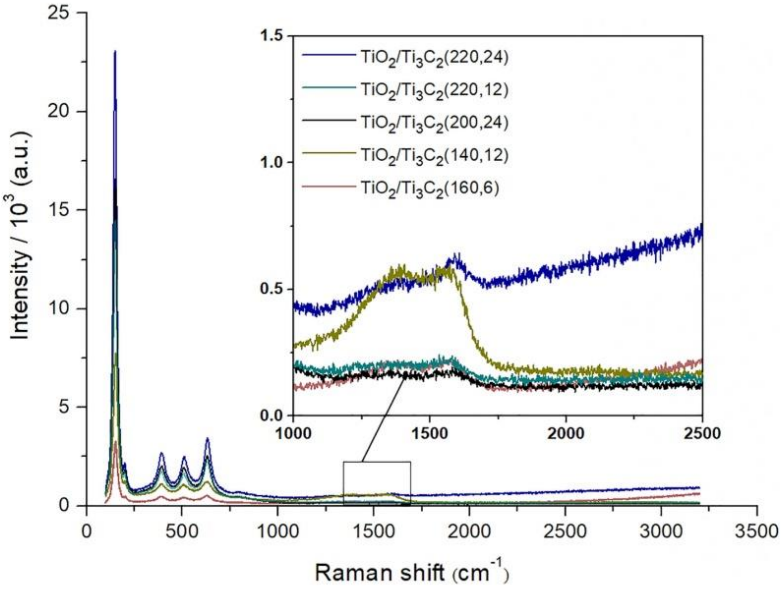

Fig. 8. Raman spectra of selected TiO_2/Ti_3C_2 composites.

Table 3
Wavenumbers of the samples with their assignment.

Band localization (cm^{-1})	Assignment
150	Eg(1)
200	Eg(2)
395	B1g(1)
512	Double signal of B1g(2) and A1g
633	Eg(3)
805	First overtone of B1g at 395 cm^{-1}
1363	D band
1584	G band

film deposited onto FTO. A similar shape of the Mott-Schottky plot was recorded by Bresolin et al. [82] and described by Bisquert [83]. When the applied potential fits the 1st and 2nd region, the space charge zone is depleted, and the capacitances of the tested electrodes are similar and overlap this of bare FTO substrate. A linear fit, indicated by the grey arrow, provides an E_{fb} of very similar value: ca. −0.3 V vs. Ag/AgCl/0.1 M KCl attributed to the FTO-dominated response. In a more cathodic range, the activity of all tested materials differs significantly, and the second flat band potential value can be distinguished, see Table 4. According to the provided data, the FTO/TiO_2/Ti_3C_2(140,12) exhibits the most positive E_{fb2} value comparing to bare FTO, FTO/ TiO_2/ Ti_3C_2(140,24), and FTO/TiO_2/Ti_3C_2(220,24). For iron-modified Ti_3C_2,

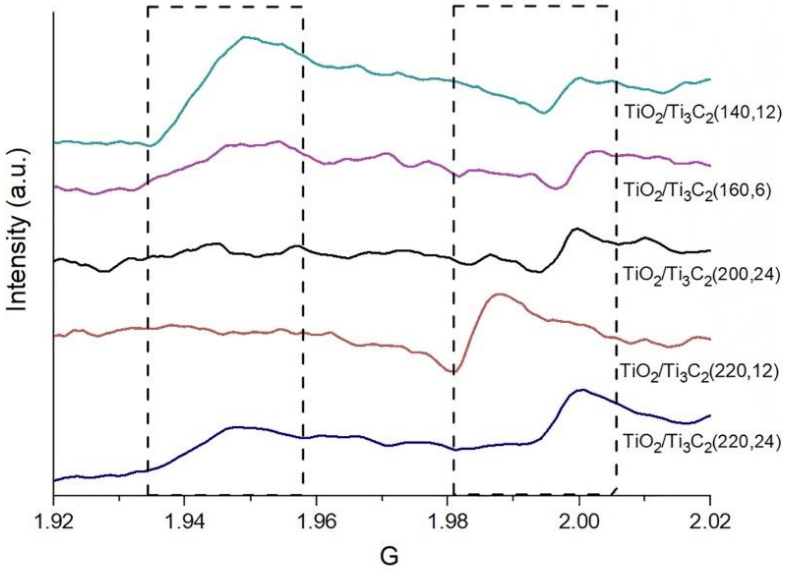

Fig. 9. The EPR spectra recorded at RT for selected TiO_2/Ti_3C_2 composites.

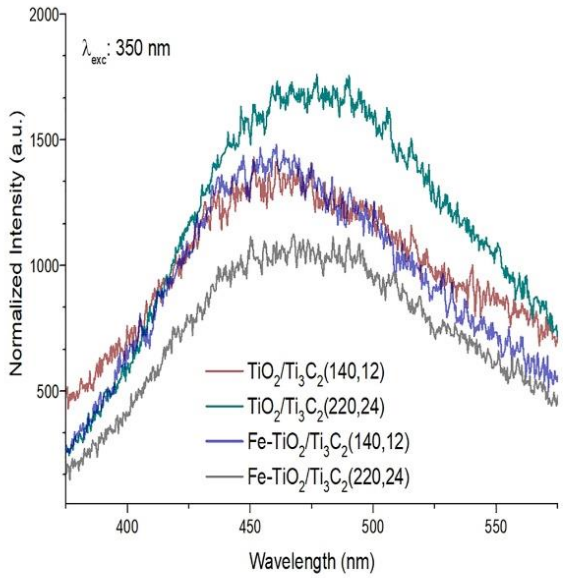

Fig. 10. Photoluminescence emission spectra of TiO_2/Ti_3C_2 and Fe-TiO_2/Ti_3C_2 photocatalysts.

only one value of flat band potential can be determined, indicating the high impact of the Fe presence on the electrochemical activity.

For n-type semiconductors, the flat band potential is almost equal to the conduction band potential. Thus, according to values of E_{fb} and E_g, the valence band (VB) edge of composites may be determined by the following equation:

$$E_{VB} = E_g + E_{CB}$$

The calculated valence band positions of TiO_2/Ti_3C_2(140,24), TiO_2/Ti_3C_2(220,24) and TiO_2/Ti_3C_2(140,12) are approximately 1.53 eV, 2.25 eV and 2.21 eV, respectively. A more positive location of VB is associated with stronger oxidation power. Thus, samples TiO_2/Ti_3C_2(220,24) and TiO_2/Ti_3C_2(140,12) exhibited enhance photocatalytic activity towards degradation of phenol and carbamazepine compared to TiO_2/Ti_3C_2(140,24).

The Mott-Schottky analysis indicated a significant increment in donor density accompanied by a positive shift of flat band potential of Fe-modified TiO_2/Ti_3C_2 samples comparing to neat TiO_2/Ti_3C_2, which is recognized to be a key factor responsible for photocatalytic oxidation reactions.

The electrochemical impedance spectroscopy Nyquist plots of the most photocatalytic active TiO_2/Ti_3C_2 and Fe-TiO_2/Ti_3C_2 photocatalysts recorded in the dark and under UV–Vis irradiation at polarization potential of + 0.5 V vs. E_{oc} are shown in Fig. 4S. a). The arc radius of iron-modified TiO_2/Ti_3C_2 in the EIS Nyquist plot was lower than unmodified TiO_2/Ti_3C_2 composites indicating improved charge carriers separation. Furthermore, the smallest arc radius was recorded for sample Fe-TiO_2/Ti_3C_2(220,24). These results indicate a larger electroactive surface area and low charge transfer resistance, implying an effective separation of the photo-generated electron-hole pairs [84].

The photocurrent response of TiO_2/Ti_3C_2 and Fe-TiO_2/Ti_3C_2 upon on–off cycles of UV–Vis light irradiation is presented in Fig. 4S b) in the Supporting Materials. For all samples, the photocurrent increases when light is switched on and decreases when the light off, indicating that the materials respond to light with good reproducibility. Furthermore, photocurrent responses maintain superior stability after ten on/off cycles, which indicates that the photocatalyst may restrain photocorrosion [85]. According to the literature, $Ti_3C_2T_x$, which acts as a metallic conductor exhibits minimal, nearly no photocurrent generation [86–88]. Photo-generated electrons in the TiO_2/Ti_3C_2 originate from TiO_2, while Ti_3C_2 is involved in the electron transfer [89]. Thus the lowest photocurrent was observed for sample TiO_2/Ti_3C_2(140,12), characterized by lower TiO_2 content. Higher photocurrent means lower recombination of photo-generated electrons and holes, higher photoelectron transfer efficiency, and more light absorbance.

Furthermore, it can be observed in absorption spectra (Fig. 7) that TiO_2/Ti_3C_2(220,24) composite have much higher absorption in the UV range what may be another proof of the generation of new v_O vacancy band locating just below the conduction band edge of pure TiO_2. The high concentration of v_o defects may lead to much higher UV light-induced photoelectron generation [90] compared to the rest of the

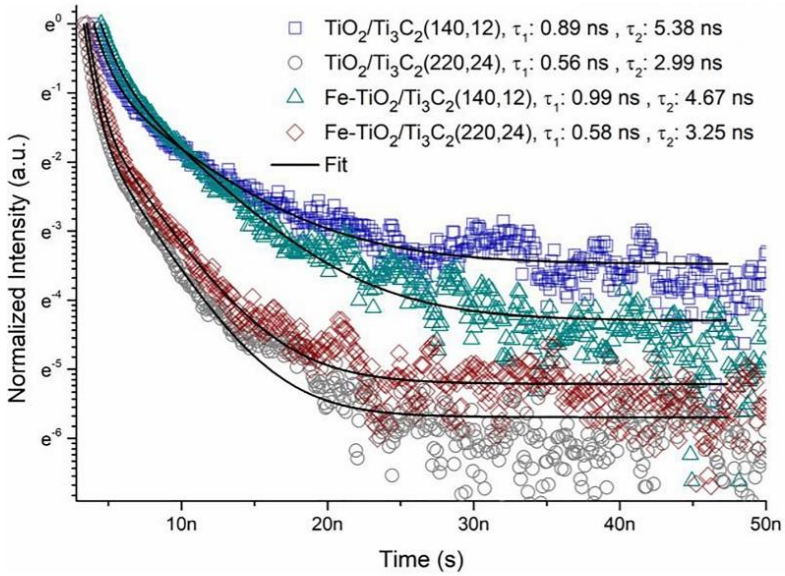

Fig. 11. Time-resolved photoluminescence decay spectra of TiO_2/Ti_3C_2 and Fe-TiO_2/Ti_3C_2 photocatalysts.

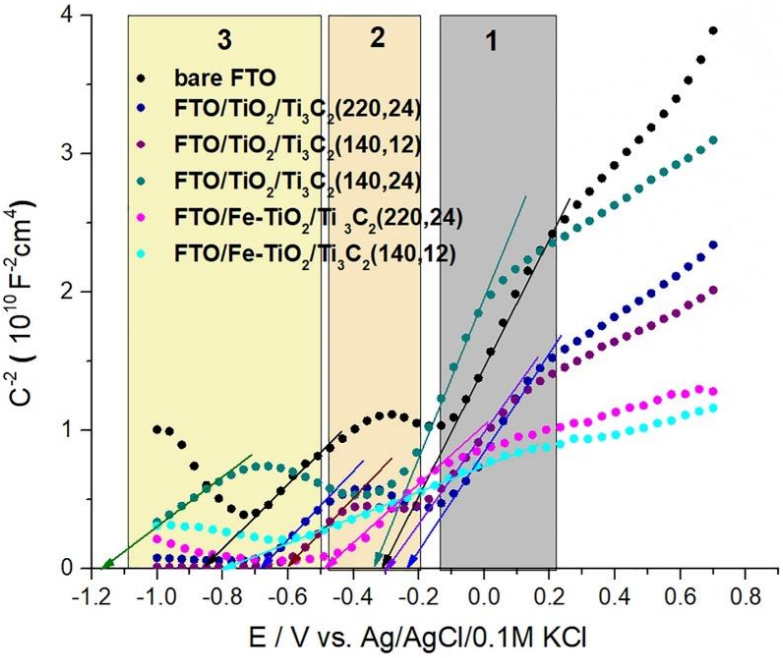

Fig. 12. Mott-Schottky plots for bare FTO and coated with samples TiO_2/Ti_3C_2(140,12), TiO_2/Ti_3C_2(140,24), TiO_2/Ti_3C_2(220,24), Fe-TiO_2/Ti_3C_2(140,12) and FeTiO_2/Ti_3C_2(220,24).

Table 4
The value of flat band potential and donor density determined for tested photocatalytic materials.

Sample	E_{fb1}	E_{fb2}	slope / 10^{10} $F^{-2}cm^4/V$	N_d / 10^{20} cm^{-3}
Bare FTO	−0.31	−0.94	–	–
FTO/ TiO_2/ Ti_3C_2(220,24)	−0.25	−0.69	2.25	1.65
FTO/ TiO_2/ Ti_3C_2(140,12)	−0.29	−0.60	2.21	1.68
FTO/ TiO_2/ Ti_3C_2(140,24)	−0.33	−1.15	1.53	2.43
FTO/ Fe-TiO_2/ Ti_3C_2(220,24)	–	−0.80	2.12	1.75
FTO/Fe-TiO_2/ Ti_3C_2(140,12)	–	−0.49	1.91	4.05

composites. Also, EPR spectra (Fig. 9) showed a strong signal at a g-value of 2.00, indicating the significant presence of v_o. This signal can be caused by electrons trapped on surface vacancies v_o [91]. A similar effect was observed by Bao et al. [86] for TiO_2/Ti_3C_2 composites obtained by calcination of Ti_3C_2 under air condition at 350, 450, 550, and 650°C, respectively. The highest photocurrent was recorded for a sample calcined at 550°C.

Additionally, the highest value of photocurrent (~0.4 μA/cm^2) was produced for the sample TiO_2/Ti_3C_2(220,24) modified with iron compared to un-modified material (~0.25 μA/cm^2). These results confirmed that Fe-modification positively influences the photocurrent values, thus indicating a more efficient separation of the photoexcited electron-hole pairs. It can also be observed that samples modified with iron species showed slower decay, indicating long charge carrier lifetimes and metastable donor states (also noticed in photoluminescence measurements).

Thermogravimetric analyzes were conducted for two of the most active TiO_2/Ti_3C_2 composites, as presented in Fig. 5S in the Supporting Materials. The thermal decomposition involved two exothermic steps. The first step with a weight loss of 0.15% in the range of 25–287 °C and 0.28% in the range of 25–235 °C. The second step with a weight loss of 1.73 in the range of 287–646 and 0.98% in the range of 235–581 °C. TGA measurements indicated the thermal stability of the compounds heated in an oxygen-rich atmosphere. It was proved by the total weight loss of 1.88% for the TiO_2/Ti_3C_2(140,12) and 1.26% for the TiO_2/Ti_3C_2(220, 24) sample.

To study the TiO_2/Ti_3C_2 photocatalysts' surface properties, the electrophoretic mobility of these photocatalysts at different pH values was investigated. The zeta potential was positive at lower pH and negative at higher pH values, as presented in Fig. 6S in the Supporting Materials. The isoelectric point (IEP) was observed at pH = 3.6 and pH = 4.7 for TiO_2/Ti_3C_2(140,12) and TiO_2/Ti_3C_2(220,24), respectively. It can be observed that the isoelectric point for TiO_2/Ti_3C_2(140,12) is shifted toward a lower pH value in comparison to the TiO_2/Ti_3C_2(220,24) sample. According to the literature, IEP for anatase TiO_2 is observed at a pH of 6 [92]. A decrease in IEP value may be attributed to the presence of MXenes, which are negatively charged. The zeta potential of an aqueous suspension of $Ti_3C_2T_X$ nanosheets was equaled to −34.75 mV [93]. Moreover, according to Kosmulski et al.[94] the presence of carbonates on the surface induces a shift in the IEP to lower pH values. The pH of carbamazepine solution during the photodegradation tests was set at 6.5. Thus, carbamazepine was primarily in the protonated form (pH < $K_{a,\ CBZ}$). As a weak acid with pKa equal to 10, phenol was present in the solution with a pH of 6.8, mainly in the molecular form. At these conditions, the Ti_3C_2 photocatalyst's surface was negatively charged, and the values of zeta potential were below −40 mV. Thus, the suspensions of all tested TiO_2/Ti_3C_2 and Fe-TiO_2/Ti_3C_2 particles were stable and did not agglomerate during the photocatalytic reaction.

3.2. Photocatalytic activity in reaction of phenol and carbamazepine degradation

The TiO_2/Ti_3C_2 composites' photocatalytic activity was studied in the photodegradation reaction of phenol as a model organic pollutant and carbamazepine belonging to the group of emerging contaminants not-susceptible to biodegradation. The results of photodegradation are presented in Table 5. The phenol decomposition efficiency ranged from 19 to 69% within 60 min of irradiation. The obtained results confirmed the crucial role of formed titanium(IV) oxide on organic compounds' oxidation efficiency.

The lowest phenol degradation rate constant ($k = 0.3 \pm 0.2 \cdot 10^{-2}$ min^{-1}) was observed for TiO_2/Ti_3C_2(140,6), which resulted from the minimal quantity of TiO_2 formed on the MXene surface. The highest photocatalytic activity was noticed for samples TiO_2/Ti_3C_2(160,6), TiO_2/Ti_3C_2(220,12), and TiO_2/Ti_3C_2(220,24) with the degradation rate constants equal to $1.8 \pm 0.05 \cdot 10^{-2}$ min^{-1}, $1.7 \pm 0.04 \cdot 10^{-2}$ min^{-1}, and $1.9 \pm 0.03 \cdot 10^{-2}$ min^{-1}, respectively. The higher the temperature and longer hydrothermal treatment time, the higher the photocatalytic activity. In this case, an increase of the TiO_2 content and crystallinity by prolonging solvothermal reaction time resulted in a more efficient generation of electrons and holes. The formation of surface heterojunction between {101} and {001} facets of decahedral anatase particles grown on Ti_3C_2 surface led to improved photoelectron transfer, which reduced charge carriers recombination. Except for the TiO_2/Ti_3C_2(220,12), TiO_2/Ti_3C_2(220,24), TiO_2/Ti_3C_2 (160,6), and TiO_2/Ti_3C_2(140,12) samples, containing titanium vacancies (Ti^{3+} centers) and oxygen or carbon vacancies at the surface, for other obtained TiO_2/Ti_3C_2 composite photocatalysts, the degradation rate constant fluctuated from 0.5 to $0.8 \cdot 10^{-2}$ min^{-1}. In all photodegradation processes, *ortho*-hydroxyphenol and *para*-hydroxyphenol were detected as the first intermediates of phenol decomposition, see Fig. 13.

The phenol degradation mainly proceeds by the attack of hydroxyl radicals on the phenyl ring, leading to *para*-hydroxyphenol and ortho-hydroxyphenol formation. For the TiO_2/Ti_3C_2(140,12) sample containing V_{Ti}, a higher concentration of *para*-hydroxyphenol than *ortho*-hydroxyphenol was noticed. In this case, electrons are accumulated on the surface (Ti^{3+} states), preventing h^+ location on the surface oxygen and further H_2O molecule oxidation to ·OH radicals. For TiO_2/Ti_3C_2(220,24) higher concentration of *ortho*-hydroxyphenol compared to sample TiO_2/Ti_3C_2(140,12) was observed. Different amounts of electrons and holes resulted in different abilities in forming ·OH, which are crucial reactive oxygen species in phenol photocatalytic decomposition.

The five samples with the highest activity in phenol decomposition were selected for evaluation of photocatalytic carbamazepine removal. The highest activity was observed for sample TiO_2/Ti_3C_2(140,12) with 96% degradation after 60 min of irradiation ($k = 5.2 \cdot 10^{-2}$ min^{-1}).

As presented in Fig. 14, the overall activity was higher than those observed for phenol decomposition. The differences in photodegradation efficiency resulted from differences in HOMO energy for phenol and carbamazepine. Higher HOMO energy (more positive value) of the decomposed compound makes it more susceptible to oxidation. According to the literature, HOMO energy calculated using the B3LYP/6–311++G method is equal to about −0.30 eV for carbamazepine [95], while for phenol −5.95 eV [96].

Shahzad et al. [97] have also reported the degradation of carbamazepine in the presence of $TiO_2/Ti_3C_2T_x$ composite with exposed {001} facets. However, the kinetic of carbamazepine degradation was slow. After 8 h of irradiation in the presence of simulated solar light, only 55% of the total carbamazepine was degraded, while in UV light, after 3 h of irradiation, almost 99% of CBZ was removed. The major detected intermediates of CBZ photodegradation were acridine, 2-aminobenzoic acid, 2-hydroxybenzoic acid, and formaldehyde-acridine [94].

In this study, formation of {001} and {101} facets in TiO_2/Ti_3C_2 layered composite markedly improved photocatalytic activity due to a surface heterojunction between {001} and {101} facets of TiO_2. After 1 h of UV–Vis light irradiation, more than 90% of carbamazepine was degraded. The co-exposed facets led to a more efficient transfer of photoinduced charge carriers. The CB and VB of {001} facets are located slightly higher than for {101} facets. It leads to the accumulation of photogenerated electrons on the {101} and holes on the {001} facets.

Moreover, modification of TiO_2/Ti_3C_2(140,12) surface with iron species resulted in complete carbamazepine degradation after 1 h of UV–Vis light irradiation with the degradation rate constant equal to $8.8 \pm 0.11 \cdot 10^{-2}$ min^{-1}, as presented in Fig. 15. The degradation efficiency for Fe-modified TiO_2/Ti_3C_2 was higher in UV–Vis than in UV light, confirming the effect of iron modification on TiO_2/Ti_3C_2 enhanced photocatalytic activity (see in Fig. 7S in the Supporting Materials). Iron oxides may increase the photocatalytic efficiency of TiO_2, as Fe ions can enact as hole and electron scavengers, thus inhibiting the recombination of the photo-generated charge carriers. Similar results were reported by Tada et al. [98] for the decomposition of 2-naphthol in the presence of surface-modified TiO_2 with highly dispersed iron oxide nanoparticles. Iron oxide-modified TiO_2 exhibited significantly higher photocatalytic activity under UV–Vis light irradiation.

For all investigated composites, hydroxycarbamazepine and small quantities of acridine were distinguished as intermediate products. The increased amount of acridine could be an indicator of the limiting step since acridine ultimately led to the formation of a stable molecule of acridone [99]. Hydroxy-carbamazepine is the first possible product of CBZ oxidation, and therefore, acts as a substrate for further oxidation. These results illustrate well intensification of the process of CBZ photocatalytic degradation.

The TiO_2/Ti_3C_2(140,12) photocatalyst and Fe-TiO_2/Ti_3C_2(140,12)

Table 5
The rate constant of phenol and carbamazepine degradation in the presence of TiO_2, TiO_2/Ti_3C_2, and Fe-TiO_2/Ti_3C_2 samples.

No.	Sample label	Phenol degradation rate constant($min^{-1} \cdot 10^{-2}$)	Carbamazepine degradation rate constant($min^{-1} \cdot 10^{-2}$)
1	TiO_2/Ti_3C_2(140,6)	0.30 ± 0.2	n.d.
2	TiO_2/Ti_3C_2(140,12)	1.05 ± 0.07	5.20 ± 0.11
3	TiO_2/Ti_3C_2(140,24)	0.60 ± 0.05	n.d.
4	TiO_2/Ti_3C_2(160,6)	1.80 ± 0.05	2.40 ± 0.15
5	TiO_2/Ti_3C_2(160,12)	0.70 ± 0.02	n.d.
6	TiO_2/Ti_3C_2(160,24)	0.70 ± 0.01	n.d.
7	TiO_2/Ti_3C_2(180,6)	0.50 ± 0.01	n.d.
8	TiO_2/Ti_3C_2(180,12)	0.70 ± 0.03	n.d.
9	TiO_2/Ti_3C_2(180,24)	0.80 ± 0.05	n.d.
10	TiO_2/Ti_3C_2(200,6)	0.70 ± 0.01	n.d.
11	TiO_2/Ti_3C_2(200,12)	0.70 ± 0.03	n.d.
12	TiO_2/Ti_3C_2(200,24)	1.60 ± 0.02	2.50 ± 0.09
13	TiO_2/Ti_3C_2(220,6)	0.70 ± 0.03	n.d.
14	TiO_2/Ti_3C_2(220,12)	1.70 ± 0.04	3.10 ± 0.16
15	TiO_2/Ti_3C_2(220,24)	1.90 ± 0.03	3.90 ± 0.14
16	Fe-TiO_2/Ti_3C_2(140,12)	n.d.	8.80 ± 0.11
17	Fe-TiO_2/Ti_3C_2(220,24)	n.d.	5.60 ± 0.07

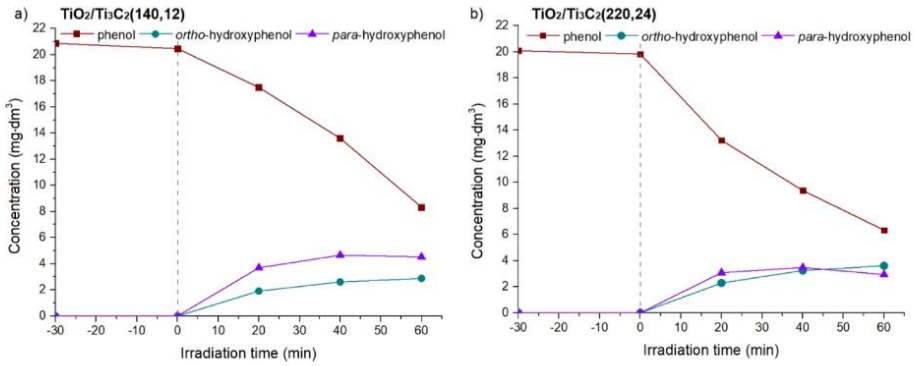

Fig. 13. Mean concentration change curves for exemplary samples TiO_2/Ti_3C_2(140,12) and TiO_2/Ti_3C_2(220,24) during phenol degradation. Detailed results for each sample are presented in Table 2S in the Supporting Materials.

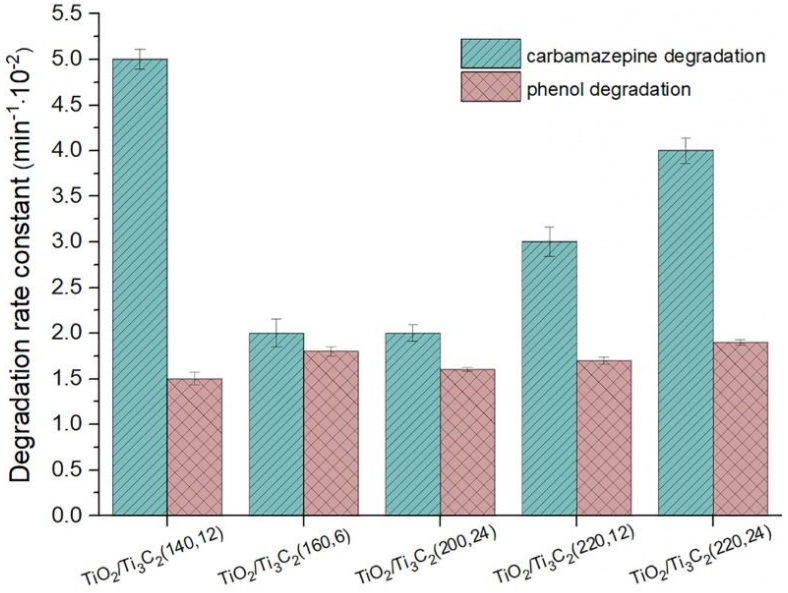

Fig. 14. Phenol and carbamazepine removal rate constant for selected TiO_2/Ti_3C_2 composites.

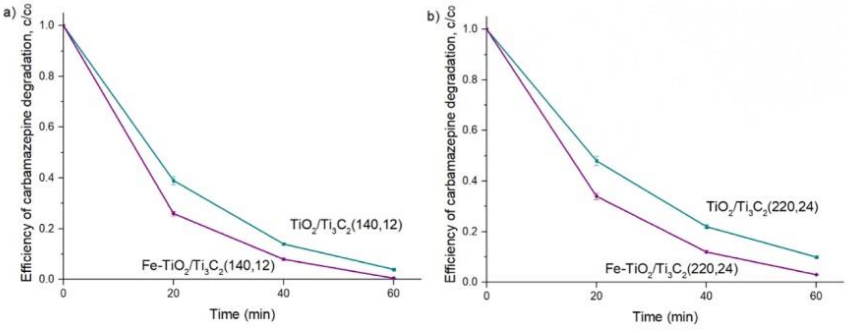

Fig. 15. Carbamazepine degradation for samples a) TiO_2/Ti_3C_2(140,12) and Fe-TiO_2/Ti_3C_2(140,12) b) TiO_2/Ti_3C_2(220,24) and Fe-TiO_2/Ti_3C_2(220,24) within 60 min of irradiation.

were selected for the reusability test. The four subsequent cycles of carbamazepine degradation were performed under UV–Vis irradiation to study the photocatalytic reusability, as presented in Fig. 8S in the Supporting Materials. At the end of each run, the photocatalyst was separated from the reaction suspension by filtration. Afterward, the separated photocatalyst was reused without any treatment. The efficiency of photocatalytic degradation after the 4th cycle decreased by about 15% compared to the 1st cycle. A slight decrease in activity after each irradiation cycle was possibly related to the photocatalyst losses due to the separation process.

Furthermore, the possible changes of photocatalyst's surface due to the deposition of intermediate products were evaluated by analyzing functional groups using the FTIR technique, as shown in Fig. 16. The FTIR spectra of Fe-TiO_2/Ti_3C_2(140,12) composite showed no notable difference between samples before and after the photocatalytic process. For photocatalyst sample before irradiation, only stretching vibrations of Ti-O bonds (620 cm^{-1}) and –OH surface groups (1625 cm^{-1} and 3430 cm^{-1}) were distinguished. In the case of Fe-TiO_2/Ti_3C_2(140,12) sample measured after the photocatalytic process, instead of –OH surface groups, –NH groups were distinguished (broad peak in the region of 3000–3400 cm^{-1}), which probably suggest adsorption of some simple intermediates of carbamazepine degradation on the photocatalyst's surface.

3.3. Mechanism of photocatalytic degradation

To further study the degradation mechanism in the presence of TiO_2-Ti_3C_2 composite, scavengers of the photo-generated electrons, holes and the main reactive oxygen species (·OH, $\cdot O_2^-$) were added into the phenol and carbamazepine solution, respectively. The results are presented in Fig. 17. Introduction of *tert*-butanol as a hydroxyl radicals (·OH) scavenger slightly retarded the photodegradation efficiency. It suggests that ·OH is one of the synergistic active species. Meanwhile, scavenging of superoxide radical anions significantly suppressed both phenol and carbamazepine decomposition rates. Thus, it indicates that $\cdot O_2^-$ plays a crucial role in the photocatalytic degradation mechanism. However, for phenol degradation, the hydroxyl radicals much more contribute to the degradation mechanism, while for carbamazepine superoxide anion radicals.

Furthermore, the addition of $AgNO_3$ as an electron scavenger remarkably increased the effectiveness of organic compounds degradation under UV–Vis light irradiation. Similar phenomena were observed by Samsudin et al. [100] for degradation of methylene blue (MB) with

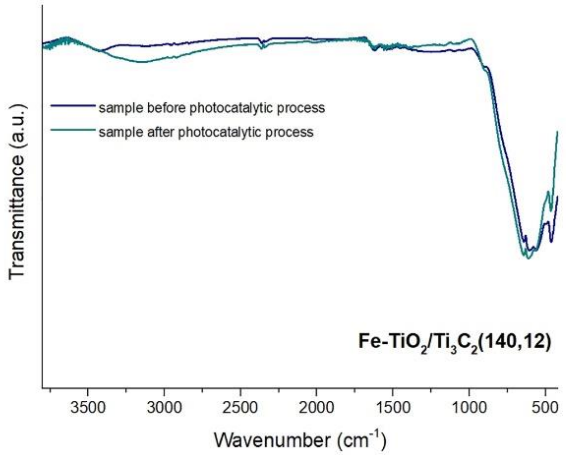

Fig. 16. The FTIR spectra for sample Fe-TiO_2/Ti_3C_2(140,12) measured before and after the photocatalytic process of carbamazepine degradation.

$BiVO_4$ photocatalyst under visible light irradiation. $BiVO_4$ photocatalyst with a higher content of (0 1 0) than (1 1 0) planes was characterized by a higher number of excited electrons located onto (0 1 0) planes. These photoexcited electrons can be easily capped by the electron scavenger leading to inhibition of the electron-hole pairs' recombination. As it was stated by Samsudin et al., when the recombination rate was reduced due to $AgNO_3$, a more significant number of photoexcited electrons may migrate and produce superoxide radicals, which further reacted with MB. Under UV–Vis light irradiation, TiO_2/Ti_3C_2 generates electrons (e^-) and holes (h^+), which participate in the generation of reactive species to decompose contaminants. Scavenging of holes resulted in a decrease in photodegradation, indicating improved electrons separation in the system.

The {0 0 1} facet with a high density of low energy O 2 s states is the only one above the valence band edge of the TiO_2 [101]. Therefore, it is suitable for the oxidation of H_2O to $\cdot OH$. The phenol degradation mechanism mainly proceeded by ·OH attack at *ortho* substitution, resulting in increased *ortho*-hydroxybenzoquinone formation. It can explain a distinct decrease of k for phenol degradation in the presence of TiO_2 with more exposed {1 0 1} facets combined with Ti_3C_2 - sample TiO_2/Ti_3C_2(140,12). Regarding carbamazepine degradation, it could be assumed that ·OH radicals played a minor role during photocatalytic oxidation reaction. The mainly exposed at TiO_2/Ti_3C_2 surface {1 0 1} facet accumulates electrons and promotes oxygen reduction to $\cdot O_2^-$.

Furthermore, superoxide radicals and hydrogen peroxide led to the formation of other reactive oxygen species: hydroxyl radicals (·OH) and singlet oxygen ($^1O_2$). In turn, it resulted in a constant increase in the degradation efficiency of CBZ. Additionally, Fe-species may readily accept excited electrons, thus reducing electron-hole recombination [102].

Fig. 18 shows a graphical presentation of the photocatalyst band edges position and charge transfer during excitation with a light greater than its bandgap energy. The potential of TiO_2/Ti_3C_2(140,12) and TiO_2/Ti_3C_2(220,24) flat band edge position recorded at −0.69 V and −0.49 V vs. Ag/AgCl/0.1 M KCl, respectively was converted to a value of −0.402 V and −0.20 V vs. NHE. The valence band edge location was estimated according to a value of the flat band edge position and bandgap energy and amounted to 2.598 V vs. NHE for TiO_2/Ti_3C_2(220,24) and 2.198 V vs. NHE for TiO_2/Ti_3C_2(140,12). According to the obtained results, TiO_2/Ti_3C_2(220,24) photocatalyst may more effectively oxidize H_2O to hydroxyl radicals, while TiO_2/Ti_3C_2(140,12) and TiO_2/Ti_3C_2(220,24) can also oxidize H_2O to oxygen and reduce oxygen into superoxide radicals.

The band structure of TiO_2/Ti_3C_2 layered composite correlates with significant inhibition of phenol and carbamazepine degradation in the presence of benzoquinone as a scavenger, suggesting that the degradation mechanism involving superoxide radicals played a crucial role. Furthermore, the presented results correspond with the EPR analysis, where the presence of a high number of Ti^{3+} sites and carbon or oxygen vacancies in the crystal lattice of the TiO_2/Ti_3C_2 was proved. These active sites, where photo-generated electrons react with oxygen, producing highly reactive superoxide anion radicals, may explain this mechanism.

A schematic illustration of the photocatalytic mechanism of carbamazepine degradation on Fe-TiO_2/Ti_3C_2 photocatalyst with co-exposed {0 0 1} and {1 0 1} TiO_2 facets was proposed and presented in Fig. 19. The Ti_3C_2 and Fe-species may readily accept excited electrons [102–103], thus reducing electron-hole recombination. However, in the case of iron oxide particles distributed on {0 0 1} TiO_2 facet, there is limited electron transfer from {1 0 1} facet, due to spatial separation, despite the iron oxide CB band position is located below TiO_2 CB position [104]. Accumulated electrons participate in superoxide anion radicals generation from oxygen as a main reactive oxygen species taking part in the photocatalytic oxidation reaction.

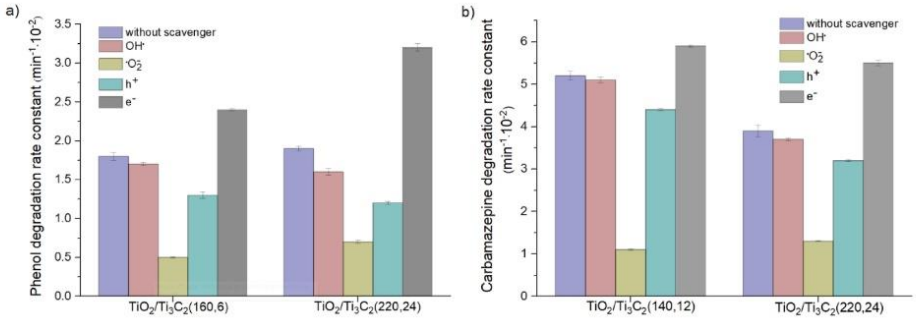

Fig. 17. Degradation rate constant in the presence of scavengers for a) phenol and b) carbamazepine removal.

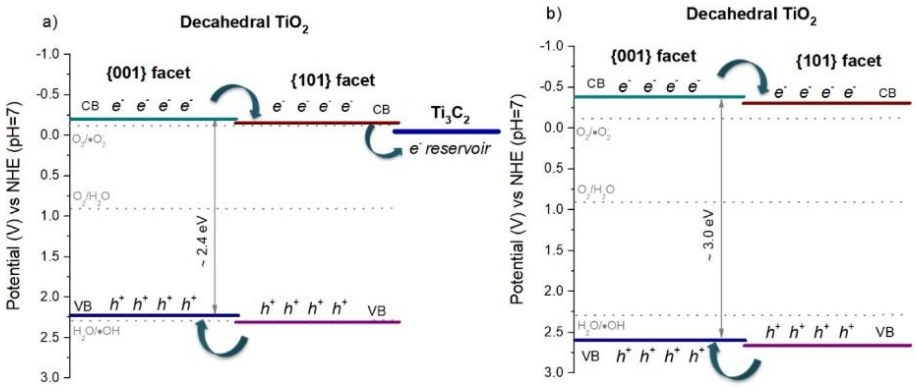

Fig. 18. Schematic representation of a)TiO$_2$/Ti$_3$C$_2$(140,12) and b) TiO$_2$/Ti$_3$C$_2$(220,24) band structure and excitation under UV–Vis light.

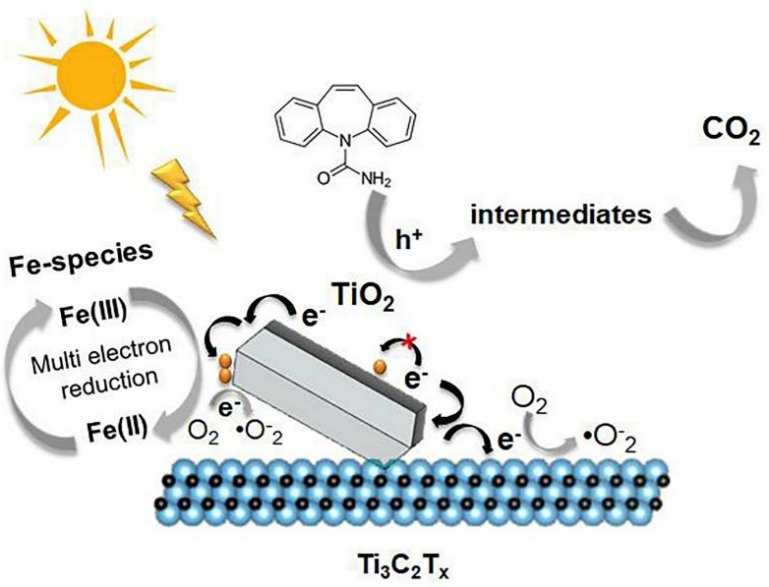

Fig. 19. Schematic illustration of the proposed mechanism of carbamazepine degradation in the presence of Fe-modified TiO$_2$/Ti$_3$C$_2$(140,12) photocatalyst with co-exposed {101} and {001} facets.

4. Conclusions

In summary, TiO_2 nanocomposites were synthesized through the solvothermal method using as a precursor accordion-like MXene compound – $Ti_3C_2T_x$. The controlled oxidation led to the formation of TiO_2 with decahedral morphology and exposed highly active {001} and {101} facets on Ti_3C_2 layer. During the study, the influence of time and temperature on the prepared composites' physicochemical and structural properties was determined. The obtained layered composite photocatalysts were characterized by a narrower bandgap ($E_g < 3$ eV), titanium vacancies (Ti^{3+} centers), carbon and oxygen vacancies. The materials synthesized under more severe conditions (the highest reaction temperature of 220°C and prolonged-time) led to the in-situ formation of TiO_2 DAPs derived from the MXene phase, while milder synthesis conditions (temperature below 200°C) led to preserved TiO_2/Ti_3C_2 structure.

The results of photocatalytic activity of phenol and carbamazepine degradation confirmed that composites prepared at lower temperature and with shorter reaction time, i.e., TiO_2/Ti_3C_2(160,6) and TiO_2/Ti_3C_2(140,12) and photocatalysts synthesized at the higher temperature (above 200 °C) and most prolonged time, i.e., TiO_2/Ti_3C_2(200,24), TiO_2/Ti_3C_2(220,12) and TiO_2/Ti_3C_2(220,24) exhibited the most excellent performance. These findings indicate the promoting effect of $Ti_3C_2T_x$ on TiO_2 activity under UV–Vis irradiation, which may act as a reservoir of photo-generated electrons, thus minimizing the recombination rate of electron-hole pairs. Moreover, the morphological properties of decahedral anatase particles with co-exposed {101} and {001} facets improve photoelectron transfer, which reduces charge carriers recombination.

The most active samples labeled TiO_2/Ti_3C_2(140,12) and TiO_2/Ti_3C_2(220,24) were further modified with iron. The ternary composite Fe-TiO_2/Ti_3C_2(140,12) showed significantly improved carbamazepine photocatalytic degradation with 100% removal after 60 min of UV–Vis irradiation. The increment in donor density and a positive shift of flat band potential of Fe-modified TiO_2/Ti_3C_2 sample compared to neat TiO_2/Ti_3C_2 contributed to superior photo-oxidation efficiency. Moreover, the photocurrent measurements, emission spectroscopy, and luminescence decay analysis confirmed that samples modified with iron species showed more efficient separation of the photoexcited electron-hole pairs and slower decay indicating long charge carrier lifetimes and metastable donor states.

Declaration of Competing Interest

The authors declare that they have no known competing financial interests or personal relationships that could have appeared to influence the work reported in this paper.

Acknowledgments

This research was financially supported by the Polish National Science Centre (grant no. NCN 2018/30/E/ST5/00845). AZJ acknowledges Polish Ministry of Science and Higher Education grant no. 0525/E-359/STYP/13/2018 Scholarships for outstanding young scientists. We also acknowledge Professor Anna Lisowska-Oleksiak from Gdańsk University of Technology for providing measuring equipment and support in electrochemical analysis.

Appendix A. Supplementary data

Supplementary data to this article can be found online at https://doi.org/10.1016/j.cej.2021.130801.

References

[1] The report "European waters - assessment of status and pressures 2018". European Environment Agency, Publications Office of the European Union, Luxembourg, 2018.
[2] A. Bhandari, R.Y. Surampalli, C.D. Adams, P. Champagne, S.K. Ong, R.D. Tyagi, T. Zhang (Eds.), Contaminants of Emerging Environmental Concern, American Society of Civil Engineers, Reston, VA, 2009.
[3] N. Callaghan, M. O'Callaghan, B. Duggan, M. Feely, Carbamazepine as a single drug in the treatment of epilepsy. A prospective study of serum levels and seizure control. J. Neurol. Neurosurg. Psychiatry 41 (10) (1978) 907–912, https://doi.org/10.1136/jnnp.41.10.907.
[4] C. Gadipelly, A. Pérez-González, G.D. Yadav, I. Ortiz, R. Ibáñez, V.K. Rathod, K. V. Marathe, Pharmaceutical Industry Wastewater: Review of the Technologies for Water Treatment and Reuse, Ind. Eng. Chem. Res. 53 (29) (2014) 11571–11592, https://doi.org/10.1021/ie501210j.
[5] Y. Zhang, S.-U. Geißen, C. Gal, Carbamazepine and diclofenac: Removal in wastewater treatment plants and occurrence in water bodies, Chemosphere 73 (8) (2008) 1151–1161, https://doi.org/10.1016/j.chemosphere.2008.07.086.
[6] Benoît Ferrari, N. Paxéus, R.L. Giudice, A. Pollio, J. Garric, Ecotoxicological impact of pharmaceuticals found in treated wastewaters: study of carbamazepine, clofibric acid, and diclofenac, Ecotoxicol. Environ. Saf. 55 (3) (2003) 359–370, https://doi.org/10.1016/S0147-6513(02)00082-9.
[7] S. Wang, J. Wang, Carbamazepine degradation by gamma irradiation coupled to biological treatment, J. Hazard. Mater. 321 (2017) 639–646, https://doi.org/10.1016/j.jhazmat.2016.09.053.
[8] M. Yao, L. Duan, J. Wei, F. Qian, S.W. Hermanowicz, Carbamazepine removal from wastewater and the degradation mechanism in a submerged forward osmotic membrane bioreactor, Bioresour. Technol. 314 (2020) 123732, https://doi.org/10.1016/j.biortech.2020.123732.
[9] M. Chtourou, M. Mallek, M. Dalmau, J. Mamo, E. Santos-Clotas, A.B. Salah, K. Walha, V. Salvadó, H. Monclús, Triclosan, carbamazepine and caffeine removal by activated sludge system focusing on membrane bioreactor, Process Saf. Environ. Prot. 118 (2018) 1–9, https://doi.org/10.1016/j.psep.2018.06.019.
[10] A.G. Pekel, E. Kurtulbaş, İ. Toprakçı, S. Şahin, Menthol-based deep eutectic solvent for the separation of carbamazepine: reactive liquid-liquid extraction, Biomass Convers. Biorefinery (2020), https://doi.org/10.1007/s13399-020-00707-z.
[11] S.K. Alharbi, W.E. Price, J. Kang, T. Fujioka, L.D. Nghiem, Ozonation of carbamazepine, diclofenac, sulfamethoxazole and trimethoprim and formation of major oxidation products, Desalin. Water Treat. 57 (60) (2016) 29340–29351, https://doi.org/10.1080/19443994.2016.1172986.
[12] L. Yang, L. Liang, L. Wang, J. Zhu, S. Gao, X. Xia, Accelerated photocatalytic oxidation of carbamazepine by a novel 3D hierarchical protonated g-C_3N_4/BiOBr heterojunction: Performance and mechanism, Appl. Surf. Sci. 473 (2019) 527–539, https://doi.org/10.1016/j.apsusc.2018.12.180.
[13] Z. Wang, C. Li, K. Domen, Recent developments in heterogeneous photocatalysts for solar driven overall water splitting, Chem. Soc. Rev. 48 (7) (2019) 2109–2125, https://doi.org/10.1039/C8CS00542G.
[14] W. Wang, C. Zhou, Y. Yang, G. Zeng, C. Zhang, Y. Zhou, J. Yang, D. Huang, H. Wang, W. Xiong, X. Li, Y. Fu, Z. Wang, Q. He, M. Jia, H. Luo, Carbon nitride based photocatalysts for solar photocatalytic disinfection, can we go further? Chem. Eng. J. 404 (2021) 126540, https://doi.org/10.1016/j.cej.2020.126540.
[15] W. Zhang, A.R. Mohamed, W. J. Ong, Z Scheme Photocatalytic Systems for Carbon Dioxide Reduction: Where Are We Now? Angew. Chem. Int. Ed. 59 (51) (2020) 22894–22915, https://doi.org/10.1002/anie.201914925.
[16] S. Zhang, B. Li, X. Wang, G. Zhao, B. Hu, Z. Lu, T. Wen, J. Chen, X. Wang, Recent developments of two-dimensional graphene-based composites in visible-light photocatalysis for eliminating persistent organic pollutants from wastewater, Chem. Eng. J. 390 (2020) 124642, https://doi.org/10.1016/j.cej.2020.124642.
[17] R. Qian, H. Zong, J. Schneider, G. Zhou, T. Zhao, Y. Li, J. Yang, D.W. Bahnemann, J.H. Pan, Charge carrier trapping, recombination and transfer during TiO_2 photocatalysis: An overview, Catal. Today 335 (2019) 78–90, https://doi.org/10.1016/j.cattod.2018.10.053.
[18] Wysocka, I., Kowalska, E., Ryl, J., Nowaczyk, G., Zielińska-Jurek, A. Morphology, Photocatalytic and Antimicrobial Properties of TiO2 Modified with Mono- and Bimetallic Copper, Platinum and Silver Nanoparticles. Nanomaterials 9 (2019) 1129. https://doi.org/10.3390/nano9081129.
[19] Y. Li, Y.-L. Li, B. Sa, R. Ahuja, Review of two-dimensional materials for photocatalytic water splitting from a theoretical perspective, Catal. Sci. Technol. 7 (3) (2017) 545–559, https://doi.org/10.1039/C6CY02178F.
[20] B. Luo, G. Liu, L. Wang, Recent advances in 2D materials for photocatalysis, Nanoscale 8 (13) (2016) 6904–6920, https://doi.org/10.1039/C6NR00546B.
[21] X. Chia, M. Pumera, Characteristics and performance of two-dimensional materials for electrocatalysis, Nat. Catal. 1 (12) (2018) 909–921, https://doi.org/10.1038/s41929-018-0181-7.
[22] Buckley, D. J., Black, N.C.G., Castanon, E.G., Melios, C., Hardman, M., Kazakova O. Frontiers of graphene and 2D material based gas sensors for environmental monitoring. 2D Mater. 7 (2020) 032002. https://doi.org/10.1088/2053-1583/ab7bc5.
[23] Y. Zhu, L. Peng, Z. Fang, C. Yan, X. Zhang, G. Yu, Structural Engineering of 2D Nanomaterials for Energy Storage and Catalysis, Adv. Mater. 30 (15) (2018) 1706347, https://doi.org/10.1002/adma.201706347.
[24] C. Du, B.o. Yan, Z. Lin, G. Yang, Enhanced carrier separation and increased electron density in 2D heavily N-doped ZnIn 2 S 4 for photocatalytic hydrogen

production, J. Mater. Chem. A 8 (1) (2020) 207–217, https://doi.org/10.1039/C9TA11318E.
[25] Y. Zhao, S. Zhang, R. Shi, G.I.N. Waterhouse, J. Tang, T. Zhang, Two-dimensional photocatalyst design: A critical review of recent experimental and computational advances, Mater. Today 34 (2020) 78–91, https://doi.org/10.1016/j.mattod.2019.10.022.
[26] S.V.P. Vattikuti, J. Shim, C. Byon, 1D Bi_2S_3 nanorod/2D e WS_2 nanosheet heterojunction photocatalyst for enhanced photocatalytic activity, J. Solid State Chem. 258 (2018) 526–535, https://doi.org/10.1016/j.jssc.2017.11.017.
[27] Y. Yang, X. Li, C. Lu, W. Huang, G C3N4 Nanosheets Coupled with TiO2 Nanosheets as 2D/2D Heterojunction Photocatalysts Toward High Photocatalytic Activity for Hydrogen Production, Catal. Lett. 149 (10) (2019) 2930–2939, https://doi.org/10.1007/s10562-019-02805-8.
[28] Y. Li, P. Zhang, D. Wan, C. Xue, J. Zhao, G. Shao, Direct evidence of 2D/1D heterojunction enhancement on photocatalytic activity through assembling MoS_2 nanosheets onto super long TiO_2 nanofibers, Appl. Surf. Sci. 504 (2020) 144361, https://doi.org/10.1016/j.apsusc.2019.144361.
[29] H. Fan, H. Zhou, W. Li, S. Gu, G. Zhou, Facile fabrication of 2D/2D step-scheme $In_2S_3/Bi_2O_2CO_3$ heterojunction towards enhanced photocatalytic activity, Appl. Surf. Sci. 504 (2020) 144351, https://doi.org/10.1016/j.apsusc.2019.144351.
[30] K. Hantanasirisakul, Y. Gogotsi, Electronic and Optical Properties of 2D Transition Metal Carbides and Nitrides (MXenes), Adv. Mater. 30 (52) (2018) 1804779, https://doi.org/10.1002/adma.201804779.
[31] C. Wei, H. Fei, Y. Tian, Y. An, H. Guo, J. Feng, Y. Qian, Isotropic Li nucleation and growth achieved by an amorphous liquid metal nucleation seed on MXene framework for dendrite free Li metal anode, Energy Storage Mater. 26 (2020) 223–233, https://doi.org/10.1016/j.ensm.2020.01.005.
[32] Y. Tian, Y. An, C. Wei, Y. Tao, Y. Zhang, H. Jiang, L. Tan, J. Feng, Y. Qian, Stable and dendrite-free lithium metal anodes enabled by carbon paper incorporated with ultrafine lithiophilic TiO2 derived from MXene and carbon dioxide, Chem. Eng. J. 406 (2021) 126836, https://doi.org/10.1016/j.cej.2020.126836.
[33] H.A. Tahini, X. Tan, S.C. Smith, The origin of low workfunctions in OH terminated MXenes, Nanoscale 9 (21) (2017) 7016–7020, https://doi.org/10.1039/C7NR01601H.
[34] R. Xiao, C. Zhao, Z. Zou, Z. Chen, L. Tian, H. Xu, H. Tang, Q. Liu, Z. Lin, X. Yang, In situ fabrication of 1D CdS nanorod/2D Ti_3C_2 MXene nanosheet Schottky heterojunction toward enhanced photocatalytic hydrogen evolution, Appl. Catal. B 268 (2020) 118382, https://doi.org/10.1016/j.apcatb.2019.118382.
[35] S. Cao, B. Shen, T. Tong, J. Fu, J. Yu, 2D/2D Heterojunction of Ultrathin MXene/Bi 2 WO 6 Nanosheets for Improved Photocatalytic CO 2 Reduction, Adv. Funct. Mater. 28 (21) (2018) 1800136, https://doi.org/10.1002/adfm.201800136.
[36] X. Xie, N. Zhang, Z.-R. Tang, M. Anpo, Y.-J. Xu, Ti3C2Tx MXene as a Janus cocatalyst for concurrent promoted photoactivity and inhibited photocorrosion, Appl. Catal. B 237 (2018) 43–49, https://doi.org/10.1016/j.apcatb.2018.05.070.
[37] L. Tie, S. Yang, C. Yu, H. Chen, Y. Liu, S. Dong, J. Sun, J. Sun, In situ decoration of ZnS nanoparticles with Ti_3C_2 MXene nanosheets for efficient photocatalytic hydrogen evolution, J. Colloid Interface Sci. 545 (2019) 63–70, https://doi.org/10.1016/j.jcis.2019.03.014.
[38] T. Cai, L. Wang, Y. Liu, S. Zhang, W. Dong, H. Chen, X. Yi, J. Yuan, X. Xia, C. Liu, S. Luo, Ag_3PO_4/Ti_3C_2 MXene interface materials as a Schottky catalyst with enhanced photocatalytic activities and anti-photocorrosion performance, Appl. Catal. B 239 (2018) 545–554, https://doi.org/10.1016/j.apcatb.2018.08.053.
[39] Y. Sun, D.i. Jin, Y. Sun, X. Meng, Y.u. Gao, Y. Dall'Agnese, G. Chen, X.-F. Wang, g-C 3 N 4 /Ti 3 C 2 T x (MXenes) composite with oxidized surface groups for efficient photocatalytic hydrogen evolution, J. Mater. Chem. A 6 (19) (2018) 9124–9131, https://doi.org/10.1039/C8TA02706D.
[40] Z. Zeng, Y. Yan, J. Chen, P. Zan, Q. Tian, P. Chen, Boosting the Photocatalytic Ability of Cu 2 O Nanowires for CO 2 Conversion by MXene Quantum Dots, Adv. Funct. Mater. 29 (2) (2019) 1806500, https://doi.org/10.1002/adfm.201806500.
[41] C. Liu, Q. Xu, Q. Zhang, Y. Zhu, M. Ji, Z. Tong, W. Hou, Y.u. Zhang, J. Xu, Layered BiOBr/Ti_3C_2 MXene composite with improved visible-light photocatalytic activity, J. Mater. Sci. 54 (3) (2019) 2458–2471, https://doi.org/10.1007/s10853-018-2990-0.
[42] H. Zhang, M. Li, J. Cao, Q. Tang, P. Kang, C. Zhu, M. Ma, 2D a Fe_2O_3 doped Ti_3C_2 MXene composite with enhanced visible light photocatalytic activity for degradation of Rhodamine B, Ceram. Int. 44 (16) (2018) 19958–19962, https://doi.org/10.1016/j.ceramint.2018.07.262.
[43] J. Low, L. Zhang, T. Tong, B. Shen, J. Yu, TiO_2/MXene Ti_3C_2 composite with excellent photocatalytic CO_2 reduction activity, J. Catal. 361 (2018) 255–266, https://doi.org/10.1016/j.jcat.2018.03.009.
[44] J. Yin, F. Zhan, T. Jiao, W. Wang, G. Zhang, J. Jiao, G. Jiang, Q. Zhang, J. Gu, Q. Peng, Facile preparation of self-assembled MXene@Au@CdS nanocomposite with enhanced photocatalytic hydrogen production activity自组装纳米复合材料MXene@Au@CdS的制备及其光催化制氢活性, Sci. China Mater. 63 (11) (2020) 2228–2238, https://doi.org/10.1007/s40843-020-1299-4.
[45] K. Li, T. Jiao, R. Xing, G. Zou, J. Zhou, L. Zhang, Q. Peng, Fabrication of tunable hierarchical MXene@AuNPs nanocomposites constructed by self-reduction reactions with enhanced catalytic performances自还原反应制备可调层状MXene@AuNPs复合材料以提高催化性能, Sci. China Mater. 61 (5) (2018) 728–736, https://doi.org/10.1007/s40843-017-9196-8.
[46] X. Huang, R. Wang, T. Jiao, G. Zou, F. Zhan, J. Yin, L. Zhang, J. Zhou, Q. Peng, Facile Preparation of Hierarchical AgNP Loaded MXene/Fe 3 O 4 /Polymer Nanocomposites by Electrospinning with Enhanced Catalytic Performance for Wastewater Treatment, ACS Omega 4 (1) (2019) 1897–1906, https://doi.org/10.1021/acsomega.8b03615.
[47] J. Yin, B. Ge, T. Jiao, Z. Qin, M. Yu, L. Zhang, Q. Zhang, Q. Peng, Self-Assembled Sandwich-like MXene-Derived Composites as Highly Efficient and Sustainable Catalysts for Wastewater Treatment, Langmuir 37 (3) (2021) 1267–1278, https://doi.org/10.1021/acs.langmuir.0c03297.s001.
[48] K. Li, T. Jiao, R. Xing, G. Zou, Q. Zhao, J. Zhou, L. Zhang, Q. Peng, Fabrication of hierarchical MXene-based AuNPs-containing core–shell nanocomposites for high efficient catalysts, Green Energy Environ. 3 (2) (2018) 147–155, https://doi.org/10.1016/j.gee.2017.11.004.
[49] M.A. Iqbal, S.I. Ali, F. Amin, A. Tariq, M.Z. Iqbal, S. Rizwan, La- and Mn-Codoped Bismuth Ferrite/Ti 3 C 2 MXene Composites for Efficient Photocatalytic Degradation of Congo Red Dye, ACS Omega 4 (5) (2019) 8661–8668, https://doi.org/10.1021/acsomega.9b00493.
[50] C.e. Cui, R. Guo, H. Xiao, E. Ren, Q. Song, C. Xiang, X. Lai, J. Lan, S. Jiang, Bi_2WO_6/Nb_2CT_x MXene hybrid nanosheets with enhanced visible-light-driven photocatalytic activity for organic pollutants degradation, Appl. Surf. Sci. 505 (2020) 144595, https://doi.org/10.1016/j.apsusc.2019.144595.
[51] Y. Li, Z. Yin, G. Ji, Z. Liang, Y. Xue, Y. Guo, J. Tian, X. Wang, H. Cui, 2D/2D/2D heterojunction of Ti_3C_2 MXene/MoS_2 nanosheets/TiO_2 nanosheets with exposed (001) facets toward enhanced photocatalytic hydrogen production activity, Appl. Catal. B 246 (2019) 12–20, https://doi.org/10.1016/j.apcatb.2019.01.051.
[52] X. An, W. Wang, J. Wang, H. Duan, J. Shi, X. Yu, The synergetic effects of Ti 3 C 2 MXene and Pt as co-catalysts for highly efficient photocatalytic hydrogen evolution over g-C 3 N 4, PCCP 20 (16) (2018) 11405–11411, https://doi.org/10.1039/C8CP01123K.
[53] J. Ran, G. Gao, F. T. Li, T. Y. Ma, A. Du, S. Z. Qiao, Ti_3C_2 MXene co-catalyst on metal sulfide photo-absorbers for enhanced visible-light photocatalytic hydrogen production, Nat. Commun. 8 (1) (2017), https://doi.org/10.1038/ncomms13907.
[54] M. Kowalkińska, S. Dudziak, J. Karczewski, J. Ryl, G. Trykowski, A. Zielińska-Jurek, Facet effect of TiO_2 nanostructures from $TiOF_2$ and their photocatalytic activity, Chem. Eng. J. 404 (2021) 126493, https://doi.org/10.1016/j.cej.2020.126493.
[55] J. Wang, B. Liu, K. Nakata, Effects of crystallinity, {001}/{101} ratio, and Au decoration on the photocatalytic activity of anatase TiO_2 crystals, Chin. J. Catal. 40 (3) (2019) 403–412, https://doi.org/10.1016/S1872-2067(18)63174-2.
[56] J. Yu, J. Low, W. Xiao, P. Zhou, M. Jaroniec, Enhanced Photocatalytic CO 2 -Reduction Activity of Anatase TiO 2 by Coexposed {001} and {101} Facets, J. Am. Chem. Soc. 136 (25) (2014) 8839–8842, https://doi.org/10.1021/ja5044787.
[57] Y. Cao, Q. Deng, Z. Liu, D. Shen, T. Wang, Q. Huang, S. Du, N. Jiang, C.-T. Lin, J. Yu, Enhanced thermal properties of poly(vinylidene fluoride) composites with ultrathin nanosheets of MXene, RSC Adv. 7 (33) (2017) 20494–20501, https://doi.org/10.1039/C7RA00184C.
[58] M. Naguib, M. Kurtoglu, V. Presser, J. Lu, J. Niu, M. Heon, L. Hultman, Y. Gogotsi, M.W. Barsoum, Two-Dimensional Nanocrystals Produced by Exfoliation of Ti_3AlC_2, Adv. Mater. 23 (37) (2011) 4248–4253, https://doi.org/10.1002/adma.201102306.
[59] Z. Wei, M. Janczarek, M. Endo, K. Wang, A. Balčytis, A. Nitta, M.G. Méndez-Medrano, C. Colbeau-Justin, S. Juodkazis, B. Ohtani, E. Kowalska, Noble metal-modified faceted anatase titania photocatalysts: Octahedron versus decahedron, Appl. Catal. B 237 (2018) 574–587, https://doi.org/10.1016/j.apcatb.2018.06.027.
[60] M. Shen, L. Zhang, M. Wang, J. Tian, X. Jin, L. Guo, L. Wang, J. Shi, Carbon-vacancy modified graphitic carbon nitride: enhanced CO 2 photocatalytic reduction performance and mechanism probing, J. Mater. Chem. A 7 (4) (2019) 1556–1563, https://doi.org/10.1039/C8TA09302D.
[61] C. Peng, H. Wang, H. Yu, F. Peng, (111) TiO 2-x /Ti 3 C 2 : Synergy of active facets, interfacial charge transfer and Ti 3+ doping for enhance photocatalytic activity, Mater. Res. Bull. 89 (2017) 16–25, https://doi.org/10.1016/j.materresbull.2016.12.049.
[62] P.K. Kalambate, Dhanjai, A. Sinha, Y. Li, Y. Shen, Y. Huang, An electrochemical sensor for ifosfamide, acetaminophen, domperidone, and sumatriptan based on self-assembled MXene/MWCNT/chitosan nanocomposite thin film, Microchim. Acta 187 (7) (2020), https://doi.org/10.1007/s00604-020-04366-9.
[63] F. Kong, X. He, Q. Liu, X. Qi, Y. Zheng, R. Wang, Y. Bai, Improving the electrochemical properties of MXene Ti_3C_2 multilayer for Li-ion batteries by vacuum calcination, Electrochim. Acta 265 (2018) 140–150, https://doi.org/10.1016/j.electacta.2018.01.196.
[64] X. Zhang, J.F. Zhang, S.X. Yang, H.Y. Cao, H.J. Huang, W. Jiang, Electrocatalytic Performance of Palladium Nanoparticle Supported by Two-dimensional Titanium Carbide-CNT Composites, J. Inorg. Mater. 33 (2018) 206–212.
[65] Y. Q. Cao, T. Q. Zi, X. R. Zhao, C. Liu, Q. Ren, J. B. Fang, W. M. Li, A. D. Li, Enhanced visible light photocatalytic activity of Fe_2O_3 modified TiO_2 prepared by atomic layer deposition, Sci. Rep. 10 (1) (2020), https://doi.org/10.1038/s41598-020-70352-z.
[66] U. Balachandran, N.G. Eror, Raman spectra of titanium dioxide, J. Solid State Chem. 42 (3) (1982) 276–282, https://doi.org/10.1016/0022-4596(82)90006-8.
[67] C.Y. Xu, P.X. Zhang, L. Yan, Blue shift of Raman peak from coated TiO_2 nanoparticles, J. Raman Spectrosc. 32 (10) (2001) 862–865, https://doi.org/10.1002/jrs.773.
[68] W. Vallejo, A. Rueda, C. Díaz Uribe, C. Grande, P. Quintana, Photocatalytic activity of graphene oxide–TiO 2 thin films sensitized by natural dyes extracted from Bactris guineensis, R. Soc. Open Sci. 6 (3) (2019) 181824, https://doi.org/10.1098/rsos.181824.
[69] S. Mohajernia, P. Andryskova, G. Zoppellaro, S. Hejazi, S. Kment, R. Zboril, J. Schmidt, P. Schmuki, Influence of Ti 3+ defect-type on heterogeneous

photocatalytic H 2 evolution activity of TiO 2, J. Mater. Chem. A 8 (3) (2020) 1432–1442, https://doi.org/10.1039/C9TA10855F.
[70] Y.i. Zhang, J. Di, P. Ding, J. Zhao, K. Gu, X. Chen, C. Yan, S. Yin, J. Xia, H. Li, Ultrathin g-C_3N_4 with enriched surface carbon vacancies enables highly efficient photocatalytic nitrogen fixation, J. Colloid Interface Sci. 553 (2019) 530–539, https://doi.org/10.1016/j.jcis.2019.06.012.
[71] X. Liang, G. Wang, X. Dong, G. Wang, H. Ma, X. Zhang, Graphitic Carbon Nitride with Carbon Vacancies for Photocatalytic Degradation of Bisphenol A, ACS Appl. Nano Mater. 2 (1) (2019) 517–524, https://doi.org/10.1021/acsanm.8b02089.
[72] Y. Li, W. Ho, K. Lv, B. Zhu, S.C. Lee, Carbon vacancy-induced enhancement of the visible light-driven photocatalytic oxidation of NO over g-C 3 N 4 nanosheets, Appl. Surf. Sci. 430 (2018) 380–389, https://doi.org/10.1016/j.apsusc.2017.06.054.
[73] H. Hirakawa, M. Hashimoto, Y. Shiraishi, T. Hirai, Photocatalytic Conversion of Nitrogen to Ammonia with Water on Surface Oxygen Vacancies of Titanium Dioxide, J. Am. Chem. Soc. 139 (31) (2017) 10929–10936, https://doi.org/10.1021/jacs.7b06634.s001.
[74] Y. Xu, S. Wu, P. Wan, J. Sun, Z.D. Hood, Introducing Ti 3+ defects based on lattice distortion for enhanced visible light photoreactivity in TiO 2 microspheres, RSC Adv. 7 (52) (2017) 32461–32467, https://doi.org/10.1039/C7RA04885H.
[75] F.J. Knorr, C.C. Mercado, J.L. McHale, Trap-State Distributions and Carrier Transport in Pure and Mixed-Phase TiO 2 : Influence of Contacting Solvent and Interphasial Electron Transfer, J. Phys. Chem. C 112 (33) (2008) 12786–12794, https://doi.org/10.1021/jp8039934.
[76] X. Wang, S. Shen, Z. Feng, C. Li, Time resolved photoluminescence of anatase/rutile TiO2 phase junction revealing charge separation dynamics, Chin. J. Catal. 37 (12) (2016) 2059–2068, https://doi.org/10.1016/S1872-2067(16)62574-3.
[77] K. Fujihara, S. Izumi, T. Ohno, M. Matsumura, Time-resolved photoluminescence of particulate TiO2 photocatalysts suspended in aqueous solutions, J. Photochem. Photobiol., A 132 (1-2) (2000) 99–104, https://doi.org/10.1016/S1010-6030(00)00204-5.
[78] A. Saha, A. Moya, A. Kahnt, D. Iglesias, S. Marchesan, R. Wannemacher, M. Prato, J.J. Vilatela, D.M. Guldi, Interfacial charge transfer in functionalized multi-walled carbon nanotube@TiO 2 nanofibres, Nanoscale 9 (23) (2017) 7911–7921, https://doi.org/10.1039/C7NR00759K.
[79] R. Brüninghoff, K. Wenderich, J.P. Korterik, B.T. Mei, G. Mul, A. Huijser, Time-Dependent Photoluminescence of Nanostructured Anatase TiO 2 and the Role of Bulk and Surface Processes, J. Phys. Chem. C 123 (43) (2019) 26653–26661, https://doi.org/10.1021/acs.jpcc.9b06890.s001.
[80] H. Cui, W. Zhao, C. Yang, H. Yin, T. Lin, Y. Shan, Y. Xie, H. Gu, F. Huang, Black TiO 2 nanotube arrays for high efficiency photoelectrochemical water splitting, J. Mater. Chem. A 2 (23) (2014) 8612–8616, https://doi.org/10.1039/C4TA00176A.
[81] P. Xu, T.J. Milstein, T.E. Mallouk, Flat-Band Potentials of Molecularly Thin Metal Oxide Nanosheets, ACS Appl. Mater. Interfaces 8 (18) (2016) 11539–11547, https://doi.org/10.1021/acsami.6b02901.s001.
[82] B.M. Bresolin, N.O. Balayeva, L.I. Granone, R. Dillert, D.W. Bahnemann, M. Sillanpää, Anchoring lead-free halide $Cs_3Bi_2I_9$ perovskite on UV100–TiO_2 for enhanced photocatalytic performance, Sol. Energy Mater. Sol. Cells 204 (2020) 1–11, https://doi.org/10.1016/j.solmat.2019.110214.
[83] Bisquert, J. Nanostructured energy devices: equilibrium concepts and kinetics. CRC Press, Boca Raton, 2014. https://doi.org/10.1201/b17613.
[84] Y. Li, D. Zhang, X. Feng, Y. Liao, Q. Wen, Q. Xiang, Truncated octahedral bipyramidal TiO2/MXen Ti3C2 hybrids with enhanced photocatalytic H2 production activity, Nanoscale Adv. 1 (2019) 1812–1818, https://doi.org/10.1039/C9NA00023B.
[85] Q. Liu, X. Tan, S. Wang, F. Ma, H. Znad, Z. Shen, L. Liu, S. Liu, MXene as a non-metal charge mediator in 2D layered CdS@Ti 3 C 2 @TiO 2 composites with superior Z-scheme visible light-driven photocatalytic activity, Environ. Sci. Nano 6 (10) (2019) 3158–3169, https://doi.org/10.1039/C9EN00567F.
[86] X. Bao, H. Li, Z. Wang, F. Tong, M.u. Liu, Z. Zheng, P. Wang, H. Cheng, Y. Liu, Y. Dai, Y. Fan, Z. Li, B. Huang, TiO2/Ti3C2 as an efficient photocatalyst for selective oxidation of benzyl alcohol to benzaldehyde, Appl. Catal. B 286 (2021) 119885, https://doi.org/10.1016/j.apcatb.2021.119885.
[87] Y. Liu, H. Zeng, Y. Chai, R. Yuan, H. Liu, Ti 3 C 2 /BiVO 4 Schottky junction as a signal indicator for ultrasensitive photoelectrochemical detection of VEGF 165, Chem. Commun. 55 (91) (2019) 13729–13732, https://doi.org/10.1039/C9CC07108C.
[88] Y. Zhuang, Y. Liu, X. Meng, Fabrication of TiO2 nanofibers/MXene Ti3C2 nanocomposites for photocatalytic H2 evolution by electrostatic self-assembly, Appl. Surf. Sci. 496 (2019) 143647, https://doi.org/10.1016/j.apsusc.2019.143647.
[89] M. Kaneko, Anatase TiO_2 adsorption on 3-aminopropyltrimethoxysilane-modified Al or glass surfaces, Heliyon 5 (2019), e01734, https://doi.org/10.1016/j.heliyon.2019.e0173.
[90] Y. Fu, F. Ding, J. Chen, M. Liu, X. Zhang, C. Du, S. Si, Label-free and near-zero-background-noise photoelectrochemical assay of methyltransferase activity based on a Bi 2 S 3 /Ti 3 C 2 Schottky junction, Chem. Commun. 56 (43) (2020) 5799–5802, https://doi.org/10.1039/D0CC01835J.
[91] M. Shah, Y. Zhu, X. Fan, J. Zhao, Y. Li, S. Asim, C. Wang, Facile Synthesis of Defective TiO 2–x Nanocrystals with High Surface Area and Tailoring Bandgap for Visible-light Photocatalysis, Sci. Rep. 5 (2015) 1–8, https://doi.org/10.1038/srep15804.
[92] C. Randorn, J.T.S. Irvine, Synthesis and visible light photoactivity of a high temperature stable yellow TiO2 photocatalyst, J. Mater. Chem. 20 (39) (2010) 8700, https://doi.org/10.1039/c0jm01370f.
[93] L.i. Ding, Y. Wei, Y. Wang, H. Chen, J. Caro, H. Wang, A Two-Dimensional Lamellar Membrane: MXene Nanosheet Stacks, Angew. Chem. Int. Ed. 56 (7) (2017) 1825–1829, https://doi.org/10.1002/anie.201609306.
[94] M. Kosmulski, P. Próchniak, J.B. Rosenholm, Letter: The IEP of Carbonate Free Neodymium(III) Oxide, J. Dispersion Sci. Technol. 30 (5) (2009) 589–591, https://doi.org/10.1080/01932690902766319.
[95] G. Serdaroğlu, J.V. Ortiz, Ab Initio Calculations on some Antiepileptic Drugs such as Phenytoin, Phenbarbital, Ethosuximide and Carbamazepine, Struct. Chem. 28 (4) (2017) 957–964, https://doi.org/10.1007/s11224-016-0898-3.
[96] X. Xiao, S. Tu, M. Lu, H. Zhong, C. Zheng, X. Zuo, J. Nan, Discussion on the reaction mechanism of the photocatalytic degradation of organic contaminants from a viewpoint of semiconductor photo-induced electrocatalysis, Appl. Catal. B 198 (2016) 124–132, https://doi.org/10.1016/j.apcatb.2016.05.042.
[97] A. Shahzad, K. Rasool, M. Nawaz, W. Miran, J. Jang, M. Moztahida, K. A. Mahmoud, D.S. Lee, Heterostructural $TiO_2/Ti_3C_2T_x$ (MXene) for photocatalytic degradation of antiepileptic drug carbamazepine, Chem. Eng. J. 349 (2018) 748–755, https://doi.org/10.1016/j.cej.2018.05.148.
[98] H. Tada, Q. Jin, H. Nishijima, H. Yamamoto, M. Fujishima, S.-I. Okuoka, T. Hattori, Y. Sumida, H. Kobayashi, Titanium(IV) Dioxide Surface Modified with Iron Oxide as a Visible Light Photocatalyst, Angew. Chem. Int. Ed. 50 (15) (2011) 3501–3505, https://doi.org/10.1002/anie.201007869.
[99] E. Donner, T. Kosjek, S. Qualmann, K.O. Kusk, E. Heath, D.M. Revitt, A. Ledin, H. R. Andersen, Ecotoxicity of carbamazepine and its UV photolysis transformation products, Sci. Total Environ. 443 (2013) 870–876, https://doi.org/10.1016/j.scitotenv.2012.11.059.
[100] M. Fakhrul Ridhwan Samsudin, L. Tau Siang, S. Sufian, R. Bashiri, N. Muti Mohamed, R. Mahirah Ramli, Exploring the role of electron hole scavengers on optimizing the photocatalytic performance of $BiVO_4$, Mater. Today:. Proc. 5 (10) (2018) 21703–21709, https://doi.org/10.1016/j.matpr.2018.07.022.
[101] K. Zhao, Q.Q. Liu, X.C. Wang, Z. Deng, Y.X. Lv, J.L. Zhu, F.Y. Li, C.Q. Jin, Superconductivity above 33 K in (Ca 1 − x Na x)Fe 2 As 2, J. Phys.: Condens. Matter 22 (22) (2010) 222203, https://doi.org/10.1088/0953-8984/22/22/222203.
[102] H. Baniamerian, M. Safavi, M. Alvarado-Morales, P. Tsapekos, I. Angelidaki, S. Shokrollahzadeh, Photocatalytic inactivation of Vibrio fischeri using Fe2O3-TiO2 based nanoparticles, Environ. Res. 166 (2018) 497–506, https://doi.org/10.1016/j.envres.2018.06.011.
[103] G. Huang, S. Li, L. Liu, L. Zhu, Q. Wang, Ti3C2 MXene-modified Bi2WO6 nanoplates for efficient photodegradation of volatile organic compounds, Appl. Surf. Sci. 503 (2020) 144183, https://doi.org/10.1016/j.apsusc.2019.144183.
[104] C. Liu, R. Tong, Z. Xu, Q. Kuang, Z. Xie, L. Zheng, RSC Adv. 6 (2016) 29794, https://doi.org/10.1039/C6RA04552A.

Supporting Information

Enhanced photocatalytic activity of accordion-like layered Ti_3C_2 (MXene) coupled with Fe-modified decahedral anatase particles exposing {1 0 1} and {0 0 1} facets

Anna Grzegórska[1], Paweł Głuchowski[2], Jakub Karczewski[3], Jacek Ryl[3], Izabela Wysocka[1], Katarzyna Siuzdak[4], Grzegorz Trykowski[5], Katarzyna Grochowska[4], Anna Zielińska-Jurek[1]**

[1] Department of Process Engineering and Chemical Technology, Faculty of Chemistry, Gdańsk University of Technology, G. Narutowicza 11/12, 80-233 Gdansk, Poland

[2] Institute of Low Temperature and Structural Research, Polish Academy of Sciences, Okólna 2, 50-422 Wrocław, Poland

[3] Institute of Nanotechnology and Materials Engineering, Faculty of Applied Physics and Mathematics, Gdańsk University of Technology, G. Narutowicza 11/12, 80-233 Gdańsk, Poland

[4] Centre for Plasma and Laser Engineering, The Szewalski Institute of Fluid-Flow Machinery, Polish Academy of Science, Fiszera 14, 80-231 Gdańsk, Poland

[5] Faculty of Chemistry, Nicolaus Copernicus University, Gagarina 7, 87-100 Toruń, Poland

* Corresponding authors: annjurek@pg.edu.pl, anna.grzegorska@pg.edu.pl

3. Results and discussion

3.1 Characterization of TiO_2/Ti_3C_2 and Fe-modified TiO_2/Ti_3C_2 photocatalysts

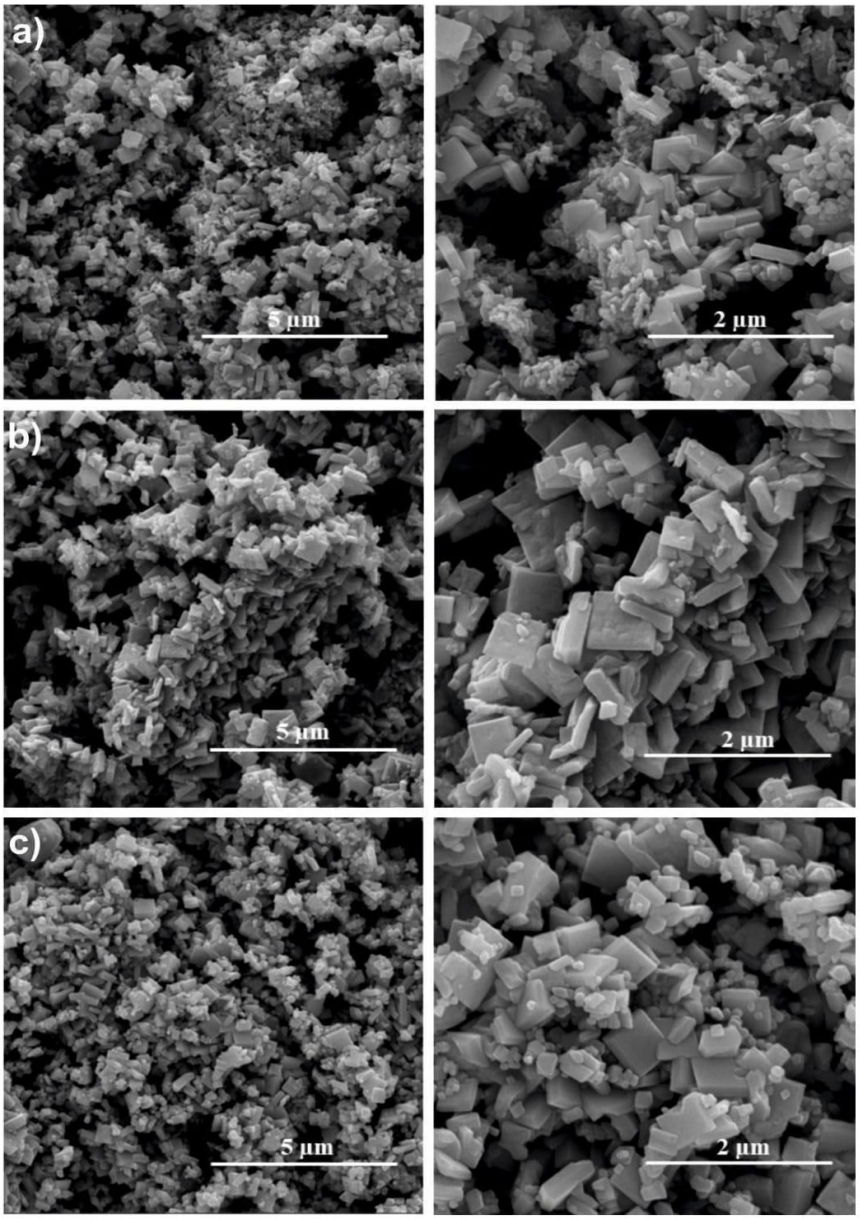

Figure 1S. SEM images of a) TiO_2/Ti_3C_2(220,24), b) TiO_2/Ti_3C_2(220,12), and c) TiO_2/Ti_3C_2(220,24)

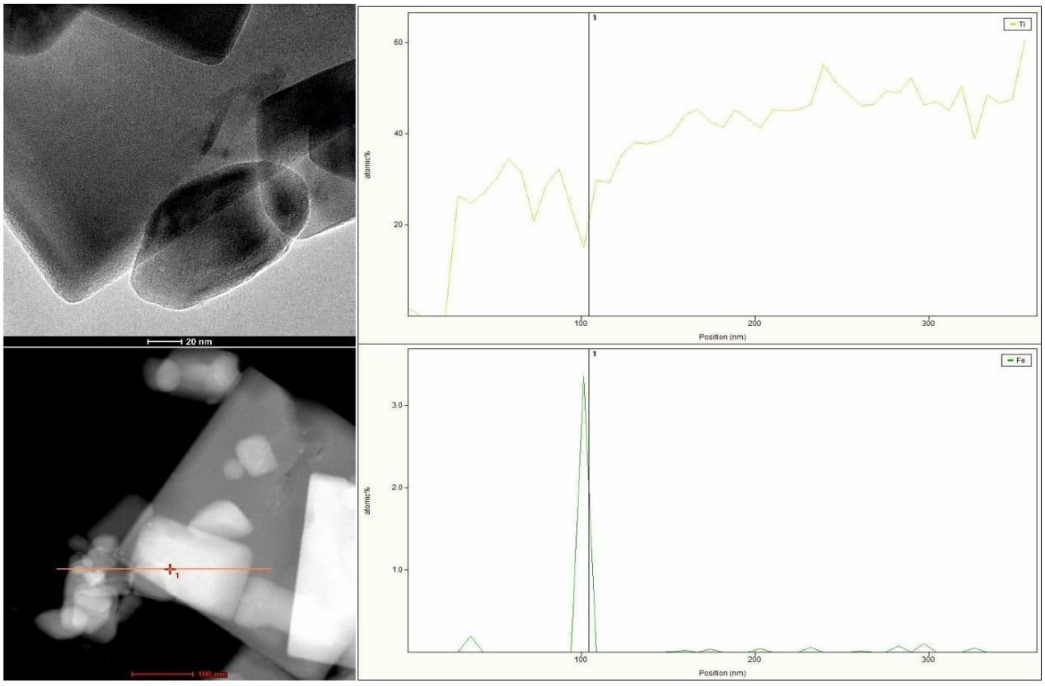

Figure 2S. The STEM images for sample Fe-TiO_2-Ti_3C_2(220,24) and the corresponding EDS line scan of iron.

3

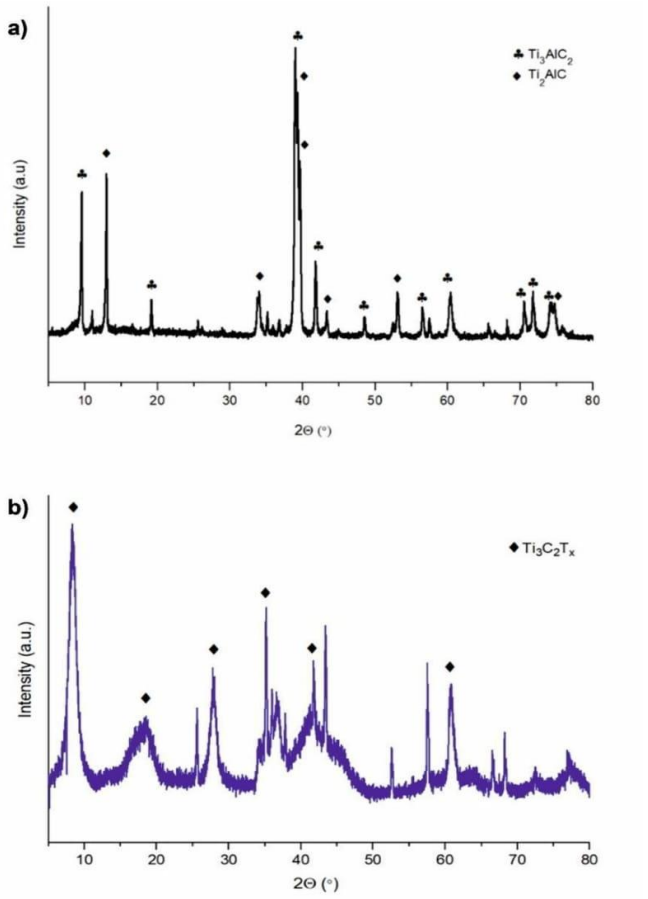

Figure 3S. XRD patterns of raw Ti_3AlC_2-Ti_2AlC (a) and $Ti_3C_2T_x$ after HF treatment (b).

Table 1S. Crystallinity (%) of selected TiO_2-Ti_3C_2 layered composites.

Sample label	Synthesis conditions		Crystalline phase content
	temperature (°C)	time (h)	(%)

4

Ti_3C_2 -TiO_2(140,12)	140	12	48.9
Ti_3C_2 -TiO_2 (160,6)	160	6	48.6
Ti_3C_2 -TiO_2(200,24)	200	24	63.6
Ti_3C_2-TiO_2 (220,12)	220	12	61.7
Ti_3C_2-TiO_2 (220,24)	220	24	65.7

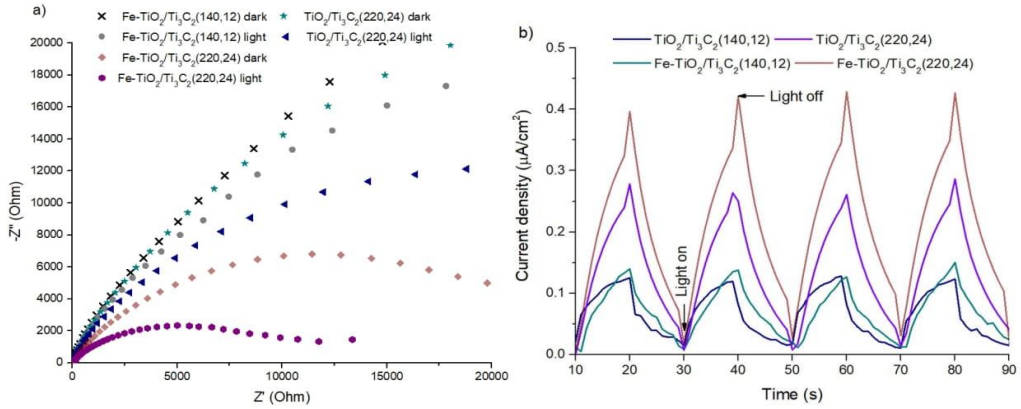

Figure 4S. (A) Nyquist plot for measured in the dark and under irradiation and (B) photocurrent response for TiO_2/Ti_3C_2 and Fe-TiO_2/Ti_3C_2 photocatalysts

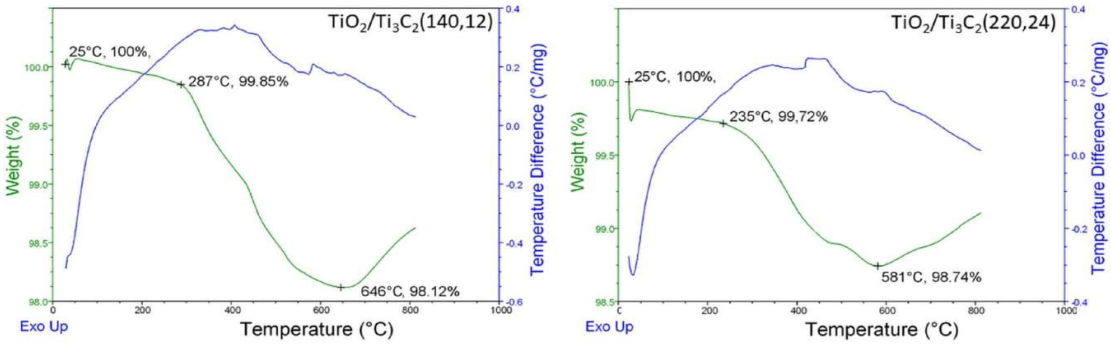

Figure 5S. TGA thermograms of selected TiO_2/Ti_3C_2 composites.

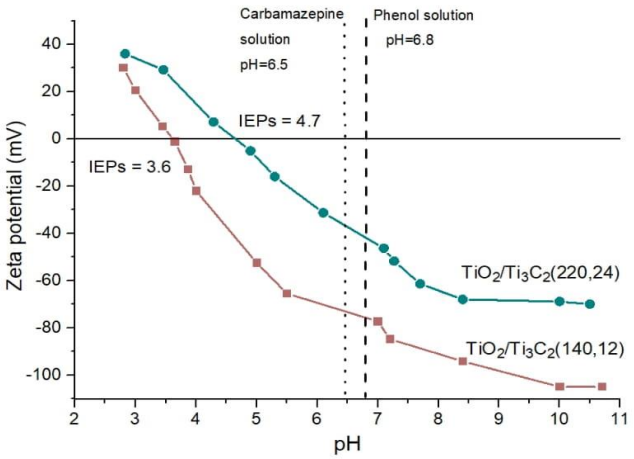

Figure 6S. Zeta potential plots versus pH for samples TiO_2/Ti_3C_2(140,12) and TiO_2/Ti_3C_2(220,24).

3.2 Photocatalytic activity in reaction of phenol and carbamazepine degradation

Table 2S. The concentration of *ortho*-hydroxyphenol and *para*-hydroxyphenol after 20, 40, and 60 minutes of irradiation.

Sample label	*Ortho*-hydroxyphenol			*Para*-hydroxyphenol		
	20 min. ($mg \cdot dm^{-3}$)	40 min. ($mg \cdot dm^{-3}$)	60 min. ($mg \cdot dm^{-3}$)	20 min. ($mg \cdot dm^{-3}$)	40 min. ($mg \cdot dm^{-3}$)	60 min. ($mg \cdot dm^{-3}$)
TiO_2/Ti_3C_2(140,6)	0.56	0.98	1.34	0.73	1.21	1.89
TiO_2/Ti_3C_2(140,12)	1.95	2.67	2.88	3.69	4.66	4.52
TiO_2/Ti_3C_2(140,24)	0.75	1.37	1.70	1.29	2.0	2.59
TiO_2/Ti_3C_2(160,6)	1.92	2.61	2.72	3.02	4.0	3.90
TiO_2/Ti_3C_2(160,12)	0.78	1.17	1.33	1.44	2.37	2.69
TiO_2/Ti_3C_2(160,24)	0.93	1.56	1.92	1.54	2.50	2.85
TiO_2/Ti_3C_2(180,6)	0.26	0.81	1.04	1.13	2.04	2.77
TiO_2/Ti_3C_2(180,12)	0.31	1.01	1.33	1.22	2.31	2.94

TiO_2/Ti_3C_2(180,24)	0.33	1.61	2.05	1.52	2.57	3.05
TiO_2/Ti_3C_2(200,6)	0.47	1.17	1.56	1.04	2.45	2.79
TiO_2/Ti_3C_2(200,12)	0.85	1.25	1.56	1.69	2.57	3.36
TiO_2/Ti_3C_2(200,24)	1.73	2.69	2.93	2.69	3.69	3.51
TiO_2/Ti_3C_2(220,6)	0.99	1.95	2.28	1.41	2.40	3.15
TiO_2/Ti_3C_2(220,12)	1.93	2.73	3.05	2.85	4.08	4.34
TiO_2/Ti_3C_2(220,24)	2.29	3.25	3.61	3.08	3.48	2.94

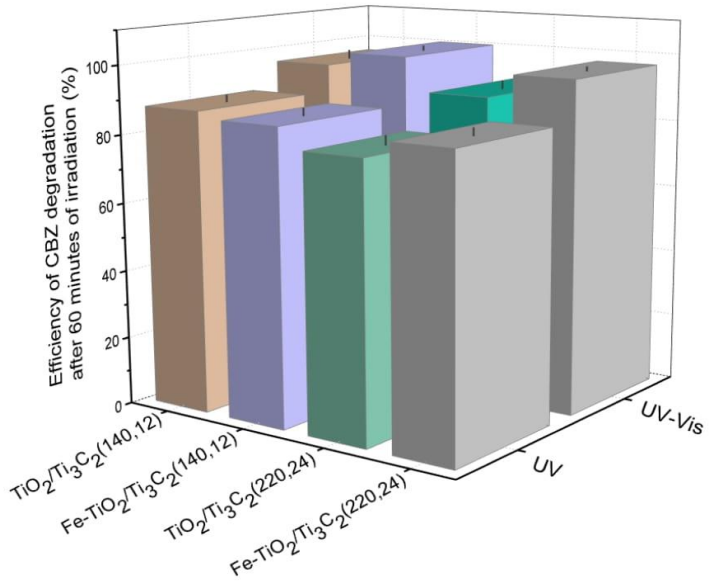

Figure 7S. The effect of irradiation light (UV 230nm<λ<400 nm; simulated solar light, UV-Vis) on photodegradation efficiency of carbamazepine.

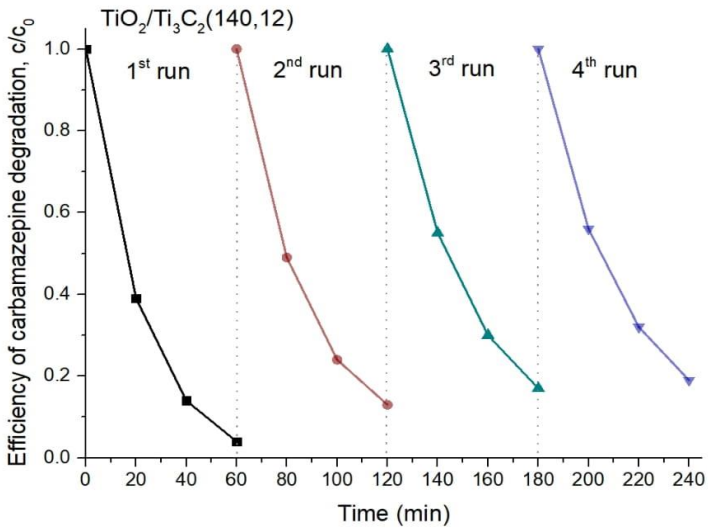

Figure 8S. The efficiency of carbamazepine degradation for sample TiO_2/Ti_3C_2(140,12) measured in the four subsequent cycles of degradation.

Rozdział IV. Design and synthesis of TiO_2/Ti_3C_2 composites for highly efficient photocatalytic removal of acetaminophen: The relationships between synthesis parameters, physicochemical properties, and photocatalytic activity

Catalysis Today 413-415 (2023) 113980

Contents lists available at ScienceDirect

Catalysis Today

journal homepage: www.elsevier.com/locate/cattod

Design and synthesis of TiO_2/Ti_3C_2 composites for highly efficient photocatalytic removal of acetaminophen: The relationships between synthesis parameters, physicochemical properties, and photocatalytic activity

Anna Grzegórska [a,*], Agnieszka Gajewicz-Skretna [b], Grzegorz Trykowski [c], Karol Sikora [d], Anna Zielińska-Jurek [a,*]

[a] Department of Process Engineering and Chemical Technology, Faculty of Chemistry, Gdańsk University of Technology, G. Narutowicza 11/12, 80-233 Gdańsk, Poland
[b] Laboratory of Environmental Chemoinformatics, Faculty of Chemistry, University of Gdansk, Wita Stwosza 63, 80-308 Gdansk, Poland
[c] Faculty of Chemistry, Nicolaus Copernicus University in Toruń, Gagarina 7, 87-100 Toruń, Poland
[d] Department of Inorganic Chemistry, Faculty of Pharmacy, Medical University of Gdańsk, Al. Gen. J. Hallera 107, 80-416 Gdańsk, Poland

ARTICLE INFO

Keywords:
Acetaminophen
Chemometrics
MXene
Photocatalysis
Ti_3C_2
TiO_2

ABSTRACT

In this study, we report the potential of TiO_2/Ti_3C_2 composite fabricated by oxidation of MXene for degradation of persistent organic pollutants. The effect of the synthesis conditions (time, temperature, and reaction environment) on the morphology, physicochemical properties, and photocatalytic activity was investigated. It was found that acetaminophen degradation was positively correlated with TiO_2 content in the composite structure. Furthermore, the findings confirmed that the synthesis reaction environment strongly influenced the obtained materials photocatalytic activity. The TiO_2/Ti_3C_2 composite obtained by solvothermal route in the presence of hydrochloric acid and ammonium fluoride exhibited the highest efficiency towards acetaminophen degradation than other composite materials, for which ACT removal reached 92 % within 60 min of irradiation under simulated solar light. The improved photocatalytic performance can be attributed to the presence of anatase-rutile polymorphs exposing highly active { 0 0 1} and { 1 0 1} facets coupled with MXene. Superoxide anion radicals and hydroxyl radicals played a major role in ACT degradation. Moreover, 3-hydroxyacetaminophen was detected as the first intermediate of ACT degradation, leading quickly to aromatic ring opening and production of aliphatic acids. Overall, this work provides an effective strategy for designing novel and efficient MXene-based photocatalysts for the degradation of emerging contaminants in water systems.

1. Introduction

Nowadays, pharmaceuticals belonging to the group of persistent organic pollutants represent a new water quality challenge, with still unknown long-term impacts on human health and ecosystems [1]. Acetaminophen (*N*-Acetyl-p-aminophenol), also known as paracetamol, is an analgesic and antipyretic drug commonly used worldwide and detected in wastewater and surface waters [2]. The annual consumption of ACT reaches 4–50 tons per million habitants; thus a high amount of this pharmaceutical may be excreted to the environment in the unchanged form or as its active metabolites [3]. Based on the studies performed from 1999 to 2018 in Latin America, the range of ACT concentration in wastewater treatment plants effluents reached 17.1–29,200 ng/dm^3, while in surface waters 3–25,200 ng/dm^3 [4].

In this regard, one of the primary challenges that societies will face during the 21st century is improving water quality by reducing pollution, minimizing the release of hazardous chemicals, and halving the proportion of untreated wastewater using the fundamentals of green chemistry and green engineering processes. This speaks for the development of new advanced treatment technologies such as photocatalysis to deal with these kinds of contaminants and improve the quality of treated wastewater before being safely discharged into public water bodies or for reuse.

MXenes are a group of materials consisting of transition metal carbides, nitrides, or carbonitrides, characterized by hydrophilic surface, good electrical conductivity, and chemical stability, which were

* Corresponding authors.
E-mail addresses: anna.grzegorska@pg.edu.pl (A. Grzegórska), annjurek@pg.edu.pl (A. Zielińska-Jurek).

https://doi.org/10.1016/j.cattod.2022.12.011
Received 27 August 2022; Received in revised form 8 November 2022; Accepted 20 December 2022
Available online 22 December 2022

discovered in 2011 [5]. The general formula of MXenes is $M_{n+1}X_nT_x$ (n = 1–4), where M is a transition metal, X represents carbon or nitrogen, and T_x refers to surface terminations (-F_x-O_y-OH) [6]. A novel and promising direction is using MXenes in photocatalysis [7,8]. MXenes may act as co-catalysts, enhancing the adsorption of the pollutants on the surface, improving the charge carriers separation, photocatalyst stability, and increasing the light absorption range [9,10]. The photocatalytic hydrogen production, CO_2 reduction as well as dyes degradation was previously described in the literature [11–13]. However, nowadays, only a few studies focus on the application of MXene materials for the photocatalytic degradation of active pharmaceutical ingredients. Jiang et al. [14] reported the application of MXene-derived C-TiO_2/Bi_4NbO_8Cl for the removal of ciprofloxacin. Liu et al. [15] investigated the potential of Ti_3C_2/TiO_2/BiOCl for the degradation of tetracycline. In the study of Liu et al. [16] the CdS@Ti_3C_2 @TiO_2 was used for the removal of sulfachloropyridazine. Yang et al. [17] proposed the application of PDI/g-C_3N_4/TiO_2@Ti_3C_2 for the photocatalytic degradation of atrazine. Shahzad et al. [18] and Grzegórska et al. [19] reported the potential of TiO_2/Ti_3C_2 and Fe-TiO_2/Ti_3C_2 composites for photocatalytic degradation of carbamazepine.

Formation of heterojunction between TiO_2 and MXene compound -$Ti_3C_2T_x$ is a promising approach to improve charge carriers separation and thus photocatalytic efficiency. MXene may form a Schottky barrier at the MXene-semiconductor heterojunction and act as a reservoir of photogenerated electrons [8]. Furthermore, depending on the synthesis conditions, different morphologies of TiO_2 with exposed crystal facets may be produced by in-situ oxidation of the MXene surface [12]. Our previous work confirmed that the formation of { 1 0 1} and { 0 0 1} facets might be particularly important in efficient photocatalytic degradation [20]. Facet-engineered TiO_2 with "surface heterojunction" which connects reductive { 1 0 1} facets and oxidative { 0 0 1} facets may effectively separate the oxidation and reduction centers of TiO_2 [19,21]. Dominant { 0 0 1} facets have a high ability to trap the photogenerated holes, while the concentration of the photogenerated electrons occurs on the { 1 0 1} facets [22]. This suggests that not only the presence of selected facets but also the ratio between them may determine the degradation rate [23]. Therefore, crystal engineering is one of the key factors affecting the efficiency of photocatalytic reactions.

In this regard, the present work represents a comprehensive investigation of the various synthesis conditions of TiO_2/Ti_3C_2 composites: (i) hydrothermal in deionized water, (ii) solvothermal in HBF_4, (iii) solvothermal in NH_4F and HCl, and (iv) simple calcination, to improve the physicochemical properties and the photocatalytic activity. For the first time, the effect of the reaction environment on the preparation of TiO_2/Ti_3C_2 composites exposing different crystal facets and applied for photocatalytic degradation of acetaminophen under simulated solar light was studied in detail. The chemometric analyses were employed to determine the relationships between synthesis parameters, physicochemical properties, and photocatalytic activity. Furthermore, for the most active sample, the possible reaction mechanism and degradation pathway were proposed.

2. Experimental

2.1. Photocatalyst preparation

The $Ti_3C_2T_x$ was obtained by etching aluminum from Ti_3AlC_2 using 48 % HF at room temperature for 24 h. TiO_2/Ti_3C_2 composites were prepared by a solvothermal method in the presence of HBF_4 (series TiO_2/Ti_3C_2_HBF_4 samples). In a typical synthesis, 60 cm^3 of HBF_4 (0.1 M) was added to 0.4 g of $Ti_3C_2T_x$, sonicated for 10 min, and mixed for 30 min (in a temperature ranging from 140° to 220°C and time from 6 to 24 h). Furthermore, the TiO_2/Ti_3C_2 composite was also obtained in deionized (DI) water during solvothermal synthesis (TiO_2/Ti_3C_2(220,24)_H_2O sample) to study the effect of the synthesis environment on morphology and photocatalytic activity. In this regard, 0.4 g of $Ti_3C_2T_x$ was added to 60 cm^3 of DI water and sonicated for 10 min. Then the suspension was mixed for 30 min and transferred into a Teflon-lined stainless steel reactor. The reaction was performed at 220 °C for 24 h. Another sample of $Ti_3C_2T_x$ was calcined at 550 °C for 2 h with a heating rate of 2 °C/min (TiO_2/Ti_3C_2(550,2) sample). Finally, the $Ti_3C_2T_x$ sample was also treated during solvothermal synthesis in HCl with NH_4F solution (TiO_2/Ti_3C_2(220,24)_NH_4F_HCl sample). In this regard, 60 cm^3 of HCl (3 M) was mixed with 0.1 g NH_4F, and 0.4 g of $Ti_3C_2T_x$ was added to the above solution and sonicated for 10 min. Then the suspension was stirred for 30 min and transferred into a Teflon-lined stainless steel reactor. The reaction was performed at 220 °C for 24 h. All resulting material was rinsed with deionized water and dried in an oven at 50 ℃.

2.2. Materials characterization

The characterization methods applied in this work can be found in subsection 2.3. in Supporting Materials.

3. Results and discussion

3.1. Physicochemical characteristics of TiO_2/Ti_3C_2 composites prepared by a solvothermal method in the presence of HBF_4

In the first step of the study, the composite synthesis was optimized to correlate the morphological and physicochemical parameters with photocatalytic activity. Firstly, TiO_2/Ti_3C_2 composites were prepared by a solvothermal method in the presence of HBF_4 at a temperature ranging from 140 °C to 220 °C for 6–24 h, as presented in Table 1 (series A). The SEM and TEM analyses confirmed the formation of the accordion-like structure of $Ti_3C_2T_x$ (see Fig. 1a-b). The solvothermal reaction in HBF_4 led to the formation of decahedral anatase particles (DAPs) on the $Ti_3C_2T_x$ layer, as shown in Fig. 1c-f. Analyzing the SEM images of all prepared TiO_2/Ti_3C_2 composites, the diversity of sample morphology can be noticed. The samples TiO_2/Ti_3C_2(140,24) and TiO_2/Ti_3C_2(180,6) presented the initial stage of TiO_2 in-situ growing and formation. Meanwhile, the sample TiO_2/Ti_3C_2(180,24) showed the most uniform DAPs, equally distributed on the MXene layers. Other samples presented a size variety, with smaller and larger DAPs. The average length and height of DAPs were calculated based on the measurements of 50 particles for each sample from the SEM images and are summarized in Table 1.

The BET surface area increased with the increase in the reaction time and temperature, as presented in Table 1. However, this trend was observed only to a certain point. Prolonged reaction time and higher temperature caused a decrease in specific surface area. The CHN analysis of MXene showed that the sample contains about 8.49 % of carbon and 2.15 % of hydrogen (as shown in Table 1S). The XRD analysis, presented in Fig. 1S in Supporting Materials, confirmed the successful etching of aluminum from the Ti_3AlC_2. For the obtained MXene materials, the characteristic diffraction peaks at $2\theta = 8.8°$, 18.1°, and 27.4° corresponding to (002), (004), and (006) planes were noticed. Furthermore, the Rietveld analysis of XRD patterns revealed that samples TiO_2/Ti_3C_2(140,6), TiO_2/Ti_3C_2(140,12), TiO_2/Ti_3C_2(160,6) are pure MXene or contain a very low content of TiO_2 because any signals corresponding to TiO_2 were not observed. Furthermore, the Rietveld analysis confirmed an increase of TiO_2 content in the composite with an increase in time and temperature. The highest content of TiO_2 was noticed for sample TiO_2/Ti_3C_2(220,48) with almost 100 % of TiO_2 and sample TiO_2/Ti_3C_2(220,24) containing 99.8 % of TiO_2 and 0.2 % of MXene.

To confirm the presence of MXene in the sample TiO_2/Ti_3C_2(220,24), the additional STEM-EDX-EELS analysis was performed. As presented in Fig. 2S in Supporting Materials for sample TiO_2/Ti_3C_2(220,24) two different areas may be distinguished. The first one with higher carbon content indicates the presence of $Ti_3C_2T_x$, and the second with negligible carbon content is TiO_2.

Table 1
Physicochemical characteristics and photocatalytic activity of TiO_2/Ti_3C_2 composites.

Sample	Synthesis conditions		BET surface area (m^2/g)	Anatase (101) crystallite size (nm)	Composition (%)				Acetaminophen degradation rate constant ($min^{-1} \cdot 10^{-2}$)
	Temperature (°C)	Time (h)			TiO_2	Ti_3C_2	h (nm)	l (nm)	
$Ti_3C_2T_x$	25	24	7.5	nd	0	100	nd	nd	0.2 ± 0.02
TiO_2/Ti_3C_2(140,6)	140	6	8.4	nd	0	100	nd	nd	0.22 ± 0.01
TiO_2/Ti_3C_2(140,12)	140	12	9.5	nd	0	100	nd	nd	0.21 ± 0.01
TiO_2/Ti_3C_2(140,24)	140	24	12.9	19	11.5	88.5	nd	nd	1.01 ± 0.03
TiO_2/Ti_3C_2(160,6)	160	6	9.9	nd	0	100	nd	nd	0.28 ± 0.01
TiO_2/Ti_3C_2(160,12)	160	12	16.0	27	18.6	81.4	35	140	1.66 ± 0.04
TiO_2/Ti_3C_2(160,24)	160	24	24.8	24	45.8	54.2	52	268	1.89 ± 0.02
TiO_2/Ti_3C_2(180,6)	180	6	16.3	24	13.5	86.5	nd	nd	0.99 ± 0.03
TiO_2/Ti_3C_2(180,12)	180	12	24.0	38	42.4	57.6	45	184	2.04 ± 0.02
TiO_2/Ti_3C_2(180,24)	180	24	21.5	40	81.7	18.3	71	328	1.22 ± 0.03
TiO_2/Ti_3C_2(200,6)	200	6	24.2	35	31.6	68.4	44	117	1.14 ± 0.03
TiO_2/Ti_3C_2(200,12)	200	12	23.0	41	69.8	30.2	64	201	1.24 ± 0.02
TiO_2/Ti_3C_2(200,24)	200	24	17.2	34	98.8	1.2	76	214	1.03 ± 0.01
TiO_2/Ti_3C_2(220,6)	220	6	22.4	41	63.9	36.1	96	289	1.37 ± 0.03
TiO_2/Ti_3C_2(220,12)	220	12	16.5	27	85.9	14.1	121	142	0.99 ± 0.02
TiO_2/Ti_3C_2(220,24)	220	24	10.0	34	99.8	0.2	88	114	2.86 ± 0.03
TiO_2/Ti_3C_2(220,48)	220	48	8.5	38	100	0	79	101	2.49 ± 0.02

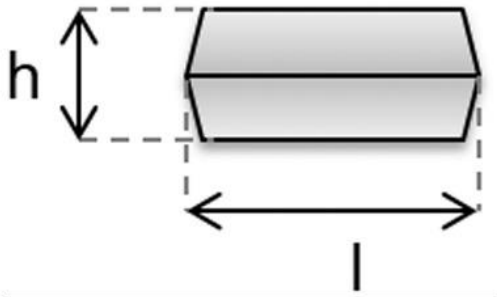

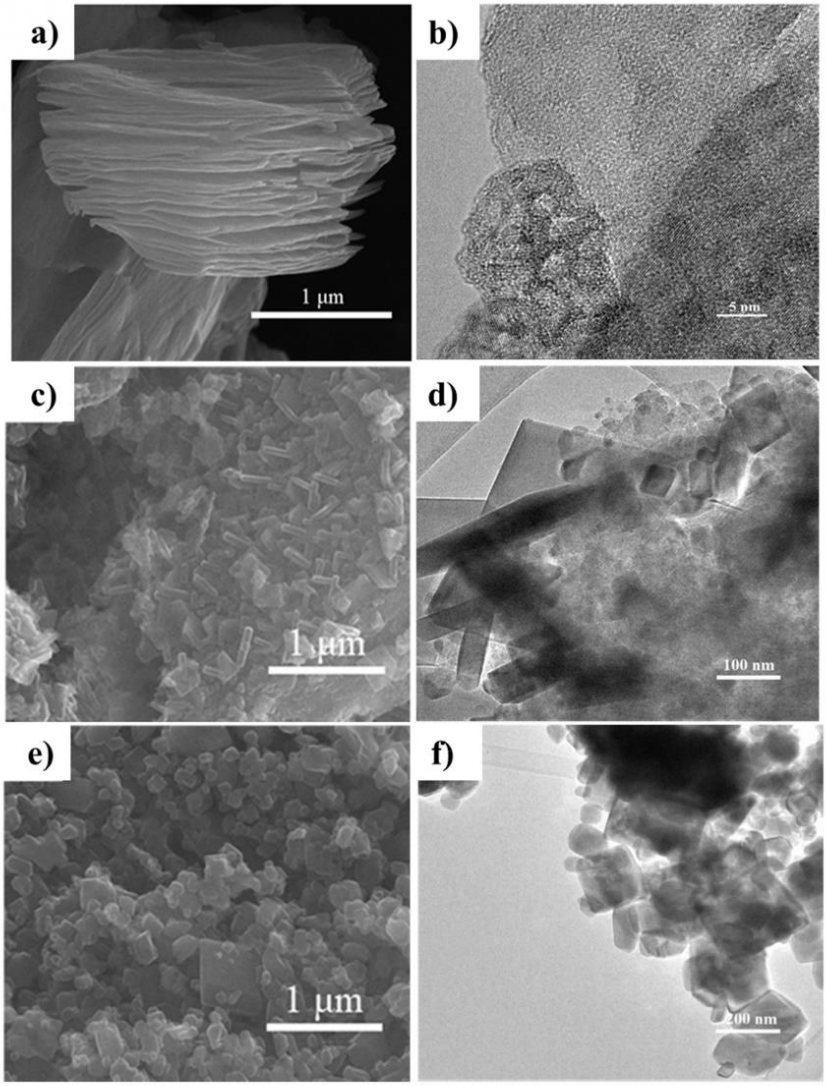

Fig. 1. The SEM and TEM images for Ti_3C_2 (a,b), TiO_2/Ti_3C_2 composite synthesized at 180 °C (c,d) and 12 h, TiO_2/Ti_3C_2 composites synthesized at 220 °C and 24 h (e,f).

In order to catch possible (dis)similarities among TiO_2/Ti_3C_2 composites, find hidden patterns in data and determine the causal relationships between the photocatalytic performance of TiO_2/Ti_3C_2 composites and the samples morphology, physicochemical properties as well as synthesis conditions, the chemometric analyses were carried out.

The tree-like graph is shown in Fig. 3S in Supporting Materials. Since the circular dendrogram for the hierarchical cluster analysis (HCA) does not identify the causal relationship between variables, hence to gain an overall idea of which MXene morphological features, physicochemical properties and/or synthesis conditions are significantly related to the enhanced photocatalytic performance of the TiO_2/Ti_3C_2 composites, the Principal Component Analysis (PCA) analysis was performed.

PCA discovers interpretable patterns and trends in the data that cannot be captured by a human eye and simultaneously simplifies the complexity in high-dimensional data. This is done by finding the orthogonal projections that maximize the variance of the data, known as the principal components (PCs). Principal components as linear combinations of the original variables (here: morphological features, physicochemical properties and/or synthesis conditions of MXene) are extracted in a way that the first principal component (PC1) explains as much variance in the original data as possible and each subsequent principal component accounts for less and less variance. Following the Kaiser criterion that states that meaningful are only those components with eigenvalues equal or higher than one, the first two principal components (PC1 and PC2) were retained for further analysis. Together, the first two PCs contain 84.83 % (62.96 % + 21.87 %) of the information (variances) contained in the data. The projection of the data onto the subspace spanned by PC1 and PC2 is shown in Fig. 2a, known as a biplot. To gain mechanistic insights into the efficiency of TiO_2/Ti_3C_2 composites towards acetaminophen degradation, the analysis of the normalized factor loadings was carried out (Fig. 2b). These loadings are, by definition, correlations between the original variables and the PCs.

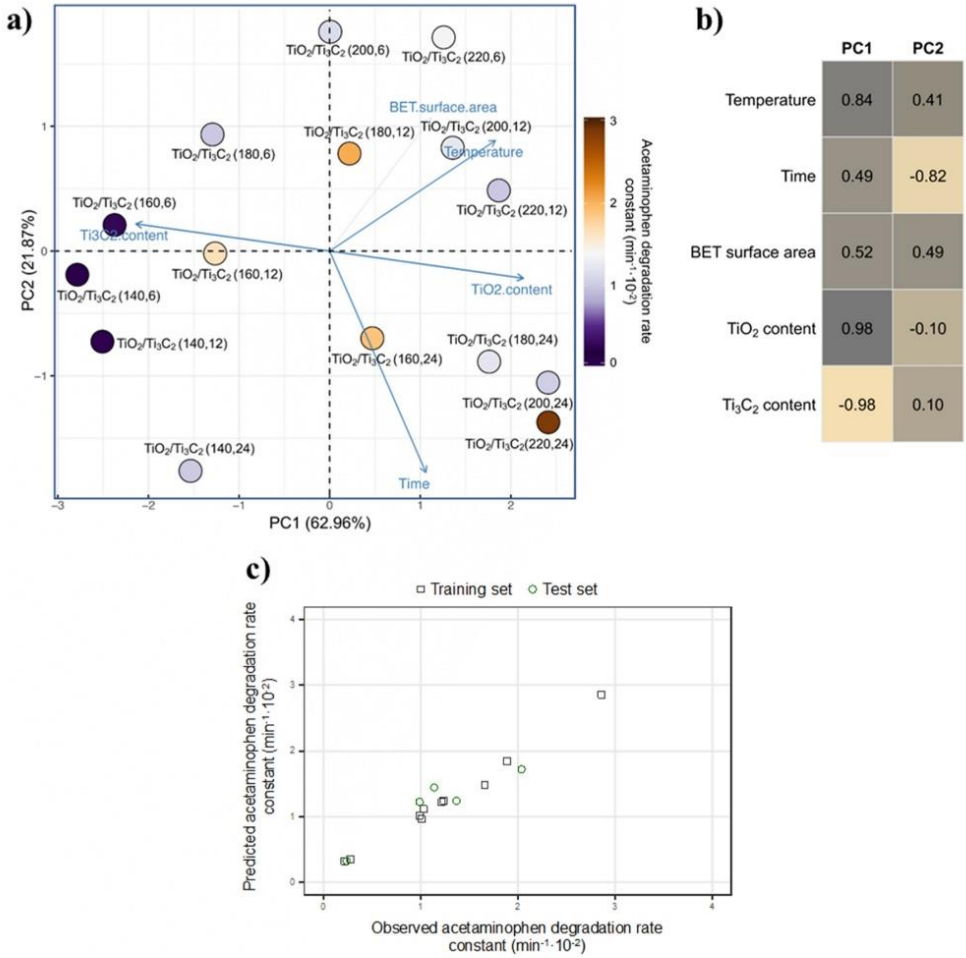

Fig. 2. (a) The PCA biplot of the first two principal components (PC1-PC2) that illustrates the grouping of TiO_2/Ti_3C_2 composites (points) in the space of explanatory variables (vectors). The color of each data point represents the value of the acetaminophen degradation rate constant ($min^{-1}\cdot10^{-2}$): dark purple means the lowest value of the photocatalytic activity, whereas dark brown – the highest photocatalytic activity; (b) The plot of normalized factor loadings utilized for providing a physical interpretation of principal components, (c) The plot of experimentally observed versus predicted values of acetaminophen degradation rate constant in the presence of TiO_2/Ti_3C_2 composites ($min^{-1}\cdot10^{-2}$). (For interpretation of the references to color in this figure legend, the reader is referred to the web version of this article.)

They quantify the extent of the relevance of original variables in explaining a given principal component. According to the so-called Malinowski rule, the statistically significant ones are only those which have absolute values equal to or higher than 0.7. A closer look at Fig. 2b reveals that the variables with the greatest influence on the first principal component (PC1) are the content of TiO_2 and the content of Ti_3C_2, followed by synthesis temperature.

The projection of the samples onto the PCs showed that the samples with the lowest photodegradation rate constant (below 0.3 $min^{-1}\cdot10^{-2}$) are furthest apart from the other composites and are located on the left side of the biplot. It is straightforward to see that these nanocomposites have low PC1 scores (X-axis), which means they are characterized by low values of the positively correlated variables (i.e., TiO_2 content and temperature), and thereby by high values of the negatively correlated variable (i.e., Ti_3C_2 content). This observation is even more obvious in the light of disclosure that these composites are pure MXene without TiO_2. In addition, these samples are characterized by the lowest surface area compared to the other TiO_2/Ti_3C_2 nanocomposites. Examining the biplot further, one can see that the samples with the highest content of TiO_2 and the lowest content of MXene were placed on the right side of the biplot. These results suggest that the greatest distances between the nanocomposites are along PC1 (X-axis), expressed by the composition and corresponding contents of TiO_2 and Ti_3C_2.

Interestingly, the samples with a higher concentration of TiO_2 than that of Ti_3C_2 were placed on the right side of the biplot and showed the differentiation along PC2 (Fig. 2a). The interpretation of PC2 (Y-axis) which reflects the synthesis conditions of nanocomposites, is not so intuitive. It is strongly negatively correlated with reaction time. As seen in Fig. 2a, composites of low and moderate values of activity of acetaminophen degradation have both low and high PC2 scores. Although PC2 does not clearly distinguish between the samples with the higher and the lower activity of acetaminophen degradation, it can be seen that the photocatalytic performance of composites slightly increases, moving downwards along the Y-axis (PC2). This observation is in line with the correlogram analysis (Fig. 4S). The temperature is strongly positively correlated with TiO_2 content ($r = 0.81$), which implies that as

temperature increases, TiO_2 content also tends to increase. A correlation between BET surface area and Ti_3C_2 content, on the other hand, indicates a weak negative correlation ($r = -0.37$), meaning that, although an increase in the first variable will likely lead to decrease in the second variable, the relationship is not very strong. As seen in Fig. 4S, the acetaminophen degradation rate constant shows a positive correlation with TiO_2 content in the composite, reaction time, synthesis temperature and BET surface area and a negative correlation with Ti_3C_2 content.

The highest photocatalytic performance with the acetaminophen degradation rate constant equal to 2.86 ± 0.03 ($min^{-1} \cdot 10^{-2}$) was obtained by the TiO_2/Ti_3C_2(220,24) sample located on the right inferior half of the biplot (Fig. 2a). This sample is composed of TiO_2 (99.8 wt%) and Ti_3C_2 (0.2 wt%). With an increase of Ti_3C_2 content up to 36.1 wt%, the photocatalytic activity of TiO_2/Ti_3C_2 composites decreased sharply and was more than 50 % less compared to the photocatalytic performance of TiO_2/Ti_3C_2(220,24) sample (Table 1). Interestingly, further increasing the Ti_3C_2 content enhanced the photocatalytic performance and resulted in higher than expected values of acetaminophen degradation rate constants.

As seen from Fig. 2a, the second, the third and the fourth composites with the highest acetaminophen degradation rate constants TiO_2/Ti_3C_2(180,12), TiO_2/Ti_3C_2(160,24), and TiO_2/Ti_3C_2(160,12) were placed nearest from the biplot origin. The composition ratio of TiO_2 to Ti_3C_2 in these composites was 42.4: 57.6 wt%, 45.8: 54.2 wt% and 18.6: 81.4 wt%, respectively. Contrary to the TiO_2/Ti_3C_2(220,24) sample, these composites were obtained at lower temperatures and, additionally, two of them also in a shorter synthesis time. This might suggest that the photocatalytic performance of TiO_2/Ti_3C_2 nanocomposites can be greatly affected not only by the chemical composition of samples but also by other factors, such as synthesis conditions (i.e., temperature, reaction time).

Finally, the computer-aided (so-called *in silico*) modelling was additionally conducted to meet the research objectives of the study. As a logical extension of experimental research, *in silico* modelling identifies the essential parameters related to a target activity or molecular property (e.g., photocatalytic activity) and enables its prediction for untested compounds from experimental training data and suitable mathematical model. Hence, before model development, the dataset of 15 experimentally tested TiO_2/Ti_3C_2 nanocomposites was split into a training set of 10 samples and a test (external assessment) set of 5 samples using the sorted response-based division algorithm (in ascending order). Considering the limited size of the available dataset, the kernel-weighted local polynomial regression (KwLPR) approach [24,25], being a pointwise iterative method, was used for *in silico* model development. Likewise, in the case of other similarity-based modelling methods, the KwLPR approach seeks to estimate the unknown regression function point by point. This means that the KwLPR algorithm approximates the (unknown) posterior molecular property using only a small fraction of the training data points that lie in the local neighbourhood of each point of estimate. It does this by fitting a polynomial at each point in the dataset to a certain (user-defined) number of k nearest neighbours, whose explanatory variables values are similar to the point of estimation. The polynomial is obtained in the distance weighted least square estimation, which allows to allocate more weight to the points near the target point being estimated and less weight to the points further away. The weights reflecting the relative importance/contribution of each of the k neighbours according to their distance to the target point are used then to estimate a weighted least squares regression local model. Finally, the regression function (i.e., local model) is applied to compute the value of a point estimate.

In this study, the best estimator's parameters that control the size and the shape of the neighbourhood (i.e., the bandwidth), the local weights (i.e., the kernel function) and the flexibility of the regression function (i.e., the degree of the local polynomial used for smoothing) were obtained through the leave-one-out validation process. To evaluate both aleatoric and epistemic uncertainty of a developed *in silico* model, i.e., to verify how well the model does fit to the training dataset and predict the activity of unseen data (outside the training set), various quality metrics were computed. The goodness-of-fit of a model was ascertained by the determination coefficient (R^2), and the root means a square error of calibration ($RMSE_C$). While the true predictive performance of the model was examined with external validation coefficients (Q^2_{F1}, Q^2_{F2}, Q^2_{F3}), concordance correlation coefficient (CCC), and root means a square error of prediction ($RMSE_P$) [26–28].

In accordance with our expectations, the chemical composition of the composite nanomaterials is not sufficient to reflect variations in the acetaminophen degradation rate constant. The overall quality metrics of such a model were disappointing (i.e., R^2, $Q^2_{F1\ F3} < 0.70$) and did not meet the commonly accepted requirements of *in silico* model. To improve the model performance and shed light on the mechanism driving acetaminophen degradation in the presence of TiO_2/Ti_3C_2 composites, the model was enriched with the synthesis conditions (i.e., with either synthesis temperature or synthesis time). Both refined models appeared to be more efficient and reliable compared to the original model (i.e., R^2, $Q^2_{F1\text{-}F3} > 0.70$). Interestingly, the model linking the acetaminophen degradation rate constant with the mass ratio of TiO_2 to Ti_3C_2 and synthesis temperature posed a better model's performance than the model using synthesis time as the explanatory variable. This can be explained by the slightly greater strength of the relationship between acetaminophen degradation rate constant and synthesis temperature ($r = 0.49$) than between acetaminophen degradation rate constant and synthesis time ($r = 0.46$) (Fig. 2b). Detailed information on the final model tuning parameters, including the kernel function applied, the calculated bandwidth for both explanatory variables, as well as the model's quality metrics, is provided in Table 2S in Supporting Materials. The analysis of the statistical metrics confirmed that the model demonstrated excellent fitting ability and external predictive power (i.e., generalization capabilities). This conclusion is clearly supported by a visual analysis of the scatter plot between the observed and predicted values of the acetaminophen degradation rate constant, shown in Fig. 2c.

As can be seen from the graph, the majority of the data points are clustered tightly around the best fit line, indicating high (close to 1) values of R^2 and Q^2. Since the developed KwLPR model fulfilled all stringent quality criteria, it has been utilized to predict the photocatalytic performance for a set of eight new TiO_2/Ti_3C_2 nanocomposites for which the experimental data have been unavailable up to now (Table 3S). The reliability of the predictions for these new composites will be subject to further experimental investigation.

3.2. The effect of reaction environment on TiO_2/Ti_3C_2 composites physicochemical properties and photocatalytic activity

In order to compare the impact of the reaction environment on the photocatalytic activity, the best parameters of the solvothermal synthesis in HBF_4 (series A, TiO_2/Ti_3C_2(220,24) sample) were applied for the preparation of the TiO_2/Ti_3C_2 composites in deionized water (TiO_2/Ti_3C_2(220,24)_H_2O sample) and in HCl and NH_4F (TiO_2/Ti_3C_2(220,24)_NH_4F_HCl sample). Furthermore, TiO_2/Ti_3C_2 nanocomposite was also obtained during the calcination of Ti_3C_2 (TiO_2/Ti_3C_2(550,2) sample) in airflow at 550 °C for 2 h (optimized calcination temperature in the range 350–650 °C).

Firstly, a comparison of structural and textural properties for the obtained TiO_2/Ti_3C_2 composites was performed. The XRD diffractograms for TiO_2/Ti_3C_2 samples synthesized at various conditions are shown in Fig. 5Sa. The diffraction patterns of TiO_2/Ti_3C_2(220,24)_HBF_4 and TiO_2/Ti_3C_2(550,2) are highly similar and correspond to the anatase phase. In the case of sample TiO_2/Ti_3C_2(220,24)_H_2O, the peaks at 8.9 ° and 18.3 ° correspond to the presence of MXene, while a minority of the rutile phase can be observed at 27.5°. For TiO_2/Ti_3C_2(220,24)_NH_4F_HCl, the characteristic signals at 25.2 ° and 27.3 °, corresponding to the (001) plane of anatase and (110) plane of rutile were

distinguished. In contrast to TiO_2/Ti_3C_2(220,24)_H_2O, the sample TiO_2/Ti_3C_2(220,24)_NH_4F_HCl is a composition of rutile (73.7 %) with a minority of anatase (26.3 %). Similar, Li and Gray [29] observed the formation of mixed-phase titanium (IV) oxide in the presence of hydrochloric acid when titanium tetra-isopropoxide was used as the titanium precursor. Furthermore, it was observed that halide ions enhanced the anatase-to-rutile phase transition [30]. The average size of anatase and rutile crystallites for TiO_2/Ti_3C_2 composites are summarized in Table 4S, while lattice parameters in Table 5S.

The DR/UV–vis spectra of the prepared composites are shown in Fig. 5Sb. The prepared samples showed absorption characteristics typical to anatase, with an absorption edge of about 400 nm extended to vis range due to $Ti_3C_2T_x$ presence. For the sample, TiO_2/Ti_3C_2(220,24)_H_2O with higher content of $Ti_3C_2T_x$, the increased absorption from 600 nm to 800 nm can be observed.

Comparing the composite morphology (Fig. 6S) it can be noticed that sample TiO_2/Ti_3C_2(220,24)_HBF_4 contains various size DAPs with the lowest surface area, about 10.0 m^2/g. For sample TiO_2/Ti_3C_2(220,24)_H_2O synthesized in the pure DI water, Ti_3C_2 sheets were covered by densely packed and irregularly shaped TiO_2 particles with the highest surface area of about 26.4 m^2/g among all prepared samples. Meanwhile, analyzing the SEM images of TiO_2/Ti_3C_2(550,2) it can be noticed that the agglomerated crystals were connected to each other to form a net shape. The sample TiO_2/Ti_3C_2(220,24)_NH_4F_HCl was a mixture of various size decahedral and octahedral TiO_2 particles exposing { 1 0 1} and { 0 0 1} facets.

The XPS analyses were performed to study the chemical states of photocatalysts surface composition, and the results are shown in Fig. 7S. The Ti 2p peak can be deconvoluted in three pairs of the doublet with peaks at 455 eV, 457 eV, and 459 eV (Ti 2p 3/2) assigned to Ti-C, substoichiometric TiC_x ($x < 1$), or titanium oxycarbides and TiO_2, respectively. However, for sample TiO_2/Ti_3C_2(550,2), notable differences from other samples can be observed. The main peak instead of TiO_2 was attributed to Ti^{3+} (457 eV), which may indicate the formation of Ti ions with a reduced charge state (Ti_xO_y). Similar phenomena were observed by Kong et al. [31] for Ti_3C_2 calcined at 700 °C. For all materials, the C1s spectra consist of five signals at 283 eV, 283.5 eV, 285 eV, 286.7 eV, and 288.5 eV assigned to Ti-C, C-Ti-O, adventitious carbon, C-O, and C-F bonds, respectively. Meanwhile, O1s signal may be deconvoluted into four signals at 528.5 eV, 530 eV, 531.5 eV, and 532.5 eV, corresponding to Ti-O-Ti, Ti-OH, C-O, and C═O.

Finally, the comparison of photocatalytic activity of the MXene-derived TiO_2/Ti_3C_2 composites prepared in different reaction environments is presented in Fig. 3a. The pure Ti_3C_2 compound showed negligible ACT photocatalytic removal. Similar very low photocatalytic activity for pure MXene was confirmed in previous studies [11,32,33]. However, in the TiO_2/Ti_3C_2 composite, MXene may act as a reservoir of photogenereted electrons and thus decrease the electron-hole recombination [34]. The highest rate constant is observed for TiO_2/Ti_3C_2(220,24)_NH_4F_HCl composite. This indicates that the bi-phase anatase-rutile structure of TiO_2 exposing highly active { 0 0 1} and { 1 0 1} facets greatly improved the photocatalytic degradation of acetaminophen. The photocatalytic activity increase can also be attributed to the morphological properties of TiO_2 consisting of decahedral and octahedral particles compared to other morphologies observed for samples obtained in different conditions. Meanwhile, sample TiO_2/Ti_3C_2(550,2) showed the lowest photocatalytic activity towards ACT degradation. This may be related to the morphology and highly defective (Ti^{3+} centers) surface of the photocatalyst. Previous studies also proved that excess defects would form the recombination center and be adverse to the separation of the charge carriers [35]. Furthermore, based on the trapping experiment in the presence of scavengers, it was noticed that the major reactive oxygen species responsible for ACT degradation are superoxide anion radicals and hydroxyl radicals (Fig. 3b).

Based on the Mott-Schottky analysis (Fig. 8S) it can be concluded that TiO_2/Ti_3C_2(220,24)_NH_4F_HCl composite showed typical characteristics for n-type semiconductor. The potential of flat band edge position was recorded at − 0.9 V vs. Ag/AgCl and converted to a value of − 0.61 V vs. NHE. According to band gap energy equal 2.8 eV the valence band (VB) edge of the composite was determined as approx. 2.19 eV. vs NHE. The proposed mechanism of acetaminophen degradation with TiO_2/Ti_3C_2(220,24)_NH_4F_HCl material is presented in the Fig. 3c. Photogenerated electrons in TiO_2 may be transferred to MXenes at the interface due to the higher potential of MXenes and inhibit recombination of photogenerated electron–hole pairs. Therefore, Ti_3C_2 may enhance the efficiency of charge separation and contribute to improved photocatalytic activity.

The proposed pathway of ACT degradation is presented in Fig. 3d. According to the LC-MS analyses, 3-hydroxyacetaminophen was detected as the first main intermediate of ACT decomposition, which suggests that hydroxylation of the benzene ring was a primary step of the degradation pathway. Moreover, based on the obtained results, 3-hydroxyacetaminophen quickly degraded within time and was further transformed through benzene ring cleavage to aliphatic acids [36,37].

Furthermore, the photocatalytic activity of the most active TiO_2/Ti_3C_2(220,24)_NH_4F_HCl composite was compared with the recently reported photocatalysts applied for photodegradation of ACT and the data are summarized in Table 6S. It was found that the photocatalyst prepared in our work has excellent performance compared with other materials with high degradation efficiency of ACT degradation within 60 min under simulated solar light.

4. Conclusions

In summary, the prepared TiO_2/Ti_3C_2 composites show good potential for photocatalytic water treatment. Based on the chemometric analyses, the photocatalytic activity was found to be significantly varied from the synthesis conditions. Chemometric analyses revealed that ACT degradation shows a positive correlation with TiO_2 content in the composite, reaction time, synthesis temperature, and BET surface area. The highest activity in this series was observed for the sample synthesized at 220 °C for 24 h. This work also demonstrates the effect of the synthesis environment on physicochemical properties and photocatalytic activity. In particular, the TiO_2/Ti_3C_2(220,24)_NH_4F_HCl displays improved photocatalytic efficiency than other composites towards ACT degradation under simulated solar light (92 % within 60 min). This phenomenon may be attributed to the formation anatase-rutile polymorphs exposing highly active { 1 0 1} facets and {0 0 1} facets coupled with MXene. Additionally, the photocatalytic mechanism was elucidated according to the band-gap energy, Mott Schottky plot and the trapping experiment. It was revealed that the main reactive oxygen species participating in photodegradation process are $\cdot O_2^-$ and ·OH. Furthermore, based on the LC/MS analyses, 3-hydroxyacetaminophen was detected as the first intermediate of photocatalytic process, and a possible degradation pathway was proposed.

Funding

The research was financially supported by Polish National Science Centre (Grant No. NCN 2018/30/E/ST5/00845.

CRediT authorship contribution statement

Anna Grzegórska: Formal analysis, Investigation, Methodology, Writing – original draft, Writing – review & editing. **Agnieszka Gajewicz-Skretna:** Formal analysis, Methodology. **Anna Zielińska-Jurek:** Conceptualization, Methodology, Resources, Supervision, Project administration,Funding acquisition, Writing – original draft, Writing – review & editing. **Grzegorz Trykowski**: Formal analysis. **Karol Sikora**: Formal analysis.

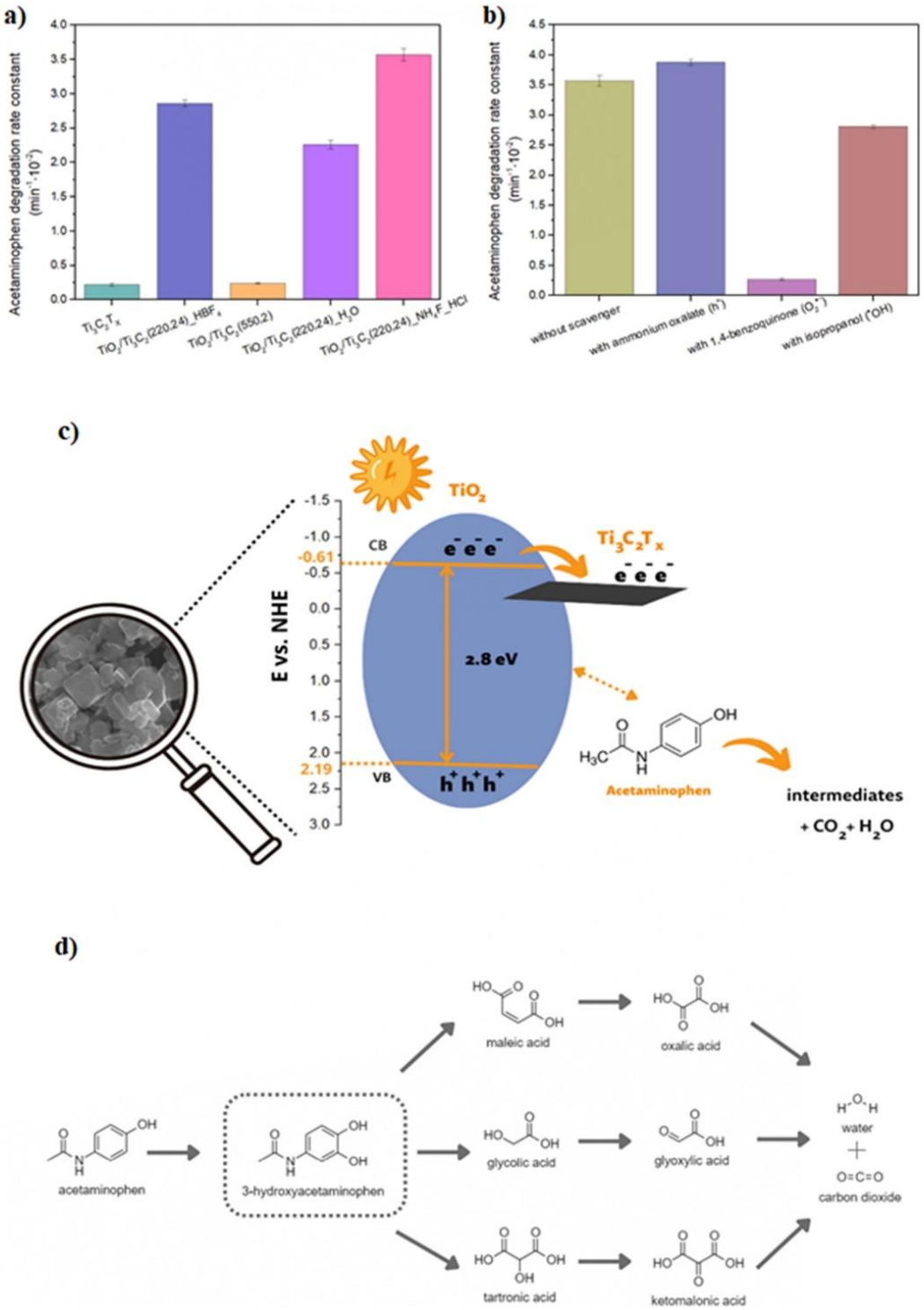

Fig. 3. The acetaminophen degradation for TiO_2/Ti_3C_2 composites (a), acetaminophen degradation with scavengers (b), proposed mechanism of ACT degradation (c), and proposed degradation pathway (d) for TiO_2/Ti_3C_2(220,24)_NH_4F_HCl.

Declaration of Competing Interest

The authors declare that they have no known competing financial interests or personal relationships that could have appeared to influence the work reported in this paper.

Data availability

Data will be made available on request.

Acknowledgements

This research was financially supported by the Polish National Science Centre (grant no. NCN 2018/30/E/ST5/00845).

Appendix A. Supporting information

Supplementary data associated with this article can be found in the online version at doi:10.1016/j.cattod.2022.12.011.

References

[1] J. Rivera Utrilla, M. Sánchez Polo, M.Á. Ferro García, G. Prados Joya, R. Ocampo-Pérez, Chemosphere 93 (2013) 1268–1287, https://doi.org/10.1016/j.chemosphere.2013.07.059.
[2] Y. Ishitsuka, Y. Kondo, D. Kadowaki, Biol. Pharm. Bull. 43 (2020) 195–206, https://doi.org/10.1248/bpb.b19-00722.
[3] R.A. Moore, N. Moore, Eur. J. Hosp. Pharm. 23 (2016) 187–188, doi.org/10.1136/ejhpharm-2016-000952.
[4] C. Peña-Guzmán, S. Ulloa-Sánchez, K. Mora, R. Helena-Bustos, E. Lopez-Barrera, J. Alvarez, M. Rodriguez-Pinzón, J. Environ. Manag. 237 (2019) 408–423, https://doi.org/10.1016/j.jenvman.2019.02.100.
[5] M. Naguib, M. Kurtoglu, V. Presser, J. Lu, J. Niu, M. Heon, L. Hultman, Y. Gogotsi, M.W. Barsoum, Adv. Mater. 23 (2011) 4248–4253, https://doi.org/10.1002/adma.201102306.
[6] P. Urbankowski, B. Anasori, T. Makaryan, D. Er, S. Kota, P.L. Walsh, M. Zhao, V. B. Shenoy, M.W. Barsoum, Y. Gogotsi, Nanoscale 8 (2016) 11385–11391, https://doi.org/10.1039/c6nr02253g.
[7] P. Kuang, J. Low, B. Cheng, J. Yu, J. Fan, J. Mater. Sci. Technol. 56 (2020) 18–44, https://doi.org/10.1016/j.jmst.2020.02.037.
[8] Q. Zhong, Y. Li, G. Zhang, Chem. Eng. J. 409 (2021), 128099, https://doi.org/10.1016/j.cej.2020.128099.
[9] L. Cheng, X. Li, H. Zhang, Q. Xiang, J. Phys. Chem. Lett. 10 (2019) 3488–3494, https://doi.org/10.1021/acs.jpclett.9b00736.
[10] J. Peng, X. Chen, W.J. Ong, X. Zhao, N. Li, Chem 5 (2019) 18–50, https://doi.org/10.1016/j.chempr.2018.08.037.
[11] M. Tahir, Energy Fuels 35 (2021) 14197–14211, https://doi.org/10.1021/acs.energyfuels.1c01340.
[12] A.A. Khan, M. Tahir, Z.Y. Zakaria, J. Environ. Chem. Eng. 9 (2021), 105244, https://doi.org/10.1016/j.jece.2021.105244.
[13] M. Tahir, A. Sherryna, R. Mansoor, A.A. Khan, S. Tasleem, B. Tahir, ACS Appl. Nano Mater. 5 (2022) 18–54, https://doi.org/10.1021/acsanm.1c03112.
[14] D. Jiang, X. Sun, X. Wu, S. Zhang, X. Qu, L. Shi, Y. Zhang, F. Du, Nanophotonics 9 (2020) 2077–2088, https://doi.org/10.1515/nanoph-2020-0088.
[15] H. Liu, C. Yang, X. Jin, J. Zhong, J. Li, Colloids Surf. A Physicochem. Eng. Asp. 603 (2020), 125239, https://doi.org/10.1016/j.colsurfa.2020.125239.
[16] Q. Liu, X. Tan, S. Wang, F. Ma, H. Znad, Z. Shen, L. Liu, S. Liu, Environ. Sci. Nano. 6 (2019) 3158–3169, https://doi.org/10.1039/c9en00567f.
[17] Yang, Chem. Eng. J. 427 (2022), 131809, https://doi.org/10.1016/j.cej.2021.131809.
[18] A. Shahzad, K. Rasool, M. Nawaz, W. Miran, J. Jang, M. Moztahida, K. A. Mahmoud, D.S. Lee, Chem. Eng. J. 349 (2018) 748–755, https://doi.org/10.1016/j.cej.2018.05.148.
[19] A. Grzegórska, P. Głuchowski, J. Karczewski, J. Ryl, I. Wysocka, K. Siuzdak, G. Trykowski, K. Grochowska, A. Zielińska-Jurek, Chem. Eng. J. 426 (2021), https://doi.org/10.1016/j.cej.2021.130801.
[20] M. Kowalkińska, S. Dudziak, J. Karczewski, J. Ryl, G. Trykowski, A. Zielińska-Jurek, Chem. Eng. J. 404 (2021), 126493, https://doi.org/10.1016/j.cej.2020.126493.
[21] S. Weon, M.-J. Suh, C. Chu, D. Huang, E. Stavitski, J.-H. Kim, ACS EST Eng. 1 (2021) 512–522, https://doi.org/10.1021/acsestengg.0c00210.
[22] R. Katal, S. Masudy-Panah, M. Tanhaei, M.H.D.A. Farahani, H. Jiangyong, Chem. Eng. J., 384 (2020) 123384. doi.org/10.1016/j.cej.2019.123384.
[23] J. Yu, J. Low, W. Xiao, P. Zhou, M. Jaroniec, J. Am. Chem. Soc. 136 (2014) 8839, https://doi.org/10.1021/ja5044787.
[24] A. Gajewicz Skretna, S. Kar, M. Piotrowska, J. Leszczynski, J. Cheminform., 13 (2021) 1–20. doi.org/10.1186/s13321-021-00484-5.
[25] A. Gajewicz-Skretna, A. Furuhama, H. Yamamoto, N. Suzuki, Chemosphere 280 (2021), 130681, https://doi.org/10.1016/j.chemosphere.2021.130681.
[26] P. Gramatica, QSAR Comb. Sci. 26 (26) (2007) 694–701, https://doi.org/10.1002/qsar.200610151.
[27] A. Tropsha, Mol. Inf. 29 (2010) 476–488, https://doi.org/10.1002/minf.201000061.
[28] N. Chirico, P. Gramatica, , J. Chem. Inf. Model. 51 (2011) 2320–2335, https://doi.org/10.1021/ci200211n.
[29] G. Li, K.A. Gray, Chem. Mater. 19 (2007) 1143–1146, https://doi.org/10.1021/cm061817f.
[30] H.A. Mahmoud, K. Narasimharao, T.T. Ali, K.M.S. Khalil, Nanoscale Res. Lett. 13 (2018), https://doi.org/10.1186/s11671-018-2465-x.
[31] F. Kong, X. He, Q. Liu, X. Qi, Y. Zheng, R. Wang, Y. Bai, Electrochim. Acta 265 (2018) 140–150, https://doi.org/10.1016/j.electacta.2018.01.196.
[32] A.A. Khan, M. Tahir, Ind. Eng. Chem. Res. 60 (2021) 16201–16223, https://doi.org/10.1021/acs.iecr.1c03242.
[33] X. Ding,Y. Li, C.Li, W. Wang, L. Wang, L. Feng, D. Han, J Mater. Sci., 54 (2019) 9385–9396. doi.org/10.1007/s10853-018-03289-4.
[34] I.A. Alsafari, S. Munir, S. Zulfiqar, M.S. Saif, M.F. Warsi, M. Shahid, Ceram. Int. 47 (2021) 28874–28883, doi.org/10.1016/j.ceramint.2021.07.048.
[35] D. Maarisetty, S.S. Baral, J. Mater. Chem. A 8 (2020) 18560–18604, https://doi.org/10.1039/d0ta04297h.
[36] T.X.H. Le, T.V. Nguyen, Z. Amadou Yacouba, L. Zoungrana, F. Avril, D.L. Nguyen, E. Petit, J. Mendret, V. Bonniol, M. Bechelany, S. Lacour, G. Lesage, M. Cretin, Chemosphere 172 (2017) 1–9, https://doi.org/10.1016/j.chemosphere.2016.12.060.
[37] M. Neamţu, M. Bobu, A. Kettrup, I. Siminiceanu, J. Environ. Sci. Health Toxic. Hazard. 48 (2013) 1264–1271, https://doi.org/10.1080/10934529.2013.776898.

Supporting Materials

Design and synthesis of TiO_2/Ti_3C_2 composites for highly efficient photocatalytic removal of acetaminophen. The relationships between synthesis parameters, physicochemical properties, and photocatalytic activity

Anna Grzegórska[1]*, Agnieszka Gajewicz-Skrętna[2], Grzegorz Trykowski[3], Karol Sikora[4], Anna Zielińska-Jurek[1]*

[1] Department of Process Engineering and Chemical Technology, Faculty of Chemistry, Gdańsk University of Technology, G. Narutowicza 11/12, 80-233 Gdańsk, Poland

[2] Laboratory of Environmental Chemoinformatics, Faculty of Chemistry, University of Gdansk, Wita Stwosza 63, 80-308 Gdansk, Poland

[3] Faculty of Chemistry, Nicolaus Copernicus University in Toruń, Gagarina 7, 87-100 Toruń, Poland

[4] Department of Inorganic Chemistry, Faculty of Pharmacy, Medical University of Gdańsk, Al. Gen. J. Hallera 107, 80-416 Gdańsk, Poland.

Keywords: acetaminophen, chemometrics, MXene, photocatalysis, Ti_3C_2, TiO_2

---

* Corresponding authors: anna.grzegorska@pg.edu.pl (AG), annjurek@pg.edu.pl (AZJ)

2. Experimental

2.2. Materials

MAX phase compound - Ti_3AlC_2 was provided by Luoyang Tongrun Info Technology Co. (China). The HF(ACS reagent, 48%) and HBF_4(48 wt.% in H_2O), NH_4F(ACS reagent, ≥98.0%) used for TiO_2/Ti_3C_2 preparation were purchased from Sigma Aldrich, and HCl(35-38%) was provided by Chempur. Acetaminophen(BioXtra, ≥99.0%) for the photocatalytic degradation process was provided by Sigma Aldrich. Scavengers for trapping experiment:

ammonium oxalate monohydrate (ACS reagent, ≥99%), isopropanol (anhydrous, 99.5%), and benzoquinone (reagent grade, ≥98%) were purchased from Sigma Aldrich. The reagents were used as received with no further purification. Deionized water (DI) was used in all experiments.

2.3. Characterization of photocatalysts

The surface crystal structure and chemical composition were determined using an X-ray powder diffractometer (XRD). XRD patterns were obtained with a powder diffractometer Rigaku Intelligent X-ray diffraction system SmartLab (Rigaku Corporation, Tokyo, Japan) with Cu Kα radiation, and in the 2θ range from 5° to 80°, with a speed 2°min^{-1} and a step of 0.01°. Brunauer-Emmett-Teller (BET) surface area was analyzed by the Micromeritics Gemini V analyzer (Norcross, GA, USA) in N_2 at a temperature of 77K (boiling point of liquid nitrogen). Prior to the measurement, the powder samples were degassed at 200°C under a constant flow of nitrogen. UV–vis reflectance spectra of the powder catalysts were recorded by a ThermoScientific Evolution 220 spectrophotometer (Waltham, MA, USA) in the wavelength range of 200–800 nm. $BaSO_4$ was applied as the reference material. The photocatalyst bandgap energy was calculated from the corresponding Kubelka-Munk function. Element analysis (H, C, N) was performed by the quantitative sample digestion at the point of combustion method in the apparatus Vario Macro CHN, Elementar Analysensysteme GmbH (Hesse, Germany). Microscopic measurements were performed using scanning electron microscope (Quanta 3D FEG, FEI Europe) with secondary electron (SE) detector (Everhart–Thornley detector) and transmission electron microscope (model Tecnai F20 X-Twin) coupled with the spectroscopic techniques (EDS, EELS). In TEM mode, a dark field (DF) detector was used for imaging. In the STEM mode, a high angle annular dark field (HAADF) detector was used for imaging, and energy dispersive

spectrometer (EDS) RTEM SN9577+, by EDAX (Pleasanton, USA), or parallel electron energy loss spectroscopy (PEELS) by Gatan (Pleasanton, USA) was used to analyze the elements.

The surface chemistry of the studied samples was analyzed by X-ray photoelectron spectroscopy (XPS) using Escalab 250Xi multispectroscope (ThermoFisher Scientific) with a monochromatic AlKα X-ray source. The high-resolution spectra were collected in the core-level binding energy range of Ti2p, C1s, and O1s, at pass energy of 20 eV. The charge compensation was provided by low-energy electron and Ar+ ions bombardment throughout the measurement, with a final calibration at adventitious carbon C1s peak (284.8 eV). Spectral deconvolution was done using Avantage 5.9921 software (ThermoFisher Scientific). The Mott-Schottky analysis was performed to determine the flat band (F_b) potential of the photocatalyst. The EIS data were recorded from the anodic towards a cathodic direction using Potentiostat/Galvanostat Autolab PGSTAT204 (Metrohm Autolab) with a Na_2SO_4 (0.5 M) as an electrolyte. EIS data were recorded for the applied frequency of 1000 Hz in the potential range from 0 to −1.5 V vs. Ag/AgCl.

2.4. Photocatalytic activity

The photocatalytic performance of the TiO_2/Ti_3C_2 was evaluated in reaction of acetaminophen degradation (20 mg/dm^3) under simulated solar light. The experiments were conducted in the 25 cm^3 reactor with a quartz window, equipped with an air supply mode. Firstly, the photocatalyst dispersed in ACT aqueous solution (2g·dm^{-3}) was stirred in the dark for 30 minutes to achieve adsorption-desorption equilibrium before irradiation. The 300 W Xe lamp (LOT Oriel, Darmstadt, Germany) was applied as a light source imitating the sunlight spectrum with the light flux in the UV range (310 nm < λ < 380 nm) equaled 30 mW·cm^{-2}. Then, reaction samples from the ACT solution were collected at regular intervals of 20 min for HPLC analysis. Furthermore, the photocatalyst particles were separated from

the solution using a 0.2 μm syringe filter. The rate of acetaminophen photodegradation was measured using reverse-phase high-performance liquid chromatography. A volume composition of the mobile phase of 0.1% formic acid, 69.9% water, and 30% methanol was used to determine acetaminophen concentration.

The acetaminophen transformation products were analyzed using high-performance LC-MS system employed consisted of an HCT Ultra spectrometer (Bruker Daltonics, Billerica, Massachusetts, US) with an ESI source coupled with an Agilent 1200 liquid chromatograph (Agilent Technologies, Santa Clara, California, US). Chromatographic separation was conducted on Eclipse XDB-C8, 4,6 x 150 mm, 5 um (Agilent) column. Mobile phase A was water with 0.1% formic acid and phase B acetonitrile with 0.1% formic acid. Gradient program was as follows: 0 min – 1% B, 5 min – 1% B, 25 min – 90% B, 30 min – 90% B, 35 min – 1% B. The flow was set at 0.4 ml/min, and the injection volume was 50 μl. Column oven temperature was set to 25°C and UV chromatograms were recorded at 220, 246 and 254 nm. Spectra were acquired in positive and negative ESI mode, the capillary voltage was set at 113V, the scanned mass range was 50–850 m/z and the accumulation time was 200,000 ms. The parameters capillary voltage, drying gas flow, nebulizing gas and source temperature was, respectively: 4.0 kV, 10 L min−1, 30 psi and 350 °C. Helium (99.999%) was used as the collision gas in the ion trap. The mass spectrometer was operated in full scan and single ion monitoring (SIM).

Furthermore, the photocatalytic process was performed in the presence of scavengers to study the mechanism of acetaminophen photodegradation. Ammonium oxalate was applied as holes scavenger (h^+), isopropyl alcohol for free hydroxyl radicals (·OH), and p-benzoquinone for superoxide radical anions ($\cdot O_2^-$). The content of each scavenger was equal to 0.03 mmol (10-fold concentration of contaminant).

2.5. Data analysis

As a first approach, unsupervised hierarchical clustering [1] (HCA) was carried out to identify distinct subgroups of TiO_2/Ti_3C_2 composites with similar features. In a nutshell, HCA seeks to group observations (here: nanocomposites) with similar features into homogenous clusters. That means that similar data observations are grouped together into one cluster. The similarity measure is a distance (e.g., Euclidean distance, Manhattan distance, Pearson correlation distance, etc.) that quantifies the level of (dis)similarity. It is assumed that two points are similar when having near-zero distance, while as the distance increases the degree of similarity decreases. Clustering was performed based upon similarity across the set of samples morphology, synthesis conditions, and physicochemical properties of TiO_2/Ti_3C_2 composites using Euclidean distance and Ward's minimum variance method. The rationale behind such a combination of distance measure and linkage method is that it tends to produce internally homogeneous and substantively interpretable clusters of approximately equal size. To get further insight into the nature of the interrelationships among the analyzed TiO_2/Ti_3C_2 composites as well as between the photocatalytic performance of the samples and their characteristics such as morphology, physicochemical properties, and synthesis conditions, the Principal Component Analysis (PCA) was performed. PCA is one of the most prevalent unsupervised pattern recognition methods for exploratory data analysis. It aims to efficiently reduce the dimensionality of the multivariate data to facilitate exploratory data analysis, visualization, and further identify the inherent patterns within the data. The theoretical foundations and applications of PCA have been detailed extensively elsewhere [2]. All statistical analyses were performed using R software (v4.1.2) with the following packages: *circlize [3]*, *dendextend [4]*, *factoextra [5]*, and *ggplot2 [6]*.

3.Results and discussion

3.1. Physicochemical characteristics of TiO_2/Ti_3C_2 composites prepared by a solvothermal method in the presence of HBF_4

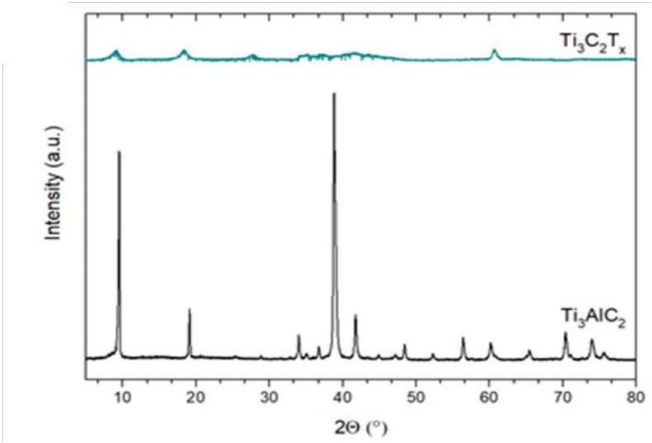

Fig 1S. The XRD diffractograms of Ti_3AlC_2 and $Ti_3C_2T_x$ after the etching process.

Table 1S. CHN analyses for $Ti_3C_2T_x$ material.

Sample	N (%)	C (%)	H (%)
$Ti_3C_2T_x$	0.196	8.486	2.147

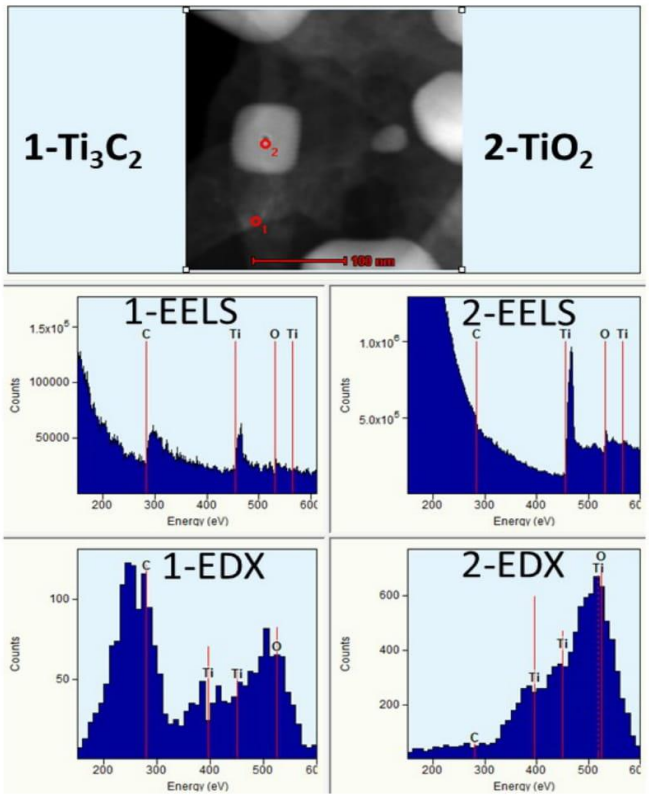

Figure 2S. STEM-EDX-EELS analysis for sample TiO_2/Ti_3C_2(220,24)

Examining the tree-like graph shown in Figure 3S in the Supporting Materials revealed that all TiO_2/Ti_3C_2 composites were clustered into four groups. The pure MXene samples, without formation of anatase, i.e., TiO_2/Ti_3C_2(140,6), TiO_2/Ti_3C_2(140,12), and TiO_2/Ti_3C_2(160,6), were grouped as one cluster (indicated with dark green). The second cluster (indicated with purple) was formed by samples composed of the evidently higher concentration of Ti_3C_2 (in the range from 54.2 to 88.5 wt%) than that of TiO_2 (in the range from 11.5 to 45.8 wt%). The composites with a mass ratio among TiO_2 and Ti_3C_2 of more than one and one-half were grouped together in the third group (indicated with gold). At the same time, the last cluster (indicated with pink) was formed by the samples synthesized at the

three highest synthesis temperatures (i.e., 180, 200, and 220°C) for 24 hours, which in addition were characterized by very low content of Ti_3C_2.

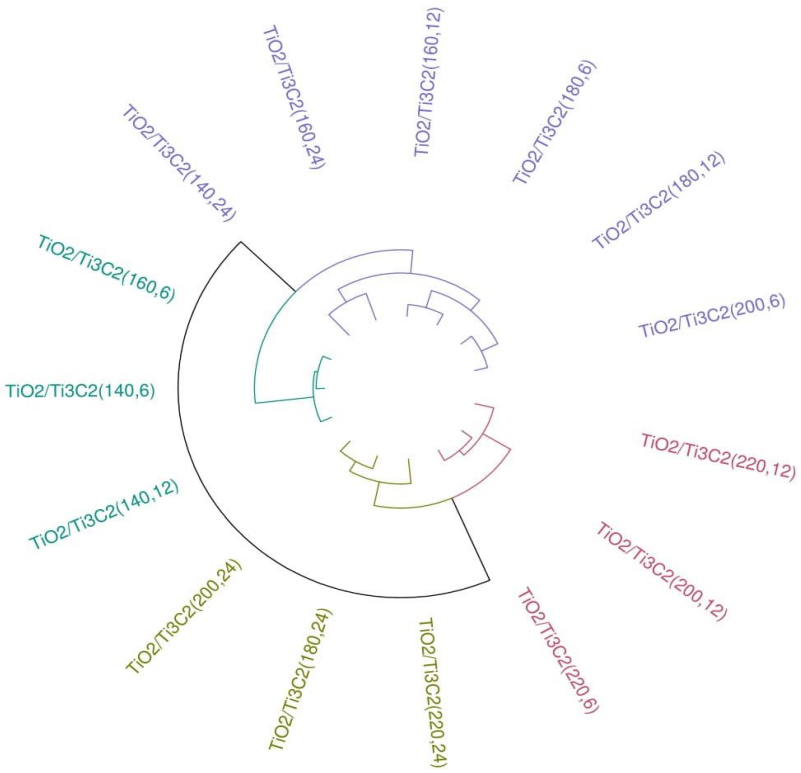

Figure 3S. Circular dendrogram for the hierarchical cluster analysis (HCA) of TiO_2/Ti_3C_2 composites results using Euclidean distance and Ward's linkage clustering.

The correlogram analysis presented in Figure 4S graphically illustrates the associations and amount of variability between variables (expressed as Pearson correlation coefficients, *r*). The interpretation of the correlogram plot provides two important pieces of information on the direction and strength of the relationship for each pair of continuous variables. The colors in the correlogram plot denote the direction of the relationship (negative or positive) between two variables. Blue gray indicates a negative correlation, meaning that increases in the value of one variable tend to be accompanied by decreases in the value of another variable.

Whereas orange represents a positive correlation which implies that the variables are directly related, and thereby when the value of one variable increases, the value of the other variable also tends to increase. The strength of a linear relationship that can be anywhere between −1 and +1 is reflected in the correlogram by the size of the circles. A correlation coefficient close to zero (indicated as small circle) suggests that no linear association exists between two variables. The further away correlation coefficient is from zero (in a positive or negative direction), the stronger the relationship between two variables. A correlation coefficient of ±1 (indicated as big circle) indicates a perfect linear relationship.

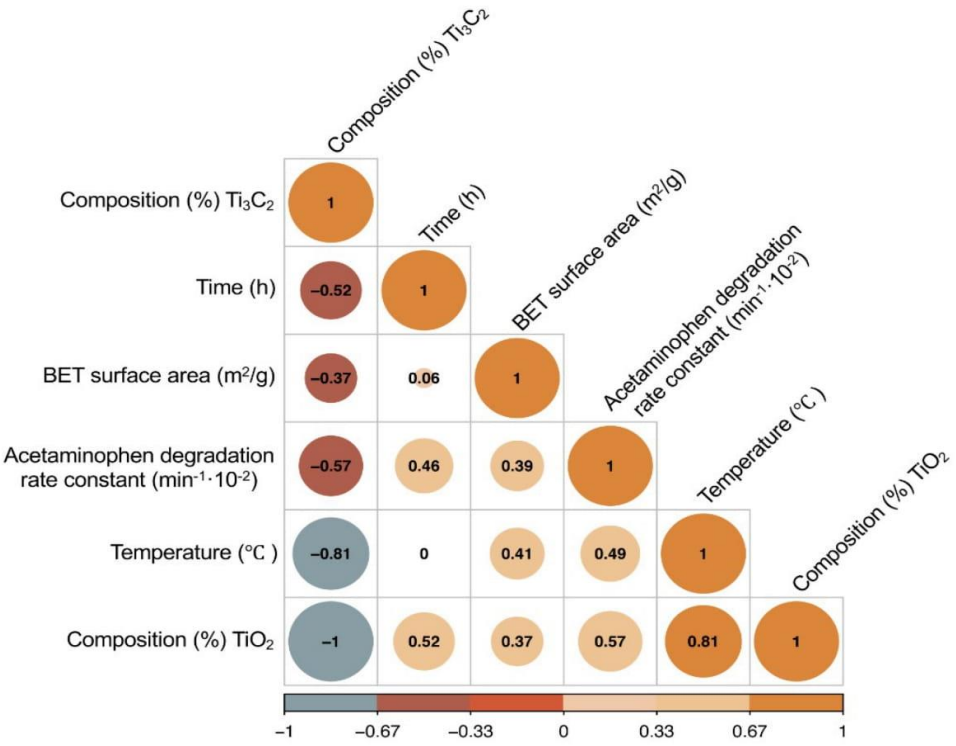

Figure 4S. Correlation matrix that illustrates the strength of a relationship between any two variables, where correlation coefficients, r (in absolute value) less than or equal to 0.35 indicate low or weak correlations, r values between 0.36 and 0.69 refer to moderate correlations, while r values greater than or equal to 0.70 are considered strong or high

correlations. The color of the circle corresponds to the directions of association: positive or negative association (or no association at all). Whereas the size of the circle indicates the strength of a linear relationship: the small circles indicate smallest (insignificant) correlation, and big circles denote highest (significant) correlation.

Table 2S. The details of the developed predictive model

Model for predicting acetaminophen degradation rate constant in the presence of TiO_2/Ti_3C_2 composites		
Kernel function:	Truncated gaussian	
Bandwidth kernel density estimation method:	Adaptive nearest-neighbour bandwidth obtained with least squares cross-validation method	
Bandwidth (the number of nearest neighbours):	Temperature	Mass ratio of TiO_2 to Ti_3C_2
	2	1
Local polynomial's degree:	0 (constant)	
Model's quality metrics:	$R^2 = 0.98$; $RMSE_C = 0.08$ $Q^2_{F1} = 0.84$; $Q^2_{F2} = 0.84$; $Q^2_{F3} = 0.90$; CCC= 0.89; $RMSE_P = 0.23$	

Table 3S. The details of the developed predictive model

ID	Composition (%)*		Temperature (°C)	Mass ratio TiO_2/Ti_3C_2	Set*	Observed acetaminophen degradation rate constant ($min^{-1} \cdot 10^{-2}$)	Predicted acetaminophen degradation rate constant ($min^{-1} \cdot 10^{-2}$)	Residuals
	TiO_2	Ti_3C_2						
TiO_2/Ti_3C_2(140,6)	0	100	140	0.00	T	0.22	0.32	-0.10
TiO_2/Ti_3C_2(140,12)	0	100	140	0.00	V	0.24	0.32	-0.08
TiO_2/Ti_3C_2(160,6)	0	100	160	0.00	T	0.28	0.35	-0.07
TiO_2/Ti_3C_2(180,6)	13.5	86.5	180	0.16	T	0.99	1.02	-0.03
TiO_2/Ti_3C_2(220,12)	85.9	14.1	220	6.09	V	0.99	1.22	-0.23
TiO_2/Ti_3C_2(140,24)	11.5	88.5	140	0.13	T	1.01	0.97	0.04
TiO_2/Ti_3C_2(200,24)	98.8	1.2	200	82.33	T	1.03	1.12	-0.09
TiO_2/Ti_3C_2(200,6)	31.6	68.4	200	0.46	V	1.14	1.44	-0.30
TiO_2/Ti_3C_2(180,24)	81.7	18.3	180	4.46	T	1.22	1.22	0.00
TiO_2/Ti_3C_2(200,12)	69.8	30.2	200	2.31	T	1.24	1.24	0.00
TiO_2/Ti_3C_2(220,6)	63.9	36.1	220	1.77	V	1.37	1.24	0.13
TiO_2/Ti_3C_2(160,12)	18.6	81.4	160	0.23	T	1.66	1.48	0.18
TiO_2/Ti_3C_2(160,24)	45.8	54.2	160	0.85	T	1.89	1.85	0.04
TiO_2/Ti_3C_2(180,12)	42.4	57.6	180	0.74	V	2.04	1.72	0.32
TiO_2/Ti_3C_2(220,24)	99.8	0.2	220	499.00	T	2.86	2.86	0.00
TiO_2/Ti_3C_2(test-1)	4	96	170	0.04	P	-	0.41	-
TiO_2/Ti_3C_2(test-2)	10	90	170	0.11	P	-	0.93	-
TiO_2/Ti_3C_2(test-3)	20	80	210	0.25	P	-	1.30	-

TiO_2/Ti_3C_2(test-4)	25	75	150	0.33	P	-	1.63	-
TiO_2/Ti_3C_2(test-5)	40	60	200	0.67	P	-	1.44	-
TiO_2/Ti_3C_2(test-6)	70	30	190	2.33	P	-	1.25	-
TiO_2/Ti_3C_2(test-7)	90	10	200	9.00	P	-	1.20	-
TiO_2/Ti_3C_2(test-8)	50	50	160	1	P	-	1.84	-

* T - training set, V - test set, P - prediction set

3.2. The effect of reaction environment on TiO_2/Ti_3C_2 composites physicochemical properties and photocatalytic activity

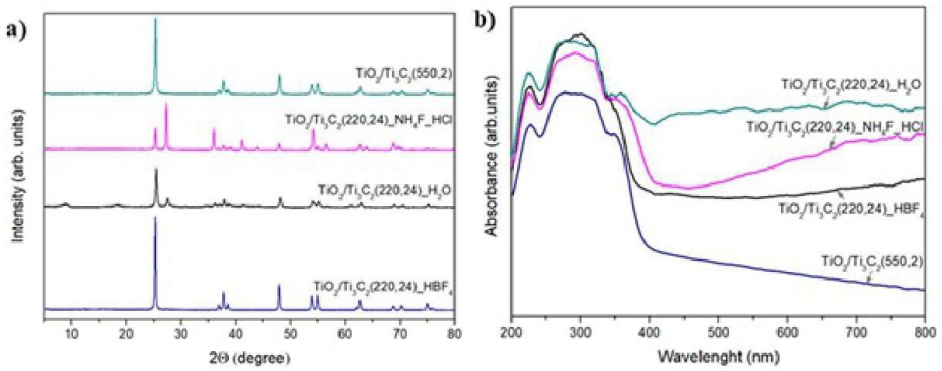

Figure 5S. The X-ray diffractograms (a) and DR/UV-vis spectra (b) for TiO_2/Ti_3C_2 composites

Table 4S. The physicochemical characteristics of prepared TiO_2/Ti_3C_2 composites

Sample	Crystallite size (nm)		Bandgap energy	BET surface area
	anatase	rutile	(eV)	(m^2/g)
TiO_2/Ti_3C_2(220,24)_HBF_4	34	-	2.98	10.0
TiO_2/Ti_3C_2(220,24)_H_2O	31	26	3.10	26.4
TiO_2/Ti_3C_2(550,2)	34	-	3.07	16.7
TiO_2/Ti_3C_2(220,24)_NH_4F_HCl	42	44	2.80	13.3

Table 5S. Lattice parameters of TiO_2/Ti_3C_2 composites

Sample	**Lattice parameters**
TiO_2/Ti_3C_2(220,24, H_2O)	**a=b (Å)**	**c (Å)**
Anatase	3.77	9.49
Rutile	4.58	2.88
TiO_2/Ti_3C_2(220,24, NH_4F, HCl)	**a=b (Å)**	**c (Å)**
Anatase	3.79	9.52
Rutile	4.61	2.97
TiO_2/Ti_3C_2(550,4)	**a=b (Å)**	**c (Å)**
Anatase	3.79	9.52
TiO_2/Ti_3C_2(220,24 HBF_4)	**a=b (Å)**	**c (Å)**
Anatase	3.79	9.51

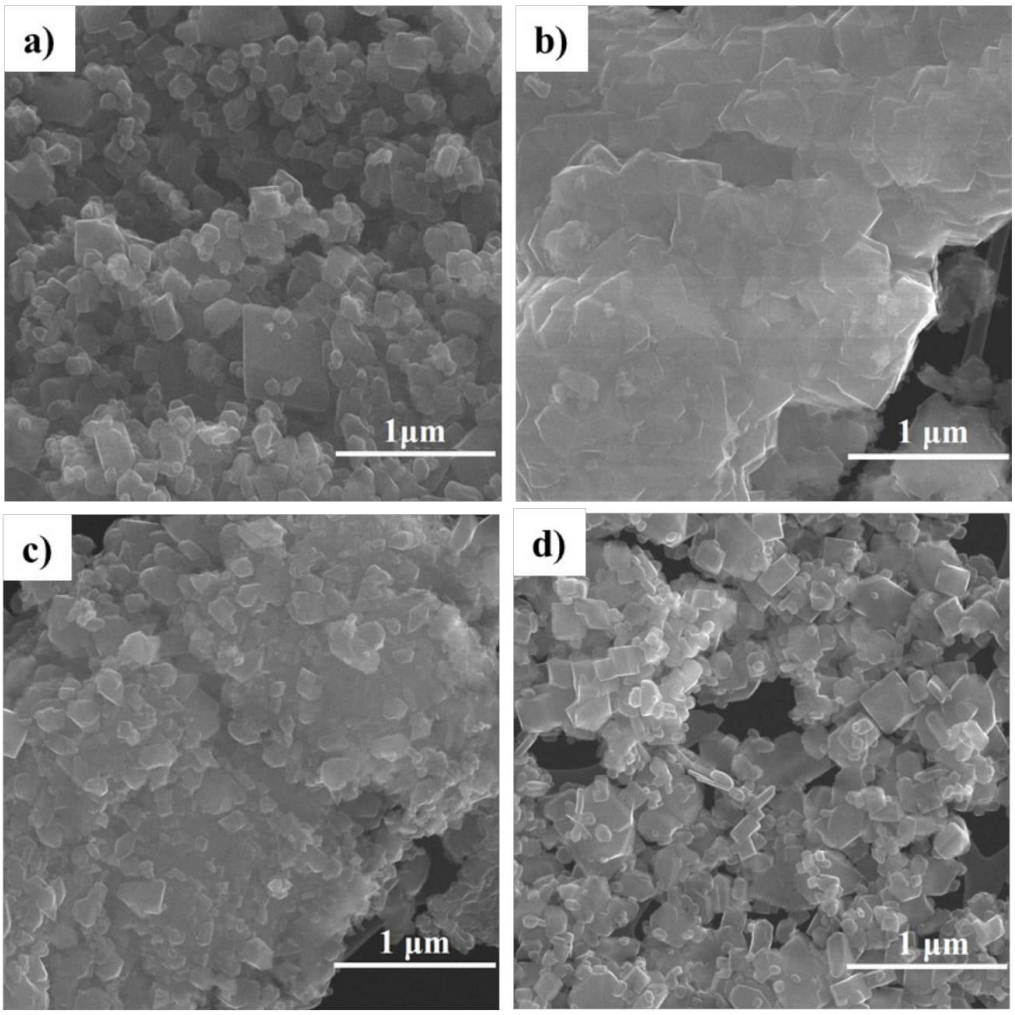

Figure 6S. The SEM images of a) $TiO_2/Ti_3C_2(220,24)\_HBF_4$, b) $TiO_2/Ti_3C_2(220,24)\_H_2O$ c) $TiO_2/Ti_3C_2(550,2)$ d) $TiO_2/Ti_3C_2(220,24)\_NH_4F\_HCl$

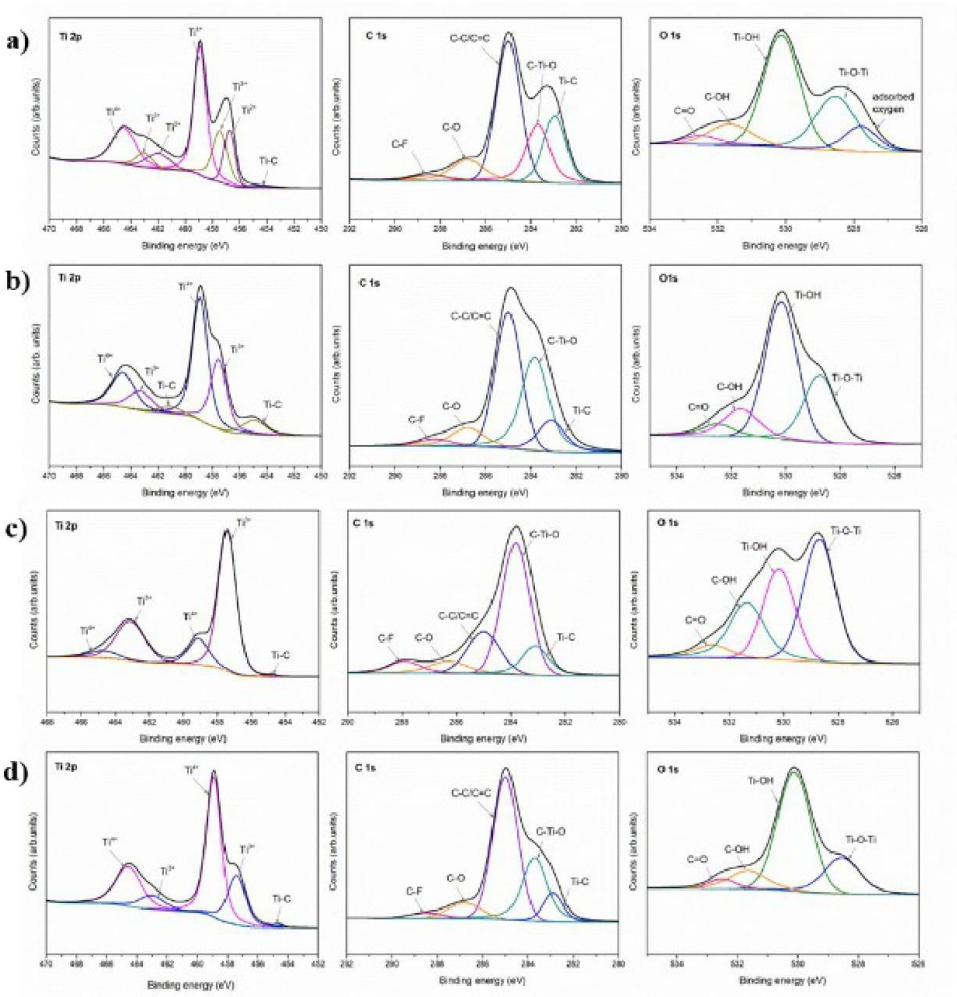

Figure 7S. The XPS spectra of Ti 2p, C1s, and O 1s regions for a) $TiO_2/Ti_3C_2(220,24)\_HBF_4$ b) $TiO_2/Ti_3C_2(220,24)\_H_2O$ c) $TiO_2/Ti_3C_2(550,2)$ d) $TiO_2/Ti_3C_2(220,24)\_NH_4F\_HCl$

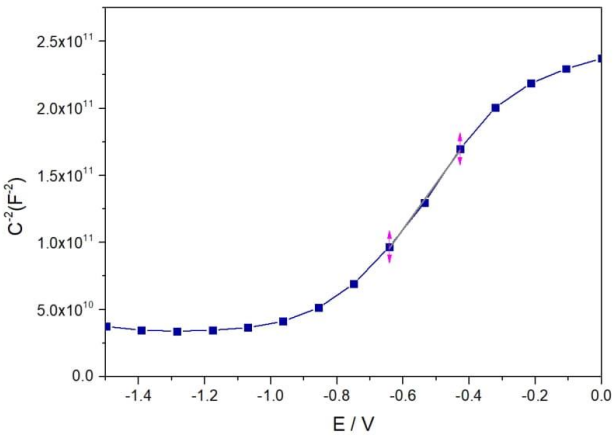

Figure 8S. The Mott-Schottky plot for sample TiO_2/Ti_3C_2(220,24)_NH_4F_HCl

Table 6S. The comparison of this work with results presented in recent literature for photocatalytic degradation of ACT

Photocatalyst	Photocatalyst loading (g/dm^3)	ACT concentration (mg/dm^3)	Light source	Degradation efficiency	Ref.
Fe_2O_3-TiO_2	1.25	30	Solar simulator	95.8% Within 3 h	[7]
Ti-Zr metal-organic-frameworks	0.25	5	Solar simulator with Xe lamp	100% within 3 h	[8]
TiO_2/Fe-C	0.25	5	Solar simulator with Xe lamp	100% within 6 h	[9]
Ag/NH_2-MIL-125	0.25	5	Solar simulator with Xe lamp	100% within 3 h	[10]
Sr@TiO_2/UiO-66-NH_2	0.25	5	Solar simulator with Xe lamp	93% within 4 h	[11]
Cu_2O/WO_3/TiO_2	0.25	1	Xe lamp	92.5% within 1 h	[12]
carbon xerogel/TiO_2	2	25	Hg lamp	96% within 4 h	[13]
TiO_2/Ti_3C_2	2	20	Xe lamp	92% within 1 h	this work

References

[1] Murtagh, F., Contreras, P., (2012) WIREs Data Min. Knowl. Discov. 2, 86–97. doi.org/10.1002/widm.53.

[2] Jolliffe, I. T., & Cadima, J. (2016). Physical and Engineering Sciences, 374, 20150202. doi.org/10.1098/rsta.2015. 0202.

[3] Gu, Z., Gu, L., Eils, R., Schlesner, M., Brors, B. (2014) Bioinformatics 30, 2811 doi.org/10.1093/bioinformatics/btu393

[4] Tal Galili (2015). dendextend: an R package for visualizing, adjusting, and comparing trees of hierarchical clustering. Bioinformatics. doi:10.1093/bioinformatics/btv428

[5] Alboukadel Kassambara and Fabian Mundt (2020). factoextra: Extract and Visualize the Results of Multivariate Data Analyses. R package version 1.0.7. https://CRAN.R-project.org/package=factoextra

[6] H. Wickham. ggplot2: Elegant Graphics for Data Analysis. Springer-Verlag New York, (2009) doi.org/10.1007/978-0-387-98141-3

[7] Khasawneh, O. F. S., Palaniandy, P., Ahmadipour, M., Mohammadi, H., & Bin Hamdan, M. R. (2021). Journal of Environmental Chemical Engineering, 9(1), 104921. doi.org/10.1016/j.jece.2020.104921

[8] Gómez-Avilés, A., Peñas-Garzón, M., Bedia, J., Dionysiou, D., Rodríguez, J., & Belver, C. (2019). Applied Catalysis B: Environmental, 253, 253-262. doi.org/10.1016/j.apcatb.2019.04.040

[9] Peñas-Garzón M, Gómez-Avilés A, Bedia J, Rodriguez JJ, Belver C. (2019) Materials 12(3), 378. doi.org/10.3390/ma12030378

[10] Muelas-Ramos, V., Belver, C., Rodriguez, J., & Bedia, J. (2021). Separation and Purification Technology, 272, 118896. doi.org/10.1016/j.seppur.2021.118896

[11] Wang, Y., Peñas-Garzón, M., Rodriguez, J., Bedia, J., & Belver, C. (2022). Chemical Engineering Journal, 446, 137229. doi.org/10.1016/j.cej.2022.137229

[12] Chau, J. H. F., Lai, C. W., Leo, B. F., Juan, J. C., & Johan, M. R. (2022). Catalysis Communications, 163, 106396. doi.org/10.1016/j.catcom.2022.106396

[13] da Cunha, R., do Carmo Batista, W. V. F., de Oliveira, H. L., dos Santos, A. C., dos Reis, P. M., Borges, K. B., Martelli, P. B., Furtado, C. A., & de Fátima Gorgulho, H. (2021). Journal of Photochemistry and Photobiology A: Chemistry, 412, 113248. doi.org/10.1016/j.jphotochem.2021.113248

Rozdział V. Magnetically recyclable TiO_2/MXene/$MnFe_2O_4$ photocatalyst for enhanced peroxymonosulphate-assisted photocatalytic degradation of carbamazepine and ibuprofen under simulated solar light

Journal of Environmental Chemical Engineering 11 (2023) 110660

Contents lists available at ScienceDirect

Journal of Environmental Chemical Engineering

journal homepage: www.elsevier.com/locate/jece

Magnetically recyclable TiO_2/MXene/$MnFe_2O_4$ photocatalyst for enhanced peroxymonosulphate-assisted photocatalytic degradation of carbamazepine and ibuprofen under simulated solar light

Anna Grzegórska [a,*], Joseph Chibueze Ofoegbu [b], Laura Cervera-Gabalda [c], Cristina Gómez-Polo [c], Diana Sannino [b], Anna Zielińska-Jurek [a,*]

[a] Department of Process Engineering and Chemical Technology, Faculty of Chemistry, Gdańsk University of Technology, G. Narutowicza 11/12, 80 233 Gdańsk, Poland
[b] Department of Industrial Engineering, University of Salerno, via Giovanni Paolo II, 132, 84084 Fisciano, Italy
[c] Departamento de Ciencias-INAMAT2, Universidad Pública de Navarra, Campus de Arrosadia, 31006 Pamplona, Spain

ARTICLE INFO

Editor: Luigi Rizzo

Keywords:
Carbamazepine
Ibuprofen
Magnetic separation
MXene
Photocatalysis
TiO_2
Ti_3C_2

ABSTRACT

In this study, a novel $TiO_2/Ti_3C_2/MnFe_2O_4$ magnetic photocatalyst with dual properties, enabling (i) improved photocatalytic degradation with PMS activation under simulated solar light and (ii) magnetic separation after the degradation process in an external magnetic field was developed and applied for the efficient photodegradation pharmaceutically active compounds (PhACs) frequently present in wastewater and surface waters worldwide. MXene was used as a Ti precursor for anatase/rutile synthesis and as a co-catalyst in the photodegradation process. Manganese ferrite with ferrimagnetic properties was coupled with the TiO_2/Ti_3C_2 composite to facilitate the magnetic separation after the purification process in an external magnetic field. Moreover, $MnFe_2O_4$ was used for PMS activation, producing $\bullet SO_4$ radicals with a strong oxidation ability and higher redox potential of 2.5–3.1 V (vs. NHE) than •OH radicals with a standard oxidation–reduction potential of 2.8 V. The effect of the manganese ferrite content in the composite structure (5 wt% and 20 wt%) on the physicochemical properties and photocatalytic activity of the magnetic photocatalyst was investigated. Furthermore, the most photocatalytic active composite of TiO_2/MXene/5%$MnFe_2O_4$ was used for peroxymonosulphate-assisted photocatalytic degradation of ibuprofen and carbamazepine. The effect of peroxymonosulphate concentration (0.0625 mM, 0.125 mM, and 0.25 mM) and the synergistic effect of PMS activation on photocatalytic degradation was studied. Based on the obtained results, it was found that TiO_2/MXene/5%$MnFe_2O_4$/PMS process is an efficient advanced treatment technology for the oxidation of emerging contaminants that are not susceptible to biodegradation. Carbamazepine and ibuprofen were completely degraded within 20 min and 10 min of the PMS-assisted photodegradation process under simulated solar light. The trapping experiments confirmed that $\bullet SO_4$ and $\bullet O_2$ are the main oxidising species involved in the CBZ degradation, while $\bullet SO_4$ and h^+ in the IBP degradation. Furthermore, introducing interfering ions of Na^+, Ca^{2+}, Mg^{2+}, Cl^-, and SO_4^{2-} in the model seawater did not affect the removal efficiency of both pharmaceuticals. In terms of reusability, the performance of the TiO_2/MXene/5% $MnFe_2O_4$/PMS photocatalyst was stable after four subsequent cycles of carbamazepine and ibuprofen degradation.

1. Introduction

Emerging contaminants in aquatic systems arising from drug residues have received great attention recently. All these compounds may be excreted into the environment as a mixture of the parent compound and its metabolites because they are only partially degraded and removed in biological wastewater treatment plants [1,2] Moreover, some of them undergo various attenuation processes, including biotransformation, photolysis, sorption, and volatilisation [3].

Among them, ibuprofen (IBP) and carbamazepine (CBZ) are the most frequently detected drugs in aquatic ecosystems [4]. Ibuprofen (IBP) is a non-steroidal anti-inflammatory drug with nearly 200 tons worldwide annual consumption. Carbamazepine (CBZ) is an anticonvulsant and antiepileptic pharmaceutical, with worldwide consumption above 1000

* Corresponding authors.
E-mail addresses: anna.grzegorska@pg.edu.pl (A. Grzegórska), annjurek@pg.edu.pl (A. Zielińska-Jurek).

https://doi.org/10.1016/j.jece.2023.110660
Received 16 May 2023; Received in revised form 20 July 2023; Accepted 27 July 2023
Available online 28 July 2023

tons per year, which is also used in the treatment of trigeminal neuralgia, a chronic pain disorder [5].

The concentrations of both pharmaceuticals in wastewater treatment plant effluents range from hundreds ng/dm^3 to tens of μg/dm^3. The effluents from Portugal WWTPs contained 1059 ng/dm^3 of CBZ and 217 ng/dm^3 of IBP [6]. Meanwhile, IBP has been detected in the Tunisia WWTPs effluent from 8 to 43 μg/dm^3. The concentration of CBZ was determined at a level between 60 and 132 μg/dm^3 [7]. Carbamazepine has also been detected in coastal and offshore seawaters of the Baltic Sea, where the concentrations were low. However, due to the long turnover time and low removal efficiency, a stock of over 55 t of carbamazepine has accumulated in the Baltic Sea waters [8]. Carbamazepine and ibuprofen can generate subtle effects on aquatic and terrestrial organisms. For example, carbamazepine and ibuprofen can modify physiological and biochemical processes in Senegalese sole (Solea senegalensis) and interfere with the biosynthesis of enzymes involved in the osmoregulatory process [9]. Therefore, improving water treatment technology is the active subject matter of actual research to protect ecosystems, increase water quality and ensure the sustainability of water cycle management.

The advanced oxidation processes (AOP), based on the in-situ generation of the strongest oxidants - hydroxyl radicals and sulphate radicals, have been recognised as a promising approach for wastewater treatment from residues of recalcitrant and emerging organic contaminants [10,11]. Among the AOPs, ozonation and UV irradiation have already been established and started at full scale for the treatment of drinking water and the facilities of water reuse. Recently, the photo-Fenton process, UV/O_3, and UV/H_2O_2 have been commonly applied to remove persistent organic compounds such as carbamazepine and ibuprofen to strengthen the oxidation capability [12–15]. Nevertheless, ozonation is restricted by the high cost of ozone and low mineralisation efficiency, while the Fenton process usually operates under a limited pH range (3–4) and generates $Fe(OH)_3$ precipitation [16–18]. The photocatalysis process is a promising intensification approach in AOPs, owing to the generation of electron-hole pairs under light irradiation and the production of reactive oxygen species. At present, solar-induced chemical processes, such as photocatalysis, are limited by low quantum efficiencies [19].

In this regard, the twofold strategy to optimise photocatalyst structure towards the degradation of selected PhACs was investigated in this study. Previously, it was reported that the hybridisation of semiconductor with graphene-related materials improve charge carriers mobility [20]. Recently, MXenes, the family of early transition metal carbides, have been proposed as advanced carbon-based materials, which may act as co-catalysts, enhancing the adsorption of the pollutants on the surface, photocatalyst stability, and increasing the light absorption range. Significantly in situ oxidation of MXene $Ti_3C_2T_x$ led to the formation of TiO_2/Ti_3C_2 composite with intimate contact providing effective charge carriers separation. Therefore, Ti_3C_2/TiO_2 composites have been proposed as advanced candidates with high efficiency in photocatalytic process [21,22]. This hybrid material with strong bonding possesses minimised defects at the interfaces [23,24]. Based on the studies performed in our group, we showed markedly enhanced photocatalytic activity of accordion-like TiO_2/Ti_3C_2 composites with exposed {1 0 1} and {0 0 1} TiO_2 crystal facets [21,22].

Furthermore, considering the difficulties of separation and recycling of photocatalyst nanoparticles from wastewater after the successful micropollutants degradation, the hybridisation of semiconductor material with magnetic particles enables efficient photocatalyst recovery from post-process suspension with the assistance of an external magnetic field [25,26]. Previously, spinel ferrites with a formula of AFe_2O_4, where A is a transition or alkaline earth metallic cation (Mn, Zn, Co, Ni, or Mg), were applied for photocatalyst separation [27,28]. Among the various studied magnetic nanomaterials, $MnFe_2O_4$ nanoparticles have attracted great attention due to their low cost, high chemical stability, and non-toxicity [29]. Simultaneously, Mn and Fe ions may activate peroxymonosulphate through an electron-transport strategy mediated by the variable-valence metal sites [30].

Therefore, in this study, TiO_2/MXene/$MnFe_2O_4$ composite was synthesised and applied for the photocatalytic degradation of the PhACs mixture under simulated solar light irradiation. To further increase the degradation efficiency of ibuprofen and carbamazepine, the photocatalytic process was combined with the PMS activation. MXene - Ti_3C_2 was used as a Ti precursor for anatase/rutile TiO_2 formation and co-catalyst, and $MnFe_2O_4$ particles embedded in the structure of TiO_2/Ti_3C_2 played a dual role of magnetic part providing easy separation after the purification process and activation of PMS, to produce $\bullet SO_4^-$ radicals.

In the presence of transition metals (Fe, Cu, Mn, Co), PMS may effectively produce sulphate radicals with strong oxidation ability [31,32]. The sulphate radical ($\bullet SO_4^-$) possesses a close or even higher redox potential of 2.5–3.1 V (vs. NHE) compared to hydroxyl radical (E_0 =1.8–2.8 V) [33,34]. Moreover, sulphate radicals have higher selectivity, longer half-life (30–40 μs), and could be activated in the broader pH range from 2 to 8 than •OH radicals [35]. The effect of PMS concentration, pH, and interfering ions on the efficiency of photocatalytic processes of CBZ and IBP mixture photodegradation was studied in detail. Furthermore, the trapping experiments with scavengers were performed to determine the major reactive species participating in the TiO_2/MXene/$MnFe_2O_4$/PMS degradation process. Finally, the composite stability and reusability were tested in subsequent cycles of PhACs photocatalytic degradation.

2. Experimental

2.1. Materials

The MAX phase compound – Ti_3AlC_2 was provided by Luoyang Tongrun Info Technology Co. (China). The hydrofluoric acid (ACS reagent, 48%), NH_4F (ACS reagent, ≥ 98.0%), $MnCl_2$ (≥99% trace metals basis), and $FeCl_3{\cdot}6\,H_2O$ (ACS reagent, 97%) were purchased from Sigma Aldrich. HCl (35–38%) and NaOH (pure p.a.) were provided by Chempur (Poland). Carbamazepine (Certified Reference Material) and Ibuprofen (≥ 98% (GC)) for the photocatalytic degradation process were provided by Sigma Aldrich. Potassium peroxymonosulphate (OXONE) was provided by Sigma Aldrich. The reagents were used as received with no further purification. Scavengers: tert-butanol (anhydrous, 99.5%), isopropanol (anhydrous, 99.5%), p-benzoquinone (reagent grade, ≥ 98%), and ammonium oxalate monohydrate (ACS reagent, ≥ 99%) for trapping experiments and reagents for model seawater: $CaCl_2$ (anhydrous, powder, 99.99% trace metals basis), $MgCl_2$ (anhydrous, ≥98%), Na_2SO_4 (ACS reagent, ≥99.0%, anhydrous, powder), and NaCl (ACS reagent, ≥99.0%) were supplied by Sigma Aldrich. Acetonitrile (HPLC grade) and H_3PO_4 (85%, HPLC grade) were used to determine the concentration of CBZ and IBU by HPLC and were provided by Sigma Aldrich. Deionised water (DI) was used in all experiments.

2.2. Synthesis of $MnFe_2O_4$

The magnetic nanoparticles were prepared by dissolving in 100 cm^3 of deionised water (DI), $FeCl_3{\cdot}6\,H_2O$ and $MnCl_2$ in the molar ratio of 2:1. Next, 0.5 M NaOH solution was added dropwise until the pH reached 10. The suspension was transferred into a Teflon-lined stainless steel reactor. The reaction was performed at 180 °C for 6 h. The resulting material was separated with a magnet, washed 3 times with DI water, and dried at 50 °C to dry mass.

2.3. Preparation of $Ti_3C_2T_x$ and TiO_2/Ti_3C_2

The $Ti_3C_2T_x$ was obtained by aluminium etching from MAX phase compound – Ti_3AlC_2. In a typical process, 10 g of Ti_3AlC_2 was added gradually to 100 cm^3 of 48% HF and mixed at room temperature for 24 h. Next, the material was centrifuged and washed with DI water until

neutral pH.

To prepare the TiO_2/Ti_3C_2 composite, 60 cm^3 of 3 M HCl was mixed with 0.1 g NH_4F. Next, 0.4 g of $Ti_3C_2T_x$ was added to the above mixture and sonicated for 10 min. Then the suspension was mixed for 30 min and transferred into a Teflon-lined stainless steel reactor. The reaction was performed at 220 °C for 24 h. The resulting material was washed several times with DI water and dried at 50 ℃ to dry mass.

2.4. Preparation of $MnFe_2O_4/TiO_2/Ti_3C_2$ composite

The composites with 5 wt% and 20 wt% of $MnFe_2O_4$ were prepared by ultrasonic-assisted self-assembly approach. In this regard, 0.5 g of TiO_2/Ti_3C_2 was dispersed in 50 cm^3 of water/ethanol mixture (1:4 v/v), while an appropriate amount of $MnFe_2O_4$ was dispersed similarly in 50 cm^3 of water/ethanol mixture (1:4 v/v), separately. Both suspensions were sonicated in the bath for 15 min. After that, $MnFe_2O_4$ dispersion was added dropwise to TiO_2/Ti_3C_2 suspension under sonication. As prepared material was mixed for 1 h using a mechanical stirrer. The prepared composite was separated with a magnet and washed 3 times with DI water. Finally, it was dried at 50 ℃ to dry mass.

2.5. Characterisation of as-obtained materials

The crystal structure of the samples was characterised by the powder X-ray diffraction method using the Rigaku Intelligent X-ray diffraction (XRD) system SmartLab (Rigaku Corporation, Tokyo, Japan). The diffractograms were obtained in a 2θ range of 5–80°, with a speed of $2°\cdot min^{-1}$ and a step of 0.01°. The quantitative phase analysis was performed using the Rietveld refinement with X'Pert HighScore Plus.

Specific surface areas were estimated through the BET model (Brunauer-Emmett-Teller) at 77 K (boiling point of liquid nitrogen) with the Micromeritics Gemini V apparatus (model 2365) (Norcross, GA, USA). Samples were degassed under N_2 at 200 °C for 2 h before the measurements.

A ThermoScientific Evolution 220 spectrophotometer (Waltham, MA, USA) was used to record the UV–vis diffuse reflectance spectra (DRS). The measurements were performed in the wavelength range from 200 nm to 800 nm, using barium sulphate as a standard reference.

The morphologies of the synthesised materials were examined by scanning electron microscopy (SEM) using SEM Microscope FEI Quanta FEG 250. Transmission electron microscope (TEM) analyses were performed using (S)TEM Titan3 G2 60–300 with detector Super-X detector (Thermo Fisher Scientific).

A SQUID magnetometer (Quantum Design MPMS XL7) was employed to magnetically characterise the samples (room temperature hysteresis loops and magnetisation versus temperature, 10 −300 K).

The X-ray photoelectron spectroscopy (XPS) measurements were performed using Escalab 250Xi multispectroscope (ThermoFisher Scientific) with a monochromatic AlKα X-ray source. The high-resolution spectra were registered in the core-level binding energy range of Ti 2p, C 1 s, and O 1 s at pass energy of 20 eV.

The photoluminescence spectra (PL) were registered using a spectrofluorometer Shimadzu RF-6000 (Kyoto, Japan). As an excitation source, a 150 W Xenon lamp was used with an excitation wavelength of 300 nm.

The Fourier-transform infrared spectroscopy (FTIR) spectra were recorded using Nicolet iS10 FT-IR Spectrometer (Thermo Fisher Scientific Inc., MA, USA) in the transmittance mode in the wavenumber range from 400 to 4000 cm^{-1}.

Electrochemical impedance spectra were registered with potentiostat/galvanostat Metrohm Autolab PGSTAT204 in the range between 10^5 and 0.1 Hz with AC voltage amplitude equal to 0.01 V. Samples were placed on the carbon screen-printed electrode with Ag reference electrode. The electrolyte solution (0.5 M Na_2SO_4) was purged with argon for 10 min prior to the measurements. The Mott Schottky analysis was performed to determine the flat band (F_b) potential of the TiO_2/Ti_3C_2 composite and $MnFe_2O_4$. The EIS data were recorded from the anodic towards a cathodic direction for the applied frequency of 1000 Hz in the potential range from 0 to − 1.8 V. Transient photocurrent response of photocatalysts was recorded at the light on/off interval equal 25 s at 0 V vs. Ag under 372 nm LED light illumination.

Thermogravimetric analysis (TGA) was performed using a thermogravimetric analyser 2 SF/1100 from Mettler Toledo. The conditions of the measurement were: airflow 10 cm^3/min, temperature range: 25–750 °C, heating rate 10 °C/min.

ICP-OES measurement was performed based on the Polish Standard PN-EN-ISO-11885_2009E. Iron Photmetric Test Kit (0.01–1 mg/dm^3) and spectrophotometer DR5000 (HACH LANGE) with a wavelength of 485 nm were used to determine iron content in the post-process solution.

2.6. Photocatalytic degradation analyses

Typically, 0.05 g of the photocatalyst was dispersed in 25 cm^3 of the mixture of carbamazepine (7 mg/dm^3) and ibuprofen (10 mg/dm^3) solution (pH 6.7, initial TOC value of 13.3 mg/dm^3). The photocatalytic experiment was performed in a 25 cm^3 reactor with a quartz window equipped with an airflow. As a light source, imitating the sunlight spectrum, a 300 W Xe lamp (LOT Oriel, Darmstadt, Germany) with a light flux in the UV range (310 nm $< \lambda <$ 380 nm) equalled 35 $mW\cdot cm^{-2}$ was operated. Before irradiation, the photocatalyst suspension was kept in the dark for 30 min to reach adsorption-desorption equilibrium. During the photodegradation process, 1 cm^3 of the suspension was collected at 0, 20, 40, and 60 min and separated using a 0.2 μm syringe filter. The rate of pharmaceutical degradation was controlled using reverse-phase high-performance liquid chromatography (Shimadzu UFLC LC-20AD (Kyoto, Japan) with a photodiode array detector (Shimadzu SPD-M20A). The analyses were performed at 45 °C and under isocratic flow conditions of 1.5 $cm^3\cdot min^{-1}$ for carbamazepine and 0.5 $cm^3\cdot min^{-1}$ for ibuprofen. A volume composition of the mobile phase of 70% acetonitrile, 29.5% water, and 0.5% orthophosphoric acid was used to determine ibuprofen concentration, while 60% water, 39.5% acetonitrile, and 0.5% orthophosphoric acid to determine carbamazepine concentration. The change in total organic carbon (TOC) during the photocatalytic process was analysed using a Shimadzu TOC analyser.

Further experiments were performed with the addition of PMS to the suspension (concentration in CBZ/IBU solution equal to 0.0625 mM, 0.125 mM, or 0.25 mM). After the addition of PMS (0.25 mM), the initial pH of the solution decreased to 5.2. The samples (1 cm^3) were collected and filtrated during the photocatalytic process, and after that 200 μL of methanol was added to quench the radical species.

Further analyses were conducted in the model seawater to evaluate the effect of interfering ions on the efficiency of photocatalytic processes of CBZ and IBP mixture removal. The model seawater contained 2.5% NaCl, 1.1% $MgCl_2$, 0.4% Na_2SO_4, and 0.16% $CaCl_2$ in DI water. Moreover, the effect of the solution pH was investigated. The solution pH was adjusted with 0.1 M HCl or 0.1 M NaOH to values 4.5 and 9.5, respectively.

The radical trapping experiments were carried out under the same conditions in the presence of scavengers (with a concentration equal to the 10-fold concentration of contaminant). Ammonium oxalate (AO) was applied as a hole scavenger (h^+), tert-butanol (t-But) for free hydroxyl radicals (•OH), isopropanol (iPr) for hydroxyl radicals and sulphate radicals (•OH and $•SO_4$) and p-benzoquinone (BQ) for superoxide radical anions ($•O_2$) scavenging test.

In order to evaluate the stability and recyclability of the photocatalyst/PMS system, after each process, the photocatalyst was separated from the solution, and a fresh portion of the pharmaceuticals mixture was poured with the addition of PMS. The photocatalyst was used without any additional treatment. The photocatalytic performance was evaluated within four subsequent cycles under the same reaction conditions.

3. Results and discussion

3.1. Characterization of $MnFe_2O_4$, TiO_2/Ti_3C_2 and $TiO_2/Ti_3C_2/MnFe_2O_4$ photocatalysts

The XRD patterns of Ti_3AlC_2 and $Ti_3C_2T_x$ after Al etching are presented in Fig. 1a. The presence of diffraction signals at $2\Theta = 8.9°$, 18.2°, and 27.5° corresponding to (002), (004), and (006) planes confirmed the successful formation of MXene. Moreover, the XRD analysis was used to determine the phase composition of the $MnFe_2O_4$, TiO_2/Ti_3C_2, and $TiO_2/Ti_3C_2/MnFe_2O_4$, as shown in Fig. 1b. The diffraction signals of $MnFe_2O_4$ are assigned to the (220), (311), (400), (422), (511), (440) planes at 29.8°, 34.8°, 42.7°, 52.8°, 56.3°, and 61.9° 2Θ. Diffractogram of TiO_2/Ti_3C_2 includes signals assigned to anatase (101), (004), (200), (211), (204), (116) planes at 25.2°, 37.7°, 47.9°, 55.0°, 62.6°, 68.8°, and rutile (110), (101), (111), (210), (211), (220) planes at 27.3°, 36.0°, 41.1°, 43.9°, 54.2°, 56.4°, respectively. In the XRD pattern of the composite material, signals for anatase, rutile, and $MnFe_2O_4$ were observed. No other signals were noticed, which confirmed the phase-pure crystallographic structure of the obtained photocatalyst. This result also demonstrates that the $MnFe_2O_4$ was successfully combined with TiO_2/Ti_3C_2. The phase distributions (percentage, wt%, of each phase) of prepared materials are listed in Table 1. Based on the Rietveld refinement, the content of the magnetic part ($MnFe_2O_4$) was about 4% for $TiO_2/Ti_3C_2/5\%MnFe_2O_4$ and 17% for $TiO_2/Ti_3C_2/5\%MnFe_2O_4$ composites. However, no signals corresponding to MXene - Ti_3C_2 were observed, probably due to the low content or well dispersion [36,37].

Therefore, to verify the presence of Ti_3C_2 in the composite after solvothermal synthesis, the XPS analysis was performed, and the results are presented in Fig. 2. The survey spectrum is presented in Fig. S2 in the Supporting Materials. The characteristic weak signals for MXene Ti-C and Ti^{3+} bonds (454.5 eV and 457.4 eV) indicated the presence of a small amount of Ti_3C_2. The most intense signal of Ti^{4+} (459 eV) confirmed that the material was almost entirely oxidised to TiO_2 [38, 39].

The C1s spectrum was deconvoluted for five peaks corresponding to Ti-C (283 eV), C-Ti-O (283.5 eV), adventitious carbon (285 eV), C-O (286.7 eV), and C-F bonds (288.5 eV). The O 1 s spectrum confirmed the presence of Ti-OH (528.5 eV) bonds and Ti-O (530 eV), as well as C═O (531.5 eV) and C-O (532.5 eV).

Furthermore, the thermogravimetric (TGA) analysis was performed to confirm the existence of Ti_3C_2 in the composite material. As can be seen in Fig. 3, the 0.7% weight gain from 250 °C to 400 °C was noticed. This change was related to the oxidation of MXene layers to form anatase.

Table 1
The phase compositions of the samples based on Rietveld refinement.

Sample	Anatase (%)	Rutile (%)	$MnFe_2O_4$ (%)
$MnFe_2O_4$	-	-	100
TiO_2/Ti_3C_2	40	60	-
$TiO_2/Ti_3C_2/5\%MnFe_2O_4$	38	58	4
$TiO_2/Ti_3C_2/20\%MnFe_2O_4$	32	51	17

The ICP-OES and SEM-EDS analyses for $TiO_2/Ti_3C_2/5\%MnFe_2O_4$ sample presented in Table S1 and Fig. S1 in the Supporting Materials confirmed the presence of Ti, Mn and Fe in the composite structure and correlated well with XRD, XPS and TGA analyses results.

The optical properties were characterised by DR/UV–vis, as presented in Fig. 4. The TiO_2/Ti_3C_2 exhibited strong absorption in the UV range with a threshold of about 420 nm. The light absorption in the range above 450 nm resulted from the presence of titanium carbide, which absorbs light within the whole light range [40]. Bandgap energy (E_g) values were calculated according to the Kubelka-Munk function, $(R)^n \cdot E_{ph}^n$ against E_{ph}, where E_{ph} is photon energy, while n has values of n = 2 and 1/2 for indirect ($MnFe_2O_4$) and direct (TiO_2) transition, respectively. The plots are presented in Fig. S3 in the Supporting Material. Furthermore, the estimated E_g values are summarised in Table 2. The manganese ferrite particles exhibited the lowest E_g value of 1.5 eV, which agrees with the literature [41].

The narrow bandgap of TiO_2/Ti_3C_2 resulted from the presence of rutile in the composite structure. Furthermore, the specific surface areas of the photocatalytic materials are presented in Table 2. It can be observed that both components and composite materials possess similar surface areas in the range of 12–13 m^2/g.

The SEM images of TiO_2/Ti_3C_2, $MnFe_2O_4$, and $TiO_2/Ti_3C_2/MnFe_2O_4$ composites are presented in Fig. 5. The TiO_2/Ti_3C_2 composite contained a mixture of various size decahedral and octahedral TiO_2 particles, exposing { 1 0 1} and { 0 0 1} facets. The morphology of the $MnFe_2O_4$ had a spherical shape (average diameter ~ 80 nm) with the presence of the agglomerates, ascribed to relatively stronger interaction among magnetic particles [42].

Furthermore, the TEM analysis was performed to characterise the morphology and microstructure of $TiO_2/Ti_3C_2/5\%MnFe_2O_4$, and the images are shown in Fig. 6. The presence of anatase, rutile, Ti_3C_2, and $MnFe_2O_4$ was noticed. In the corresponding HRTEM image, the d-spacing was ~0.258 nm and ~0.482 nm, respectively, which corresponded to the (111) and (311) planes of $MnFe_2O_4$. For anatase, d-spacing of ~0.351 nm was assigned to the (101) planes, while for rutile, ~0.215 nm and ~0.323 nm were assigned to the (111) and (110)

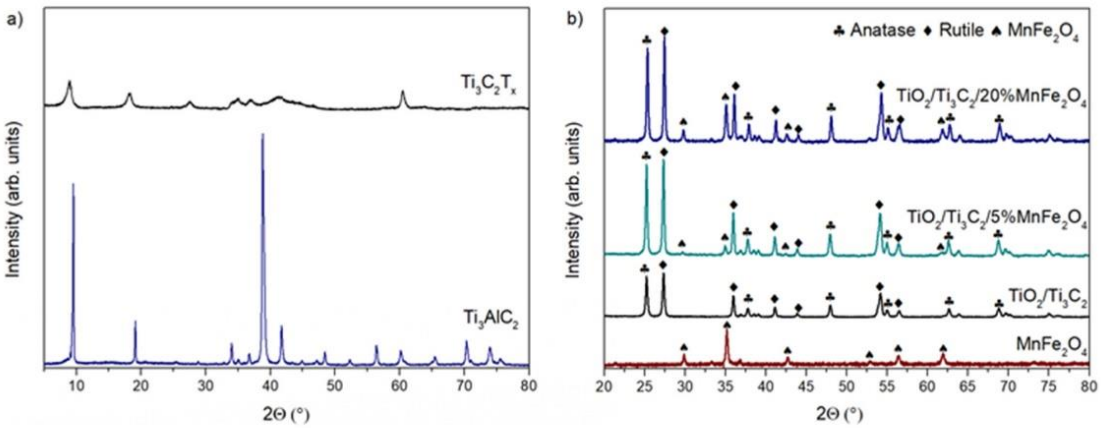

Fig. 1. The XRD diffractograms for Ti_3AlC_2 and $Ti_3C_2T_x$ (a) and prepared materials (b).

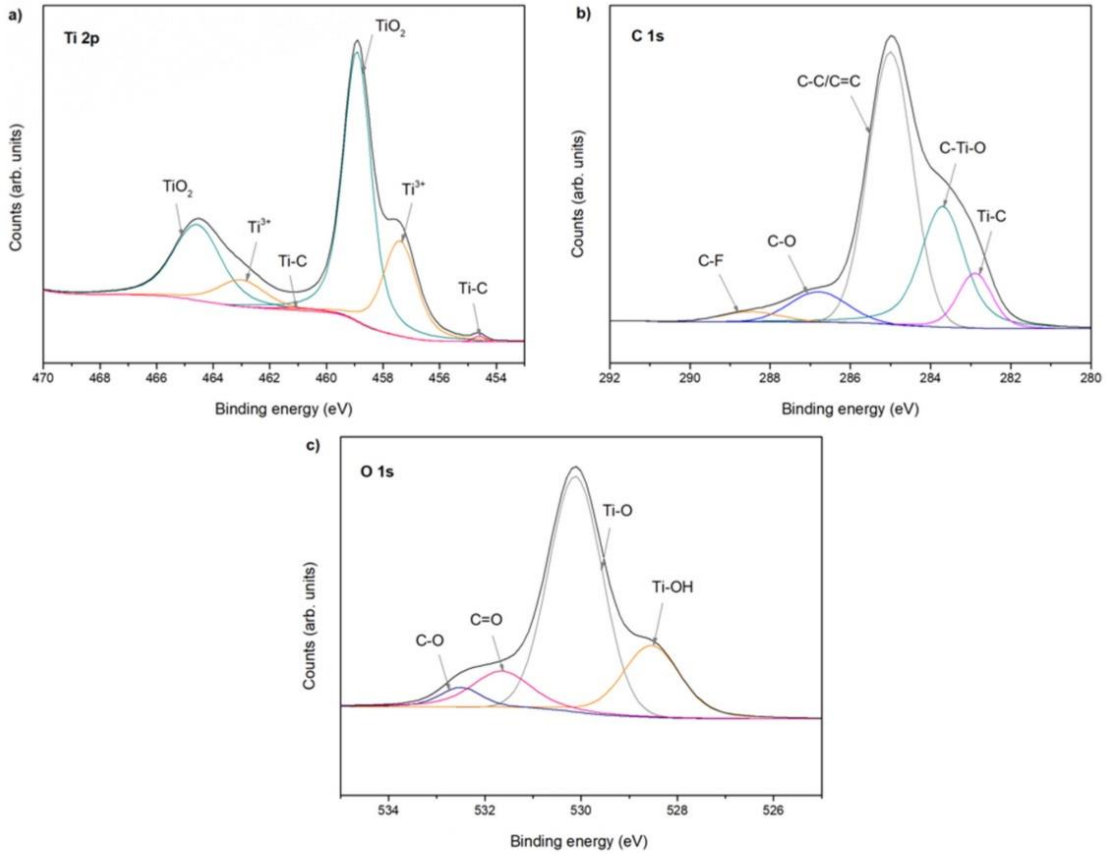

Fig. 2. XPS spectra for Ti 2p (a), C 1 s (b) and O 1 s (c) regions for TiO_2/Ti_3C_2 composite.

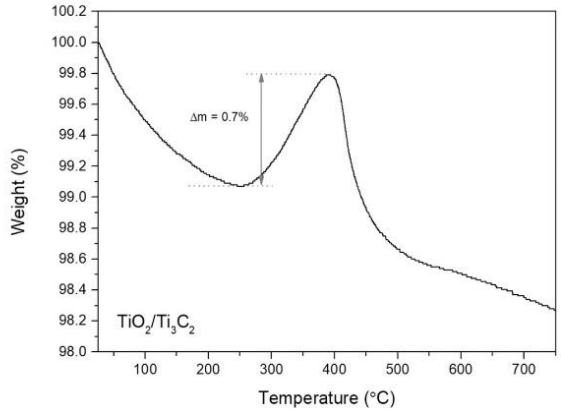

Fig. 3. TG curve of TiO_2/Ti_3C_2.

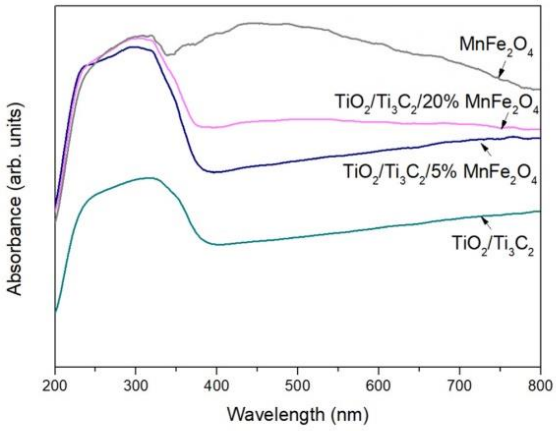

Fig. 4. The DR/UV–vis spectra for prepared materials.

planes, respectively [43]. STEM-EDS elemental mapping proved that $MnFe_2O_4$ particles were uniformly distributed in the composite material with some agglomerates (see Fig. 6 and Fig. S4 in the Supporting Materials).

The photoluminescence spectra of TiO_2/Ti_3C_2 and TiO_2/Ti_3C_2/5% $MnFe_2O_4$ were analysed under an excitation of 300 nm (Fig. 7). The materials showed a broad visible emission band between 400 and 700 nm with a maximum of 465 nm associated with the multi-photon process occurring due to the participation of various electronic states within the band gap. Both spectra are similar and broad with no clear shift. Only, a slight decrease in the photoluminescence intensity for $TiO_2/Ti_3C_2/MnFe_2O_4$ composites, compared with TiO_2/Ti_3C_2 was

Table 2
BET surface area and calculated bandgap energy for prepared materials.

Sample	BET surface area (m^2/g)	E_g (eV)
$MnFe_2O_4$	13.4	1.5
TiO_2/Ti_3C_2	12.5	3.0
$TiO_2/Ti_3C_2/5\%MnFe_2O_4$	12.9	2.99
$TiO_2/Ti_3C_2/20\%MnFe_2O_4$	12.1	3.05

noticed.

Furthermore, the Gaussian fitting and deconvolution of PL spectra for $TiO_2/Ti_3C_2/5\%MnFe_2O_4$ are shown in Fig. 8. The deconvolution of the spectrum reveals ten components centered at 425 nm, 443 nm, 465 nm 482 nm, 492 nm, 516 nm, 573 nm, 639 nm, 692 nm, and 732 nm. The first band (violet-blue) at 425 nm may be attributed to the self-trapped excitons of TiO_6 octahedra [44]. The bands in the blue and green region may correspond to the shallow trap due to the Ti^{3+} states just below the conduction band and singly ionised oxygen vacancies, respectively. The band at 573 nm may be ascribed to intrinsic defects or the recombination of electrons and holes on the amorphous carbon of MXene [44,45]. The orange-red region emission may be assigned to surface oxygen and hydroxyl species [44] There is no significant difference in the deconvolution of pure TiO_2/Ti_3C_2 and $TiO_2/Ti_3C_2/MnFe_2O_4$ composites (Fig. S5 in the Supporting Materials). For $MnFe_2O_4$ very weak emission was observed. Characteristic blue emission may be attributed to the radiative defects related to the interface traps existing at the grain boundaries. Green emissions may correspond to oxygen vacancies [46]. The yellow-orange signal may be related to the Mn d-d emission [47].

Fig. 9 shows the room temperature hysteresis loops (magnetisation, M, versus applied magnetic field, m_0H) of pure $MnFe_2O_4$ and $TiO_2/Ti_3C_2/MnFe_2O_4$ composites. Pure $MnFe_2O_4$ had the highest saturation magnetisation of 68 emu/g. Meanwhile, the magnetic properties of the composite were reduced in comparison to $MnFe_2O_4$ to about 12 emu/g for $TiO_2/Ti_3C_2/20\%$ $MnFe_2O_4$ and 5 emu/g for $TiO_2/Ti_3C_2/5\%$ $MnFe_2O_4$, as a consequence of the presence of a relatively high fraction of non-magnetic component of TiO_2/Ti_3C_2. Nevertheless, the coercive field, H_c, is not significantly modified after the preparation of the final composites (see inset of Figure 8, H_c 60 Oe in the three samples). It is important to notice that, as can be seen in the image in Fig. 8, even the sample with the lowest magnetic component ($TiO_2/Ti_3C_2/5\%$ $MnFe_2O_4$) can be effectively separated from the liquid using a magnet bar and thus possess good properties for recovery and recycling.

The magnetic response of the samples was further analysed through the temperature dependence of the magnetisation. Fig. 10a shows M versus temperature at the applied magnetic field of 6 T for the manganese ferrite and the TiO_2/Ti_3C_2 composites. As concluded from the hysteresis loops, an overall reduction in M is found in the composites due to the non-magnetic nature of TiO_2/Ti_3C_2. However, if the magnetic response of this component is analysed in further detail under similar experimental conditions (see inset of Fig. 10a), negative magnetisation is found to be linked to its diamagnetic nature. Such a negative contribution (low in absolute value) would not contribute significantly to the net magnetisation. Anyway, the magnetisation was estimated considering the magnetic contribution of each component, that is, $M_{composite} = (\%) * M_{MnFe2O4} + (1 - \%) * M_{TiO2/Ti3C2}$, considering % from the Rietveld refinement (4% and 17%, see Table 1). As shown in Fig. 10a, a close

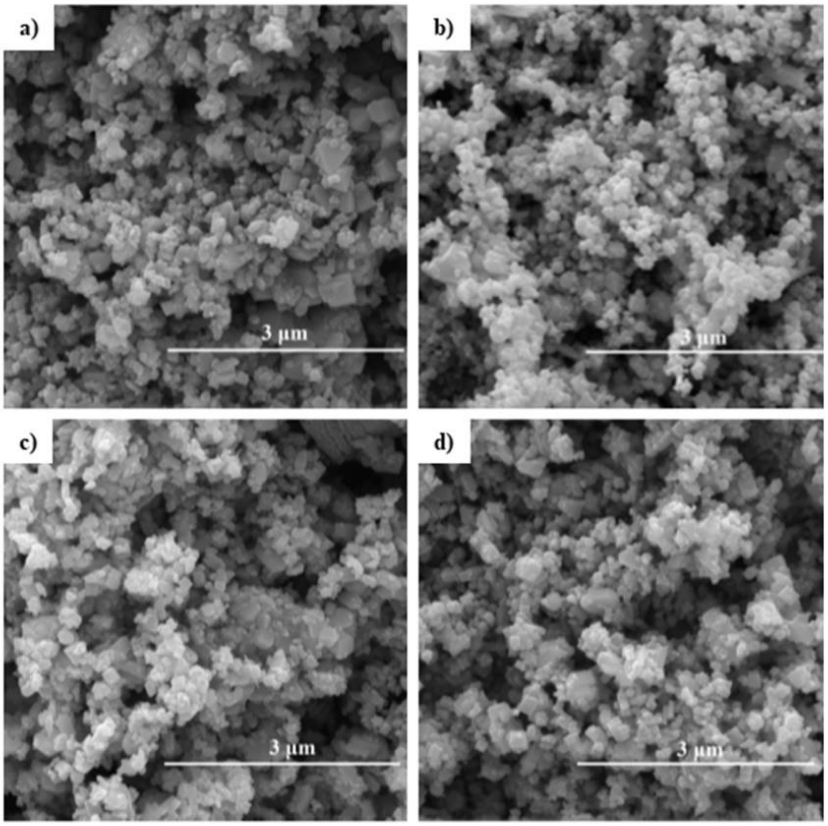

Fig. 5. The SEM image of pure $MnFe_2O_4$ (a), TiO_2/Ti_3C_2 (b), $TiO_2/Ti_3C_2/5\%MnFe_2O_4$ (c), $TiO_2/Ti_3C_2/20\%MnFe_2O_4$ (d).

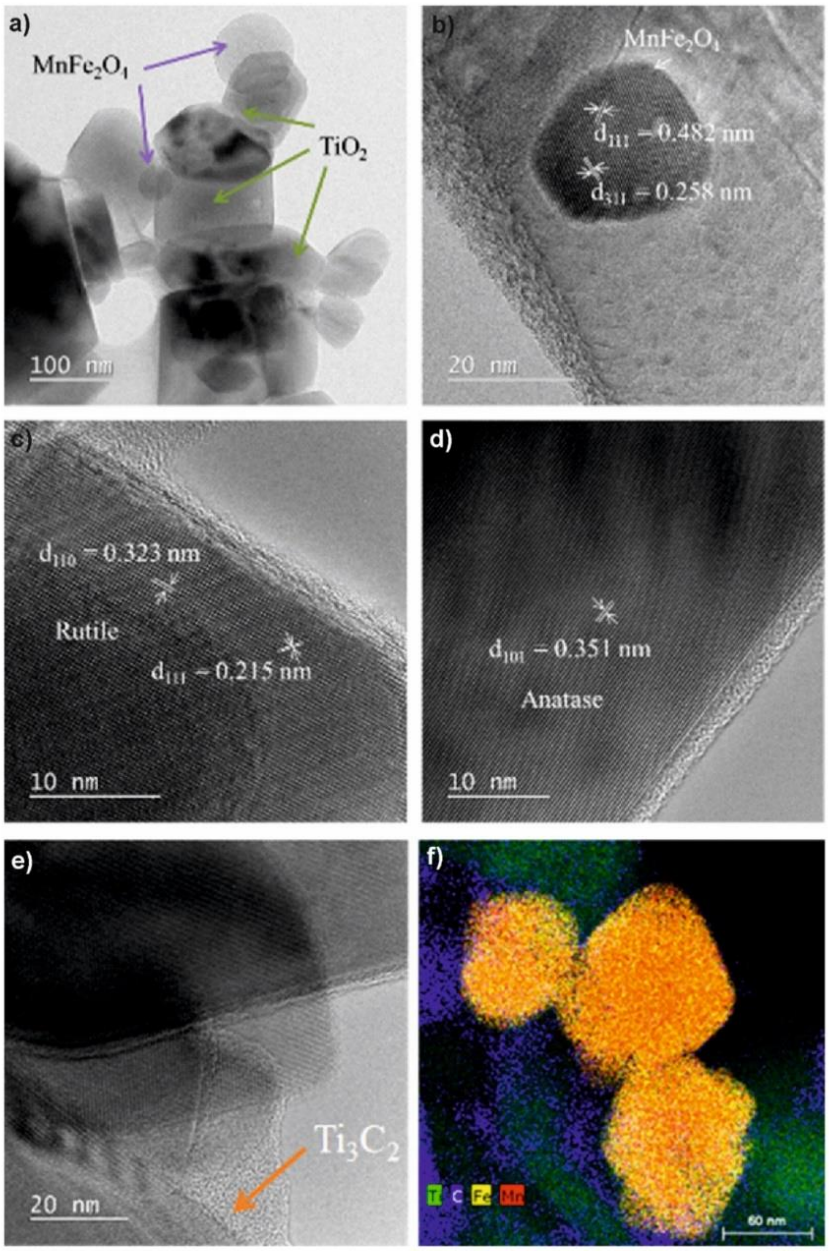

Fig. 6. The TEM image of $TiO_2/Ti_3C_2/5\%MnFe_2O_4$ (a), HRTEM with marked lattice spacing for $MnFe_2O_4$ (b), rutile (c) and anatase (d), TEM image for Ti_3C_2 (e), STEM-EDS elemental mapping of $TiO_2/Ti_3C_2/5\%MnFe_2O_4$ (f).

agreement between this estimation (line) and the experimental magnetisation (symbols) is found. Finally, regarding the magnetic characterisation, the Zero-Field-Cooled (ZFC)-Field-Cooled (FC) magnetisation curves are displayed in Fig. 10b for the three analysed samples, where the magnetisation for the composites is normalised (M/%) to comparatively analyse their magnetic response. Typical curves of superparamagnetic nanoparticles with Blocking temperatures slightly above room temperature are obtained in all the samples. The proximity of the Blocking temperature to the operation temperature (300 K) guarantees an optimum magnetic behaviour of the magnetic composites in aqueous dispersions, that is, low Hc and magnetisation at the remanence to avoid magnetic interparticle interactions and high magnetic susceptibility to allow and efficient recovery through the action of an external magnetic field.

The EIS Nyquist plots are shown in Fig. 11a. It can be seen that $TiO_2/Ti_3C_2/5\%$ $MnFe_2O_4$ showed the minimum radius of arc in comparison to other samples, which suggests that coupling between TiO_2/Ti_3C_2 and 5% of $MnFe_2O_4$ decreased the charge-transfer resistance. As shown in Fig. 11b, all samples present a stable photocurrent within 5 on/off cycles, indicating that these materials can be excited to generate

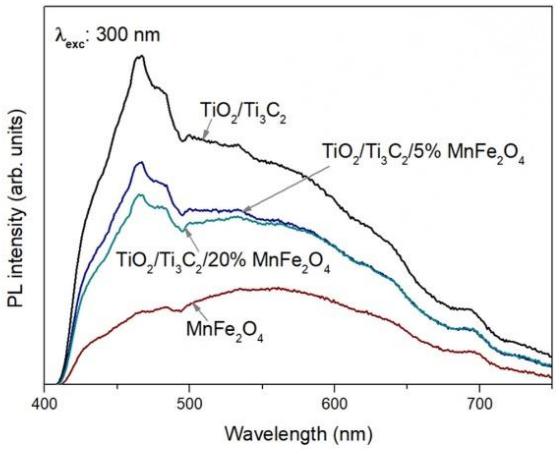

Fig. 7. The PL spectra of the prepared materials.

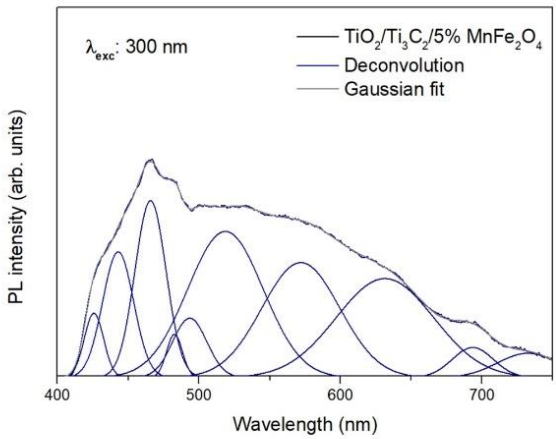

Fig. 8. The Gaussian fitting and deconvolution of PL spectra of the $TiO_2/Ti_3C_2/5\%MnFe_2O_4$.

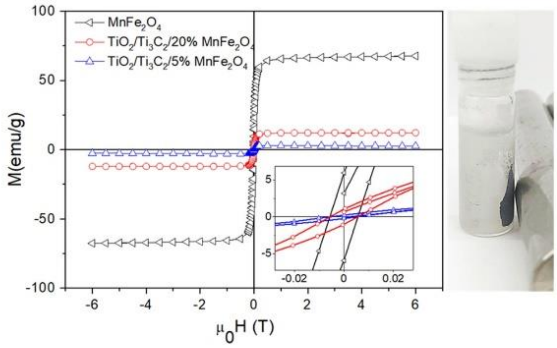

Fig. 9. Room temperature hysteresis loops for pure $MnFe_2O_4$ and composites. Inset: enlargement of the low field region.

electron–hole pairs. However, for pure $MnFe_2O_4$ the photocurrent response is very weak, which is related to the low number of generated charge carriers. For $TiO_2/Ti_3C_2/5\%$ $MnFe_2O_4$, slightly higher photocurrent density was observed than TiO_2/Ti_3C_2, suggesting efficient transfer and improved electron-hole separation.

According to the slope of Mott Schottky plots (Fig. 12), both TiO_2/Ti_3C_2 and $MnFe_2O_4$ presented n-type semiconductor characteristics. The potential of TiO_2/Ti_3C_2 and $MnFe_2O_4$ flat band edge position, which for n-type semiconductors is almost equal to the conduction band potential, were recorded at − 1.21 and − 1.4 vs Ag. These values were converted to a value of − 0.41 V and − 0.62 V vs. NHE. Considering the bandgap value for TiO_2/Ti_3C_2 and $MnFe_2O_4$ equal to 3.0 eV and 1.5 eV, respectively, the valence band edge position were calculated as 2.59 V and 0.88 V vs. NHE.

3.2. Photocatalytic activity in reaction of ibuprofen and carbamazepine degradation

Firstly, the photolysis of ibuprofen and carbamazepine was analysed to notice the differences between processes with or without photocatalyst and verify the effect of PMS addition. As shown in Fig. 13, the photolysis of CBZ reached 23% within 60 min, while for IBP 49% within 60 min under simulated solar light irradiation. In these cases, the mineralisation measured as TOC reduction was not observed. After the addition of PMS (0.25 mM), the degradation for both pharmaceuticals increased to about 90% within 60 min. Nevertheless, the TOC concentration did not decrease.

The efficiency of carbamazepine and ibuprofen photodegradation for composite materials is presented in Fig. 14. The photocatalytic activity of pure $MnFe_2O_4$ was inefficient, which confirmed that although the lowest band gap, magnetic material did not show the ability for photodegradation and could only absorb a low amount of CBZ and IBP in the dark reaction (see Fig. S6 in the Supporting Materials). This may be explained by the fast recombination of electron-hole pairs [48]. Based on XRD analysis, the TiO_2/Ti_3C_2 composite sample contained TiO_2 as a mixture of anatase and rutile. Therefore due to the difference in the position of band gaps, the formation of heterojunction in TiO_2 material can be noticed. According to our previous work [22] focusing on the influence of the solvothermal reaction environment on morphology and photocatalytic activity, it was found that at the same hydrothermal reaction time and temperature, higher activity in reaction of acetaminophen degradation revealed sample obtained in NH_4F/HCl solution consisting of anatase and rutile combined with trace amounts of Ti_3C_2 compared to the sample of anatase modified with Ti_3C_2 prepared in HBF_4/H_2O solution. The direct contact between these two crystalline TiO_2 polymorphs may facilitate the interparticle transfer of the photogenerated charges in the photocatalytic processes and improve the photocatalytic activity [49–51]. The introduction of 5 wt% of manganese ferrite into the TiO_2/Ti_3C_2 photocatalyst structure did not affect the degradation efficiency of both pharmaceuticals, which reached 100% after 60 min of irradiation. However, the incorporation of a higher amount of $MnFe_2O_4$ (20%) significantly decreased the photocatalytic activity. This phenomenon may be attributed to the excessive amount of magnetic light diffusing particles that may hinder the contact between the photocatalyst and the light or become a new electron-hole recombination centre, which reduces the lifetime of the photogenerated charge carriers [52,53].

The TOC reduction efficiency during the photodegradation process is presented in Fig. 15. For TiO_2/Ti_3C_2 and $TiO_2/Ti_3C_2/5\%$ $MnFe_2O_4$ composite, the mineralisation efficiency was about 40% within 60 min of irradiation. In the case of $TiO_2/Ti_3C_2/20\%$ $MnFe_2O_4$ composite and $MnFe_2O_4$, the mineralisation was not observed.

Furthermore, as presented in Fig. 16, the addition of PMS resulted in a significant increase in the degradation of both pharmaceuticals. Moreover, the combination of the photocatalytic degradation process for sample $TiO_2/Ti_3C_2/5\%MnFe_2O_4$ with PMS activation led to superior

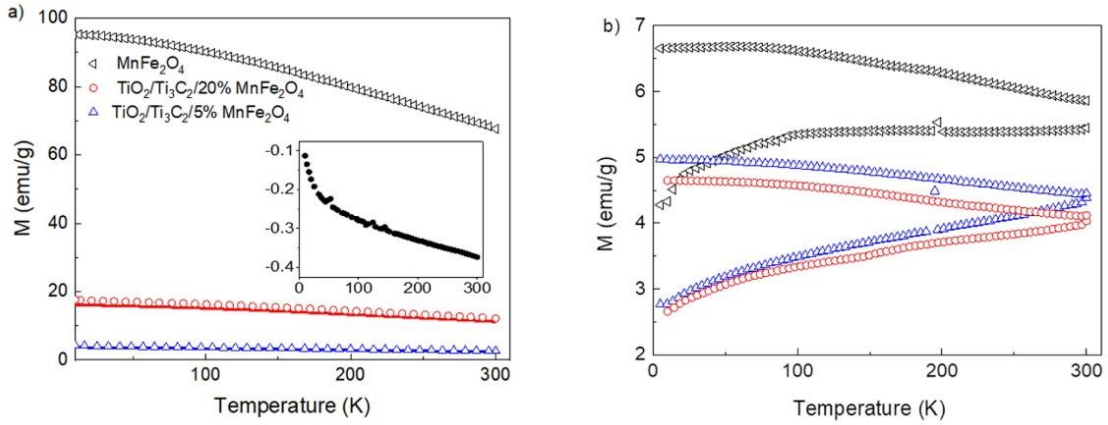

Fig. 10. High field magnetisation, M, (applied magnetic field $m_0H = 6$ T) for $MnFe_2O_4$ and prepared magnetic composites (a). Inset: M versus T at 6 T for the TiO_2/Ti_3C_2 component) and ZFC-FC magnetization curves for $MnFe_2O_4$ the prepared samples (applied magnetic field H = 50 Oe). M values for the composites were normalised to the relative fraction (%) (b).

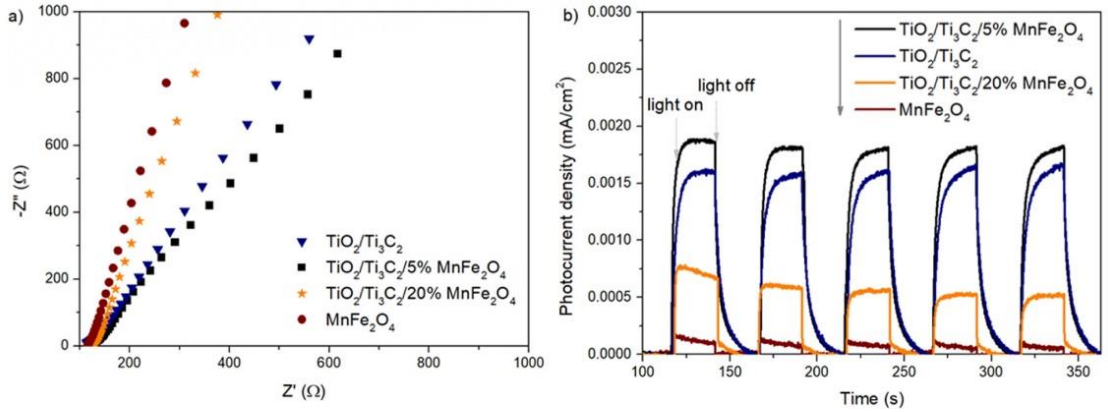

Fig. 11. The EIS Nyquist plots (a) and generated photocurrent (b) for prepared materials.

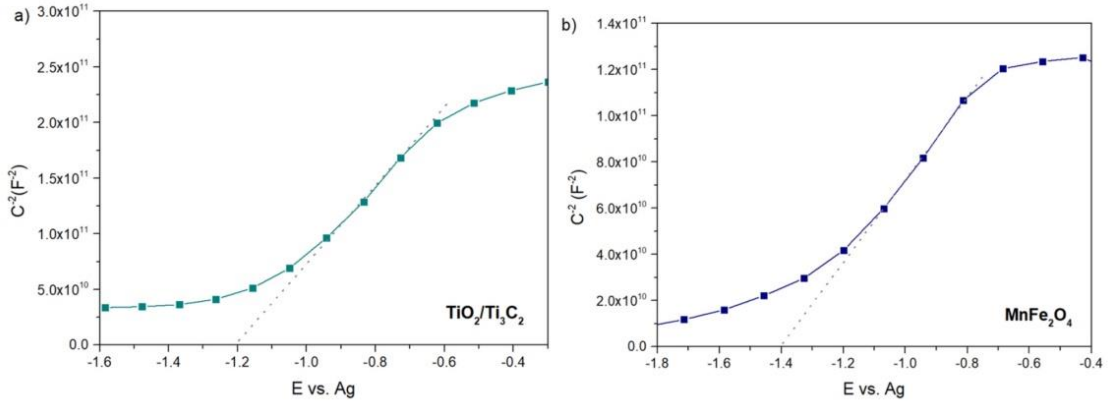

Fig. 12. The Mott Schottky plots for TiO_2/Ti_3C_2 (a) and $MnFe_2O_4$ (b).

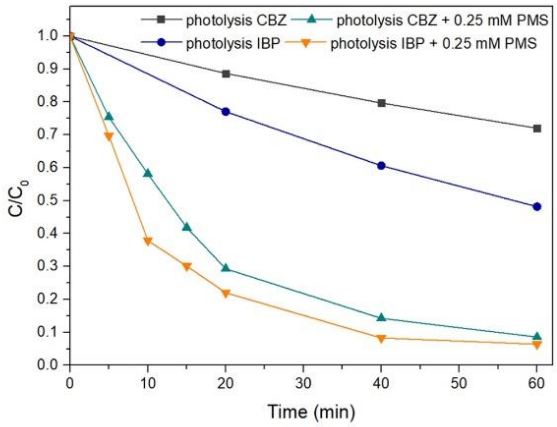

Fig. 13. The efficiency of carbamazepine and ibuprofen degradation in the CBZ/IBP mixture for photolysis and photolysis with PMS (0.25 mM).

photodegradation of the pharmaceutical mixture. In the case of the $MnFe_2O_4$, both Mn and Fe may activate PMS to produce sulphate radicals [54]. The effect of PMS concentration in the range of 0.065–0.25 mM for IBU and CBZ degradation and mineralisation was observed (see Figs. 16–17). The degradation rate was promoted with the increased concentration of the PMS. It can be explained by the fact that more PMS as a source of active species may improve pharmaceuticals degradation [55]. However, above a certain concentration, $\bullet SO_4^-$ might be consumed by the excess PMS and produce less active $SO_5^{\bullet-}$ [56]. Therefore, the highest degradation efficiency was observed for $TiO_2/Ti_3C_2/5\%MnFe_2O_4$ photocatalytic process combined with the activation of PMS with a concentration of 0.25 mM. After 20 min and 10 min of the advanced treatment process, 100% of CBZ and IBP were degraded, respectively.

Furthermore, a mineralisation efficiency measured as a TOC reduction was also improved for the sample $TiO_2/Ti_3C_2/5\%$ $MnFe_2O_4$/PMS compared to the sample without PMS (Fig. 17). The rate constant increased from 8.9 ± 0.27 $min^{-1} \cdot 10^{-2}$ to $28.6 \pm 0.98 \cdot 10^{-2}$ min^{-1} for CBZ, and from $7.0 \pm 0.18 \cdot 10^{-2}$ min^{-1} to 53.0 ± 1.4 $min^{-1} \cdot 10^{-2}$, after the introduction of PMS into the reaction environment (Table S2 in the Supporting Materials). Therefore, the synergetic effect on the CBZ and IBP mixture degradation efficiency for peroxymonosulphate-assisted photocatalytic degradation over $TiO_2/Ti_3C_2/5\%$ $MnFe_2O_4$ photocatalyst was noticed.

The amount of the photocatalyst is another important factor determining the photocatalytic activity. The amount of $TiO_2/Ti_3C_2/5\%$ $MnFe_2O_4$ photocatalyst ranged from 0.5 to 2 $g \cdot dm^{-3}$, with PMS concentration equal to 0.25 mM. As presented in Fig. 18, the highest degradation efficiency was observed for 2 $g \cdot dm^{-3}$. However, the reduction of photocatalyst amount to 0.5 $g \cdot dm^{-3}$ enables degradation above 90% of CBZ and near 100% of IBP within 20 min of irradiation and TOC reduction of about 47%. The TOC removal was summarised in Table S3 in the Supporting Materials.

The effect of pH on the CBZ/IBP degradation was investigated at constant photocatalyst amount ($2 g \cdot dm^{-3}$) and PMS concentration (0.25 mM) by adjusting the initial pH of the solution. As shown in Fig. 19, a decrease in CBZ degradation can be noticed at a pH of 6.7 compared to 4.5, whereas the photodegradation efficiency of IBU was efficient at both pH values. However, increasing pH to 9.5 resulted in markedly decreased degradation of CBZ and IBP. The TOC removal was summarised in Table S3 in the Supporting Materials. Similarly, the lowest mineralisation efficiency of IBU and CBZ was observed under alkaline conditions, in which PMS may undergo self-decomposing without the production of reactive species. Moreover, in alkaline conditions, standard redox potentials of sulfate and hydroxyl radicals are lower as well as their lifetimes are shorter than in acidic conditions [57,

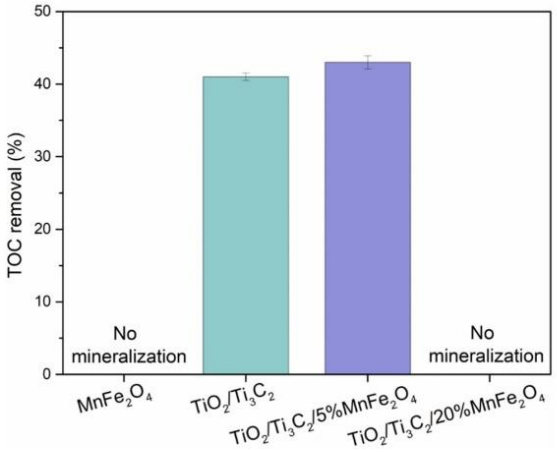

Fig. 15. TOC removal in the photodegradation process for obtained photocatalysts.

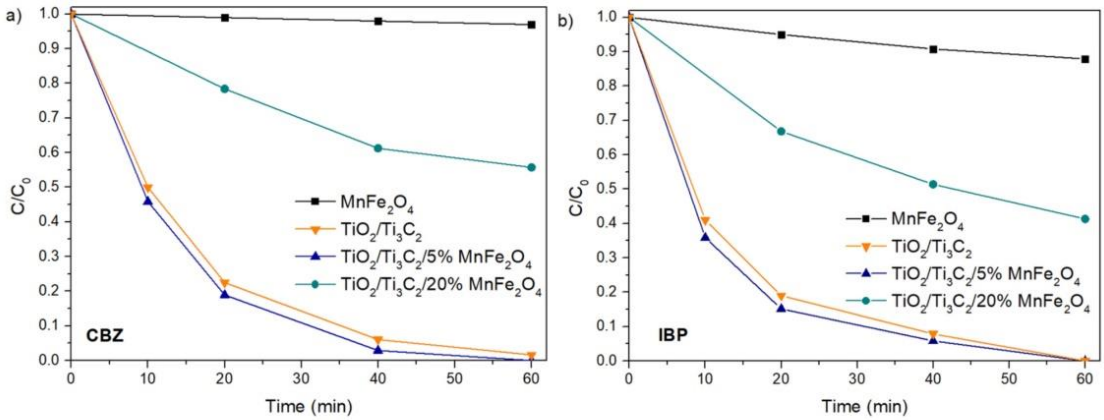

Fig. 14. The efficiency of carbamazepine (a) and ibuprofen (b) photocatalytic degradation in the CBZ/IBP mixture under simulated solar light.

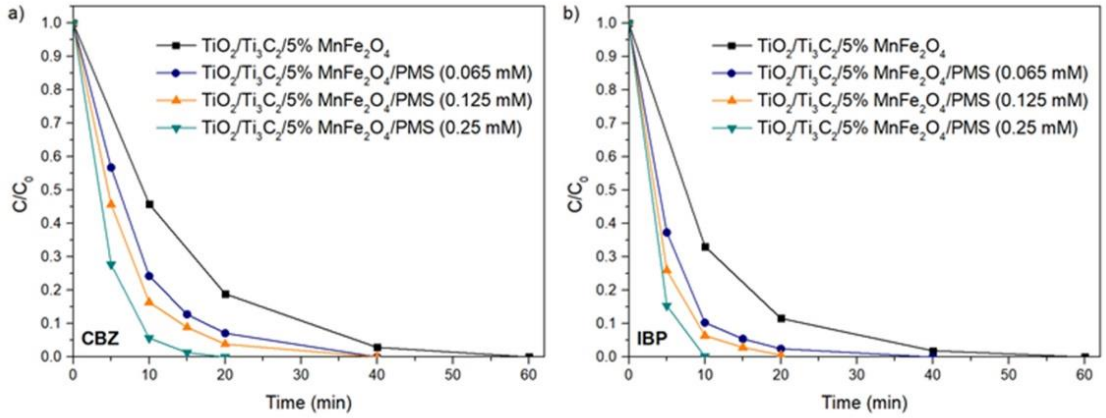

Fig. 16. The effect of PMS concentration on the carbamazepine (a) and ibuprofen (b) degradation efficiency in the CBZ/IBP mixture for TiO_2/Ti_3C_2/5% $MnFe_2O_4$/PMS system.

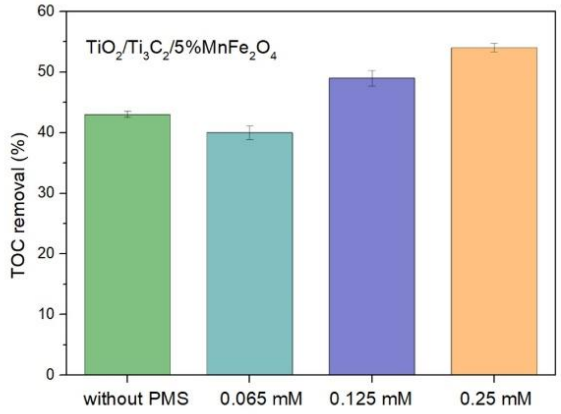

Fig. 17. The effect of PMS concentration on the carbamazepine (a) and ibuprofen (b) mineralisation efficiency measured as TOC removal for TiO_2/Ti_3C_2/5% $MnFe_2O_4$/PMS system after 60 min of irradiation.

58].

Furthermore, additional experiments were performed in the model seawater to evaluate the effect of interfering ions (Mg^{2+}, Ca^{2+}, Na^{+} cations and Cl^{-} and SO_4^{2-}) on the efficiency of CBZ and IBU photodegradation (Fig. 20).

Interestingly, for CBZ removal, significant improvement was observed. After 5 min of irradiation, about 100% of CBZ was degraded, whereas in DI water within 20 min. The TOC removal efficiency is also summarised in Table S3 in the Supporting Materials. Also, a slight improvement in the mineralisation efficiency was observed in the model seawater. Huang et al. [59] reported that chloride ions could facilitate the Acid Orange 7 photocatalytic degradation in the presence of PMS. The enhancement could be related to the generation of reactive chlorine species from the reaction between Cl and $\bullet SO_4$ [60].

Meanwhile, for IBP, the degradation was slightly limited. The slower photodegradation of IBU in seawater compared with the DI water may be attributed to the presence of inorganic species in seawater acting as hydroxyl radical scavengers and therefore reducing photocatalytic activity [61].

In order to explain the mechanism of CBZ and IBP photodegradation with TiO_2/Ti_3C_2/5%$MnFe_2O_4$/PMS system, the trapping experiments with reactive species scavengers were performed. The results are shown in Fig. 21. The highest inhibition of CBZ degradation efficiency was

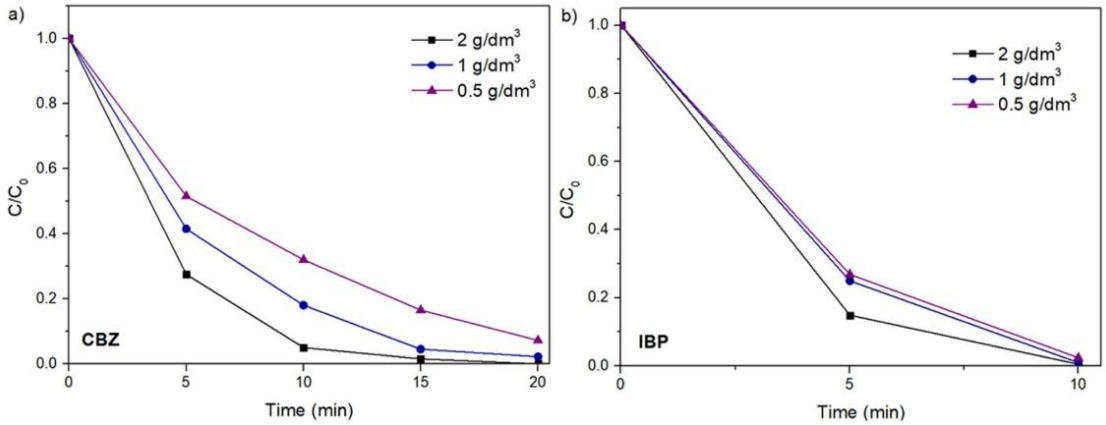

Fig. 18. The effect of photocatalyst amount on the efficiency of carbamazepine (a) and ibuprofen (b) degradation in the CBZ/IBP mixture for TiO_2/Ti_3C_2/5% $MnFe_2O_4$/PMS system.

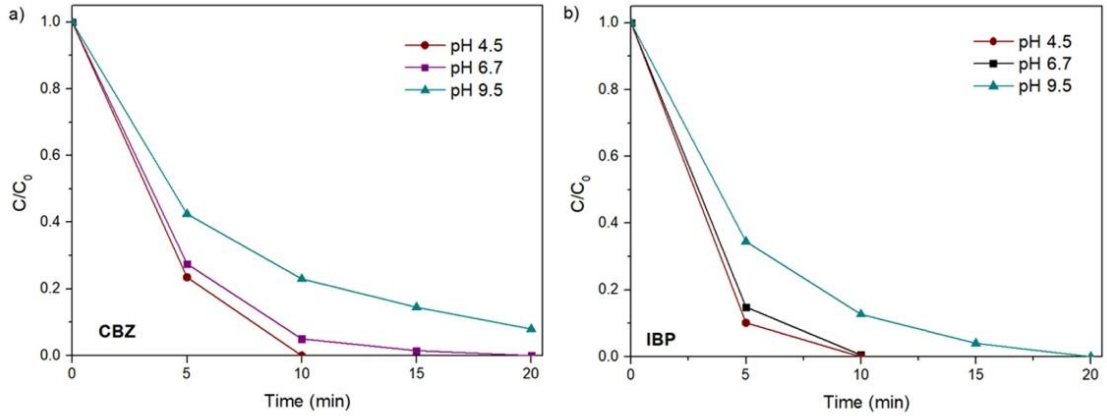

Fig. 19. The effect of pH on the efficiency of carbamazepine (a) and ibuprofen (b) degradation (C/C_0) in the CBZ/IBP mixture for $TiO_2/Ti_3C_2/5\%$ $MnFe_2O_4$/PMS system.

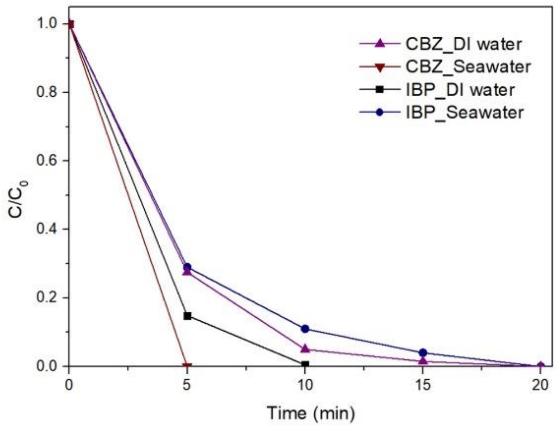

Fig. 20. The efficiency of carbamazepine and ibuprofen degradation (C/C_0) in the CBZ/IBP mixture for $TiO_2/Ti_3C_2/5\%$ $MnFe_2O_4$/PMS system in deionised water (DI) water and model seawater.

observed with the addition of benzoquinone, which indicates that superoxide anion radicals are the main oxidising species taking part in the removal of pharmaceuticals. Meanwhile, the degradation of IBP was significantly limited in the presence of ammonium oxalate. In this case, the h^+ were mainly involved in the photodegradation process. Furthermore, for both pharmaceuticals, a decrease in photocatalytic activity was observed with the addition of isopropanol, suggesting that the presence of $\bullet SO_4^-$ significantly affects the pharmaceuticals removal efficiency.

Different reactive species may play the dominant role in the photodegradation mechanism depending on the nature and physicochemical properties of both pharmaceuticals and photocatalyst. According to Dudziak et al. [62], for carbamazepine with a low energy position of LUMO orbital, the process efficiency is not exactly dependent on the stability of h^+ generated organic radical, which is frequently indicated as an initial reactive form. Meanwhile, direct h^+ transfer from the surface to the pollutant appears essential for IBU degradation, which also agrees with its preferred surface adsorption and negative charge. In the study of Georgaki et al. [63], the hole-dominated surface reaction was also observed for IBP, while for CBZ solution-phase mechanism.

The possible mechanism of pharmaceuticals degradation with $TiO_2/Ti_3C_2/5\%$ $MnFe_2O_4$/PMS is presented in Fig. 22. In the presence of light, the promotion of electrons from the valence band (VB) of $MnFe_2O_4$ and TiO_2 to its CB was attained in the nanocomposite, leaving behind the same number of holes in the corresponding VB. The photogenerated

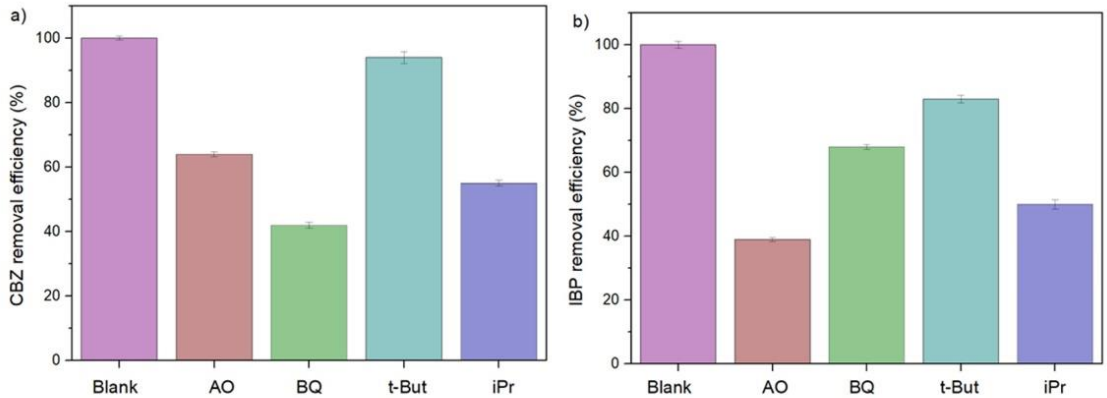

Fig. 21. The trapping experiments for carbamazepine (a) and ibuprofen (b) degradation in the CBZ/IBP mixture for $TiO_2/Ti_3C_2/5\%$ $MnFe_2O_4$/PMS system.

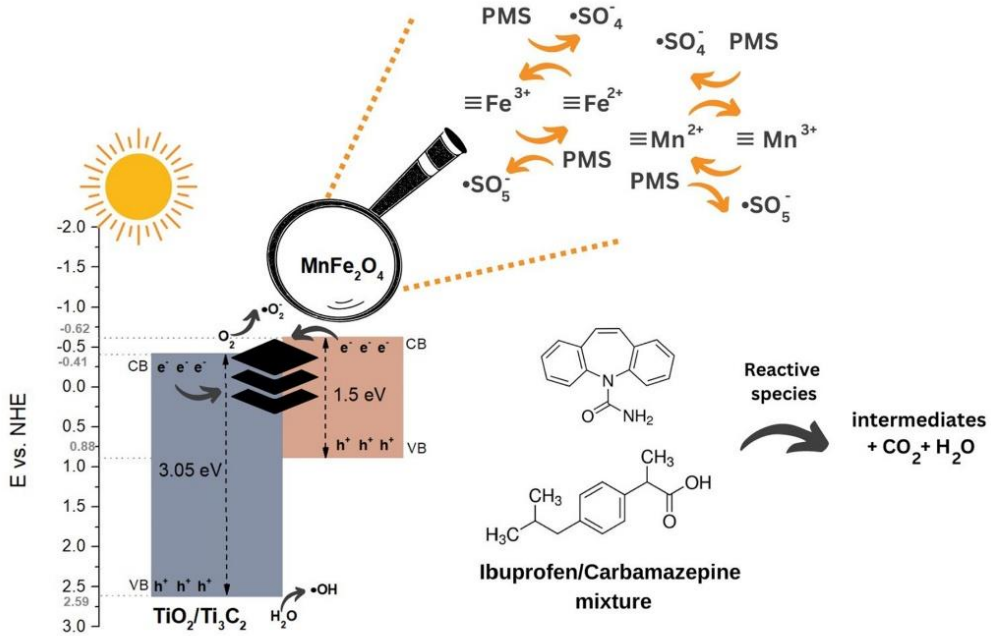

Fig. 22. The possible mechanism of IBP/CBZ mixture degradation in the presence of $TiO_2/Ti_3C_2/5\%MnFe_2O_4$/PMS.

electrons are transported to the conductive MXene at the interface, which elongates the lifetime of holes in the VB of TiO_2 and inhibits the recombination of photogenerated charge carriers. Accumulated electrons participate in superoxide anion radical generation from oxygen, whereas photogenerated holes participate in hydroxyl radicals production as a main reactive oxygen species taking part in the photocatalytic degradation of CBZ and IBP.

Furthermore, the presence of Mn and Fe may activate PMS to produce sulphate radicals. Electron transfer from PMS to Fe^{3+} and Fe^{2+} caused the regeneration of Fe^{3+} and cycling between Fe^{3+} and Fe^{2+} (Eqs. 1–2). Similarly, there was also the regeneration of Mn^{2+} and cycling between Mn^{2+} and Mn^{3+} (Eqs. 3–4). This redox cycles $Mn^{2+}\rightarrow Mn^{3+}\rightarrow Mn^{2+}$ and $Fe^{2+}\rightarrow Fe^{3+}\rightarrow Fe^{2+}$ are the rate-limiting steps in the PMS activation [64]. Furthermore, $\bullet SO_5$ radicals may react with each other to form $\bullet SO_4^-$ (Eq. 5). While, $\bullet SO_4^-$ may further react with OH^- to generate •OH (Eq. 6) [65].

$$Fe^{3+} + HSO_5^- \rightarrow Fe^{2+} + \bullet SO_5^- + H^+ \quad (1)$$

$$Fe^{2+} + HSO_5^- \rightarrow Fe^{3+} + \bullet SO_4^- + OH^- \quad (2)$$

$$Mn^{2+} + HSO_5^- \rightarrow Mn^{3+} + \bullet SO_4^- + OH^- \quad (3)$$

$$Mn^{3+} + HSO_5^- \rightarrow Fe^{2+} + \bullet SO_5^- + H^+ \quad (4)$$

$$\bullet SO_5^- + \bullet SO_5^- \rightarrow 2\ \bullet SO_4^- + O_2 \quad (5)$$

$$\bullet SO_4^- + OH^- \rightarrow SO_4^{2-} + \bullet OH \quad (6)$$

Based on the ICP-OES analysis and iron photometric measurement, the levels of metal lixiviation were determined for the $TiO_2/Ti_3C_2/5\%$ $MnFe_2O_4$/PMS system with the highest PMS concentration. The results are presented in Table S4 in the Supporting Materials. The metal lixiviation using $TiO_2/Ti_3C_2/5\%$ $MnFe_2O_4$/PMS (0.25 mM) system to the post-process solution was below LOD for Ti, not exceeding the permissible limit for Fe (0.08 $mg{\cdot}dm^{-3}$) in surface and drinking water, while exceeded for Mn (0.4 $mg{\cdot}dm^{-3}$) in drinking water. Despite that, the photocatalyst showed good stability and reusability in the four subsequent cycles of photodegradation. After each cycle, the composite material was separated and reused with no additional treatment. As presented in Fig. 23a, the degradation efficiency of CBZ and IBP remained stable and maintained at 100% within 10 min for IBP and 100% within 20 min for CBZ, respectively, confirming good stability and recyclability. Besides, the XRD characteristic peaks of the used composite are unchanged compared to the fresh material (Fig. 24a). Similarly, FTIR spectra (Fig. 24b) for $TiO_2/Ti_3C_2/5\%$ $MnFe_2O_4$ fresh sample and after the 4th photocatalytic cycle do not differ. A broad band observed in the range between 3650 and 3000 cm^{-1} with a maximum at 3430 cm^{-1} is ascribed to the stretching mode of the hydroxyl group. The characteristic signal at 1630 cm^{-1} is related to the bending vibrations of the hydroxyl group. The broad band between 882 and 400 cm^{-1} corresponds to the Ti-O stretching vibrations and Ti-O-Ti bridging stretching mode.

The results presented in the present study were compared with recent publications concerning photocatalytic degradation of IBP and CBZ enhanced by PMS activation. The comparison is presented in Table 3. However, any studies considering photocatalyst/PMS/sunlight irradiation system for IBP degradation have not been found.

4. Conclusions

For the first time, the ternary magnetic composites $TiO_2/Ti_3C_2/MnFe_2O_4$ were successfully fabricated and applied for the degradation of pharmaceuticals, the mixture of carbamazepine and ibuprofen. The present work provided a new approach to the application of MXene compound as a precursor for photocatalyst synthesis and co-catalyst. The $TiO_2/Ti_3C_2/MnFe_2O_4$ magnetic composite was easily recovered from the post-process suspension after the photodegradation process by an external magnetic field. The magnetic composite revealed excellent photocatalytic activity in the wide pH range and in the presence of inorganic ions. For both pharmaceuticals, nearly 100% degradation was obtained within 60 min in the photocatalytic degradation process. The synergetic effect of the combination of photodegradation process in the presence of $TiO_2/Ti_3C_2/5\%MnFe_2O_4$ composite with PMS activation under simulated solar light was noticed. The coupling of photocatalysis

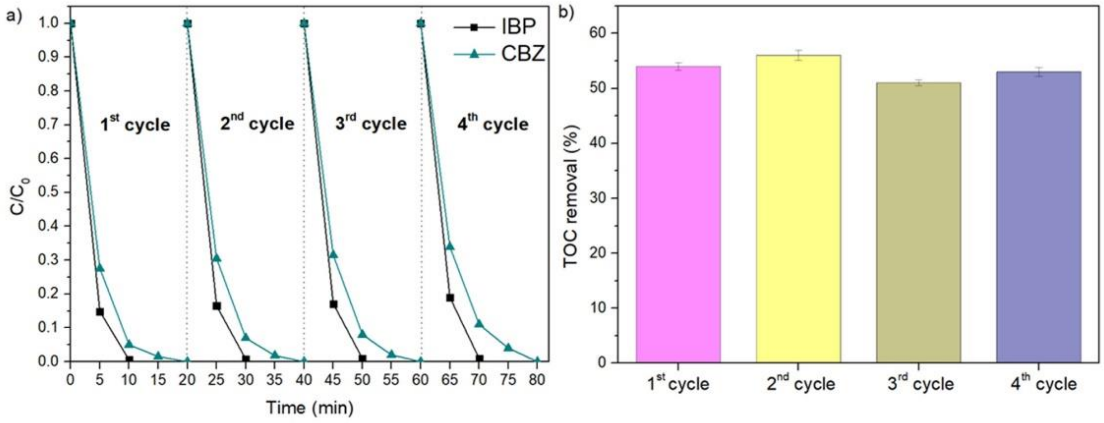

Fig. 23. The stability and reusability analyses in the four subsequent cycles of CBZ/IBP mixture photodegradation (a) and mineralisation efficiency measure as TOC reduction in the four subsequent cycles after 60 min of irradiation (b) for TiO_2/Ti_3C_2/5% $MnFe_2O_4$/PMS.

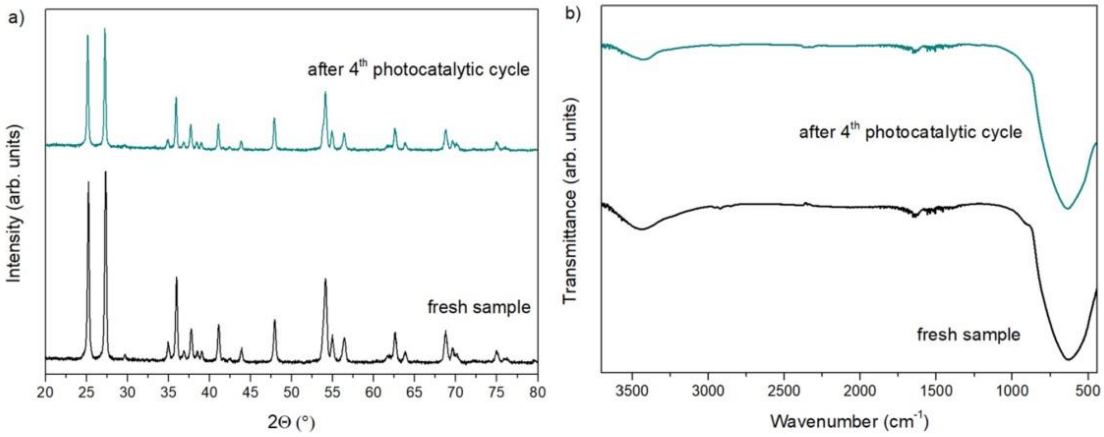

Fig. 24. The comparison of XRD diffractograms (a) and FTIR spectra (b) for TiO_2/Ti_3C_2/5% $MnFe_2O_4$ fresh sample and sample after the fourth photodegradation cycle.

Table 3
The comparison of this work with results presented in recent related papers.

Photocatalyst	Dosage (g/dm^3)	Pharmaceutical concentration (mg/dm^3)	PMS concentration	Light source	Degradation efficiency	Ref.
BiOCl	0.6	10 (CBZ)	1 mM	simulated solar light ($\lambda > 300$ nm)	100% within 20 min	[66]
β-FeOOH on g-C_3N_4	0.1	10 (CBZ)	0.2 mM	simulated sunlight	100% within 30 min	[67]
Si doped TiO_2	0.1	10 (CBZ)	1 mM	A metal halide lamp with a 300 nm cut-off filter	100% within 60 min	[68]
TiO_2/Ti_3C_2/5% $MnFe_2O_4$	2	7 (CBZ) 10 (IBP)	0.25 mM	Xe lamp	100% within 20 min 100% within 10 min	this work

with relatively low PMS concentration led to a significant increase in the kinetic of the reaction. The degradation efficiency was 100% within 20 min for carbamazepine and 10 min for ibuprofen without significant change in the pH of the solution. Therefore, considering the economic aspects related to energy saving by reducing the photocatalytic process time, combining the photocatalytic degradation process with PMS activation seems beneficial. Therefore, the results presented in this work have the potential to provide new insights into the development of combined magnetic photocatalyst/PMS processes. However, it is important to find the compromise between high degradation efficiency in AOP-based processes and the possibility of secondary pollutants generation, for example, acidification of the treated wastewater or metal ions lixiviation into the water environment. In our study, due to the relatively low PMS concentration, we did not observe a significant change in the pH of the solution after the photodegradation process. However, for the highest PMS concentration of 0.25 mM, lixiviation of a trace amount of Fe and Mn can be noticed.

CRediT authorship contribution statement

Anna Zielińska-Jurek: Conceptualization, Methodology, Supervision, Writing – review & editing, Project administration, Funding acquisition. **Anna Grzegórska:** Formal analysis, Investigation, Visualization, Writing – review & editing. **Joseph Chibueze Ofoegbu:** Formal analysis. Diana Sannino: Writing – review & editing. **Laura Cervera-Gabalda:** Formal analysis. **Cristina Gómez-Polo:** Writing – review & editing..

Declaration of Competing Interest

The authors declare that they have no known competing financial interests or personal relationships that could have appeared to influence the work reported in this paper.

Data Availability

Data will be made available on request.

Acknowledgements

The research was financially supported by Polish National Science Centre (Grant No. NCN 2021/43/B/ST5/02983) and MCIN/AEI/10.13039/501100011033, grant PID2020-116321RB-C21.

Appendix A. Supporting information

Supplementary data associated with this article can be found in the online version at doi:10.1016/j.jece.2023.110660.

References

[1] D. Camacho-Muñoz, B. Petrie, L. Lopardo, K. Proctor, J. Rice, J. Youdan, R. Barden, B. Kasprzyk-Hordern, Stereoisomeric profiling of chiral pharmaceutically active compounds in wastewaters and the receiving environment – a catchment-scale and a laboratory study, Environ. Int 127 (2019) 558–572, https://doi.org/10.1016/j.envint.2019.03.050.

[2] S. Afsa, K. Hamden, P.A. Lara Martin, H. ben Mansour, Occurrence of 40 pharmaceutically active compounds in hospital and urban wastewaters and their contribution to Mahdia coastal seawater contamination, Environ. Sci. Pollut. Res. 27 (2020) 1941–1955, https://doi.org/10.1007/s11356-019-06866-5.

[3] M. Kumar, D.D. Snow, R. Honda, S. Mukherjee, Springer Transactions in Civil and Environmental Engineering Contaminants in Drinking and Wastewater Sources Challenges and Reigning Technologies, n.d. ⟨http://www.springer.com/series/13593⟩.

[4] N.S.P. Batucan, L.A. Tremblay, G.L. Northcott, C.D. Matthaei, Medicating the environment? A critical review on the risks of carbamazepine, diclofenac and ibuprofen to aquatic organisms, Environ. Adv. 7 (2022), 100164, https://doi.org/10.1016/j.envadv.2021.100164.

[5] S. Zhu, B. Dong, Y. Wu, L. Bu, S. Zhou, Degradation of carbamazepine by vacuum-UV oxidation process: kinetics modeling and energy efficiency, J. Hazard Mater. 368 (2019) 178–185, https://doi.org/10.1016/j.jhazmat.2019.01.043.

[6] P. Paíga, M. Correia, M.J. Fernandes, A. Silva, M. Carvalho, J. Vieira, S. Jorge, J. G. Silva, C. Freire, C. Delerue-Matos, Assessment of 83 pharmaceuticals in WWTP influent and effluent samples by UHPLC MS/MS: hourly variation, Sci. Total Environ. 648 (2019) 582–600, https://doi.org/10.1016/j.scitotenv.2018.08.129.

[7] H. Khazri, S. ben Hassine, I. Ghorbel-Abid, R. Kalfat, M. Trabelsi-Ayadi, Presence of carbamazepine, naproxen, and ibuprofen in wastewater from northern Tunisia, Environ. Forensics 20 (2019) 121–128, https://doi.org/10.1080/15275922.2019.1597779.

[8] B. Björlenius, M. Ripszám, P. Haglund, R.H. Lindberg, M. Tysklind, J. Fick, Pharmaceutical residues are widespread in Baltic Sea coastal and offshore waters – screening for pharmaceuticals and modelling of environmental concentrations of carbamazepine, Sci. Total Environ. 633 (2018) 1496–1509, https://doi.org/10.1016/j.scitotenv.2018.03.276.

[9] A. González-Mira, A. Torreblanca, F. Hontoria, J.C. Navarro, E. Mañanós, I. Varó, Effects of ibuprofen and carbamazepine on the ion transport system and fatty acid metabolism of temperature conditioned juveniles of Solea senegalensis, Ecotoxicol. Environ. Saf. 148 (2018) 693–701, https://doi.org/10.1016/j.ecoenv.2017.11.023.

[10] D. Ghime, P. Ghosh, Advanced oxidation processes: a powerful treatment option for the removal of recalcitrant organic compounds, in: Advanced Oxidation Processes - Applications, Trends, and Prospects, IntechOpen, 2020, https://doi.org/10.5772/intechopen.90192.

[11] A. Fiszka Borzyszkowska, A. Pieczyńska, A. Ofiarska, W. Lisowski, K. Nikiforow, E. M. Siedlecka, Photocatalytic degradation of 5-fluorouracil in an aqueous environment via Bi–B co-doped TiO_2 under artificial sunlight, Int. J. Environ. Sci. Technol. 17 (2020) 2163–2176, https://doi.org/10.1007/s13762-019-02604-z.

[12] H. Farzaneh, K. Loganathan, J. Saththasivam, G. McKay, Ozone and ozone/hydrogen peroxide treatment to remove gemfibrozil and ibuprofen from treated sewage effluent: factors influencing bromate formation, Emerg. Contam. 6 (2020) 225–234, https://doi.org/10.1016/j.emcon.2020.06.002.

[13] J.-K. Im, I.-H. Cho, S.-K. Kim, K.-D. Zoh, Optimization of carbamazepine removal in O_3/UV/H_2O_2 system using a response surface methodology with central composite design, Desalination 285 (2012) 306–314, https://doi.org/10.1016/j.desal.2011.10.018.

[14] S. Sun, H. Yao, W. Fu, F. Liu, X. Wang, W. Zhang, Enhanced degradation of carbamazepine in FeOCl based Photo-Fenton reaction, J. Environ. Chem. Eng. 9 (2021), 104501, https://doi.org/10.1016/j.jece.2020.104501.

[15] A. Fiszka Borzyszkowska, A. Sulowska, I. Zekker, J. Karczewski, K. Bester, A. Zielińska-Jurek, Environmentally friendly fabrication of high-efficient Fe-ZnO/citric acid-modified cellulose composite and the enhancement of photocatalytic activity in the presence of H_2O_2, Catalysts 12 (2022) 1370, https://doi.org/10.3390/catal12111370.

[16] S. Sun, H. Yao, W. Fu, F. Liu, X. Wang, W. Zhang, Enhanced degradation of carbamazepine in FeOCl based Photo-Fenton reaction, J. Environ. Chem. Eng. 9 (2021), 104501, https://doi.org/10.1016/j.jece.2020.104501.

[17] S. Venkatesh, K. Venkatesh, A.R. Quaff, Dye decomposition by combined ozonation and anaerobic treatment: cost effective technology, J. Appl. Res. Technol. 15 (2017) 340–345, https://doi.org/10.1016/j.jart.2017.02.006.

[18] J. Gomes, R. Costa, R.M. Quinta-Ferreira, R.C. Martins, Application of ozonation for pharmaceuticals and personal care products removal from water, Sci. Total Environ. 586 (2017) 265–283, https://doi.org/10.1016/j.scitotenv.2017.01.216.

[19] R. Saravanan, F. Gracia, A. Stephen, Basic principles (in:), Mech., Chall. Photocatal. (2017) 19–40, https://doi.org/10.1007/978-3-319-62446-4_2.

[20] R. Marschall, Semiconductor composites: strategies for enhancing charge carrier separation to improve photocatalytic activity, Adv. Funct. Mater. 24 (2014) 2421–2440, https://doi.org/10.1002/adfm.201303214.

[21] A. Grzegórska, P. Głuchowski, J. Karczewski, J. Ryl, I. Wysocka, K. Siuzdak, G. Trykowski, K. Grochowska, A. Zielińska-Jurek, Enhanced photocatalytic activity of accordion-like layered Ti_3C_2 (MXene) coupled with Fe-modified decahedral anatase particles exposing {1 0 1} and {0 0 1} facets, Chem. Eng. J. 426 (2021), https://doi.org/10.1016/j.cej.2021.130801.

[22] A. Grzegórska, A. Gajewicz-Skretna, G. Trykowski, K. Sikora, A. Zielińska-Jurek, Design and synthesis of TiO_2/Ti_3C_2 composites for highly efficient photocatalytic removal of acetaminophen: the relationships between synthesis parameters, physicochemical properties, and photocatalytic activity, Catal. Today (2022), https://doi.org/10.1016/j.cattod.2022.12.011.

[23] C. Peng, X. Xie, W. Xu, T. Zhou, P. Wei, J. Jia, K. Zhang, Y. Cao, H. Wang, F. Peng, R. Yang, X. Yan, H. Pan, H. Yu, Engineering highly active Ag/Nb_2O_5@Nb_2CT_x (MXene) photocatalysts via steering charge kinetics strategy, Chem. Eng. J. 421 (2021), https://doi.org/10.1016/j.cej.2021.128766.

[24] Y. Wang, X. Hu, H. Song, Y. Cai, Z. Li, D. Zu, P. Zhang, D. Chong, N. Gao, Y. Shen, C. Li, Oxygen vacancies in actiniae like Nb_2O_5/Nb_2C MXene heterojunction boosting visible light photocatalytic NO removal, Appl. Catal. B. 299 (2021), https://doi.org/10.1016/j.apcatb.2021.120677.

[25] A.M. Chávez, R.R. Solís, F.J. Beltrán, Magnetic graphene TiO_2-based photocatalyst for the removal of pollutants of emerging concern in water by simulated sunlight aided photocatalytic ozonation, Appl. Catal. B. 262 (2020), 118275, https://doi.org/10.1016/j.apcatb.2019.118275.

[26] Z. Lendzion-Bieluń, A. Wojciechowska, J. Grzechulska-Damszel, U. Narkiewicz, Z. Śniadecki, B. Idzikowski, Effective processes of phenol degradation on Fe_3O_4–TiO_2 nanostructured magnetic photocatalyst, J. Phys. Chem. Solids 136 (2020), 109178, https://doi.org/10.1016/j.jpcs.2019.109178.

[27] K.K. Kefeni, B.B. Mamba, Photocatalytic application of spinel ferrite nanoparticles and nanocomposites in wastewater treatment: Review, Sustain. Mater. Technol. 23 (2020), e00140, https://doi.org/10.1016/j.susmat.2019.e00140.

[28] R. Suresh, S. Rajendran, P.S. Kumar, D.-V.N. Vo, L. Cornejo-Ponce, Recent advancements of spinel ferrite based binary nanocomposite photocatalysts in wastewater treatment, Chemosphere 274 (2021), 129734, https://doi.org/10.1016/j.chemosphere.2021.129734.

[29] B. Mandal, J. Panda, P.K. Paul, R. Sarkar, B. Tudu, $MnFe_2O_4$ decorated reduced graphene oxide heterostructures: nanophotocatalyst for methylene blue dye degradation, Vacuum 173 (2020), https://doi.org/10.1016/j.vacuum.2019.109150.

[30] W. Han, D. Li, M. Zhang, H. Ximin, X. Duan, S. Liu, S. Wang, Photocatalytic activation of peroxymonosulfate by surface-tailored carbon quantum dots, J. Hazard Mater. 395 (2020), https://doi.org/10.1016/j.jhazmat.2020.122695.

[31] W. Shi, Y. Liu, W. Sun, Y. Hong, X. Li, X. Lin, F. Guo, J. Shi, Assembling g-C_3N_4 nanosheets on rod-like $CoFe_2O_4$ nanocrystals to boost photocatalytic degradation of ciprofloxacin with peroxymonosulfate activation, Mater. Today Commun. 29 (2021), https://doi.org/10.1016/j.mtcomm.2021.102871.

[32] J. Li, X. Cheng, H. Zhang, J. Gou, X. Zhang, D. Wu, D.D. Dionysiou, Insights into performance and mechanism of ZnO/$CuCo_2O_4$ composite as heterogeneous photoactivator of peroxymonosulfate for enrofloxacin degradation, J. Hazard Mater. 448 (2023), 130946, https://doi.org/10.1016/j.jhazmat.2023.130946.

[33] M.G. Antoniou, A.A. de la Cruz, D.D. Dionysiou, Degradation of microcystin-LR using sulfate radicals generated through photolysis, thermolysis and e− transfer mechanisms, Appl. Catal. B. 96 (2010) 290–298, https://doi.org/10.1016/j.apcatb.2010.02.013.

[34] V. Hasija, P. Raizada, V.K. Thakur, T. Ahamad, S.M. Alshehri, S. Thakur, V. H. Nguyen, Q. van Le, P. Singh, An overview on photocatalytic sulfate radical formation via doped graphitic carbon nitride for water remediation, Curr. Opin. Chem. Eng. 37 (2022), 100841, https://doi.org/10.1016/j.coche.2022.100841.
[35] X. Tan, J. Bai, J. Zheng, Y. Zhang, J. Li, T. Zhou, L. Xia, Q. Xu, B. Zhou, Photocatalytic fuel cell based on sulfate radicals converted from sulfates in situ for wastewater treatment and chemical energy utilisation, Catal. Today 335 (2019) 485–491, https://doi.org/10.1016/j.cattod.2019.02.014.
[36] B. Cao, S. Wan, Y. Wang, H. Guo, M. Ou, Q. Zhong, Highly-efficient visible-light-driven photocatalytic H_2 evolution integrated with microplastic degradation over MXene/$Zn_xCd_{1-x}S$ photocatalyst, J. Colloid Interface Sci. 605 (2022) 311–319, https://doi.org/10.1016/j.jcis.2021.07.113.
[37] S. Cao, B. Shen, T. Tong, J. Fu, J. Yu, 2D/2D heterojunction of ultrathin MXene/Bi_2WO_6 nanosheets for improved photocatalytic CO_2 reduction, Adv. Funct. Mater. 28 (2018), 1800136, https://doi.org/10.1002/adfm.201800136.
[38] Y. Cao, Q. Deng, Z. Liu, D. Shen, T. Wang, Q. Huang, S. Du, N. Jiang, C. T. Lin, J. Yu, Enhanced thermal properties of poly(vinylidene fluoride) composites with ultrathin nanosheets of MXene, RSC Adv. 7 (2017) 20494–20501, https://doi.org/10.1039/C7RA00184C.
[39] W.Y. Chen, X. Jiang, S.-N. Lai, D. Peroulis, L. Stanciu, Nanohybrids of a MXene and transition metal dichalcogenide for selective detection of volatile organic compounds, Nat. Commun. 11 (2020) 1302, https://doi.org/10.1038/s41467-020-15092-4.
[40] D. Xu, Z. Li, L. Li, J. Wang, Insights into the photothermal conversion of 2D MXene nanomaterials: synthesis, mechanism, and applications, Adv. Funct. Mater. 30 (2020), 2000712, https://doi.org/10.1002/adfm.202000712.
[41] P. Kommu, R. Dash, G.P. Singh, A.S. Bhattacharyya, Mixed transitional metal oxide of $MnFe_2O_4$ synthesised by solution combustion method and their electrochemical applications, Energy Storage (2022), https://doi.org/10.1002/est2.423.
[42] F. Jelokhani, S. Sheibani, A. Ataie, Adsorption and photocatalytic characteristics of cobalt ferrite-reduced graphene oxide and cobalt ferrite-carbon nanotube nanocomposites, J. Photochem. Photobio. A Chem. 403 (2020), 112867, https://doi.org/10.1016/j.jphotochem.2020.112867.
[43] H. Qin, Y. Yang, W. Shi, Y. She, Heterogeneous Fenton degradation of ofloxacin catalysed by magnetic nanostructured $MnFe_2O_4$ with different morphologies, Environ. Sci. Pollut. Res. 28 (2021) 26558–26570, https://doi.org/10.1007/s11356-021-12548-y.
[44] A. Iqbal, U. Saidu, S. Sreekantan, M.N. Ahmad, M. Rashid, N.M. Ahmed, W. H. Danial, L.D. Wilson, Mesoporous TiO_2 implanted ZnO QDs for the photodegradation of tetracycline: material design, structural characterisation and photodegradation mechanism, Catalysts 11 (2021) 1205, https://doi.org/10.3390/catal11101205.
[45] Y. Sun, Y. Sun, X. Meng, Y. Gao, Y. Dall'Agnese, G. Chen, C. Dall'Agnese, X.-F. Wang, Eosin Y-sensitized partially oxidised Ti_3C_2 MXene for photocatalytic hydrogen evolution, Catal. Sci. Technol. 9 (2019) 310–315, https://doi.org/10.1039/C8CY02240B.
[46] T.M. Hammad, J.K. Salem, A.A. Amsha, N.K. Hejazy, Optical and magnetic characterisations of zinc substituted copper ferrite synthesised by a co-precipitation chemical method, J. Alloy. Compd. 741 (2018) 123–130, https://doi.org/10.1016/j.jallcom.2018.01.123.
[47] N. Pradhan, Red-tuned Mn d-d emission in doped semiconductor nanocrystals, ChemPhysChem 17 (2016) 1087–1094, https://doi.org/10.1002/cphc.201500953.
[48] B. Boutra, N. Güy, M. Özacar, M. Trari, Magnetically separable $MnFe_2O_4$/TA/ZnO nanocomposites for photocatalytic degradation of Congo Red under visible light, J. Magn. Magn. Mater. 497 (2020), 165994, https://doi.org/10.1016/j.jmmm.2019.165994.
[49] J. Qu, J. He, H. Li, Q. Jiang, M. Li, Q. Kong, M. Shi, R. Li, C. Li, Unraveling the role of interface in photogenerated charge separation at the anatase/rutile heterophase junction, J. Phys. Chem. C. 127 (2023) 768–775, https://doi.org/10.1021/acs.jpcc.2c07482.
[50] W.K. Wang, J.J. Chen, X. Zhang, Y.X. Huang, W.W. Li, H.Q. Yu, Self-induced synthesis of phase-junction TiO_2 with a tailored rutile to anatase ratio below phase transition temperature, Sci. Rep. 6 (2016) 20491, https://doi.org/10.1038/srep20491.
[51] R. Quesada Cabrera, C. Sotelo Vazquez, J.C. Bear, J.A. Darr, I.P. Parkin, Photocatalytic evidence of the rutile-to-anatase electron transfer in titania, Adv. Mater. Interfaces 1 (2014), 1400069, https://doi.org/10.1002/admi.201400069.
[52] Y. Chen, Z. Jiang, L. Xu, C. Liu, Y. Cheng, Y. Zou, Q. Zhang, Composite magnetic photocatalyst $Bi_{24}O_{31}Br_{10}$/$NiFe_2O_4$: Hydrothermal preparation, characterisation and photocatalytic mechanism, Mater. Sci. Semicond. Process 126 (2021), https://doi.org/10.1016/j.mssp.2021.105669.
[53] M. Li, C. Song, Y. Wu, M. Wang, Z. Pan, Y. Sun, L. Meng, S. Han, L. Xu, L. Gan, Novel Z-scheme visible-light photocatalyst based on $CoFe_2O_4$/BiOBr/Graphene composites for organic dye degradation and Cr(VI) reduction, Appl. Surf. Sci. 478 (2019) 744–753, https://doi.org/10.1016/j.apsusc.2019.02.017.
[54] H.L. So, K.Y. Lin, W. Chu, H. Gong, Degradation of triclosan by recyclable $MnFe_2O_4$-activated PMS: process modification for reduced toxicity and enhanced performance, Ind. Eng. Chem. Res 59 (2020) 4257–4264, https://doi.org/10.1021/acs.iecr.9b05481.
[55] G. Chen, X. Zhang, Y. Gao, G. Zhu, Q. Cheng, X. Cheng, Novel magnetic MnO_2/$MnFe_2O_4$ nanocomposite as a heterogeneous catalyst for activation of peroxymonosulfate (PMS) toward oxidation of organic pollutants, Sep Purif. Technol. 213 (2019) 456–464, https://doi.org/10.1016/j.seppur.2018.12.049.
[56] L. Zhu, Z. Shi, L. Deng, Y. Duan, Efficient degradation of sulfadiazine using magnetically recoverable $MnFe_2O_4$/δ-MnO_2 hybrid as a heterogeneous catalyst of peroxymonosulfate, Colloids Surf. A Physicochem Eng. Asp. 609 (2021), 125637, https://doi.org/10.1016/j.colsurfa.2020.125637.
[57] M. Ahmadi, F. Ghanbari, M. Moradi, Photocatalysis assisted by peroxymonosulfate and persulfate for benzotriazole degradation: effect of pH on sulfate and hydroxyl radicals, Water Sci. Technol. 72 (2015) 2095–2102, https://doi.org/10.2166/wst.2015.437.
[58] X. Liu, J. Zhou, D. Liu, L. Li, W. Liu, S. Liu, C. Feng, Construction of Z scheme $CuFe_2O_4$/MnO_2 photocatalyst and activating peroxymonosulfate for phenol degradation: synergistic effect, degradation pathways, and mechanism, Environ. Res 200 (2021), 111736, https://doi.org/10.1016/j.envres.2021.111736.
[59] Y. Huang, Q. Jiang, X. Yu, H. Gan, X. Zhu, S. Fan, Y. Su, Z. Xu, C. He, A combined radical and non-radical oxidation processes for efficient degradation of Acid Orange 7 in the homogeneous Cu(II)/PMS system: important role of chloride, Environ. Sci. Pollut. Res. 28 (2021) 51251–51264, https://doi.org/10.1007/s11356-021-14262-1.
[60] H. Ming, D. Wei, Y. Yang, B. Chen, C. Yang, J. Zhang, Y. Hou, Photocatalytic activation of peroxymonosulfate by carbon quantum dots functionalised carbon nitride for efficient degradation of bisphenol A under visible-light irradiation, Chem. Eng. J. 424 (2021), 130296, https://doi.org/10.1016/j.cej.2021.130296.
[61] C.C. Yang, C.L. Huang, T.C. Cheng, H.T. Lai, Inhibitory effect of salinity on the photocatalytic degradation of three sulfonamide antibiotics, Int Biodeterior. Biodegrad. 102 (2015) 116–125, https://doi.org/10.1016/j.ibiod.2015.01.015.
[62] S. Dudziak, A. Fiszka Borzyszkowska, A. Zielińska Jurek, Photocatalytic degradation and pollutant-oriented structure-activity analysis of carbamazepine, ibuprofen and acetaminophen over faceted TiO_2, J. Environ. Chem. Eng. 11 (2023), 109553, https://doi.org/10.1016/j.jece.2023.109553.
[63] I. Georgaki, E. Vasilaki, N. Katsarakis, A study on the degradation of carbamazepine and ibuprofen by TiO_2 & ZnO Photocatalysis upon UV/visible-light irradiation, Am. J. Anal. Chem. 05 (2014) 518–534, https://doi.org/10.4236/ajac.2014.58060.
[64] Z. Xie, D.D. Dionysiou, S. Luo, M. Chen, Z. Wei, Dual reaction center catalyst based on common metals Cu Mg Al for synergistic peroxymonosulfate adsorption-activation in Fenton-like process, Appl. Catal. B. 327 (2023), 122468, https://doi.org/10.1016/j.apcatb.2023.122468.
[65] M. Long, D. Li, H. Li, X. Ma, Q. Zhao, Q. Wen, F. Song, Synergetic effect of photocatalysis and peroxymonosulfate activated by MFe_2O_4 (M = Co, Mn, or Zn) for enhanced photocatalytic activity under visible light irradiation, RSC Adv. 12 (2022) 20946–20955, https://doi.org/10.1039/D2RA03558H.
[66] Y. Fang, H. Wang, X. Wang, Y. Zhou, L. Wu, W. Duo Wu, Z. Wu, Constructing thin BiOCl nanoplates for highly efficient photocatalytic peroxymonosulfate activation: in-depth understanding of the activation process, Sep Purif. Technol. 307 (2023), 122771, https://doi.org/10.1016/j.seppur.2022.122771.
[67] X. Wang, W. Lu, Z. Zhao, H. Zhong, Z. Zhu, W. Chen, In situ stable growth of β-FeOOH on g-C_3N_4 for deep oxidation of emerging contaminants by photocatalytic activation of peroxymonosulfate under solar irradiation, Chem. Eng. J. 400 (2020), 125872, https://doi.org/10.1016/j.cej.2020.125872.
[68] Y. Zhou, H. Zhang, L. Wu, Y. Zhang, X. Wang, Z. Wu, Hollow hemispherical Si-doped anatase for efficient carbamazepine degradation via photocatalytic activation of peroxymonosulfate, Chem. Eng. J. 457 (2023), 141234, https://doi.org/10.1016/j.cej.2022.141234.

Supporting Information

Magnetically recyclable TiO_2/MXene/$MnFe_2O_4$ photocatalyst for enhanced peroxymonosulphate-assisted photocatalytic degradation of carbamazepine and ibuprofen under simulated solar light

Anna Grzegórska[1], Joseph Chibueze Ofoegbu[2], Laura Cervera-Gabalda[3], Cristina Gómez-Polo[3], Diana Sannino[2], Anna Zielińska-Jurek[1]**

[1] Department of Process Engineering and Chemical Technology, Faculty of Chemistry, Gdańsk University of Technology, G. Narutowicza 11/12, 80-233 Gdańsk, Poland

[2] Department of Industrial Engineering, University of Salerno, via Giovanni Paolo II, 132, 84084 Fisciano, Italy

[3] Departamento de Ciencias-INAMAT[2], Universidad Pública de Navarra, Campus de Arrosadia, 31006 Pamplona, Spain

* Corresponding authors: *annjurek@pg.edu.pl, anna.grzegorska@pg.edu.pl*

3. Results and discussion

3.1 Characterization of $MnFe_2O_4$, TiO_2/Ti_3C_2 and $TiO_2/Ti_3C_2/MnFe_2O_4$ photocatalysts

Table S1. ICP-OES measurements for the $TiO_2/Ti_3C_2/5\%MnFe_2O_4$.

Element	Content (wt%)
Ti	33.9930±2.0554
Mn	0.9436±0.0632
Fe	2.0062±0.1147

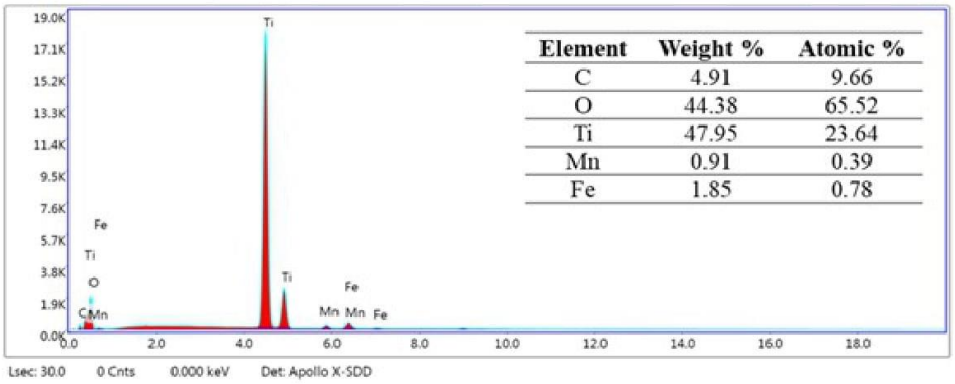

Element	Weight %	Atomic %
C	4.91	9.66
O	44.38	65.52
Ti	47.95	23.64
Mn	0.91	0.39
Fe	1.85	0.78

Figure S1. SEM area EDS spectrum with atomic and weight percentage of elements.

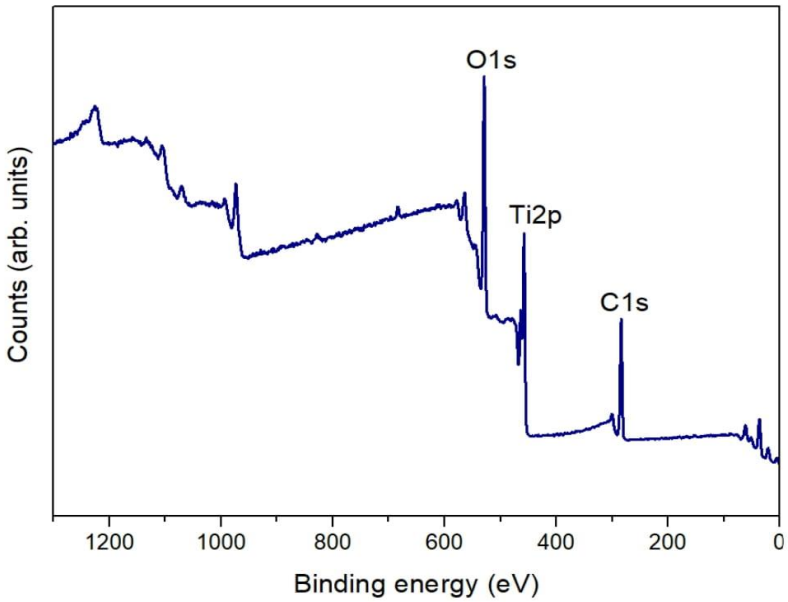

Figure S2. Survey XPS spectra for TiO_2/Ti_3C_2 composite.

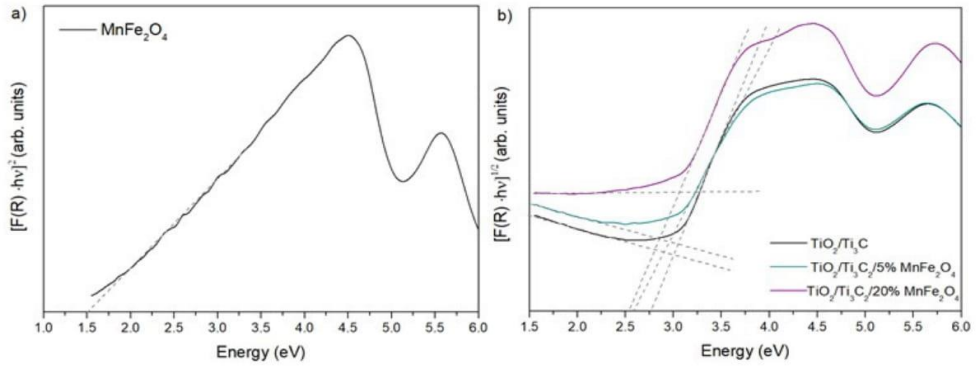

Figure S3. The band gap determination from Kubelka Munk function for various photocatalysts.

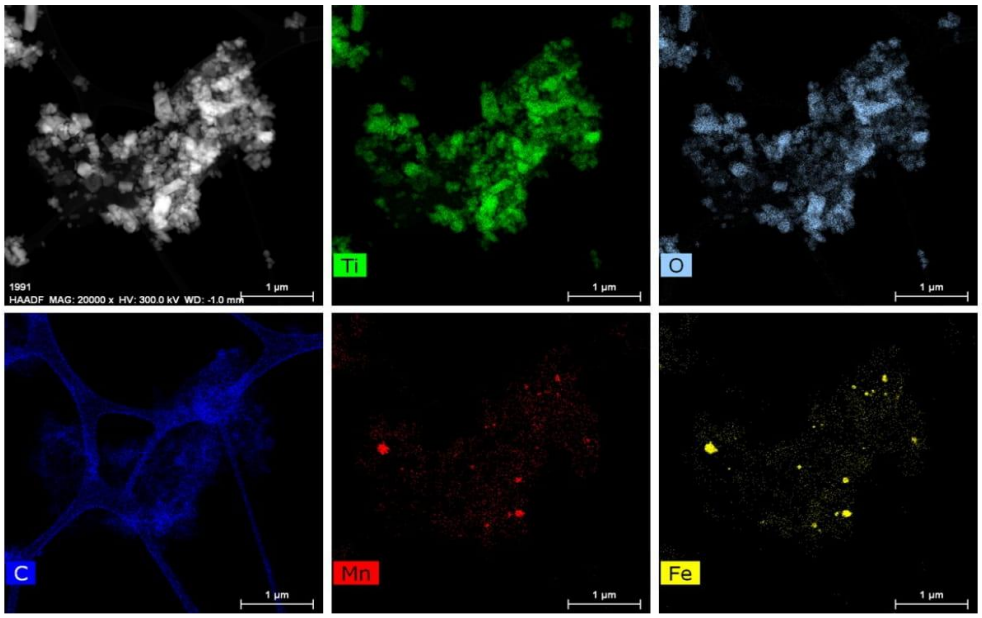

Figure S4. HAADF-STEM image and STEM-EDS elemental mapping of $TiO_2/Ti_3C_2/5\%MnFe_2O_4$.

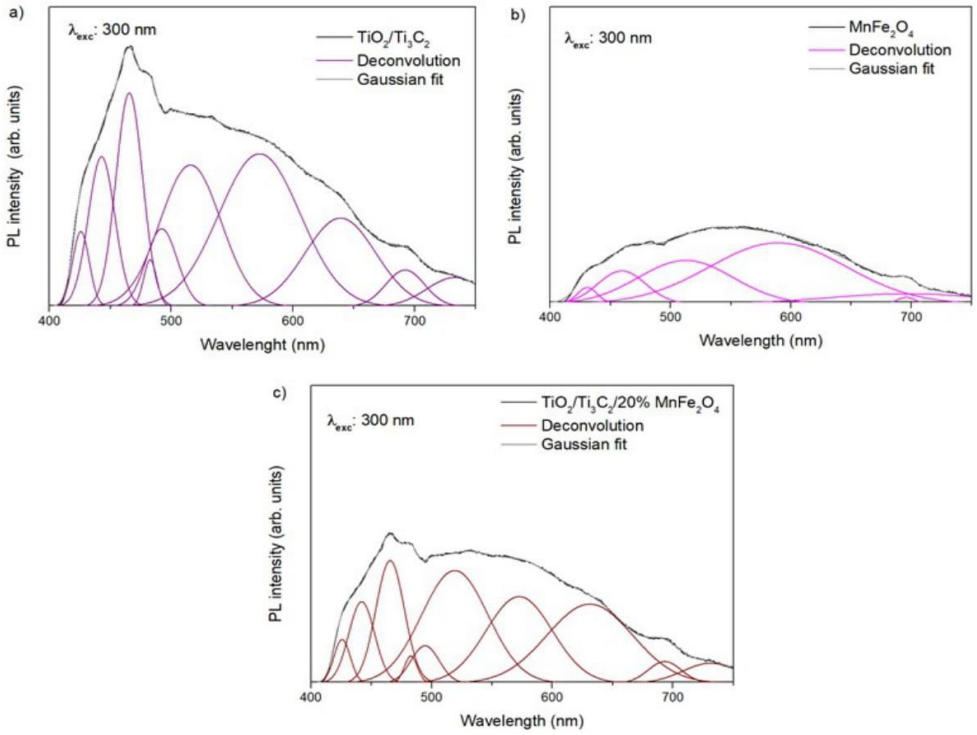

Figure S5. The Gaussian fitting and deconvolution of PL spectra of the TiO_2/Ti_3C_2 (a), $MnFe_2O_4$ (b), and $TiO_2/Ti_3C_2/20\%MnFe_2O_4$ (c)

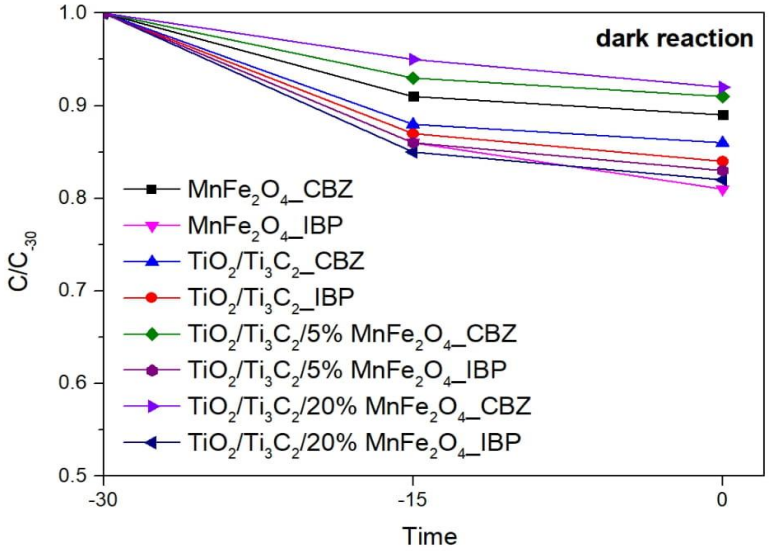

Figure S6. CBZ and IBP adsorption (dark reaction) for prepared materials.

Table S2. The rate constant of CBZ and IBP degradation in the CBZ/IBU mixture for selected processes.

Sample	CBZ degradation rate constant ($min^{-1} \cdot 10^{-2}$)	IBP degradation rate constant ($min^{-1} \cdot 10^{-2}$)
Photolysis	0.5±0.02	1.2±0.05
Photolysis/PMS	4.8±0.14	5.2±0.23
TiO_2/Ti_3C_2	6.9±0.19	6.2±0.24
TiO_2/Ti_3C_2/5% $MnFe_2O_4$	8.9±0.27	7.0±0.18
TiO_2/Ti_3C_2/5% $MnFe_2O_4$/PMS (0.25 mM)	28.6±0.98	53.0±1.4

Table S3. The TOC removal (%) in the CBZ/IBU mixture for selected processes.

Sample	TOC removal (%)
TiO_2/Ti_3C_2/5% $MnFe_2O_4$/PMS (0.25 mM) Amount of photocatalyts - 2g/dm^3	54±1.7%
TiO_2/Ti_3C_2/5% $MnFe_2O_4$/PMS (0.25 mM) Amount of photocatalyts - 1g/dm^3	51±0.6%
TiO_2/Ti_3C_2/5% $MnFe_2O_4$/PMS (0.25 mM) Amount of photocatalyts - 0.5 g/dm^3	47±1.3%
TiO_2/Ti_3C_2/5% $MnFe_2O_4$/PMS (0.25 mM) pH 4.5	57±0.8%
TiO_2/Ti_3C_2/5% $MnFe_2O_4$ /PMS (0.25 mM) pH 9.5	43.1±1.1%
TiO_2/Ti_3C_2/5% $MnFe_2O_4$/PMS (0.25 mM) Seawater	60.3±2.1%

Table S4. The metal lixiviation results for a post-process solution using TiO_2/Ti_3C_2/5% $MnFe_2O_4$/PMS (0.25 mM) and amount of photocatalyst – 2 g/dm^3.

Element	ICP-OES (mg/dm^3)	Iron Photometric Test (mg/dm^3)
Ti	<LOD	-
Mn	0.423±0.032	-
Fe	0.089±0.010	0.08

Rozdział VI. Modelling and optimisation of MXene-derived TiO_2/Ti_3C_2 synthesis parameters using Response Surface Methodology based on the Box–Behnken factorial design. Enhanced carbamazepine degradation by the Cu-modified TiO_2/Ti_3C_2 photocatalyst

Process Safety and Environmental Protection 179 (2023) 449–461

Contents lists available at ScienceDirect

Process Safety and Environmental Protection

journal homepage: www.journals.elsevier.com/process-safety-and-environmental-protection

Modelling and optimisation of MXene-derived TiO_2/Ti_3C_2 synthesis parameters using Response Surface Methodology based on the Box–Behnken factorial design. Enhanced carbamazepine degradation by the Cu-modified TiO_2/Ti_3C_2 photocatalyst

Anna Grzegórska [a,*], Jakub Karczewski [b], Anna Zielińska-Jurek [a,*]

[a] Department of Process Engineering and Chemical Technology, Faculty of Chemistry, Gdańsk University of Technology, G. Narutowicza 11/12, 80-233 Gdańsk, Poland
[b] Institute of Nanotechnology and Materials Engineering, Faculty of Applied Physics and Mathematics, Gdańsk University of Technology, G. Narutowicza 11/12, 80-233 Gdańsk, Poland

ARTICLE INFO

Keywords:
Box-Behnken
Carbamazepine
Cu species
MXene
Photocatalysis
Optimisation
RSM
Ti_3C_2
TiO_2

ABSTRACT

In the present study, a hydrothermal method in a water/ethanol environment was used for the first time to obtain novel Cu/TiO_2/Ti_3C_2 composites with high photocatalytic activity for the degradation of carbamazepine (CBZ) under simulated solar light. The Box–Behnken factorial design was coupled with Response Surface Methodology (RSM) for synthesis parameter optimisation. The effect of different synthesis parameters, including temperature, time and water/ethanol ratio, was for the first time studied in detail. The analysis of variance (ANOVA) was used to verify the adequacy of the proposed model. The water/ethanol ratio was the most influential parameter for anatase crystallite growth and the efficiency of carbamazepine degradation. The TiO_2/Ti_3C_2 sample prepared under the optimised conditions (synthesis time of 17 h, temperature of 220 °C, and water/ethanol ratio of 58:42 v/v) revealed almost 100% of CBZ degradation within 60 min. Furthermore, the surface modification of this sample with 0.25% - 1 wt% of copper resulted in improved photocatalytic activity. For TiO_2/Ti_3C_2 modified with 0.5% of Cu, almost complete CBZ degradation was observed in 40 min of the photodegradation process. Finally, the combination of the photodegradation process with the activation of peroxymonosulphate (PMS) by Cu-TiO_2/Ti_3C_2 resulted in markedly improved carbamazepine degradation and reached 100% within 20 min under simulated solar light irradiation. The degradation mechanism of CBZ was proposed based on trapping experiments, which revealed that $\bullet O_2^-$ and $\bullet SO_4^-$ are the main oxidising species involved in carbamazepine degradation. Moreover, the hybrid system exhibited high recyclability and stability during subsequent photodegradation cycles.

1. Introduction

The water demand in many places worldwide has surpassed its supply and continues to grow. Population growth, climate change, industrialisation, and destruction of the environment contribute to a greater demand for water (Rathi et al., 2021). Therefore, the recycling of water is crucial. Recently, anthropogenic activities have led to high levels of water resource pollution with emerging contaminants such as endocrine-disrupting compounds, personal care products and pharmaceuticals, which are not biodegradable in conventional wastewater treatment plants. The presence of these substances and their transformation products in aquatic systems may cause serious environmental and health concerns. For example, carbamazepine (CBZ) is the most frequently detected pharmaceutical in water bodies. This antiepileptic drug is a recalcitrant compound that is not susceptible to biodegradation and is not efficiently removed by wastewater treatment plants (WWTPs) or naturally occurring photolysis process. The human body metabolises approximately 72% of CBZ, while 28% is unchanged and subsequently discharged through faeces to the environment, along with its main metabolites, such as 3-hydroxycarbamazepine and carbamazepine-10, 11-epoxide, which are more toxic to daphnids than the parent compound (Zind et al., 2021; Gubitosa et al., 2022). Moreover, it exhibits high water solubility, biomagnification, and bioaccumulation in aquatic organisms. Mezzelani et al. (2020) observed that CBZ was the most

* Corresponding authors.
E-mail addresses: anna.grzegorska@pg.edu.pl (A. Grzegórska), annjurek@pg.edu.pl (A. Zielińska-Jurek).

https://doi.org/10.1016/j.psep.2023.09.028
Received 12 July 2023; Received in revised form 29 August 2023; Accepted 12 September 2023
Available online 16 September 2023

frequently detected pharmaceutical in more than 95% of Mediterranean mussels collected over 4 years from 14 sites along the Adriatic and Tyrrhenian Sea. Almeida et al. (2021) reported that CBZ, at environmentally relevant concentrations (up to 1 μg/dm^3), may alter biological responses (physiological, cellular, molecular) in marine bivalves. According to European legislation on the classification and labelling of chemicals (92/32/EEC), carbamazepine is classified as R52/53 substance, which is hazardous to aquatic organisms and may cause long-term adverse effects in the aquatic environment (Zhang et al., 2008). Furthermore, carbamazepine has been proposed as an anthropogenic marker for water bodies. In Germany, CBZ has been detected in WWTPs effluents, surface water, and groundwater at concentrations of 1075–6300 ng·dm^{-3}, 81–1100 ng·dm^{-3}, and 1–100 ng·dm^{-3}, respectively. In the United Kingdom, the concentrations are found to be 152–4596 ng·dm^{-3}, 9–327 ng·dm^{-3}, and 425–3600 ng·dm^{-3} (Hai et al., 2018).

Therefore, the occurrence, fate, transformation, and transfer of the emerging pollutants in the environment must be identified. Moreover, a significant issue to address is the degradation of persistent and emerging contaminants by the application of advanced treatment technologies such as ozonation, Fenton, photo-Fenton, and photocatalysis (Rivera-Utrilla et al., 2013). The selection of a treatment method depends on the specific characteristics of the wastewater and the physicochemical properties of the pharmaceuticals. It is particularly important to consider the potential environmental and human health impacts of each treatment method and select an efficient and sustainable technology.

In this regard, photocatalysis is a significant approach as an efficient green remediation technology for the degradation of persistent and emerging organic pollutants. In this process, the generation of electrons and holes leads to the formation of reactive oxygen species (ROS) such as hydroxyl radicals (OH•), superoxide radical anions (•O_2^-), singlet oxygen ($^1O_2$), and hydrogen peroxide (H_2O_2), which can selectively or non-selectively oxidise and mineralise a wide range of contaminants in water and air (Wolski et al., 2019; Afreen et al., 2020). Among a wide group of semiconductor materials, titanium(IV) oxide is a commonly used photocatalyst with low cost, strong oxidising potential, and chemical stability (Simamora et al., 2012). Nevertheless, its activity limited to UV irradiation and fast charge carrier recombination enforces the search for alternative approaches (Dong et al., 2015). The combination of TiO_2 with highly conductive carbonaceous materials is a potential strategy to inhibit the fast recombination of photogenerated electrons and holes (Asencios et al., 2022). Among carbonaceous materials, MXenes have attracted attention in various fields because of their unique properties, including non-toxicity, excellent mechanical strength, large interlayer spacing, extraordinary electrical and thermal conductivity, hydrophilicity, rich surface chemistry, and biocompatibility (Im et al., 2021; Zhang et al., 2020). Moreover, the in situ oxidation of MXene led to the formation of MXene/metal oxide composite, i.e. Ti_3C_2/TiO_2, with intimate contact, which provides highly efficient charge carriers separation (Grzegórska et al., 2021).

In this study, we focused for the first time on the effect of the synthesis parameters, including temperature, time, water/ethanol ratio and modification with copper species on the photocatalytic degradation of carbamazepine in the presence of TiO_2/Ti_3C_2 under simulated solar light. The Box–Behnken factorial design was coupled with Response Surface Methodology (RSM) for optimisation of temperature, water/ethanol ratio, and hydrothermal reaction Then, ANOVA was used to study the statistically significant parameters and their interactions. Furthermore, the TiO_2/Ti_3C_2 sample obtained under optimal conditions was modified with copper species to improve charge carriers separation and enhanced photocatalytic activity under simulated solar light. Among transition metals, copper is an inexpensive metal, almost 100 times and 6000 times cheaper than Ag and Au, with excellent thermal and electrical conductivity (Gawande et al., 2016). Highly reactive copper species can promote various reactions via both one- and two-electron pathways, owing to their wide range of oxidation states (Cu^0, Cu^+, Cu^{2+}, and Cu^{3+}) (Muscetta et al., 2020).

Table 1
Experimental range and levels of the independent variables in the Box–Behnken statistical experimental design.

Variable design	Factors	Coded level		
		-1	0	+1
A	Temperature (°C)	180	200	220
B	Time (hours)	6	15	24
C	Amount of ethanol (vol%)	0	50	100

Table 2
The Box-Behnken design with experimental values for the independent variables and optimum conditions determined based on the response optimisation for CBZ degradation.

Experiment symbol	Coded level of variables			Actual level of variables		
	A	B	C	A	B	C
S1	-1	-1	0	180	6	50
S2	+1	-1	0	220	6	50
S3	-1	+1	0	180	24	50
S4	+1	+1	0	220	24	50
S5	-1	0	-1	180	15	0
S6	+1	0	-1	220	15	0
S7	-1	0	+1	180	15	100
S8	+1	0	+1	220	15	100
S9	0	-1	-1	200	6	0
S10	0	+1	-1	200	24	0
S11	0	-1	+1	200	6	100
S12	0	+1	+1	200	24	100
S13	0	0	0	200	15	50
S14	0	0	0	200	15	50
S15	0	0	0	200	15	50
S16	optimum conditions			220	17	42

In addition, copper species may effectively activate peroxymonosulphate (PMS) to produce sulphate radicals, a promising alternative to hydroxyl radicals. The •SO_4^- radicals have a higher redox potential (E_0 = 2.5–3.1 V) than OH• (1.8–2.8 V) radicals. Moreover, sulphate radicals reveal a longer half-life (4×10^{-5} s) than that of OH• radicals (2×10^{-5} s). Notably, during •SO_4^- based oxidation processes, secondary oxidants such as •OH, •O_2^-, and $^1O_2$ can also be produced, which accelerates the degradation rate of organic contaminants (Hasija et al., 2022). Therefore, a promising strategy of photocatalysis assisted by peroxymonosulphate (PMS) activation for enhanced CBZ degradation is proposed in this study.

2. Materials

Ti_3AlC_2 was purchased from Luoyang Tongrun Info Technology Co. (China). HF (ACS reagent, 50%), ethanol (anhydrous, 99.8%), copper (II) nitrate trihydrate (p.a., 99–104%), potassium peroxymonosulphate (OXONE, monopersulphate compound), and carbamazepine (Pharmaceutical Secondary Standard; Certified Reference Material) were provided by Sigma Aldrich. Beznoquinone (reagent grade, ≥ 98%), ammonium oxalate (ACS reagent, ≥ 99%), isopropanol (anhydrous, 99.5%), and tert-butanol (anhydrous, 99.5%) were supplied by Sigma Aldrich. Acetonitrile (HPLC grade) and H_3PO_4 (85%, HPLC grade) applied to determine the CBZ concentration by HPLC were provided by Sigma Aldrich. All reagents were used as received without additional treatment. Deionised (DI) water was used in all experiments.

3. Methods

3.1. Experiment design

The statistical software Minitab version 21.1 (Minitab USA, 2021) was used to design and analyse the effects of various synthesis

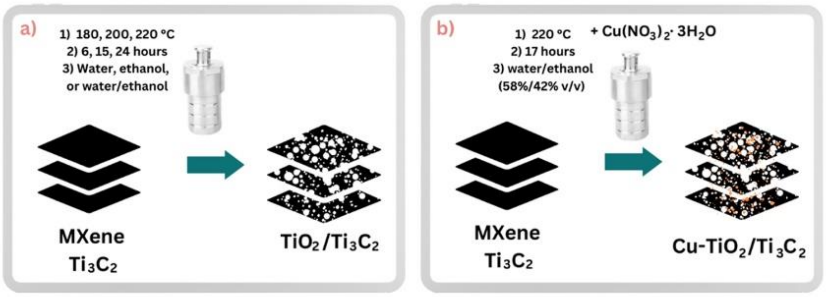

Fig. 1. Schematic representation of the synthesis procedure.

parameters on the physicochemical properties of the materials and the photodegradation of CBZ. A three-factor three-level Box-Behnken experimental design (BBD), along with RSM, was used to correlate the interactions among the variables and responses. Based on the BBD design, 15 runs were performed to obtain precise results. The coefficients were analysed using analysis of variance (ANOVA). Each of the parameters was analysed on the three levels: low (−1), high (+1), and centre point (0). Table 1. represents the levels and ranges of the selected independent variables. The Box-Behnken experimental design, with three independent variables, is presented in Table 2.

3.2. Preparation of MXene – $Ti_3C_2T_x$

First, 10 g of Ti_3AlC_2 was gradually added to 100 cm^3 of HF. The suspension was mixed for 24 h at room temperature. The sample was then centrifuged and washed with DI water until the pH of the washing solution was neutral.

3.3. Synthesis of TiO_2/Ti_3C_2 composite

In a typical procedure, 0.4 g $Ti_3C_2T_x$ was dispersed in water (60 cm^3), a water-ethanol mixture (1:1 v/v), or ethanol. The mixture was sonicated for 10 min to obtain a homogeneous dispersion and then mixed for another 30 min. The suspension was transferred to a Teflon-lined stainless-steel autoclave reactor and held in an oven for 6, 15, or 24 h at 180, 200, or 220 °C, according to the parameters summarised in Tables 1 and 2.

3.4. Preparation of Cu-deposited TiO_2/Ti_3C_2 composites

The TiO_2/Ti_3C_2 composites were modified with Cu particles using the one-pot synthesis method, as presented in Fig. 1. In the first step, 0.4 g $Ti_3C_2T_x$ was dispersed in 60 cm^3 of a water/ethanol mixture (58:42 v/v). Then, a proper volume of $Cu(NO_3)_2 \cdot 3\ H_2O$ aqueous solution corresponding to 0.25 wt%, 0.5 wt% and 1 wt% of Cu was added. Next, the sample was sonicated for 10 min and mixed for 30 min. The suspension was transferred to a Teflon-lined stainless steel autoclave reactor and held in an oven for 17 h at 220 °C.

3.5. Characterisation methods

The prepared materials were characterised using X-ray powder diffraction (XRD). This technique was used to determine the composition of the prepared photocatalysts and the crystallite size. XRD patterns were obtained with a powder diffractometer Rigaku Intelligent X-ray diffraction system SmartLab (Rigaku Corporation, Tokyo, Japan) with Cu Kα radiation, and in the 2θ range from 5° to 80°, with a speed of 2°min^{-1} and a step of 0.01°. UV–vis reflectance spectra of the powdered photocatalysts were recorded using a Thermo Scientific Evolution 220 spectrophotometer (Waltham, MA, USA). $BaSO_4$ was used as the reference material. Absorbance was recorded in the wavelength range of 200–800 nm. The Brunauer-Emmett-Teller (BET) surface area was determined using a Micromeritics Gemini V analyser (Norcross, GA, USA) in liquid nitrogen. Before the measurements, the powder samples (approximately 0.1 g) were degassed at 200 °C for 2 h under constant nitrogen flow. Scanning electron microscopy (SEM) was used to determine the morphologies of the prepared composites. The SEM images were obtained using an SEM microscope (FEI Quanta FEG 250). Transmission electron microscopy (TEM) analyses were conducted using a Thermo Fisher (formerly FEI) Titan Themis G2 200 Probe Cs Corrected Scanning Transmission Electron Microscope (STEM). Photoluminescence (PL) spectra were recorded on a spectrofluorometer Shimadzu RF-6000 (Kyoto, Japan). A 150 W Xenon lamp with an excitation wavelength of 300 nm was used as the excitation source. XPS analyses were performed using a multi-chamber UHV PREVAC system. The photoelectron excitation source was an X-ray tube VG Scienta SAX 100 with an aluminum anode equipped with a monochromator VG Scienta XM 780, emitting radiation with the characteristic line of Al Kα and an energy of 1486.6 eV. Spectral deconvolution was performed using CasaXPS Version 2.3.25 PR1. Electrochemical measurements were performed using an Autolab Potentiostat/Galvanostat Autolab (model PGSTAT204). The photocatalytic materials were placed on carbon screen-printed electrodes with an Ag reference electrode. The electrolyte solution (0.5 M Na_2SO_4) was purged with Ar for 10 min prior to the measurements. Electrochemical impedance spectra (EIS) Nyquist plots were recorded in the range of 10^5 Hz to 0.1 Hz with an AC voltage amplitude of 0.01 V. Mott Schottky plots were registered for the applied frequency of 1000 Hz in the potential range from − 1.5–0 V. The transient photocurrent response of the photocatalysts was recorded at a light on/off interval of 25 s at 0 V vs. Ag under 372 nm LED light illumination.

3.6. Photocatalytic activity

In a typical procedure, a photocatalyst suspension (2 g/dm^3) was prepared in a carbamazepine solution (14 mg/dm^3) in a 25 cm^3 glass reactor with a quartz window. The suspension was aerated throughout the experiment. Prior to photodegradation, the suspension was mixed in the dark for 30 min to achieve adsorption-desorption equilibrium. Subsequently, the photocatalytic experiment was performed using a 300 W Xenon lamp emitting simulated solar light irradiation. The spectrum of the used Xe lamp is presented in Fig. S1 in Supporting Materials. The reaction temperature was maintained at 20 °C. The samples were collected at 0, 20, 40, and 60 min of the process. Furthermore, the photocatalyst was separated from the solution using a 0.2 μm syringe filter. The progress of pollutant photodegradation was analysed using reverse-phase high-performance liquid chromatography (HPLC) (Shimadzu UFLC LC-20AD (Kyoto, Japan) with a photodiode array detector (Shimadzu SPD-M20A). Measurements were performed at 45 °C under isocratic flow conditions of 1.5 $cm^3 \cdot min^{-1}$. The volume

Table 3
Box-Behnken experimental results: carbamazepine degradation (%), TOC removal (%), specific surface area (m^2/g), and average anatase crystallite size (nm) of anatase TiO_2 particles.

Sample no.	Sample label	BET surface area (m^2/g)	Anatase crystallite size (nm)	Efficiency of degradation (%)	Degradation rate constant ($min^{-1} \cdot 10^{-2}$)	TOC removal (%)
S1	T180/EtOH-H_2O/6 h	34.1	12	66	1.84 ± 0.09	9.2
S2	T220/EtOH-H_2O/6 h	42.6	13.5	83	2.93 ± 0.12	16.4
S3	T180/EtOH-H_2O/ 24 h	38.1	13	88	3.54 ± 0.05	18.3
S4	T220/EtOH-H_2O/ 24 h	50.6	17	95	4.86 ± 0.07	21.2
S5	T180/H_2O/15 h	24.3	18	57	1.46 ± 0.06	3.7
S6	T220/H_2O/15 h	29.1	24	84	2.77 ± 0.08	11.0
S7	T180/EtOH/15 h	57.6	13	48	1.11 ± 0.05	9.2
S8	T220/EtOH/15 h	33.2	15	83	2.68 ± 0.09	12.8
S9	T200/H_2O/6 h	37.2	19	79.5	2.57 ± 0.04	7.3
S10	T200/H_2O/24 h	30.3	25	81	2.63 ± 0.05	17.3
S11	T200/EtOH/15 h	42.9	11.5	50	1.19 ± 0.07	10.1
S12	T200/EtOH/24 h	69.6	13	52	1.28 ± 0.03	13.5
S13	T200/EtOH-H_2O/ 15 h	38.3	13	97	5.34 ± 0.09	22.4
S14	T200/EtOH-H_2O/ 15 h	42.4	13	96.5	5.21 ± 0.13	22.9
S15	T200/EtOH-H_2O/ 15 h	39.5	13	97	5.39 ± 0.11	23.8
S16	T220/EtOH-H_2O/ 17 h	38.2	18	99.5	6.56 ± 0.13	25.2

composition of the mobile phase was 39.5% acetonitrile, 60% water, and 0.5% orthophosphoric acid. Determination of CBZ concentration was performed using the C18 column, with the injection volume of 10 µL, and the detection wavelength was set at 285 nm. The mean retention time of CBZ was 4.6 min. The calibration curve for the determination of CBZ concentration is presented in Fig. S2 in Supporting Materials.

For the photodegradation process coupled with PMS activation, after reaching the adsorption-desorption equilibrium, 0.5 mM of PMS was added to the photoreactor. The samples were collected at 0, 5, 10, 20, 30, 40, and 60 min of the process. Subsequently, after photocatalyst separation, 200 µL of methanol was added to each sample to quench the generated radical species.

Furthermore, trapping experiments were performed to analyse the mechanism of the CBZ degradation. Benzoquinone was used as a superoxide anion radicals scavenger, ammonium oxalate as holes scavenger, isopropanol as a hydroxyl radicals and sulphate radicals scavenger, and tert-butanol as a hydroxyl radicals scavenger. The concentration of the scavengers was 10-times higher than that of the CBZ in the solution.

4. Results and discussion

4.1. Box–Behnken design (BBD) and characteristic of TiO_2/Ti_3C_2 composites

Firstly, a three-factor three-level Box-Benkhen design (BBD) was developed to optimise the synthesis parameters and describe the photocatalytic degradation of carbamazepine in an aqueous solution. Carbamazepine is a persistent pharmaceutical compound not susceptible to biodegradation. Therefore, in this study, we investigated the effect of photocatalyst synthesis parameters on carbamazepine degradation to propose a highly efficient advanced treatment process.

The results obtained from the 15 experiments planned using the BBD are presented in Table 3. The responses were the efficiency of carbamazepine degradation (%), TOC removal efficiency (%), BET-specific surface area (m^2/g), and average anatase crystallite size (nm). According to the results presented in Table 3, polynomial equations in an uncoded form showing the empirical relationship between the responses (CBZ degradation, TOC removal, BET surface area, and crystallite size) and independent variables were determined.

The surface area of a photocatalyst is an important factor affecting the efficiency of the photocatalytic degradation process. A higher specific surface area with more reactive sites and a shorter migration distance may reduce the recombination rate of photogenerated electron-hole pairs (Isac et al., 2022). Furthermore, materials with higher surface areas exhibit better adsorption properties (Danish et al., 2021).

The polynomial equation representing the empirical relationship between the BET surface area and the independent variables is shown in Eq. 1. The coefficient of determination (R^2) of the model was 0.88.

$$BET\ surface\ area\ (m^2/g) = -400 + 4{\cdot}23{\cdot}A - 3{\cdot}55{\cdot}B + 1{\cdot}386{\cdot}C - 0{\cdot}00984{\cdot}A^2 + 0{\cdot}0643{\cdot}B^2 - 0{\cdot}00004{\cdot}C^2 + 0{\cdot}0055{\cdot}A{\cdot}B - 0{\cdot}00731{\cdot}A{\cdot}C + 0{\cdot}01902{\cdot}B{\cdot}C \quad (1)$$

The highest surface areas of 50.6 $m^2{\cdot}g^{-1}$, 57.6 $m^2{\cdot}g^{-1}$, and 69.6 $m^2{\cdot}g^{-1}$ were noticed for samples S4 (T220/EtOH-H_2O/24 h), S7 (T180/EtOH/15 h) and S12 (T200/EtOH/24 h), respectively. By analysing the 3D surface plots presented in Fig. 2, an increase in the BET surface area with an increase in the synthesis time and amount of ethanol used as a reaction medium was observed. The BET surface area increased with an increase in the hydrothermal reaction temperature to 200 °C, and decreased above this temperature. The ANOVA results and Pareto chart in Table S1 and Fig. S3 in the Supporting Materials show that the amount of ethanol (C) had the highest influence on the BET surface area. Only for this variable, the p-value was lower than the significance level ($p \leq \alpha$), and exceeded the red vertical line (2.571) in the Pareto chart.

Crystallite size is also one of the parameters involved in controlling photocatalytic activity. The crystallite size was calculated based on the XRD analyses presented in Fig. S4 in Supporting Materials. For all the obtained samples (S1-S15), the characteristic signals for both the anatase and MXene phases were identified. The main signals at 8.9°, 18.3°, 27.6°, and 60.6° were assigned to the (002), (004), (006), and (110) planes of MXene, respectively, and at 25.3°, 48.0°, 53.8°, and 55.0° to the (101), (200), (105), and (211) planes of anatase, respectively. The largest anatase crystallite size was observed for the samples prepared in water as a reaction medium (S5, S6, and S10) and the smallest was obtained with the addition of ethanol, which enabled the control of anatase particle nucleation and growth (samples S1, S7, and S11) (Dudziak et al., 2021).

The polynomial equation representing the empirical relationship

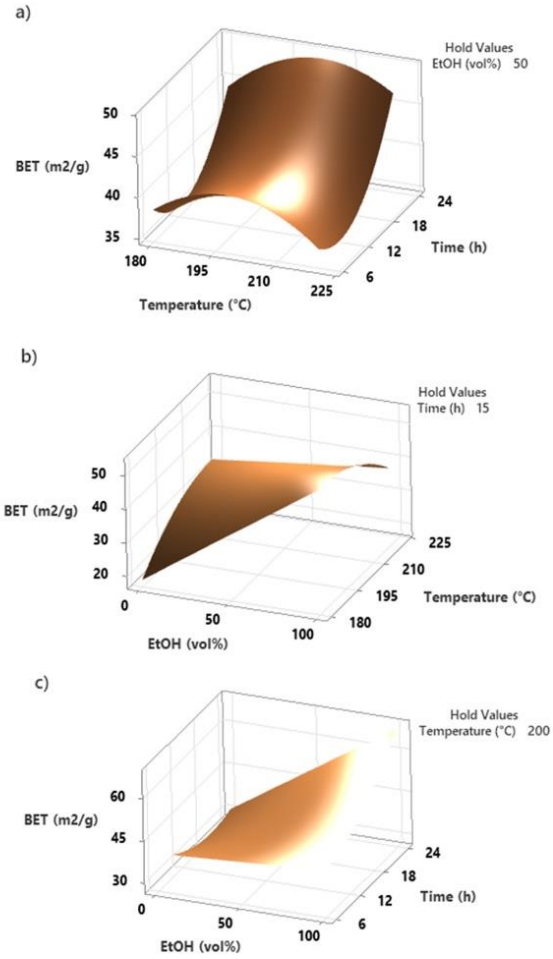

Fig. 2. 3D surface plots showing the effects of (a) temperature and synthesis time, (b) amount of ethanol and temperature, and (c) amount of ethanol and synthesis time on the BET surface area development.

between the anatase crystallite size and the independent variables is shown in Eq. 2.

The coefficient of determination (R^2) of the model was 0.98. ANOVA results and a Pareto chart (Table S2 and Fig. S5 in the Supporting Materials) showed that the amount of ethanol (C and C^2), temperature (A), and time (B) had the highest impact on the crystallite size.

$$\textit{Crystallite size (nm)} = 44{\cdot}8 - 0{\cdot}369{\cdot}A - 0{\cdot}262{\cdot}B + 0{\cdot}017{\cdot}C + 0{\cdot}00116{\cdot}A^2 + 0{\cdot}00015{\cdot}B^2 + 0{\cdot}001535{\cdot}C^2 + 0{\cdot}00264{\cdot}A{\cdot}B - 0{\cdot}001100{\cdot}A{\cdot}C - 0{\cdot}00233{\cdot}B{\cdot}C \quad (2)$$

As presented in Fig. 3, the average anatase crystallite size was positively correlated with the hydrothermal reaction temperature, time, and ethanol concentration. It was found that a longer time and higher temperature facilitated the anatase grain growth. In contrast, the average crystallite size decreased with increasing ethanol concentration. The presence of ethanol suppressed the hydrothermal oxidation of $Ti_3C_2T_x$. Furthermore, according to Zhang et al. (2017), without ethanol, TiO_2 nuclei readily grow into TiO_2 grains because of complete contact with water. Furthermore, the presence of ethyl alcohol resulted in steric hindrance, limiting grain growth and leading to the formation of smaller anatase nanoparticles.

The DR/UV–vis spectra of the selected TiO_2/Ti_3C_2 composites are

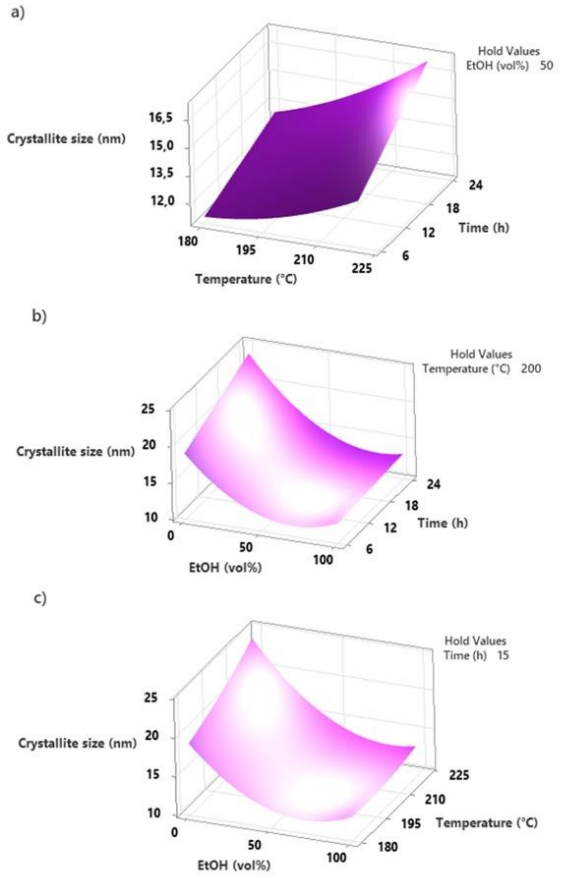

Fig. 3. 3D surface plots presenting the effects of (a) temperature and synthesis time, (b) amount of ethanol and temperature, and (c) amount of ethanol and synthesis time on TiO_2 crystallite size.

presented in Fig. S6 in Supporting Materials. All samples showed a characteristic absorption band for TiO_2 in the range of 200–350 nm. The significant increase in the absorption in the range of 400–800 nm may be attributed to the presence of MXene and its full-spectrum absorption.

Finally, scanning electron microscopy (SEM) images of the TiO_2/Ti_3C_2 composites synthesised under different conditions are shown in Fig. 4. The layered structure of MXene was preserved after the solvothermal treatment. The MXene surface was uniformly covered with fine TiO_2 nanoparticles. Furthermore, increasing the synthesis temperature led to complete coverage of the MXene sheets with the TiO_2 agglomerates.

The polynomial equation representing the empirical relationship between CBZ degradation (%) and the independent variables is presented in Eq. 3. The coefficient of determination (R^2) of the model was 0.87.

$$\textit{CBZ degradation (\%)} = -667 + 6{\cdot}56{\cdot}A + 6{\cdot}32{\cdot}B + 0{\cdot}29{\cdot}C - 0{\cdot}0148{\cdot}A^2 - 0{\cdot}10001{\cdot}B^2 - 0{\cdot}00933{\cdot}C^2 - 0{\cdot}0142{\cdot}A{\cdot}B - 0{\cdot}00231{\cdot}A{\cdot}C + 0{\cdot}0004{\cdot}B{\cdot}C \quad (3)$$

By analysing the 3D surface plots (Fig. 5), it can be observed that the efficiency of CBZ degradation increased with an increase in the synthesis temperature. An opposite effect was observed for the amount of ethanol in the reaction environment. The addition of ethanol improved the photocatalytic activity; however, above the optimal amount of ethanol, the degradation efficiency decreased. Based on 15 experiments, the

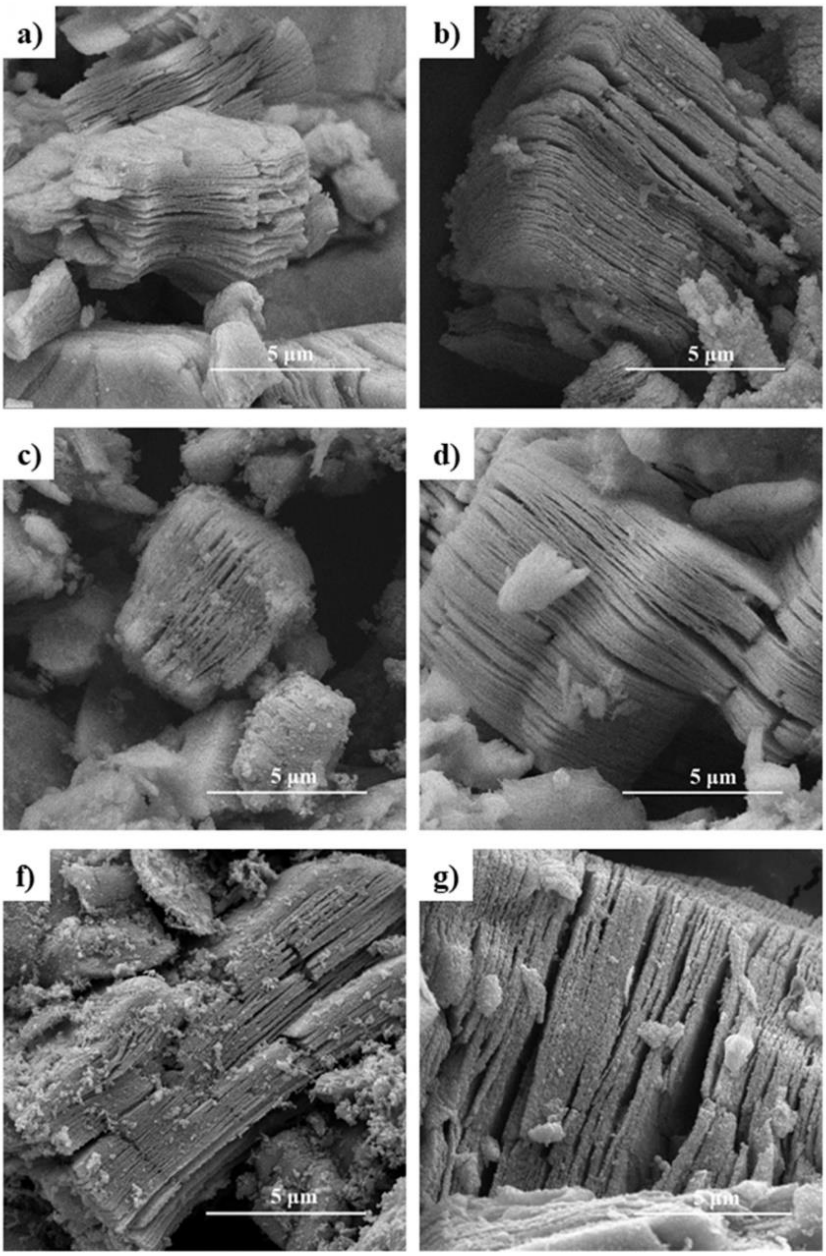

Fig. 4. SEM images of S13 (T200/EtOH-H_2O/15 h) (a), S10 (T200/H_2O/24 h) (b), S4 (T220/EtOH-H_2O/24 h) (c), S12 (T200/EtOH/24 h) (e), S16 (T220/EtOH-H_2O/17 h) (f), and 0.5% Cu-S16 (Cu-modified T220/EtOH-H_2O/17 h) (g).

highest photocatalytic activity towards CBZ degradation was observed for sample S15 (T200/EtOH-H_2O/15 h), synthesised at 200 °C for 15 h with an ethanol/water ratio of 50:50 v/v. The degradation of CBZ reached 97% within 60 min under simulated solar light irradiation. ANOVA results and Pareto chart (Table S3 and Fig. S7 in the Supporting Materials) showed that the amount of ethanol (C^2) and temperature (A) had the highest impact on the photocatalytic CBZ degradation. Only for these two variables, the p-value was lower than the significance level ($p \leq \alpha$) and exceeded the red vertical line, indicating a minimum statistically significant effect (2.571) in the Pareto chart.

To further improve CBZ degradation, optimisation of the response was performed, and the synthesis parameters were predicted to be 220 °C, 17 h, and a water–ethanol mixture with a ratio of 58:42 v/v. Furthermore, to confirm the predictions, the photocatalyst was synthesised under these conditions. The photocatalytic activity experiment confirmed that the degradation was the highest among all analysed samples for this composite, reaching nearly 100% within 60 min of irradiation.

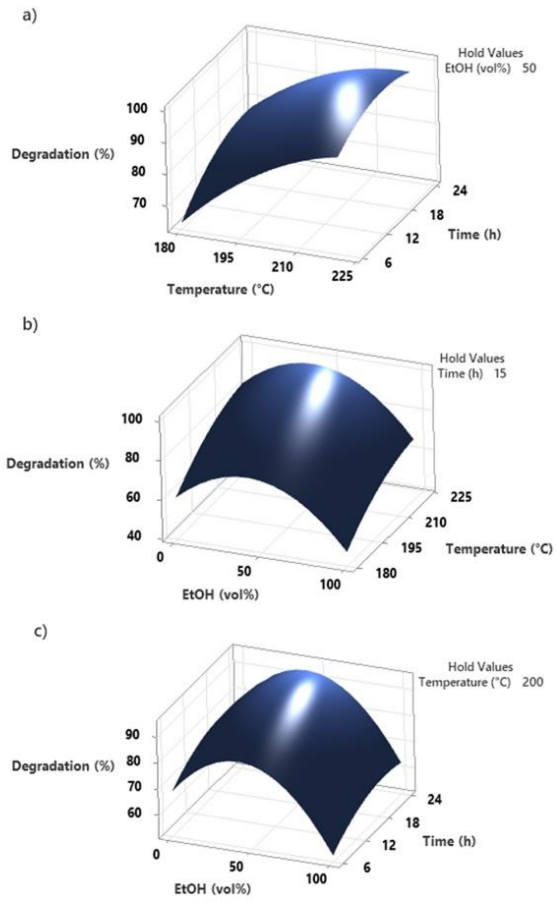

Fig. 5. 3D surface plots presenting the effects of (a) temperature and synthesis time, (b) amount of ethanol and temperature, and (c) amount of ethanol and synthesis time on CBZ degradation (%).

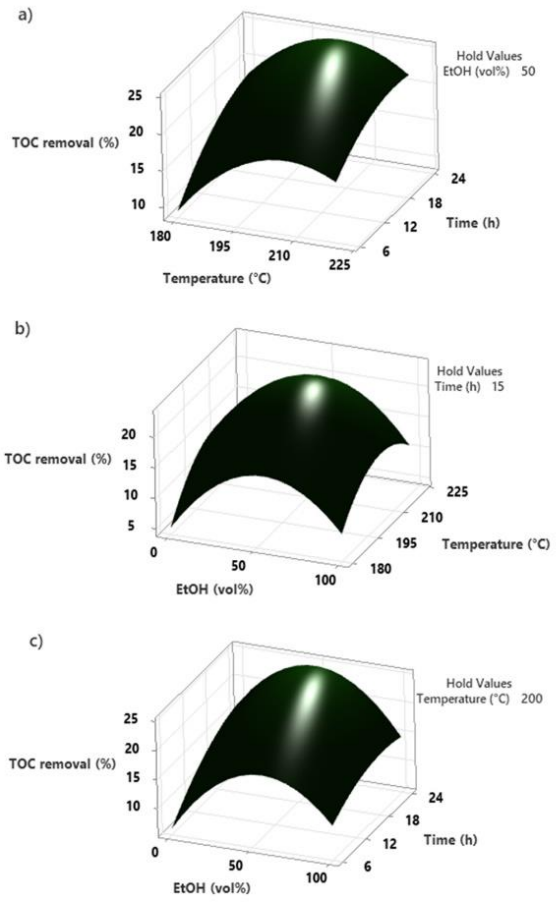

Fig. 6. 3D surface plots presenting the effects of (a) temperature and synthesis time, (b) amount of ethanol and temperature, and (c) amount of ethanol and synthesis time on TOC removal.

The progress in the photodegradation process also reflects the mineralisation of organic compounds to CO_2 and H_2O. This process may be evaluated by the determination of the total organic carbon (TOC) removal after the degradation process. The polynomial equation representing the empirical relationship between TOC removal after the photocatalytic process (%) and the independent variables is shown in Eq. 4. The coefficient of determination (R^2) of the model was 0.98.

$$TOC\ removal\ (\%) = -535{\cdot}7 + 5{\cdot}084{\cdot}A + 2{\cdot}467{\cdot}B + 0{\cdot}617{\cdot}C - 0{\cdot}01204{\cdot}A^2 - 0{\cdot}02397{\cdot}B^2 - 0{\cdot}003617{\cdot}C^2 - 0{\cdot}00597{\cdot}A{\cdot}B - 0{\cdot}000925{\cdot}C - 0{\cdot}00367{\cdot}B{\cdot}C \quad (4)$$

Based on the 3D surface plots presented in Fig. 6, it can be observed that the reduction in TOC concentration, similar to the photocatalytic activity, increased with increasing synthesis temperature and time.

The amount of ethanol in the synthesis above the optimal value caused a decrease in TOC removal after the photocatalytic process. The ANOVA results and Pareto chart (Table S4 and Fig. S8 in Supporting Materials) showed that the amount of ethanol (C^2) had the greatest influence on TOC removal, followed by synthesis time, and temperature. For these variables, the p-value was lower than the significance level ($p \leq \alpha$) and exceeded the red vertical line (2.571) in the Pareto chart.

Table 4
The anatase crystallite size, BET surface area, and band gap energy for Cu-S16 composites.

Sample	Crystallite size (nm)	BET surface area (m^2/g)	Band gap (eV)
0.25% Cu-S16	19	41.2	3.13
0.5% Cu-S16	17	40.9	3.10
1% Cu-S16	17	40.3	3.09

4.2. Characterisation of Cu-modified TiO_2/Ti_3C_2 composites

In the next step, the sample synthesised under optimised conditions (sample S16 with a synthesis time of 17 h, temperature of 220 °C, and water/ethanol ratio of 58:42 v/v) was modified with different amounts of Cu in the range from 0.25 wt% to 1 wt%.

The BET surface areas of the composite materials in the series Cu-S16 were similar and equalled 40–41 $m^2{\cdot}g^{-1}$, slightly higher than that of pure S16 sample (38.2 m^2/g). The band gap energy of the S16 composite was 3.14 eV, and similar values (Table 4) were obtained for Cu-modified samples, as presented in Table 4.

Based on the XRD analysis, only the signals corresponding to TiO_2 and Ti_3C_2 were noticed, as presented in Fig. 7. Any copper species were

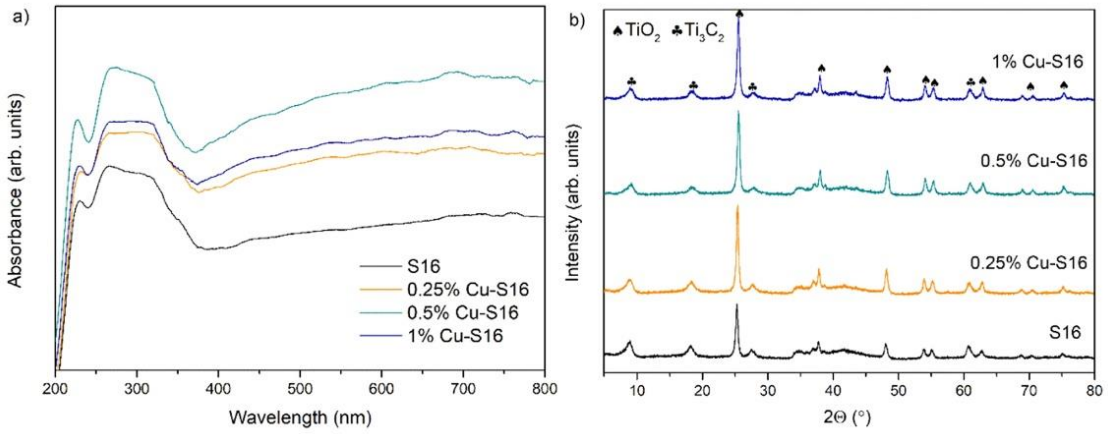

Fig. 7. DR/UV–vis spectra (a) and XRD diffractograms (b) of the S16 (T220/EtOH-H_2O/17 h) and Cu-modified T220/EtOH-H_2O/17 h samples with different amounts of copper.

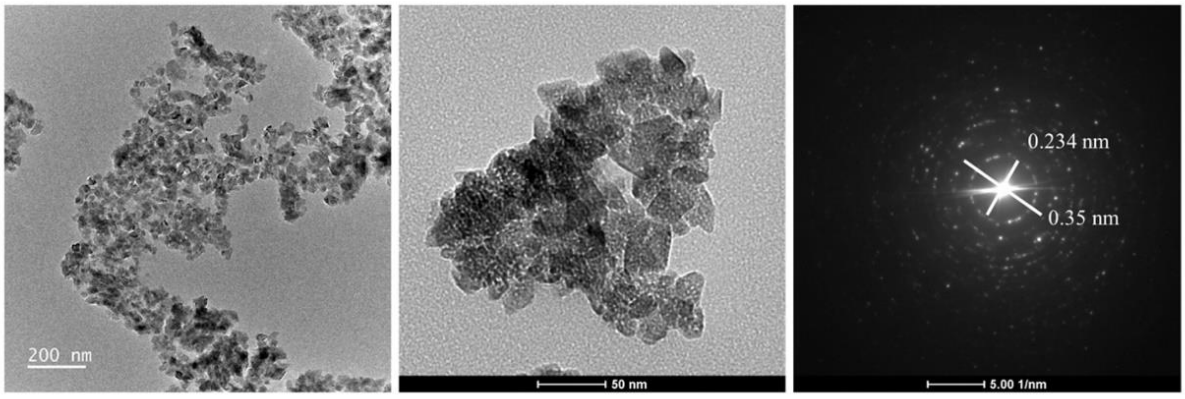

Fig. 8. TEM images and SAED pattern of 0.5% Cu-S16 sample.

detected in the composite materials. It may be related to the low amount of Cu in the composite structure or suggests that copper was uniformly distributed on the TiO_2/Ti_3C_2 surface. Because the radius of Cu^{2+} (0.087 nm) is considerably larger than that of Ti^{4+} (0.0745 nm) and there is a large difference in the valence state, copper should not replace titanium in the crystal lattice (Yan et al., 2015).

Furthermore, SEM-EDS analysis confirmed the presence of copper on the Ti_3C_2/TiO_2 composite surface, as shown in Fig. S9 in the Supporting Materials. The copper content for the 0.5% Cu-S16 sample was about 0.51 wt% (0.19 at%), which is consistent with the amount used for modification. TEM images are presented in Fig. 8. The formation of small TiO_2 nanoparticles on the MXene surface was visible. Based on the TEM with the corresponding SAED pattern, d-spacing values equalled 0.35 nm and 0.234 nm were ascribed to the anatase (101) and $Ti_3C_2T_x$ (103) planes, respectively (Verma et al., 2017; Huang et al., 2022).

XPS analysis was performed to identify the oxidation states of the elements and are presented in Fig. 9. The Ti $2p_{3/2}$ components at 455.2 eV, 456.5 eV, 457.9 eV, and 459.5 eV correspond to Ti bound to C, Ti(II), Ti(III) and Ti(IV), respectively (Zhu et al., 2016). For the O 1 s region, peaks at 530.7 eV and 532.3 eV are ascribed to Ti–O–Ti in TiO_2 and Ti-OH, respectively. The OH terminates on the surface of Ti_3C_2 (Ding et al., 2019). The C 1 s spectrum was deconvoluted into nine peaks fitted at 282 eV, 284.4 eV, 285 eV, 285.6 eV, 286.2 eV, 287 eV, 287.9 eV, 289.1 eV, and 289.8 eV. These peaks were assigned to the Ti-C, C═C, C-H, C-C, C-OH, C-O-C, C═O, C-F, and O═C-O bonds, respectively (Ahmed et al., 2016; Kalambate et al., 2020). XPS analysis revealed the presence of copper (0.1 at%) in the composite material. The peak was deconvoluted for two signals at 932.3 eV and 934.1 eV corresponding to Cu(0) and/or Cu(I), and Cu(II), respectively. Only based on the XPS spectrum in the Cu 2p region, it is difficult to distinguish between metallic Cu and Cu(I) due to the similar BE values (Biesinger et al., 2010; Shaaban and Li, 2022). The prevailing quantity of Cu(0)/Cu (I) over Cu(II) indicates the partial self-reduction of copper on the MXene surface without an external reducing agent. This phenomenon occurs due to the strong reductive activity of low-valence Ti(II) and Ti (III) species and the presence of negatively charged terminal groups (Wang et al., 2023; Zou et al., 2016). Similarly, a self-reduction process on the $Ti_3C_2T_x$ surface was observed for Ag, Au, Ni, and Cu (Li et al., 2022; Zhou et al., 2022; Zhang et al., 2016; Li et al., 2018).

The photoluminescence spectra are presented in Fig. 10. The spectra show a broad band between 400 and 650 nm, with a maximum photoluminescence intensity at 460 nm. The incorporation of copper into the composite material led to a decrease in photoluminescence. Furthermore, the highest decrease was observed for the 0.5% Cu-S16 sample, possibly due to the lowest recombination of photoexcited charge carriers, thus improving photocatalytic efficiency. Meanwhile, for the sample modified with 1% of copper, the PL peak intensity was stronger than that of the sample modified with 0.5% of copper, indicating that an

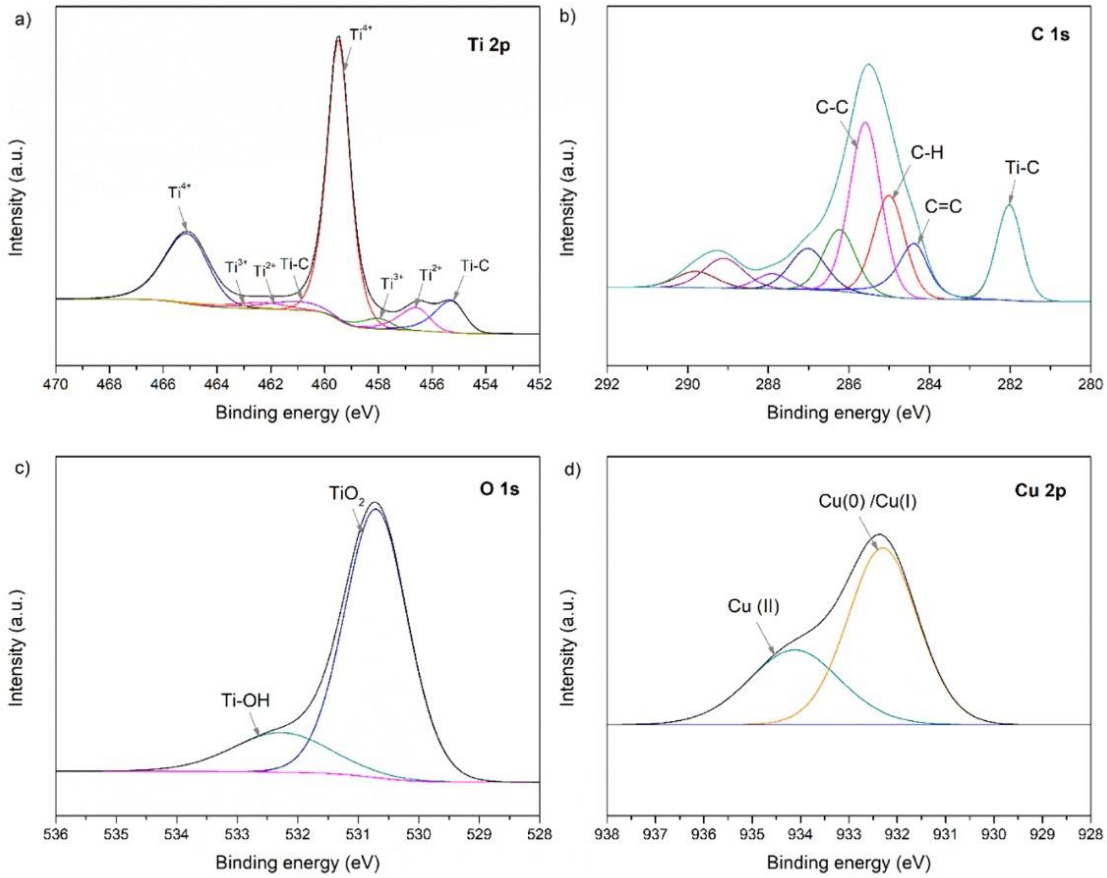

Fig. 9. XPS spectra of Ti 2p (a), C 1 s (b), O 1 s (c), and Cu 2p (d) regions for sample 0.5% Cu-S16.

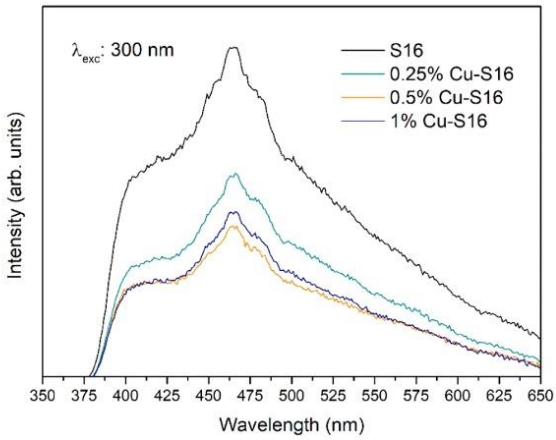

Fig. 10. Photoluminescence spectra of Cu-modified composite materials.

excessive amount of Cu negatively affected the charge carriers separation. Excessive Cu agglomerates can form new recombination centres for photogenerated charge carriers.

Electrochemical impedance spectroscopy is a suitable method to characterise the charge transfer resistance. The EIS Nyquist plots of the prepared materials are presented in Fig. 11a. The diameter of the semicircle in the EIS Nyquist plot correlates with the charge transfer resistance and separation efficiency of the photogenerated electron-hole pairs at the interface between the material and the electrolyte solution. It can be seen that the 0.5% Cu-S16 sample showed the smallest impedance arc radius compared with the other Cu-modified samples and pure TiO_2/Ti_3C_2. This is related to the excellent electronic conductivity of Cu, and enhancement in the Cu-modified composite conductivity compared to pure TiO_2/Ti_3C_2. The direct contact between deposited Cu species and TiO_2/Ti_3C_2 results in efficient photogenerated charge carriers separation, faster and easier electron transfer and lower electron-hole recombination rate (Vattikuti et al., 2018). Similar effect was also confirmed in previous studies for Cu-TiO_2 (Hua et al., 2016) and Cu-$BiVO_4$ (Wu et al., 2022). A lower resistance is correlated with a higher photocurrent response for samples modified with copper. For both samples, a photocurrent was instantly generated once the light was turned on. The photocurrent response of the composite modified with copper was improved compared to TiO_2/Ti_3C_2 sample (Fig. 11b). The photocurrent density for 0.5% Cu-S16 was 12.76 μA/cm^2, while for S16 was 3.46 μA/cm^2, which was above 3.5 times greater for copper-modified TiO_2/Ti_3C_2. The higher the photocurrent, the higher is the charge carriers separation efficiency (Shen et al., 2018). In the five-cycle measurement, similar photocurrent values were obtained for each switch on/off cycle, showing the excellent reproducibility of the materials. According to the Mott Schottky plot (Fig. 12), the conduction

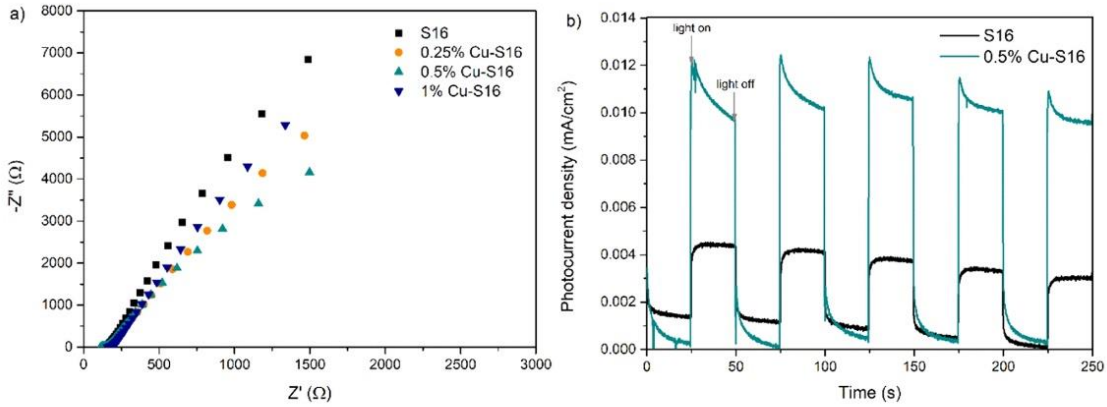

Fig. 11. EIS Nyquist plots (a) and photocurrent density (b) of prepared materials.

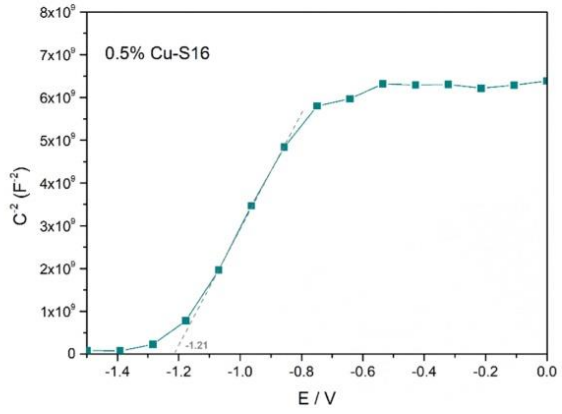

Fig. 12. Mott Schottky plot for 0.5% Cu-S16 composite.

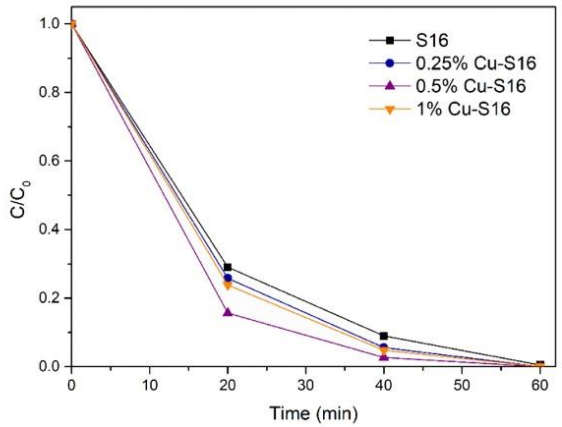

Fig. 13. CBZ degradation efficiency for samples modified with various copper amounts under UV–vis irradiation.

band, which is almost equal to the flat band potential for n-type semiconductors, was determined at − 1.21 V versus Ag and converted to − 0.41 V versus NHE.

Table 5
CBZ degradation rate constant and mineralisation measured as TOC removal efficiency.

Sample	CBZ degradation rate constant ($min^{-1} \cdot 10^{-2}$)	TOC removal (%)
Photolysis	0.2 ± 0.03	0
S16	6.6 ± 0.19	25.2
0.25% Cu S16	7.2 ± 0.34	42.3
0.5% Cu S16	9.0 ± 0.15	61.5
1% Cu-S16	7.6 ± 0.20	46.4
Photolysis + PMS	4.9 ± 0.17	2.1
S16 + PMS	8.3 ± 0.16	27.8
0.5% Cu-S16 + PMS	33.5 ± 1.54	65.3

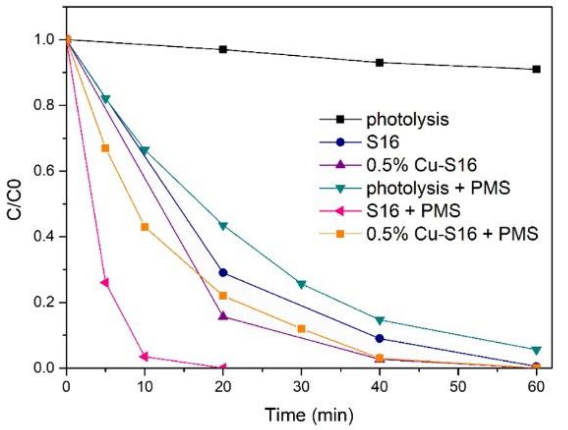

Fig. 14. CBZ degradation efficiency for processes with and without PMS addition.

The photocatalytic activity of the prepared samples was investigated in reaction of carbamazepine degradation, as presented in Fig. 13. Pure sample S16 (T220/EtOH-H_2O/17 h) synthesised under optimal conditions was compared with those modified with different amounts of copper from 0.25 wt% to 1 wt%. The incorporation of copper led to an increase in the photocatalytic activity of the composite. The optimal amount of copper was about 0.5 wt%. For this sample, 100% of CBZ was degraded within 60 min under simulated solar light. Compared with the S16 sample, the constant rate for the 0.5%-S16 sample increased from

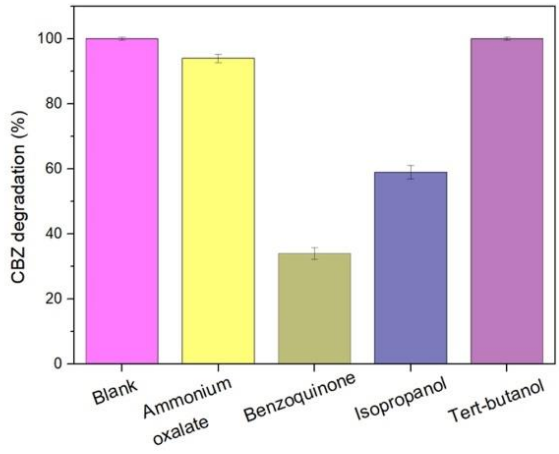

Fig. 15. Degradation of CBZ in the presence of scavengers for 0.5% Cu-S16/PMS.

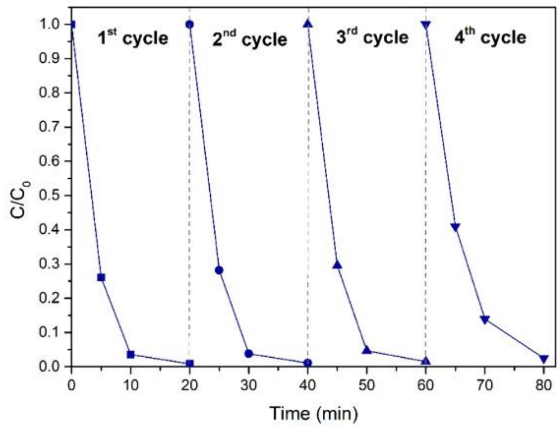

Fig. 16. CBZ degradation efficiency in the 4 subsequent cycles for 0.5% Cu-S16/PMS.

6.0 $min^{-1}\cdot10^{-2}$ to 9.0 $min^{-1}\cdot10^{-2}$ (see in Table 5). Moreover, the TOC removal efficiency increased from 25% to 61%.

In the next step, the photodegradation process in the presence of 0.5% Cu-S16 was combined with PMS activation. The results are shown in Fig. 14. It can be seen that PMS may be activated by light irradiation. The rate constant for photolysis with PMS increased from 0.2 $min^{-1}\cdot10^{-2}$ to 4.9 $min^{-1}\cdot10^{-2}$, compared with photolysis. A synergetic effect of the combination of the photocatalytic process and PMS activation for the degradation of CBZ was observed. The rate constant increased from 9.0 $min^{-1}\cdot10^{-2}$ for 0.5% Cu-S16 without PMS to 33.5 $min^{-1}\cdot10^{-2}$ for 0.5% Cu-S16 with PMS (Table 5). It can be explained by the fact that some transition metal ions, such as copper, can induce the generation of reactive sulphate radicals by coupling with PMS.

To verify the mechanism of CBZ degradation by 0.5% Cu-S16 in the presence of PMS, trapping experiments using radical scavengers were performed. As shown in Fig. 15, superoxide anion radicals ($\bullet O_2$) and sulphate radicals ($\bullet SO_4$) were the main reactive species involved in the efficient photodegradation process.

The stability and recyclability of the 0.5% Cu-S16/PMS system were evaluated in the four subsequent photodegradation cycles (Fig. 16). It can be observed that 0.5% Cu-S16/PMS may be effectively reusable, with nearly 100% degradation of CBZ within 20 min after the fourth cycle. Moreover, the XRD and FTIR analyses confirmed no changes in the material structure after the degradation processes (Fig. 17).

According to the Mott Schottky plot and band gap determined from the Kubelka Munk function, the conduction and valence bands were determined as − 0.41 V and 2.69 V, respectively. As presented in Fig. 18 the prepared photocatalyst can easily reduce oxygen to superoxide radicals (−0.18 V vs. NHE). According to XPS analysis, copper exists in two oxidation states: Cu(I) and Cu(II). Both of these species can activate PMS (Zhu et al., 2021). The following reactions may occur during PMS activation by Cu(II), which is considered a direct one-electron transfer reaction:

$$Cu^{2+} + HSO_5^- \rightarrow Cu^{3+} + \bullet SO_4^- + OH^- \quad (5)$$

Meanwhile, in the case of Cu(I), there are two possible routes: one-electron oxidation of Cu(I) or two-electron oxidation of Cu(I) to produce Cu(II) or Cu(III), respectively (Wang et al., 2020; Ding et al., 2022).

$$Cu^{+} + HSO_5^- \rightarrow Cu^{2+} + \bullet SO_4^- + OH^- \quad (6)$$

$$Cu^{+} + HSO_5^- \rightarrow Cu^{3+} + SO_4^{2-} + OH^- \quad (7)$$

Previous studies show that activating PMS using Cu (II) to generate ROS is difficult because this reaction is thermodynamically

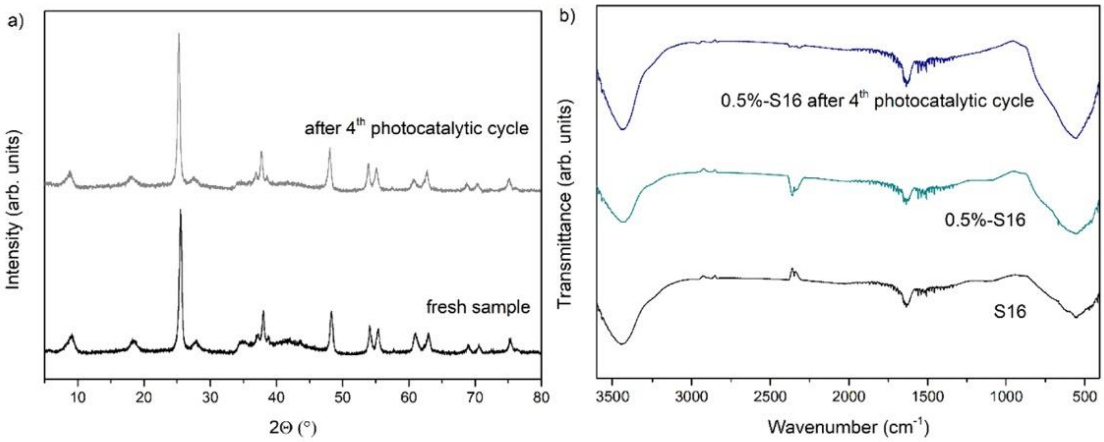

Fig. 17. The XRD diffractograms (a) and FTIR spectra (b) of fresh and used 0.5%Cu-S16 composites.

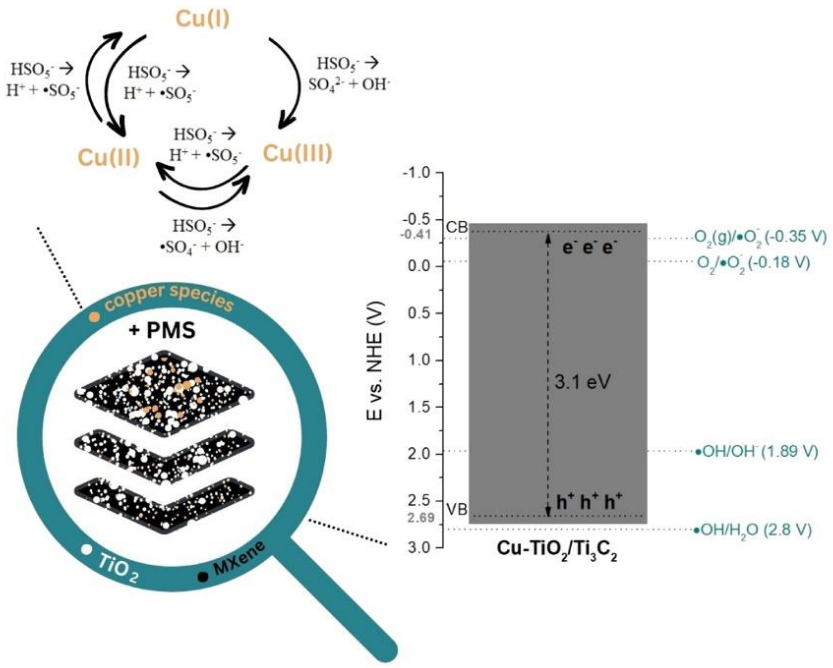

Fig. 18. Proposed scheme of degradation mechanism for the Cu-TiO_2/Ti_3C_2/PMS system.

unfavourable. Moreover, the degradation rate of pollutants by Cu(II) is slow, and the time is relatively long (Zhang et al., 2022). Furthermore, Cu(I) may effectively activate PMS to generate highly active radicals and promote the rapid decomposition of pollutants, owing to its stronger electron donation capacity.

5. Conclusions

In this work, the temperature, water/ethanol ratio, and hydrothermal reaction time were optimised using the Box- Behnken method to maximise carbamazepine photodegradation efficiency under simulated solar light. ANOVA was used to study the statistically significant parameters and their interactions. According to the RSM and ANOVA analyses, the optimum synthesis conditions were 220 °C, 17 h, and 58:42 v/v water/ethanol ratio, and the most important parameter affecting the synthesis of the highly photocatalytic active TiO_2/Ti_3C_2 composite material was the water/ethanol ratio. The optimised TiO_2/Ti_3C_2 sample exhibited the highest CBZ photodegradation efficiency, and complete CBZ degradation was observed within 60 min under simulated solar light irradiation.

Further analysis revealed that modification with copper species led to markedly improved photocatalytic activity, and the optimal copper content was 0.5 wt%. The combination of the photocatalytic process using the 0.5% Cu-S16 sample with PMS (0.5 mM) activation led to complete CBZ degradation within 20 min of irradiation under simulated solar light. The superoxide anion radicals and sulphate radicals were the main reactive species involved in the degradation process.

Declaration of Competing Interest

The authors declare that they have no known competing financial interests or personal relationships that could have appeared to influence the work reported in this paper.

Acknowledgements

The research was financially supported by Polish National Science Centre (Grant No. NCN 2021/43/B/ST5/02983).

Appendix A. Supporting information

Supplementary data associated with this article can be found in the online version at doi:10.1016/j.psep.2023.09.028.

References

Afreen, G., Shoeb, M., Upadhyayula, S., 2020. Effectiveness of reactive oxygen species generated from rGO/CdS QD heterostructure for photodegradation and disinfection of pollutants in waste water. Mater. Sci. Eng.: C. 108, 110372 https://doi.org/10.1016/j.msec.2019.110372.

Ahmed, B., Anjum, D.H., Hedhili, M.N., Gogotsi, Y., Alshareef, H.N., 2016. H_2O_2 assisted room temperature oxidation of Ti_2C MXene for Li-ion battery anodes. Nanoscale 8, 7580–7587. https://doi.org/10.1039/C6NR00002A.

Almeida, Â., Soares, A.M.M., Esteves, V.I., Freitas, R., 2021. Occurrence of the antiepileptic carbamazepine in water and bivalves from marine environments: a review. Environ. Toxicol. Pharm. 86, 103661 https://doi.org/10.1016/j.etap.2021.103661.

Asencios, Y.J.O., Lourenço, V.S., Carvalho, W.A., 2022. Removal of phenol in seawater by heterogeneous photocatalysis using activated carbon materials modified with TiO_2, 388–389 Catal. Today 247–258. https://doi.org/10.1016/j.cattod.2020.06.064.

Biesinger, M.C., Lau, L.W.M., Gerson, A.R., 2010. Resolving surface chemical states in XPS analysis of first row transition metals, oxides and hydroxides: Sc, Ti, V, Cu and Zn. Appl. Surf. Sci. 257, 887–898. https://doi.org/10.1016/j.apsusc.2010.07.086.

Danish, M.S.S., Estrella, L.L., Alemaida, I.M.A., Lisin, A., Moiseev, N., Ahmadi, M., Nazari, M., Wali, M., Zaheb, H., Senjyu, T., 2021. Photocatalytic applications of metal oxides for sustainable environmental remediation. Met. (Basel) 11, 80. https://doi.org/10.3390/met11010080.

Ding, X., Li, Y., Li, C., Wang, W., Wang, L., Feng, L., Han, D., 2019. 2D visible light driven TiO_2@Ti_3C_2/g-C_3N_4 ternary heterostructure for high photocatalytic activity. J. Mater. Sci. 54, 9385–9396. https://doi.org/10.1007/s10853-018-03289-4.

Ding, Y., Fu, L., Peng, X., Lei, M., Wang, C., Jiang, J., 2022. Copper catalysts for radical and nonradical persulfate based advanced oxidation processes: certainties and uncertainties. Chem. Eng. J. 427, 131776 https://doi.org/10.1016/j.cej.2021.131776.

Dong, H., Zeng, G., Tang, L., Fan, C., Zhang, C., He, X., He, Y., 2015. An overview on limitations of TiO_2-based particles for photocatalytic degradation of organic pollutants and the corresponding countermeasures. Water Res. 79, 128–146. https://doi.org/10.1016/j.watres.2015.04.038.

Dudziak, S., Kowalkińska, M., Karczewski, J., Pisarek, M., Siuzdak, K., Kubiak, A., Siwińska-Ciesielczyk, K., Zielińska-Jurek, A., 2021. Solvothermal growth of {0 0 1} exposed anatase nanosheets and their ability to mineralise organic pollutants. The effect of alcohol type and content on the nucleation and growth of TiO_2 nanostructures. Appl. Surf. Sci. 563, 150360 https://doi.org/10.1016/j.apsusc.2021.150360.

Gawande, M.B., Goswami, A., Felpin, F.X., Asefa, T., Huang, X., Silva, R., Zou, X., Zboril, R., Varma, R.S., 2016. Cu and Cu-based nanoparticles: synthesis and applications in catalysis. Chem. Rev. 116, 3722–3811. https://doi.org/10.1021/acs.chemrev.5b00482.

Grzegórska, A., Gluchowski, P., Karczewski, J., Ryl, J., Wysocka, I., Siuzdak, K., Trykowski, G., Grochowska, K., Zielińska Jurek, A., 2021. Enhanced photocatalytic activity of accordion-like layered Ti_3C_2 (MXene) coupled with Fe-modified decahedral anatase particles exposing {1 0 1} and {0 0 1} facets. Chem. Eng. J. 426, 130801 https://doi.org/10.1016/j.cej.2021.130801.

Gubitosa, J., Mongiovi', C., Romita, R., Cosma, P., Nuzzo, S., Rizzi, V., Fini, P., 2022. Removal of emerging contaminants from water using cyclodextrin-based polymers and advanced oxidation processes: the case of carbamazepine. Processes 10, 1703. https://doi.org/10.3390/pr10091703.

Hai, F., Yang, S., Asif, M., Sencadas, V., Shawkat, S., Sanderson-Smith, M., Gorman, J., Xu, Z.Q., Yamamoto, K., 2018. Carbamazepine as a possible anthropogenic marker in water: occurrences, toxicological effects, regulations and removal by wastewater treatment technologies. Water (Basel) 10, 107. https://doi.org/10.3390/w10020107.

Hasija, V., Raizada, P., Thakur, V.K., Ahamad, T., Alshehri, S.M., Thakur, S., Nguyen, V. H., van Le, Q., Singh, P., 2022. An overview on photocatalytic sulfate radical formation via doped graphitic carbon nitride for water remediation. Curr. Opin. Chem. Eng. 37, 100841 https://doi.org/10.1016/j.coche.2022.100841.

Hua, Z., Dai, Z., Bai, X., Ye, Z., Wang, P., Gu, H., Huang, X., 2016. Copper nanoparticles sensitised TiO_2 nanotube arrays electrode with enhanced photoelectrocatalytic activity for diclofenac degradation. Chem. Eng. J. 283, 514–523. https://doi.org/10.1016/j.cej.2015.07.072.

Huang, W.X., Li, Z.P., Li, D.D., Hu, Z.H., Wu, C., Lv, K.L., Li, Q., 2022. Ti_3C_2 MXene: recent progress in its fundamentals, synthesis, and applications. Rare Met. 41, 3268–3300. https://doi.org/10.1007/s12598-022-02058-2.

Im, J.K., Sohn, E.J., Kim, S., Jang, M., Son, A., Zoh, K.D., Yoon, Y., 2021. Review of MXene based nanocomposites for photocatalysis. Chemosphere 270, 129478. https://doi.org/10.1016/j.chemosphere.2020.129478.

Isac, L., Cazan, C., Andronic, L., Enesca, A., 2022. CuS-based nanostructures as catalysts for organic pollutants photodegradation. Catalysts 12, 1135. https://doi.org/10.3390/catal12101135.

Kalambate, P.K., Sinha Dhanjai, A., Li, Y., Shen, Y., Huang, Y., 2020. An electrochemical sensor for ifosfamide, acetaminophen, domperidone, and sumatriptan based on self-assembled MXene/MWCNT/chitosan nanocomposite thin film. Microchim. Acta 187, 402. https://doi.org/10.1007/s00604 020 04366 9.

Li, K., Jiao, T., Xing, R., Zou, G., Zhou, J., Zhang, L., Peng, Q., 2018. Fabrication of tunable hierarchical MXene@AuNPs nanocomposites constructed by self-reduction reactions with enhanced catalytic performances. Sci. China Mater. 61, 728–736. https://doi.org/10.1007/s40843-017-9196-8.

Li, X., Peng, W., Li, L., Chen, S., Ye, L., Peng, C., 2022. Simple synthesis of copper/MXene/polyacrylamide hydrogel catalyst for 4-nitrophenol reduction. Mater. Lett. 324, 132705 https://doi.org/10.1016/j.matlet.2022.132705.

Mezzelani, M., Fattorini, D., Gorbi, S., Nigro, M., Regoli, F., 2020. Human pharmaceuticals in marine mussels: evidence of sneaky environmental hazard along Italian coasts. Mar. Environ. Res. 162, 105137 https://doi.org/10.1016/j.marenvres.2020.105137.

Muscetta, M., Clarizia, L., Garlisi, C., Palmisano, G., Marotta, R., Andreozzi, R., di Somma, I., 2020. Hydrogen production upon UV-light irradiation of Cu/TiO2 photocatalyst in the presence of alkanol-amines. Int. J. Hydrog. Energy 45, 26701–26715. https://doi.org/10.1016/j.ijhydene.2020.07.002.

Rathi, B.S., Kumar, P.S., Show, P.L., 2021. A review on effective removal of emerging contaminants from aquatic systems: current trends and scope for further research. J. Hazard. Mater. 409, 124413 https://doi.org/10.1016/j.jhazmat.2020.124413.

Rivera-Utrilla, J., Sánchez-Polo, M., Ferro-García, M.Á., Prados-Joya, G., Ocampo-Pérez, R., 2013. Pharmaceuticals as emerging contaminants and their removal from water. A review. Chemosphere 93, 1268–1287. https://doi.org/10.1016/j.chemosphere.2013.07.059.

Shaaban, E., Li, G., 2022. Probing active sites for carbon oxides hydrogenation on Cu/TiO_2 using infrared spectroscopy. Commun. Chem. 5, 32 https://doi.org/10.1038/s42004-022-00650-2.

Shen, R., Xie, J., Guo, P., Chen, L., Chen, X., Li, X., 2018. Bridging the g-C_3N_4 nanosheets and robust CuS cocatalysts by metallic acetylene black interface mediators for active and durable photocatalytic H_2 production. ACS Appl. Energy Mater. 1, 2232–2241. https://doi.org/10.1021/acsaem.8b00311.

Simamora, A.J., Hsiung, T.L., Chang, F.C., Yang, T.C., Liao, C.Y., Wang, H.P., 2012. Photocatalytic splitting of seawater and degradation of methylene blue on CuO/nano TiO_2. Int. J. Hydrog. Energy 37, 13855–13858. https://doi.org/10.1016/j.ijhydene.2012.04.091.

Vattikuti, S.V.P., Reddy, P.A.K., Shim, J., Byon, C., 2018. Visible-light-driven photocatalytic activity of SnO_2 –ZnO quantum dots anchored on g-C_3N_4 nanosheets for photocatalytic pollutant degradation and H_2 production. ACS Omega 3, 7587–7602. https://doi.org/10.1021/acsomega.8b00471.

Verma, R., Gangwar, J., Srivastava, A.K., 2017. Multiphase TiO_2 nanostructures: a review of efficient synthesis, growth mechanism, probing capabilities, and applications in bio-safety and health. RSC Adv. 7, 44199–44224. https://doi.org/10.1039/C7RA06925A.

Wang, L., Xu, H., Jiang, N., Wang, Z., Jiang, J., Zhang, T., 2020. Trace cupric species triggered decomposition of peroxymonosulfate and degradation of organic pollutants: Cu(III) being the primary and selective intermediate oxidant. Environ. Sci. Technol. 54, 4686–4694. https://doi.org/10.1021/acs.est.0c00284.

Wang, Y., Zhao, P., Gao, B., Yuan, M., Yu, J., Wang, Z., Chen, X., 2023. Self-reduction of bimetallic nanoparticles on flexible MXene graphene electrodes for simultaneous detection of ascorbic acid, dopamine, and uric acid. Microchem. J. 185, 108177 https://doi.org/10.1016/j.microc.2022.108177.

Wolski, L., Walkowiak, A., Ziolek, M., 2019. Formation of reactive oxygen species upon interaction of Au/ZnO with H_2O_2 and their activity in methylene blue degradation. Catal. Today 333, 54–62. https://doi.org/10.1016/j.cattod.2018.04.004.

Wu, L., Yue, X., Chang, Y., Wang, K., Zhang, J., Sun, J., Wei, Z., Kowalska, E., 2022. Photocatalytic degradation of tetracycline under visible light irradiation on $BiVO_4$ microballs modified with noble metals. Catalysts 12, 1293. https://doi.org/10.3390/catal12111293.

Yan, H., Zhao, T., Li, X., Hun, C., 2015. Synthesis of Cu-doped nano-TiO_2 by detonation method. Ceram. Int. 41, 14204–14211. https://doi.org/10.1016/j.ceramint.2015.07.046.

Zhang, B., Han, Z., Xin, Y., Zhang, Y., Li, W., Li, B., Ding, A., Ma, J., He, X., 2022. Peroxymonosulfate activation by vacuum ultraviolet and trace copper ions: a new way to boost Cu(II)/Cu(I) redox cycle. Chem. Eng. J. 450, 138097 https://doi.org/10.1016/j.cej.2022.138097.

Zhang, X., Liu, Y., Dong, S., Ye, Z., Guo, Y., 2017. One-step hydrothermal synthesis of a TiO_2-$Ti_3C_2T_x$ nanocomposite with small sized TiO_2 nanoparticles. Ceram. Int. 43, 11065–11070. https://doi.org/10.1016/j.ceramint.2017.05.151.

Zhang, Y., Geißen, S.U., Gal, C., 2008. Carbamazepine and diclofenac: removal in wastewater treatment plants and occurrence in water bodies. Chemosphere 73, 1151–1161. https://doi.org/10.1016/j.chemosphere.2008.07.086.

Zhang, Y.Z., El-Demellawi, J.K., Jiang, Q., Ge, G., Liang, H., Lee, K., Dong, X., Alshareef, H.N., 2020. MXene hydrogels: fundamentals and applications. Chem. Soc. Rev. 49, 7229–7251. https://doi.org/10.1039/D0CS00022A.

Zhang, Z., Li, H., Zou, G., Fernandez, C., Liu, B., Zhang, Q., Hu, J., Peng, Q., 2016. Self-reduction synthesis of new MXene/Ag composites with unexpected electrocatalytic activity. ACS Sustain Chem. Eng. 4, 6763–6771. https://doi.org/10.1021/acssuschemeng.6b01698.

Zhou, S., Zhao, Y., Shi, R., Wang, Y., Ashok, A., Héraly, F., Zhang, T., Yuan, J., 2022. Vacancy rich MXene immobilized Ni single atoms as a high performance electrocatalyst for the hydrazine oxidation reaction. Adv. Mater. 34, 2204388 https://doi.org/10.1002/adma.202204388.

Zhu, J., Tang, Y., Yang, C., Wang, F., Cao, M., 2016. Composites of TiO_2 nanoparticles deposited on Ti_3C_2 MXene nanosheets with enhanced electrochemical performance. J. Electrochem Soc. 163, A785–A791. https://doi.org/10.1149/2.0981605jes.

Zhu, Y., Li, D., Zuo, S., Guan, Z., Ding, S., Xia, D., Li, X., 2021. Cu_2O/CuO induced non-radical/radical pathway toward highly efficient peroxymonosulfate activation. J. Environ. Chem. Eng. 9, 106781 https://doi.org/10.1016/j.jece.2021.106781.

Zind, H., Mondamert, L., Remaury, Q.B., Cleaon, A., Leitner, N.K.V., Labanowski, J., 2021. Occurrence of carbamazepine, diclofenac, and their related metabolites and transformation products in a French aquatic environment and preliminary risk assessment. Water Res 196, 117052. https://doi.org/10.1016/j.watres.2021.117052.

Zou, G., Zhang, Z., Guo, J., Liu, B., Zhang, Q., Fernandez, C., Peng, Q., 2016. Synthesis of MXene/Ag composites for extraordinary long cycle lifetime lithium storage at high rates. ACS Appl. Mater. Interfaces 8, 22280–22286. https://doi.org/10.1021/acsami.6b08089.

Modelling and optimisation of MXene-derived TiO_2/Ti_3C_2 synthesis parameters using Response Surface Methodology based on the Box–Behnken factorial design. Enhanced carbamazepine degradation by the Cu-modified TiO_2/Ti_3C_2 photocatalyst.

Anna Grzegórska[1], Jakub Karczewski[2], Anna Zielińska-Jurek[1]

[1] Department of Process Engineering and Chemical Technology, Faculty of Chemistry, Gdańsk University of Technology, G. Narutowicza 11/12, 80-233 Gdańsk, Poland

[2] Institute of Nanotechnology and Materials Engineering, Faculty of Applied Physics and Mathematics, Gdańsk University of Technology, G. Narutowicza 11/12, 80-233 Gdańsk, Poland

* *Corresponding authors: annjurek@pg.edu.pl, anna.grzegorska@pg.edu.pl*

Keywords: Box-Behnken, carbamazepine, Cu species, MXene, photocatalysis, optimisation, RSM, Ti_3C_2, TiO_2

3. Methods

3.6. Photocatalytic activity

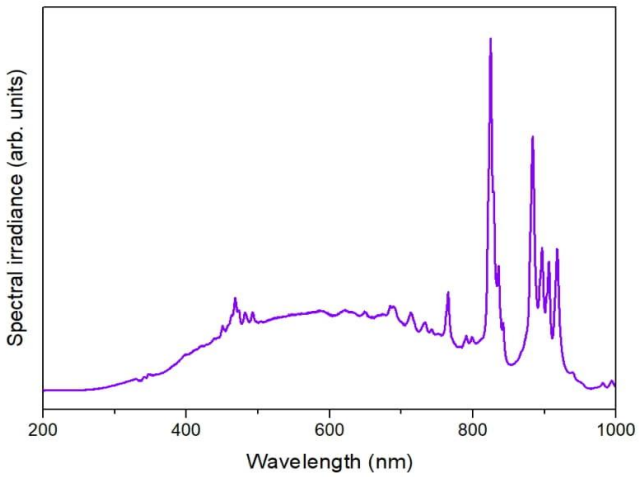

Figure S1. Spectrum of 300 W Xenon lamp

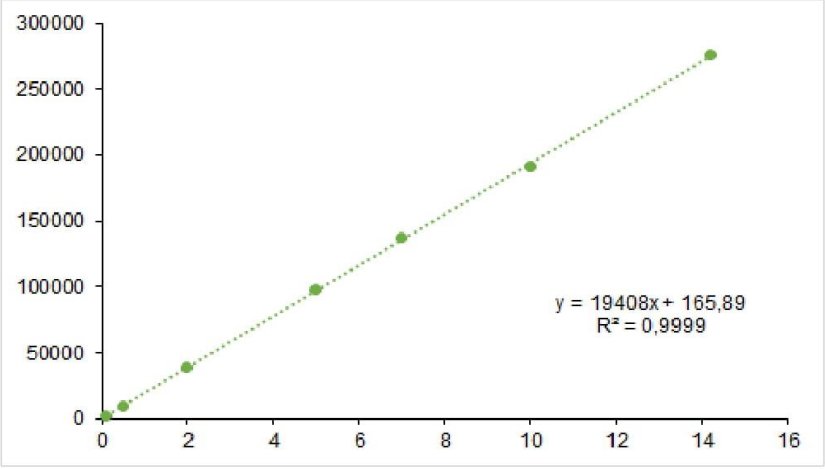

Figure S2. Calibration curve for quantification of CBZ concentration

4. Results and discussion

4.1 Box–Behnken design (BBD) and characteristic of TiO_2/Ti_3C_2composites

Table S1. ANOVA results of the quadratic model for BET surface area

Source	Degrees of freedom (df)	Sum of squares (SS)	Mean square (MS)	F-value	p-value
Regression	9	1636.16	181.796	3.99	0.071
Linear	3	954.95	318.317	**6.99**	**0.031**
A	1	0.28	0.281	0.01	0.940
B	1	120.51	120.513	2.65	0.165
C	1	834.16	834.157	**18.32**	**0.008**
Square	3	170.29	56.762	1.25	0.386
A^2	1	57.22	57.221	1.26	0.313
B^2	1	100.26	100.256	2.20	0.198
C^2	1	0.04	0.044	0.00	0.976
2-way interaction	3	510.93	170.308	3.74	0.095
AB	1	3.94	3.940	0.09	0.780
AC	1	213.89	213.891	4.70	0.082
BC	1	293.09	293.094	6.44	0.052
Residual error	5	227.61	45.522		
Lack of fit	3	218.47	72.824	15.94	0.060
R^2		0.8779			

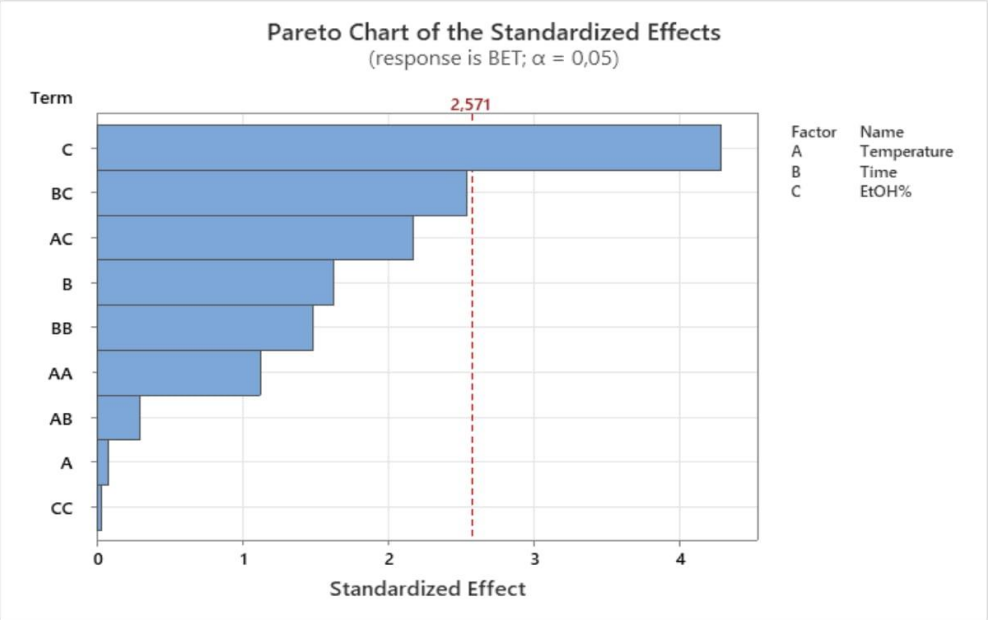

Figure S3. Pareto chart of the standardized effects for the BET surface area

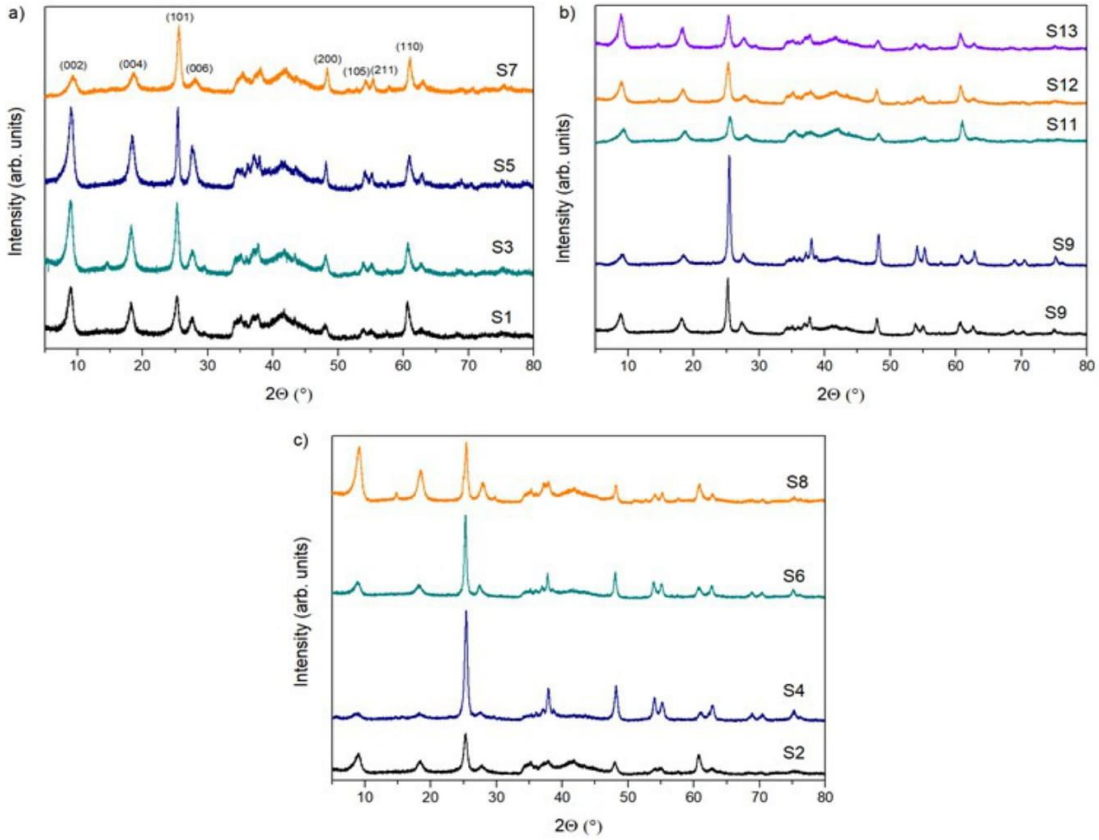

Figure S4. XRD diffractograms of prepared samples synthesized at 180 °C (a), 200 °C (b), and 220 °C (c)

Table S2. ANOVA results of the quadratic model for anatase crystallite size

Source	Degrees of freedom (df)	Sum of squares (SS)	Mean square (MS)	F-value	p-value
Regression	9	242.693	26.966	**27.36**	**0.001**
Linear	3	177.738	59.246	**60.12**	**0.000**
A	1	19.531	19.531	**19.82**	**0.007**
B	1	15.401	15.401	**15.63**	**0.011**
C	1	142.805	142.805	**144.91**	**0.000**
Square	3	54.802	18.267	**18.54**	**0.004**
A^2	1	0.790	0.790	0.80	0.412
B^2	1	0.001	0.001	0.00	0.982
C^2	1	54.374	54.374	**55.17**	**0.001**
2-way interaction	3	10.152	3.384	3.43	0.109

AB	1	0.903	0.903	0.92	0.383
AC	1	4.840	4.840	4.91	0.078
BC	1	4.410	4.410	4.47	0.088
Residual error	5	4.927	0.985	-	-
Lack of fit	3	4.907	1.636	**163.58**	**0.006**
R^2		0.9801			

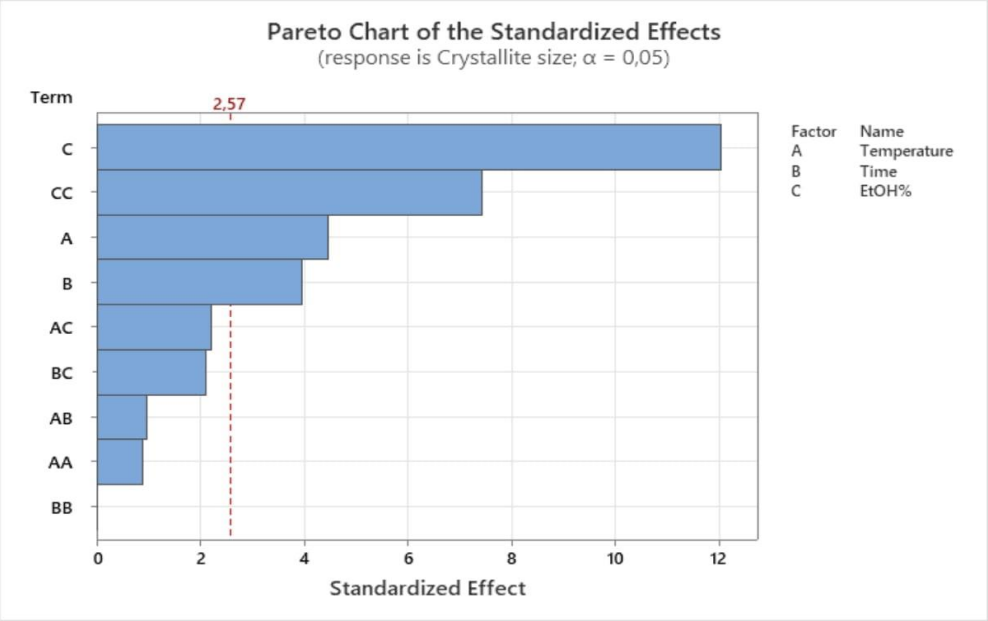

Figure S5. Pareto chart of the standarized effects for the anatase crystallite size

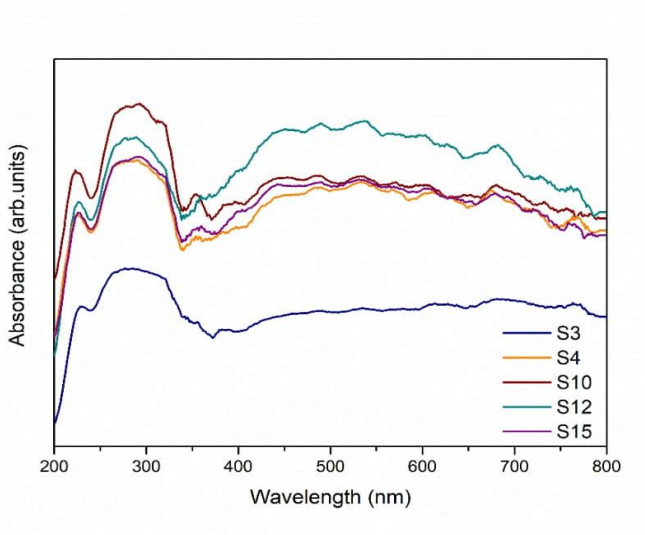

Figure S6. DR/UV-vis spectra of selected materials

Table S3. ANOVA results of the quadratic model for carbamazepine degradation

Source	Degrees of freedom (df)	Sum of squares (SS)	Mean square (MS)	F-value	p-value
Regression	9	3892.49	432.5	3.71	0.081
Linear	3	1638.62	546.21	4.68	0.065
A	1	895.49	895.49	**7.68**	**0.039**
B	1	169.37	169.37	1.45	0.282
C	1	573.76	573.76	4.92	0.077
Square	3	2206.38	735.46	**6.31**	**0.038**
A^2	1	130.24	130.24	1.12	0.339
B^2	1	242.65	242.65	2.08	0.209
C^2	1	2007.39	2007.39	**17.22**	**0.009**
2-way interaction	3	47.49	15.83	0.14	0.935
AB	1	25.96	25.96	0.22	0.657
AC	1	21.39	21.39	0.18	0.686
BC	1	0.14	0.14	0.00	0.974
Residual error	5	582.94	116.59	-	-
Lack of fit	3	582.70	194.23	**1574.86**	**0.001**
R^2		0.8697			

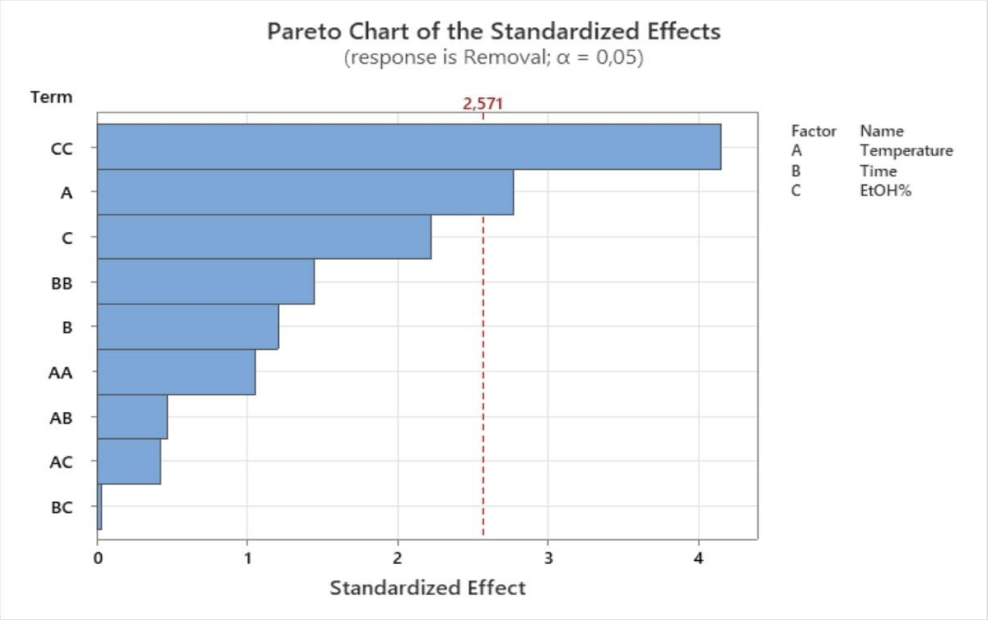

Figure S7. Pareto chart of the standardized effects for the carbamazepine degradation

Table S4. ANOVA results of the quadratic model for TOC removal

Source	Degrees of freedom (df)	Sum of squares (SS)	Mean square (MS)	F-value	p-value
Regression	9	540.500	60.056	30.86	**0.001**
Linear	3	153.248	51.083	26.25	**0.002**
A	1	55.125	55.125	28.33	**0.003**
B	1	93.161	93.161	47.88	**0.001**
C	1	4.961	4.961	2.55	0.171
Square	3	368.318	122.773	63.10	**0.000**
A^2	1	85.663	85.663	44.02	**0.001**
B^2	1	13.920	13.920	7.15	0.044
C^2	1	301.853	301.853	155.13	**0.000**
2-way interaction	3	18.935	6.312	3.24	0.119

AB	1	4.622	4.622	2.38	0.184
AC	1	3.422	3.422	1.76	0.242
BC	1	10.890	10.890	5.60	0.064
Residual error	5	9.729	1.946	-	-
Lack of fit	3	8.723	2.908	5.78	0.151
R^2		0.9823			

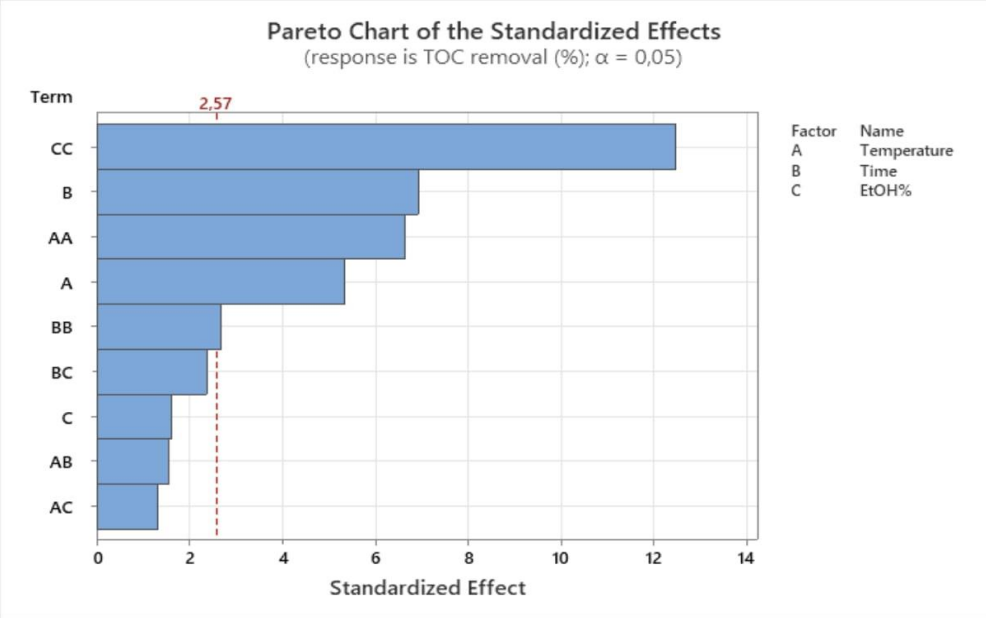

Figure S8. Pareto chart of the standardized effects for the TOC removal

4.2. Characterisation of Cu-modified TiO_2/Ti_3C_2 composite

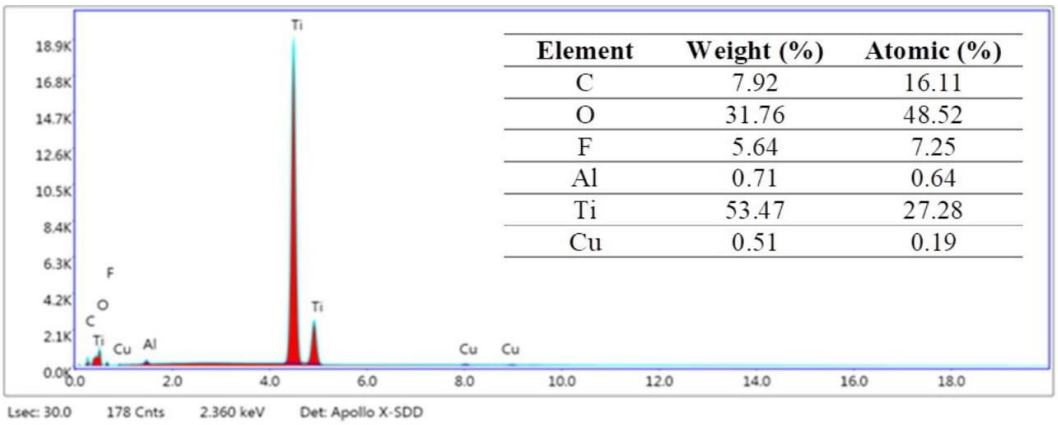

Element	Weight (%)	Atomic (%)
C	7.92	16.11
O	31.76	48.52
F	5.64	7.25
Al	0.71	0.64
Ti	53.47	27.28
Cu	0.51	0.19

Figure S9. The SEM-EDX analysis

Rozdział VII: Podsumowanie i wnioski

Przeprowadzone badania, których rezultaty przedstawiono w 5 publikacjach naukowych opublikowanych w czasopismach z listy JCR, pogłębiają stan wiedzy na temat zastosowania związków z grupy MXenów w procesach fotokatalitycznych. Etapy pracy badawczej przedstawionej w każdej z publikacji obejmowały syntezę materiałów, charakterystykę właściwości fizykochemicznych oraz analizę aktywności fotokatalitycznej. Potwierdzono postawione tezy badawcze, między innymi zasadność zastosowania MXenu $Ti_3C_2T_x$ jako ko-katalizatora i jako prekursora do otrzymywania kompozytów TiO_2/Ti_3C_2. Powyższe założenie potwierdzono uzyskując materiały charakteryzujące się wysoką aktywnością fotokatalityczną w procesach degradacji trzech aktywnych substancji farmaceutycznych: karbamazepiny, acetaminofenu, i ibuprofenu.

Wykazano, że aktywność otrzymanych kompozytów TiO_2/Ti_3C_2 zależy od szeregu parametrów regulowanych w procesie syntezy (czas, temperatura, środowisko reakcji). W przypadku zastosowania jako ko-katalizator istotny wpływ ma zawartość węglika w kompozycie. Dodatkowo zaproponowano możliwość poprawy aktywności fotokatalitycznej kompozytów poprzez wprowadzenie cząstek metali przejściowych takich jak Cu i Fe z zastosowaniem prostych metod modyfikacji. Otrzymane wyniki wskazują na wysoki potencjał aplikacyjny otrzymanych materiałów ze względu na doskonałą stabilność oraz wysoką aktywność fotokatalityczną w szerokim przedziale pH, czy w obecności nieorganicznych jonów przeszkadzających.

Ponadto, otrzymywanie potrójnego kompozytu poprzez wprowadzenie cząstek o właściwościach magnetycznych ($TiO_2/Ti_3C_2/MnFe_2O_4$) pozwala na zapewnienie efektywnej separacji fotokatalizatora po procesie, z wykorzystaniem zewnętrznego pola magnetycznego.

W ostatnim etapie prac zaproponowano połączenie dwóch metod należących do grupy AOP – fotokatalizy i aktywacji PMS prowadzącej do wytworzenia wysoce reaktywnych rodników siarczanowych. Osiągnięcie synergistycznego efektu degradacji aktywnych substancji farmaceutycznych było możliwe dzięki obecności w kompozytach cząstek Cu i $MnFe_2O_4$ wykazujących zdolność aktywacji PMS.

Do nowości naukowych zaproponowanych w cyklu prac naukowych w ramach mojej pracy doktorskiej zaliczam:

- Wykazanie możliwości zastosowania MXenu jako ko-katalizatora wpływającego na efektywny transfer ładunku oraz zmniejszenie rekombinacji par elektron-dziura;
- Określenie wpływu czas i temperatury procesu utleniania powierzchni MXenów na skład kompozytu, właściwości fizykochemiczne i morfologię, a w konsekwencji na aktywność fotokatalityczną;
- Otrzymanie fotokatalizatorów o zdefiniowanej morfologii i wykazanie wpływu środowiska reakcji na właściwości fizykochemiczne i aktywność fotokatalityczną kompozytów TiO_2/Ti_3C_2;
- Wykazanie, że kompozyty TiO_2/Ti_3C_2 charakteryzują się wysoką stabilnością w szerokim zakresie pH, w obecności nieorganicznych jonów przeszkadzających oraz aktywnością w kolejnych cyklach degradacji, co wskazuje na ich potencjał do zastosowania jako efektywnych fotokatalizatorów do degradacji uporczywych zanieczyszczeń organicznych obecnych w wodach powierzchniowych;
- Określenie wpływu modyfikacji kompozytów TiO_2/Ti_3C_2 za pomocą żelaza lub miedzi na wzrost efektywności fotokatalitycznej degradacji farmaceutyków;
- Wykazanie, że wprowadzenie ferrytu manganowego do kompozyt TiO_2/Ti_3C_2 pozwala na łatwe odzyskanie fotokatalizatora z zawiesiny po procesie oczyszczania w zewnętrznymo polu magnetycznym;
- Optymalizację metody syntezy fotokatalizatorów o zdefiniowanej morfologii;
- Wykazanie, że połączenie procesu fotokatalizy z aktywację PMS wpływa na synergiczny efekt degradacji substancji farmaceutycznych w ponad 4-krotnie krótszym czasie. W tym odniesieniu, uwzględniając aspekty ekonomiczne procesu związane z oszczędnością energii poprzez skrócenie czasu procesu fotodegradacji, korzystne wydaje się połączenie fotokatalizy z aktywacją za pomocą PMS.

Oświadczenia współautorów

Grenoble, October 20th 2023

Dr Laura Cervera-Gabalda
SpLine - Spanish CRG BM25 Beamline (ICMM)
The European Synchrotron
71, Avenue des Martyrs
38000 Grenoble, France
cerverag@esrf.fr

Statement of contribution

I declare that I have contributed to the publication, which constitues a part of the PhD dissertation of M.Sc. Eng Anna Grzegórska:

1. A. Grzegórska, J. Chibueze Ofoegbu, L. Cervera-Gabalda, C. Gómez-Polo, D. Sannino, A. Zielińska-Jurek, Magnetically recyclable TiO_2/MXene/$MnFe_2O_4$ photocatalyst for enhanced peroxymonosulphate-assisted photocatalytic degradation of carbamazepine and ibuprofen under simulated solar light. J. Environ. Chem. Eng. 11 (2023) 110660.

In the above study, I measured the magnetic properties of the photocatalysts and analyzed and described the results.

.....
Dr Laura Cervera-Gabalda

Salerno 17/10/2023

Joseph Chibueze Ofoegbu
Department of Industrial Engineering
University of Salerno
via Giovanni Paolo II 132
84084 Fisciano, SA, Italy
j.ofoegbu@studenti.unisa.it

Statement of contribution

I declare that I have contributed to the publication, which constitues a part of the PhD dissertation of M. Sc. Eng. Anna Grzegórska:

1. A. Grzegórska, J. Chibueze Ofoegbu, L. Cervera-Gabalda, C. Gómez-Polo, D. Sannino, A. Zielińska-Jurek, Magnetically recyclable TiO_2/MXene/$MnFe_2O_4$ photocatalyst for enhanced peroxymonosulphate-assisted photocatalytic degradation of carbamazepine and ibuprofen under simulated solar light. J. Environ. Chem. Eng. 11 (2023) 110660.

In the above study, I have performed the preliminary analyses regarding the characteristics of materials and their photocatalytic activity.

……
Joseph Chibueze Ofoegbu

Uniwersytet Gdański | Związek Uczelni Fahrenheita

Gdańsk, 17.10.2023 r.

dr hab. AGNIESZKA GAJEWICZ-SKRĘTNA
Uniwersytet Gdański, Wydział Chemii
Katedra Chemii i Radiochemii Środowiska
Pracownia Chemoinformatyki Środowiska

Oświadczenie o udziale w publikacji

Oświadczam, że mój indywidualny wkład w publikację stanowiącą część rozprawy doktorskiej mgr inż. Anny Grzegórskiej:

> *A. Grzegórska, A. Gajewicz-Skrętna, G. Trykowski, K. Sikora, A. Zielińska-Jurek, Design and synthesis of TiO_2/Ti_3C_2 composites for highly efficient photocatalytic removal of acetaminophen: The relationships between synthesis parameters, physicochemical properties, and photocatalytic activity. Catal. Today 413-415 (2023) 113980.*

obejmował opracowanie koncepcji badań w zakresie badań komputerowych, w tym: dobór metodyki; wykonanie analiz chemometrycznych i modelowania *in silico*; interpretację uzyskanych wyników, napisanie wybranych fragmentów manuskryptu; przygotowanie rysunków: 2, 3S i 4S; korektę manuskryptu po recenzjach.

Agnieszka Gajewicz-Skrętna

Uniwersytet Gdański, Wydział Chemii,
Katedra Chemii i Radiochemii Środowiska
Pracownia Chemoinformatyki Środowiska
ul. Wita Stwosza 63
80-308 Gdańsk

e-mail: agnieszka.gajewiczi@ug.edu.pl

www.ug.edu.pl

CHEMIA UG

Wrocław, 19.10.2023

dr Paweł Głuchowski
Instytut Niskich Temperatur i Badań Strukturalnych
im. Włodzimierza Trzebiatowskiego
Polskiej Akademii Nauk
ul. Okólna 2
50-422 Wrocław
p.gluchowski@intibs.pl

Oświadczenie o udziale w publikacjach

Oświadczam, że mój indywidualny wkład w publikacje stanowiące część rozprawy doktorskiej mgr inż. Anny Grzegórskiej:

1. A. Grzegórska, I. Wysocka, P. Głuchowski, J. Ryl, J. Karczewski, A. Zielińska-Jurek, Novel composite of Zn/Ti-layered double hydroxide coupled with MXene for the efficient photocatalytic degradation of pharmaceuticals, Chemosphere 308 (2022) 136191.

obejmował wykonanie pomiarów fotoluminescencji, wyznaczenie czasu życia nośników ładunku dla fotokatalizatorów, przygotowanie rysunku 3 a-b, analizę i opis uzyskanych wyników;

2. A. Grzegórska, P. Głuchowski, J. Karczewski, J. Ryl, I. Wysocka, K. Siuzdak, G. Trykowski, K. Grochowska, A. Zielińska-Jurek, Enhanced photocatalytic activity of accordion-like layered Ti_3C_2 (MXene) coupled with Fe-modified decahedral anatase particles exposing {1 0 1} and {0 0 1} facets, Chem. Eng. J. 426 (2021) 130801.

obejmował wykonanie pomiarów fotoluminescencji, wyznaczenie czasu życia nośników ładunku dla fotokatalizatorów, przygotowanie rysunków 10 i 11, analizę i opis uzyskanych wyników.

Paweł Głuchowski
dr Paweł Głuchowski

upna
Universidad Pública de Navarra
Nafarroako Unibertsitate Publikoa

Pamplona, 20 October 2023

Prof. Cristina Gómez-Polo
Departamento de Ciencias-INAMAT[2]
Universidad Pública de Navarra
Campus de Arrosadia
31006 Pamplona, Spain
gpolo@unavarra.es

Statement of contribution

I declare that I have contributed to the publication, which constitues a part of the PhD dissertation of M.Sc. Eng Anna Grzegórska:

1. A. Grzegórska, J. Chibueze Ofoegbu, L. Cervera-Gabalda, C. Gómez-Polo, D. Sannino, A. Zielińska-Jurek, Magnetically recyclable TiO_2/MXene/$MnFe_2O_4$ photocatalyst for enhanced peroxymonosulphate-assisted photocatalytic degradation of carbamazepine and ibuprofen under simulated solar light. J. Environ. Chem. Eng. 11 (2023) 110660.

In the above study, I supervised magnetic properties measurements of the photocatalysts, analyzed and described the results.

Prof. Cristina Gomez Polo

Gdańsk, 20.10.2023

dr hab. Katarzyna Grochowska
Pracownia Materiałów Funkcjonalnych
INSTYTUT MASZYN PRZEPŁYWOWYCH
im. Roberta Szewalskiego
POLSKIEJ AKADEMII NAUK
ul. Fiszera 14
80-231 Gdańsk
kgrochowska@imp.gda.pl

Oświadczenie o udziale w publikacji

Oświadczam, że mój indywidualny wkład w publikację stanowiącą część rozprawy doktorskiej mgr inż. Anny Grzegórskiej:

1. A. Grzegórska, P. Głuchowski, J. Karczewski, J. Ryl, I. Wysocka, K. Siuzdak, G. Trykowski, K. Grochowska, A. Zielińska-Jurek, Enhanced photocatalytic activity of accordion-like layered Ti_3C_2 (MXene) coupled with Fe-modified decahedral anatase particles exposing {1 0 1} and {0 0 1} facets, Chem. Eng. J. 426 (2021) 130801.

obejmował osadzenia żelaza na próbkach fotokatalizatorów z wykorzystaniem systemu napylania magnetronowego.

dr hab. Katarzyna Grochowska

POLITECHNIKA GDAŃSKA

WYDZIAŁ CHEMICZNY

Gdańsk, 17.10.2023

mgr inż. Anna Grzegórska
Katedra Inżynierii Procesowej i Technologii Chemicznej
Wydział Chemiczny
Politechnika Gdańska
ul. Narutowicza 11/12
80-233 Gdańsk
anna.grzegorska@pg.edu.pl

Oświadczenie o udziale w publikacjach

Oświadczam, że mój indywidualny wkład w publikacje stanowiące część rozprawy doktorskiej mgr inż. Anny Grzegórskiej:

1. A. Grzegórska, I. Wysocka, P. Głuchowski, J. Ryl, J. Karczewski, A. Zielińska-Jurek, Novel composite of Zn/Ti-layered double hydroxide coupled with MXene for the efficient photocatalytic degradation of pharmaceuticals, Chemosphere 308 (2022) 136191.
2. A. Grzegórska, P. Głuchowski, J. Karczewski, J. Ryl, I. Wysocka, K. Siuzdak, G. Trykowski, K. Grochowska, A. Zielińska-Jurek, Enhanced photocatalytic activity of accordion-like layered Ti_3C_2 (MXene) coupled with Fe-modified decahedral anatase particles exposing {1 0 1} and {0 0 1} facets, Chem. Eng. J. 426 (2021) 130801.
3. A. Grzegórska, A. Gajewicz-Skrętna, G. Trykowski, K. Sikora, A. Zielińska-Jurek, Design and synthesis of TiO_2/Ti_3C_2 composites for highly efficient photocatalytic removal of acetaminophen: The relationships between synthesis parameters, physicochemical properties, and photocatalytic activity. Catal. Today 413-415 (2023) 113980.
4. A. Grzegórska, J. Chibueze Ofoegbu, L. Cervera-Gabalda, C. Gómez-Polo, D. Sannino, A. Zielińska-Jurek, Magnetically recyclable $TiO_2/MXene/MnFe_2O_4$ photocatalyst for enhanced peroxymonosulphate-assisted photocatalytic degradation of carbamazepine and ibuprofen under simulated solar light. J. Environ. Chem. Eng. 11 (2023) 110660.
5. A. Grzegórska, J. Karczewski, A. Zielińska-Jurek, Modelling and optimisation of MXene-derived TiO_2/Ti_3C_2 synthesis parameters using Response Surface Methodology based on the Box–Behnken factorial design. Enhanced carbamazepine degradation by the Cu-modified TiO_2/Ti_3C_2 photocatalyst, Process Saf. Environ. Prot. 179 (2023) 449.

obejmował przegląd literatury dotyczącej tematyki badań; syntezę i charakterystykę fotokatalizatorów; badanie aktywności fotokatalitycznej materiałów; analizę, interpretację i opis uzyskanych wyników; przygotowanie manuskryptów, oraz korektę manuskryptów po recenzjach.

Anna Grzegórska

mgr inż. Anna Grzegórska

POLITECHNIKA GDAŃSKA

WYDZIAŁ FIZYKI TECHNICZNEJ I MATEMATYKI STOSOWANEJ

Gdańsk, 17.10.2023

dr hab. inż. Jakub Karczewski, prof. PG
Instytut Nanotechnologii i Inżynierii Materiałowej
Wydział Fizyki Technicznej i Matematyki Stosowanej
Politechnika Gdańska
ul. Narutowicza 11/12
80-233 Gdańsk
jakub.karczewski@pg.edu.pl

Oświadczenie o udziale w publikacjach

Oświadczam, że mój indywidualny wkład w publikacje stanowiące część rozprawy doktorskiej mgr inż. Anny Grzegórskiej:

1. A. Grzegórska, I. Wysocka, P. Głuchowski, J. Ryl, J. Karczewski, A. Zielińska-Jurek, Novel composite of Zn/Ti-layered double hydroxide coupled with MXene for the efficient photocatalytic degradation of pharmaceuticals, Chemosphere 308 (2022) 136191.

2. A. Grzegórska, P. Głuchowski, J. Karczewski, J. Ryl, I. Wysocka, K. Siuzdak, G. Trykowski, K. Grochowska, A. Zielińska-Jurek, Enhanced photocatalytic activity of accordion-like layered Ti_3C_2 (MXene) coupled with Fe-modified decahedral anatase particles exposing {1 0 1} and {0 0 1} facets, Chem. Eng. J. 426 (2021) 130801.

3. A. Grzegórska, J. Karczewski, A. Zielińska-Jurek, Modelling and optimisation of MXene-derived TiO_2/Ti_3C_2 synthesis parameters using Response Surface Methodology based on the Box–Behnken factorial design. Enhanced carbamazepine degradation by the Cu-modified TiO_2/Ti_3C_2 photocatalyst, Process Saf. Environ. Prot. 179 (2023) 449.

obejmował wykonanie analiz fotokatalizatorów za pomocą skaningowego mikroskopu elektronowego (SEM).

.....

dr hab. inż. Jakub Karczewski, prof. PG

Fisciano, 18 October 2023

Prof. Diana Sannino
Department of Industrial Engineering
University of Salerno
via Giovanni Paolo II 132
84084 Fisciano, Italy
dsannino@unisa.it

Statement of contribution

I declare that I have contributed to the publication, which constitues a part of the PhD dissertation of M.Sc. Eng. Anna Grzegórska:

1. A. Grzegórska, J. Chibueze Ofoegbu, L. Cervera-Gabalda, C. Gómez-Polo, D. Sannino, A. Zielińska-Jurek, Magnetically recyclable TiO_2/MXene/$MnFe_2O_4$ photocatalyst for enhanced peroxymonosulphate-assisted photocatalytic degradation of carbamazepine and ibuprofen under simulated solar light. J. Environ. Chem. Eng. 11 (2023) 110660.

In the above study, I have made corrections in the manuscript.

Diana Sannino
.....
Prof. Diana Sannino

Gdańsk,18.10.2023

dr Karol Sikora
Katedra i Zakład Chemii Nieorganicznej
Wydział Farmaceutyczny
Gdański Uniwersytet Medyczny
Aleja Generała Józefa Hallera 107
80-416 Gdańsk
karol.sikora@gumed.edu.pl

Oświadczenie o udziale w publikacji

Oświadczam, że mój indywidualny wkład w publikację stanowiącą część rozprawy doktorskiej mgr inż. Anny Grzegórskiej:

1. A. Grzegórska, A. Gajewicz-Skrętna, G. Trykowski, K. Sikora, A. Zielińska-Jurek, Design and synthesis of TiO_2/Ti_3C_2 composites for highly efficient photocatalytic removal of acetaminophen: The relationships between synthesis parameters, physicochemical properties, and photocatalytic activity. Catal. Today 413-415 (2023) 113980.

obejmował wykonanie analiz produktów degradacji acetaminofenu za pomocą LC-MS.

Katedra i Zakład Chemii Nieorganicznej
Gdański Uniwersytet Medyczny
dr Karol Sikora
Adiunkt
dr Karol Sikora

Gdańsk, 19.10.2023

dr hab. inż. Katarzyna Siuzdak, Profesor IMP PAN
Pracownia Materiałów Funkcjonalnych
INSTYTUT MASZYN PRZEPŁYWOWYCH
im. Roberta Szewalskiego
POLSKIEJ AKADEMII NAUK
ul. Fiszera 14
80-231 Gdańsk
katarzyna.siuzdak@imp.gda.pl

Oświadczenie o udziale w publikacji

Oświadczam, że mój indywidualny wkład w publikację stanowiącą część rozprawy doktorskiej mgr inż. Anny Grzegórskiej:

1. A. Grzegórska, P. Głuchowski, J. Karczewski, J. Ryl, I. Wysocka, K. Siuzdak, G. Trykowski, K. Grochowska, A. Zielińska-Jurek, Enhanced photocatalytic activity of accordion-like layered Ti_3C_2 (MXene) coupled with Fe-modified decahedral anatase particles exposing {1 0 1} and {0 0 1} facets, Chem. Eng. J. 426 (2021) 130801.

wykonanie analizy fotokatalizatorów za pomocą spektroskopii Ramana wraz z przygotowaniem rysunku nr 8 i dyskusją uzyskanych wyników; analizy Motta-Schottky'ego wraz z przygotowaniem rysunku nr 12 oraz dyskusją uzyskanych wyników.

dr hab. inż. Katarzyna Siuzdak

POLITECHNIKA GDAŃSKA

WYDZIAŁ FIZYKI TECHNICZNEJ I MATEMATYKI STOSOWANEJ

Gdańsk, ... 17.10.2023

dr hab. inż. Jacek Ryl, prof. PG
Instytut Nanotechnologii i Inżynierii Materiałowej
Wydział Fizyki Technicznej i Matematyki Stosowanej
Politechnika Gdańska
ul. Narutowicza 11/12
80-233 Gdańsk
jacryl@pg.edu.pl

Oświadczenie o udziale w publikacjach

Oświadczam, że mój indywidualny wkład w publikacje stanowiące część rozprawy doktorskiej mgr inż. Anny Grzegórskiej:

1. A. Grzegórska, I. Wysocka, P. Głuchowski, J. Ryl, J. Karczewski, A. Zielińska-Jurek, Novel composite of Zn/Ti-layered double hydroxide coupled with MXene for the efficient photocatalytic degradation of pharmaceuticals, Chemosphere 308 (2022) 136191.

obejmował wykonanie pomiarów rentgenowskiej spektroskopii fotoelektronów (XPS) dla fotokatalizatorów;

2. A. Grzegórska, P. Głuchowski, J. Karczewski, J. Ryl, I. Wysocka, K. Siuzdak, G. Trykowski, K. Grochowska, A. Zielińska-Jurek, Enhanced photocatalytic activity of accordion-like layered Ti_3C_2 (MXene) coupled with Fe-modified decahedral anatase particles exposing {1 0 1} and {0 0 1} facets, Chem. Eng. J. 426 (2021) 130801.

obejmował wykonanie pomiarów elektrochemicznej spektroskopii impedancyjnej (EIS) i fotoprądów dla fotokatalizatorów.

.....

dr hab. inż. Jacek Ryl, prof. PG

UNIWERSYTET MIKOŁAJA KOPERNIKA W TORUNIU
Wydział Chemii

UCZELNIA BADAWCZA
INICJATYWA DOSKONAŁOŚCI

Toruń, 17 października 2023 r.

dr Grzegorz Trykowski
Katedra Chemii Materiałów, Adsorpcji i Katalizy
Wydział Chemii
Uniwersytet Mikołaja Kopernika w Toruniu
ul. Gagarina 7, 87-100 Toruń
tryki@umk.pl

Oświadczenie o udziale w publikacjach

Oświadczam, że mój indywidualny wkład w publikacje stanowiące część rozprawy doktorskiej mgr inż. Anny Grzegórskiej:

1. A. Grzegórska, P. Głuchowski, J. Karczewski, J. Ryl, I. Wysocka, K. Siuzdak, G. Trykowski, K. Grochowska, A. Zielińska-Jurek, Enhanced photocatalytic activity of accordion-like layered Ti3C2 (MXene) coupled with Fe-modified decahedral anatase particles exposing {1 0 1} and {0 0 1} facets, Chem. Eng. J. 426 (2021) 130801.

obejmował wykonanie analiz fotokatalizatorów za pomocą transmisyjnego mikroskopu elektronowego (TEM), analiz termograwimetrycznych (TGA) i spektroskopii fourierowskiej w podczerwieni (FTIR);

2. A. Grzegórska, A. Gajewicz-Skrętna, G. Trykowski, K. Sikora, A. Zielińska-Jurek, Design and synthesis of TiO2/Ti3C2 composites for highly efficient photocatalytic removal of acetaminophen: The relationships between synthesis parameters, physicochemical properties, and photocatalytic activity. Catal. Today 413-415 (2023) 113980.

obejmował wykonanie analiz fotokatalizatorów za pomocą transmisyjnego mikroskopu elektronowego (TEM) i skaningowego mikroskopu elektronowego (SEM), oraz analizy elementarnej (CHN).

Grzegorz Trykowski

dr Grzegorz Trykowski

POLITECHNIKA GDAŃSKA

WYDZIAŁ CHEMICZNY

Gdańsk, 17.10.2023

dr inż. Izabela Wysocka
Katedra Inżynierii Procesowej i Technologii Chemicznej
Wydział Chemiczny
Politechnika Gdańska
ul. Narutowicza 11/12
80-233 Gdańsk
izabela.wysocka@pg.edu.pl

Oświadczenie o udziale w publikacjach

Oświadczam, że mój indywidualny wkład w publikacje stanowiące część rozprawy doktorskiej mgr inż. Anny Grzegórskiej:

1. A. Grzegórska, I. Wysocka, P. Głuchowski, J. Ryl, J. Karczewski, A. Zielińska-Jurek, Novel composite of Zn/Ti-layered double hydroxide coupled with MXene for the efficient photocatalytic degradation of pharmaceuticals, Chemosphere 308 (2022) 136191.

2. A. Grzegórska, P. Głuchowski, J. Karczewski, J. Ryl, I. Wysocka, K. Siuzdak, G. Trykowski, K. Grochowska, A. Zielińska-Jurek, Enhanced photocatalytic activity of accordion-like layered Ti_3C_2 (MXene) coupled with Fe-modified decahedral anatase particles exposing {1 0 1} and {0 0 1} facets, Chem. Eng. J. 426 (2021) 130801.

obejmował udział w dyskusji i opisie wyników.

Izabela Wysocka

dr inż. Izabela Wysocka

POLITECHNIKA GDAŃSKA

WYDZIAŁ CHEMICZNY

Gdańsk, 17.10.2023

dr hab. inż. Anna Zielińska-Jurek, prof. PG
Katedra Inżynierii Procesowej i Technologii Chemicznej
Wydział Chemiczny
Politechnika Gdańska
ul. Narutowicza 11/12
80-233 Gdańsk
annjurek@pg.edu.pl

Oświadczenie o udziale w publikacjach

Oświadczam, że mój indywidualny wkład w publikacje stanowiące część rozprawy doktorskiej mgr inż. Anny Grzegórskiej:

1. A. Grzegórska, I. Wysocka, P. Głuchowski, J. Ryl, J. Karczewski, A. Zielińska-Jurek, Novel composite of Zn/Ti-layered double hydroxide coupled with MXene for the efficient photocatalytic degradation of pharmaceuticals, Chemosphere 308 (2022) 136191.
2. A. Grzegórska, P. Głuchowski, J. Karczewski, J. Ryl, I. Wysocka, K. Siuzdak, G. Trykowski, K. Grochowska, A. Zielińska-Jurek, Enhanced photocatalytic activity of accordion-like layered Ti_3C_2 (MXene) coupled with Fe-modified decahedral anatase particles exposing {1 0 1} and {0 0 1} facets, Chem. Eng. J. 426 (2021) 130801.
3. A. Grzegórska, A. Gajewicz-Skrętna, G. Trykowski, K. Sikora, A. Zielińska-Jurek, Design and synthesis of TiO_2/Ti_3C_2 composites for highly efficient photocatalytic removal of acetaminophen: The relationships between synthesis parameters, physicochemical properties, and photocatalytic activity. Catal. Today 413-415 (2023) 113980.
4. A. Grzegórska, J. Chibueze Ofoegbu, L. Cervera-Gabalda, C. Gómez-Polo, D. Sannino, A. Zielińska-Jurek, Magnetically recyclable TiO_2/MXene/$MnFe_2O_4$ photocatalyst for enhanced peroxymonosulphate-assisted photocatalytic degradation of carbamazepine and ibuprofen under simulated solar light. J. Environ. Chem. Eng. 11 (2023) 110660.
5. A. Grzegórska, J. Karczewski, A. Zielińska-Jurek, Modelling and optimisation of MXene-derived TiO_2/Ti_3C_2 synthesis parameters using Response Surface Methodology based on the Box–Behnken factorial design. Enhanced carbamazepine degradation by the Cu-modified TiO_2/Ti_3C_2 photocatalyst, Process Saf. Environ. Prot. 179 (2023) 449.

obejmował zainicjowanie tematyki badawczej, opracowanie koncepcji i metodyki badań, koordynację prac badawczych, dyskusję wyników, redagowanie publikacji oraz pozyskanie funduszy na badania.

Anna Zielińska-Jurek

dr hab. inż. Anna Zielińska-Jurek, prof. PG